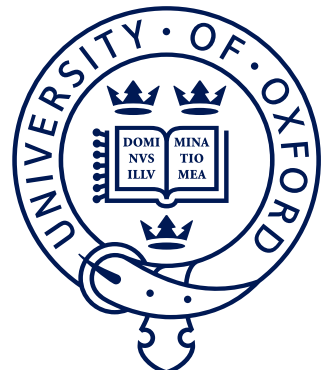


<sup>1</sup> **CP violation in  $B^\pm \rightarrow Dh^\pm$  decays**  
<sup>2</sup> **where  $D \rightarrow K_S^0 h'^+ h'^-$**

<sup>3</sup> *A measurement of the CKM angle  $\gamma$  at LHCb and understanding  
<sup>4</sup> the impact of neutral kaon CP violation*



<sup>6</sup> Mikkel Bjørn  
<sup>7</sup> St. Anne's College  
<sup>8</sup> University of Oxford

<sup>9</sup> A thesis submitted for the degree of  
<sup>10</sup> *Doctor of Philosophy*  
<sup>11</sup> Trinity 2020

<sup>12</sup>

## Acknowledgements

<sup>13</sup> suitable thank you's

# Abstract

14

<sup>15</sup> World's best measurement of  $\gamma$ . Details to be added.

# Contents

16

17	Preface	vii
18	1 Introduction	1
19	1.1 Structure of the thesis . . . . .	1
20	2 Theoretical background	2
21	2.1 The C, P and T symmetries and their violation . . . . .	2
22	2.2 CP violation in the Standard Model . . . . .	4
23	2.2.1 The CKM matrix and the Unitarity Triangle . . . . .	4
24	2.2.2 Measuring $\gamma$ in tree level decays . . . . .	9
25	2.3 Measuring $\gamma$ using multi-body D final states . . . . .	12
26	2.3.1 Dalitz plots and the phase space of multi-body decays . . . . .	12
27	2.3.2 The GGSZ method to measure $\gamma$ . . . . .	14
28	2.3.3 A model-independent approach . . . . .	16
29	2.3.4 Measuring strong-phase inputs at charm factories . . . . .	18
30	2.3.5 Global CP asymmetry and the relation to GLW and ADS measurements . . . . .	22
31	2.4 Strategy for the LHCb measurement . . . . .	26
33	3 The LHCb experiment	29
34	3.1 Subdetectors . . . . .	29
35	3.1.1 The VELO . . . . .	29
36	3.1.2 Magnet and tracking stations . . . . .	29
37	3.1.3 The RICH . . . . .	29
38	3.1.4 Calorimeters . . . . .	29
39	3.1.5 Muon detectors . . . . .	29
40	3.2 Track reconstruction . . . . .	29
41	3.3 The LHCb triggering system . . . . .	29
42	3.3.1 The level-0 hardware trigger . . . . .	29
43	3.3.2 High-level triggers . . . . .	29
44	3.3.3 Offline data filtering: the LHCb stripping . . . . .	29
45	3.4 Simulation . . . . .	29

<sup>46</sup>	<b>4 Neutral kaon <math>CP</math> violation and material</b>	
<sup>47</sup>	<b>interaction in BPGGSZ measurements</b>	<b>31</b>
<sup>48</sup>	4.1 $CP$ violation and material interaction of neutral kaons . . . . .	31
<sup>49</sup>	4.1.1 A first look at the impact on $\gamma$ measurements . . . . .	35
<sup>50</sup>	4.2 Impact on BPGGSZ measurements of $\gamma$ :	
<sup>51</sup>	principles . . . . .	37
<sup>52</sup>	4.2.1 Modified symmetry relations . . . . .	37
<sup>53</sup>	4.2.2 Relationship between the $K_S^0$ and $K_L^0$ amplitudes . . . . .	38
<sup>54</sup>	4.2.3 Modification of the BPGGSZ yield equations . . . . .	39
<sup>55</sup>	4.3 Impact on BPGGSZ measurements of $\gamma$ :	
<sup>56</sup>	LHCb and Belle II measurements . . . . .	42
<sup>57</sup>	4.3.1 Detector geometries . . . . .	43
<sup>58</sup>	4.3.2 Kaon momentum distributions . . . . .	44
<sup>59</sup>	4.3.3 Experimental time acceptance . . . . .	45
<sup>60</sup>	4.3.4 Detector material budget . . . . .	46
<sup>61</sup>	4.3.5 Calculation procedure . . . . .	48
<sup>62</sup>	4.3.6 Results . . . . .	49
<sup>63</sup>	4.3.7 Coupled $B^\pm \rightarrow DK^\pm$ and $B^\pm \rightarrow D\pi^\pm$ measurements . . . . .	51
<sup>64</sup>	4.4 Concluding remarks . . . . .	52
<sup>65</sup>	<b>5 A BPGGSZ measurement of <math>\gamma</math> with <math>B^\pm \rightarrow Dh^\pm</math> decays</b>	<b>54</b>
<sup>66</sup>	5.1 Candidate reconstruction and selection . . . . .	54
<sup>67</sup>	5.1.1 Initial requirements . . . . .	55
<sup>68</sup>	5.1.2 Boosted decision tree . . . . .	57
<sup>69</sup>	5.1.3 Particle-identification requirements . . . . .	62
<sup>70</sup>	5.1.4 Final requirements . . . . .	63
<sup>71</sup>	5.1.5 Selected candidates . . . . .	63
<sup>72</sup>	5.2 Signal selection efficiencies . . . . .	64
<sup>73</sup>	5.2.1 Efficiency of the PID requirements . . . . .	66
<sup>74</sup>	5.2.2 Efficiency profile over the Dalitz plot . . . . .	67
<sup>75</sup>	5.3 Background studies . . . . .	69
<sup>76</sup>	5.3.1 Charmless decays . . . . .	69
<sup>77</sup>	5.3.2 Background from four-body $D$ decays . . . . .	71
<sup>78</sup>	5.3.3 Semi-leptonic backgrounds . . . . .	73
<sup>79</sup>	5.3.4 Cross-feed from other $D \rightarrow K_S^0 h^+ h^-$ decays . . . . .	79
<sup>80</sup>	5.3.5 Swapped-track backgrounds . . . . .	79
<sup>81</sup>	5.4 Signal and background mass shapes . . . . .	81
<sup>82</sup>	5.4.1 Signal decays . . . . .	82
<sup>83</sup>	5.4.2 Cross-feed between $B^\pm \rightarrow Dh^\pm$ channels . . . . .	84

84	5.4.3	Partially reconstructed backgrounds . . . . .	86
85	5.4.4	Combinatorial background . . . . .	91
86	5.4.5	Fit results . . . . .	93
87	5.5	Measurement of the CP-violation observables . . . . .	94
88	5.5.1	Fit setup . . . . .	95
89	5.5.2	Main results . . . . .	98
90	5.5.3	Cross checks . . . . .	99
91	5.6	Systematic uncertainties . . . . .	109
92	5.6.1	Strong phase uncertainties . . . . .	109
93	5.6.2	Efficiency-profile-related systematic uncertainties . . . . .	110
94	5.6.3	Mass shapes . . . . .	113
95	5.6.4	$CP$ violation and material interaction of the $K_S^0$ . . . . .	118
96	5.6.5	Impact of $D$ mixing . . . . .	119
97	5.6.6	PID efficiencies . . . . .	119
98	5.6.7	Dalitz-coordinate resolution . . . . .	119
99	5.6.8	The fixed yield fractions . . . . .	120
100	5.6.9	Systematic uncertainty due to backgrounds that are not modelled in fit . . . . .	121
101	5.6.10	Bias correction . . . . .	123
102	5.6.11	Charmless backgrounds . . . . .	123
103	5.6.12	Summary of systematic uncertainties . . . . .	124
104	5.7	Obtained constraints on $\gamma$ . . . . .	125
105	5.7.1	Statistical approach . . . . .	126
106	5.7.2	Interpretation results . . . . .	128
107	5.7.3	Compatibility with other measurements . . . . .	129
109	<b>6</b>	<b>Conclusions</b>	<b>138</b>
110	<b>Appendices</b>		
111	<b>A</b>	<b>Projections of main fit to data</b>	<b>140</b>

# Preface

112

113 The work presented in this thesis has been resulted in two papers, either under  
114 review or published in the Journal of High Energy Physics. These are

115 [?] *Measurement of the CKM angle  $\gamma$  using  $B^\pm \rightarrow [K_S^0 h^+ h^-]_D h^\pm$  decays,*

116 submitted to JHEP.

117 This paper describes a measurement of the CKM angle  $\gamma$  using  $pp$  collision  
118 data taken with the LHCb experiment during the Run 1 of the LHC, in 2011  
119 and 2012, and during the full Run 2, in 2015–2018. The measurement uses the  
120 decay channels  $B^\pm \rightarrow D h^\pm$  where  $D \rightarrow K_S^0 h'^+ h'^-$ , in which  $h$  and  $h'$  denotes  
121 pions or kaons. It obtains a value of  $\gamma = (? \pm ?)^\circ$ , which constitutes the world’s  
122 best single-measurement determination of  $\gamma$ . The work is the main focus of  
123 this thesis and described in detail in Chapter 5.

124 [?] *CP violation and material interaction of neutral kaons in measurements*  
125 *of the CKM angle  $\gamma$  using  $B^\pm \rightarrow D K^\pm$  decays where  $D \rightarrow K_S^0 \pi^+ \pi^-$* , JHEP  
126 19 (2020) 106.

127 This paper describes a phenomenological study of the impact of neutral  
128 kaon  $CP$  violation and material interaction on measurements of  $\gamma$ . With the  
129 increased measurement precision to come in the near future, an understanding  
130 of these effects is crucial, especially in the context of  $B \rightarrow D\pi$  decays; however  
131 no detailed study had been published at the start of this thesis. The study is  
132 the subject of Chapter 4. Some text excerpts and figures from the paper have  
133 been reproduced in the thesis.

134 All of the work described in this thesis is my own, except where clearly referenced  
135 to others. Furthermore, I contributed significantly to an analysis of  $B^\pm \rightarrow D K^\pm$   
136 decays with LHCb data taken in 2015 and 2016, now published in

137 [?] *Measurement of the CKM angle  $\gamma$  using  $B^\pm \rightarrow D K^\pm$  with  $D \rightarrow K_S^0 \pi^+ \pi^-$*   
138  *$K_S^0 K^+ K^-$  decays*, JHEP 08 (2018) 176.

139 I was responsible for the analysis of the signal channel, whereas the control channel  
140 was analysed by Nathan Jurik. The measurement is superseded by that of Ref. [?]  
141 and is not described in detail in the thesis.

# 1

<sup>142</sup>

<sup>143</sup>

## Introduction

<sup>144</sup> All the big picture stuff: constraints on New Physics from high precision measurements, a small nod to matter-antimatter asymmetry questions etc.

<sup>146</sup> Do mention the Belle [?] and BaBar [?] combinations of  $\gamma$  measurements,  
<sup>147</sup> including which decay channels they include (maybe).

### <sup>148</sup> 1.1 Structure of the thesis

# 2

149

150

## Theoretical background

151 This chapter lays out the theoretical framework of the thesis. Section 2.1 introduces  
152 charge and parity symmetry violation in general, while Section 2.2 covers the  
153 description in the Standard Model and the general theory behind charge-parity  
154 symmetry violation measurements in charged  $B$  decays. Section 2.3 focuses on  
155 the theory of measurements using  $B^\pm \rightarrow Dh^\pm$  decays with multi-body  $D$  final  
156 states, after which the specific analysis strategy for the measurement described  
157 in the thesis is outlined out in Section 2.4.

### 158 2.1 The C, P and T symmetries and their vio- 159 lation

160 The concept of symmetry play a fundamental role in modern physics. By Noether's  
161 theorem [?], the simple assumption of invariance of our physical laws under universal  
162 temporal and spatial translations leads to the very non-trivial prediction of conserved  
163 energy and momentum; within the field of particle physics, the interactions and  
164 dynamics of the Standard Model (SM) follow completely simply from requiring  
165 the fundamental particle fields to satisfy a local  $U(1) \times SU(2) \times SU(3)$  gauge  
166 symmetry [?]; and one of the short-comings of the SM, is that it fails to explain  
167 the apparent *lack* of symmetry in our matter-dominated universe [?]. Indeed, it is  
168 important to experimentally establish the symmetries of our world at a fundamental  
169 level, and the degree to which they are broken.

170 Three discrete symmetries of importance are the symmetries under

I'll  
adjust  
this para-  
graph  
when  
I've  
written  
the intro-  
duction.

- 171     1. The charge operator  $C$ , which conjugates all internal quantum numbers of a  
 172       quantum state and thus converts particles into their anti-particle counter parts.  
 173       For example,  $C$  transforms the electric charge of a particle state  $Q \rightarrow -Q$ .
- 174     2. The parity operator  $P$ , which inverts the spatial dimensions of space time:  
 175        $\vec{x} \rightarrow -\vec{x}$ . As such, it transforms left-handed particle fields into right-handed  
 176       particle fields and vice versa.
- 177     3. The time-inversion operator  $T$ , which inverts the temporal dimension of space  
 178       time:  $t \rightarrow -t$ .

179     These are fundamentally related by the *CPT* theorem [?], which states that any  
 180       Lorentz-invariant Quantum Field Theory (QFT) must be symmetric under the  
 181       simultaneous application of *all* three operators. However, any one of the symmetries  
 182       can be broken individually, and experiments have shown the physical laws of our  
 183       world to violate each of the  $C$ ,  $P$ , and  $T$  symmetries.

184     Such a symmetry-breaking effect was established for the first time in 1956, when  
 185       Chien-Shiung Wu observed parity violation in weak decays of Co-60 nuclei [?], after  
 186       carrying out an experiment that was proposed by Yang Chen-Ning and Tsung-Dao  
 187       Lee [?]. While this experiment established the breaking of  $P$  symmetry, it left open  
 188       the possibility that the physical laws are invariant under a combination of a charge-  
 189       and parity inversion; that they are  $CP$  symmetric. However, this was disproved in  
 190       1964 when Kronin and Fitch observed that long-lived kaons, which predominantly  
 191       decay to the  $CP$ -odd  $3\pi$  state, could also decay to the  $CP$ -even  $\pi\pi$  states [?].

192     Since then  $CP$  violation has been found in the  $B^0$  system by the BaBar and Belle  
 193       collaborations [?, ?] during the early 2000's; the  $B$  factories, along with CDF, also saw  
 194       evidence for  $CP$  violation in  $B^\pm$  decays [?, ?, ?, ?, ?, ?, ?] later confirmed by LHCb [?],  
 195       and  $CP$  violation was measured for the  $B_s^0$  meson by LHCb in 2013 [?]; within the  
 196       last year and a half, the first observation of  $CP$ -violation in  $D^0$  decays has also been  
 197       made by the LHCb collaboration [?], and most recently evidence for  $CP$ -violation in  
 198       the neutrino sector has been reported by the T2K collaboration [?]. The observed  
 199       effects can be divided into distinct classes. The conceptually simplest case is

- 200     1.  *$CP$ -violation in decay*, where  $|A/\bar{A}| \neq 1$  for some decay amplitude  $A$ , and the  
 201       amplitude  $\bar{A}$  of the  $CP$ -conjugate decay. The result is different decay rates in  
 202       two  $CP$ -conjugate decays

$$\Gamma(M \rightarrow f) \neq \Gamma(\bar{M} \rightarrow \bar{f}). \quad (2.1)$$

203     This type of  $CP$  violation was not seen until the late 1980ies [?, ?], more than  
 204       20 years after the first observation of  $CP$  violation, and only finally established  
 205       around the year 2000 [?, ?]. Also this discovery was made in  $K \rightarrow \pi\pi$  decays.

206  $CP$ -violation in decay is the only type possible for charged initial states, and  
207 it is thus the main focus of the thesis. Two additional  $CP$ -violating effect are  
208 possible for neutral initial states (a situation that will be the main focus of  
209 Chapter 4). These effects are

210 2.  *$CP$ -violation in mixing*, which denotes the case where the mixing rates between  
211 the  $M^0$  and  $\bar{M}^0$  states differ

$$\Gamma(M^0 \rightarrow \bar{M}^0) \neq \Gamma(\bar{M}^0 \rightarrow M^0). \quad (2.2)$$

212 The  $CP$  violation first observed by Kronin and Fitch in the neutral kaon  
213 sector [?] is (dominantly) of this type.

214 3.  *$CP$ -violation in interference between mixing and decay*, which can be present  
215 for a neutral initial states  $M^0$  decaying into a final state  $f$  common to both  
216  $M^0$  and  $\bar{M}^0$ . The decay rate includes an interference term between two  
217 amplitudes: the amplitude for a direct  $M^0 \rightarrow f$  decay and the amplitude  
218 for a decay after mixing:  $M^0 \rightarrow \bar{M}^0 \rightarrow f$ . Even in the absence of the two  
219 aforementioned effects, the rates  $\Gamma(M^0 \rightarrow f)$  and  $\Gamma(\bar{M}^0 \rightarrow \bar{f})$  can differ due  
220 to the interference term. Such  $CP$  asymmetries have been measured in eg.  
221  $B^0 \rightarrow J/\psi K$  by LHCb and the  $B$  factories, and in  $B_s^0 \rightarrow J/\psi \phi$  decays by the  
222 LHC and Tevatron experiments [?].

223  $CP$  violation measurements thus have a long, rich, and still-developing history.

## 224 2.2 **CP violation in the Standard Model**

225 All existing measurements of  $CP$  violation in the quark sector are naturally explained  
226 in the SM; indeed, the need to explain the observation  $CP$  violation in neutral  
227 kaons was a driving force in the development of the model in the first place, when  
228 it lead Kobayashi and Maskawa to predict the existence of then-unknown particles  
229 in 1973 [?] (now known to be the third generation quarks).

### 230 2.2.1 **The CKM matrix and the Unitarity Triangle**

231 The SM contains three generations of quarks, each consisting of an up-type quark ( $u$ ,  
232  $c$ , and  $t$ ) and a down-type quark ( $d$ ,  $s$ , and  $b$ ). The charged weak interaction of the  
233  $W^\pm$  boson couples up and down-type quarks. The quark states that couple to the  $W$   
234 are not (a priori) identical to the mass eigenstates, and can be denoted ( $u'$ ,  $c'$ , and  $t'$ )  
235 and ( $d'$ ,  $s'$ , and  $b'$ ). A basis for the quark states can be chosen such that the weakly

<sup>236</sup> coupling up-quark states are identical to the propagating quark states,  $u = u'$ , but  
<sup>237</sup> then the down-type quark state are different:  $d' \neq d$ . The two bases of the down-type  
<sup>238</sup> quarks are related via the Cabibbo-Kobayashi-Maskawa (CKM) matrix [?, ?]<sup>1</sup>

$$\begin{pmatrix} d' \\ s' \\ t' \end{pmatrix} = V \begin{pmatrix} d \\ s \\ t \end{pmatrix} = \begin{pmatrix} V_{ud} & V_{us} & V_{ub} \\ V_{cd} & V_{cs} & V_{cb} \\ V_{td} & V_{ts} & V_{tb} \end{pmatrix} \begin{pmatrix} d \\ s \\ t \end{pmatrix}. \quad (2.3)$$

<sup>239</sup> Thus the Lagrangian terms representing the coupling of a  $W^\pm$  boson with a  $u$ -  
<sup>240</sup> and a  $d$ -type quark is

$$\mathcal{L}_{W^+} = -\frac{g}{\sqrt{2}} V_{ud} (\bar{u} \gamma^\mu W_\mu^+ d) \quad \mathcal{L}_{W^-} = -\frac{g}{\sqrt{2}} V_{ud}^* (\bar{d} \gamma^\mu W_\mu^- u) \quad (2.4)$$

<sup>241</sup> where  $g$  is the weak coupling constant,  $\gamma_u$  are the Dirac matrices, and  $u$  and  $d$   
<sup>242</sup> represent the left-handed components of the physical quark states.

<sup>243</sup> The CKM matrix is a unitary complex  $3 \times 3$  matrix, and hence has  $3^2 = 9$   
<sup>244</sup> independent, real parameters. However, 5 of these can be absorbed into non-physical  
<sup>245</sup> phases of the quark states (both mass and weak eigenstates) and hence the matrix  
<sup>246</sup> has 4 real, physical parameters: 3 mixing angles and a single phase. Chau and  
<sup>247</sup> Keung [?] proposed the parameterisation

$$\begin{aligned} V &= \begin{pmatrix} 1 & 0 & 0 \\ 0 & c_{23} & s_{23} \\ 0 & -s_{23} & c_{23} \end{pmatrix} \begin{pmatrix} c_{13} & 0 & s_{13}e^{-i\delta_{CP}} \\ 0 & 1 & 0 \\ -s_{13}e^{-i\delta_{CP}} & 0 & c_{13} \end{pmatrix} \begin{pmatrix} c_{12} & s_{12} & 0 \\ -s_{12} & c_{12} & 1 \\ 0 & 0 & 1 \end{pmatrix} \\ &= \begin{pmatrix} c_{12}c_{13} & s_{12}c_{13} & s_{13}e^{-i\delta_{CP}} \\ -s_{12}c_{23} - c_{12}s_{23}s_{13}e^{i\delta_{CP}} & c_{12}c_{23} - s_{12}s_{23}s_{13}e^{i\delta_{CP}} & s_{23}c_{13} \\ s_{12}s_{23} - c_{12}c_{23}s_{13}e^{i\delta_{CP}} & -c_{12}s_{23} - s_{12}c_{23}s_{13}e^{i\delta_{CP}} & c_{23}c_{13} \end{pmatrix} \end{aligned} \quad (2.5)$$

<sup>248</sup> which is the preferred standard by the PDG [?]. Here,  $s_{ij} \equiv \sin \theta_{ij}$  and  $c_{ij} \equiv \cos \theta_{ij}$   
<sup>249</sup> denote the sine and cosine of three rotation angles in quark space;  $\theta_{12} = \theta_C$  being  
<sup>250</sup> the usual Cabibbo angle [?].

<sup>251</sup> The presence of the complex phase  $\delta_{CP}$  in the Lagrangian term of the  $W$  coupling  
<sup>252</sup> causes  $CP$  violation because, as evident from Eq. (2.4), if  $\delta_{CP}$  enters the amplitude  
<sup>253</sup> for some decay mediated by a  $W$  boson,  $A = |A|e^{i(\delta_0 + \delta_{CP})}$ , then it will enter the  
<sup>254</sup>  $CP$  conjugate decay amplitude with the opposite sign:  $\bar{A} = |A|e^{i(\delta_0 - \delta_{CP})}$ . In these  
<sup>255</sup> expressions,  $\delta_0$  denotes a  $CP$  conserving phase that is not caused by complex terms  
<sup>256</sup> in the Lagrangian, but arises due to potential intermediate states in the decay

---

<sup>1</sup> A basis for the quarks can of course be chosen, such that neither the up-quarks or the down-quarks are expressed in their mass eigenstates. In that case the CKM matrix is recovered as  $V = U_u^* U_d$ , where  $U_{u/d}$  is the unitary transformation matrices that brings the  $u/d$  quarks into their mass eigenstates.

amplitude.<sup>2</sup> Usually the underlying mechanism is due to QCD effects, and these  $CP$  conserving phases are therefore generally dubbed *strong* phases, as opposed to the  $CP$  violating *weak* phase of the  $W$  coupling [?]. This terminology will be applied throughout the thesis.

Experimentally, it has been observed that the CKM matrix elements of Eq. (2.5) satisfy  $s_{13} \ll s_{23} \ll s_{12}$ . This motivates an often used, alternative parameterisation of the matrix, where the elements are expressed as power series in a parameter  $\lambda$  that naturally incorporates this hierarchy: the Wolfenstein parameterisation [?].

The definitions

$$\begin{aligned} s_{12} &\equiv \lambda \\ s_{23} &\equiv \lambda^2 A \\ s_{13} &\equiv \lambda^3(\rho - i\eta) \end{aligned} \tag{2.6}$$

are made, after which the unitarity conditions (or Eq. 2.5) determine the remaining elements to any order in  $\lambda$ .<sup>3</sup> To  $\mathcal{O}(\lambda^5)$  the Wolfenstein parameterisation of the CKM matrix is [?, ?]

$$V = \begin{pmatrix} 1 - \frac{\lambda^2}{2} - \frac{\lambda^4}{8} & \lambda & A\lambda^3(\rho - i\eta) \\ -\lambda + \frac{\lambda^5}{2}A^2(1 - 2(\rho + i\eta)) & 1 - \frac{\lambda^2}{2} - \frac{\lambda^4}{8}(1 + 4A^2) & A\lambda^2 \\ A\lambda^3(1 - (\rho + i\eta)(1 - \frac{\lambda^2}{2})) & -A\lambda^2(1 - \frac{\lambda^2}{2}(1 - 2(\rho + i\eta))) & 1 - \frac{1}{2}A^2\lambda^4 \end{pmatrix}. \tag{2.7}$$

The unitarity condition  $V^\dagger V = \mathbb{1}$  of the CKM matrix defines 9 relations between the CKM elements of the form

$$\sum_j V_{jq}^* V_{jq} = 1 \quad , \quad q \in \{d, s, b\} \quad \text{along the diagonal} \tag{2.8a}$$

$$\sum_j V_{jq}^* V_{jq'} = 0 \quad , \quad q, q' \in \{d, s, b\}, q \neq q' \quad \text{off-diagonal.} \tag{2.8b}$$

The off-diagonal conditions constrain three complex numbers to sum to zero, and can thus be visualised as triangles in the complex plane, the so-called unitarity triangles. Of these, the triangle corresponding to the  $(d, b)$  elements plays a special role, because all three sides are of the same order of magnitude,  $\mathcal{O}(\lambda^3)$ . When expressed in the form

$$\frac{V_{ud}^* V_{ub}}{V_{cd}^* V_{cb}} + \frac{V_{td}^* V_{tb}}{V_{cd}^* V_{cb}} + 1 = 0, \tag{2.9}$$

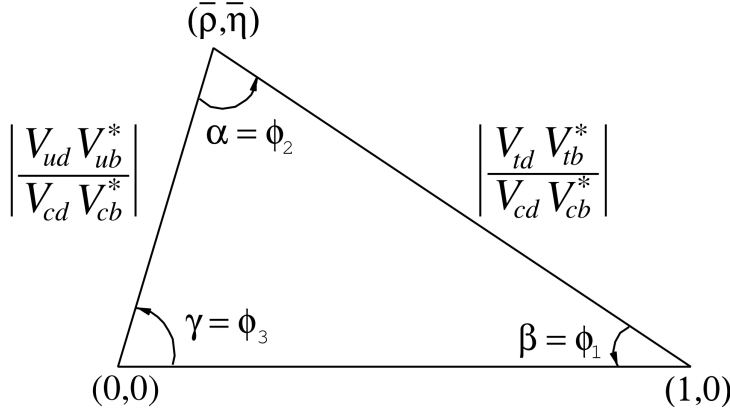


**Figure 2.1:** Definition of the lengths and sides of the Unitarity Triangle. Figure is taken from the *CKM Quark-Mixing Matrix* review of the PDG [?].

it is often referred to as the singular Unitarity Triangle, illustrated in Fig. 2.1 where the usual names for the three angles are also given.

Over-constraining the unitarity triangle by making separate measurements of all sides and angles, in as many different decay channels as possible, is an important, and non-trivial test of the SM. The current experimental constraints are in agreement with the SM predictions, as visualised in Fig. 2.2. The CKM angle

$$\gamma \equiv \arg(-V_{ud}V_{ub}^*/V_{cd}V_{cb}^*) = \arg(-V_{cb}V_{cd}^*/V_{ub}V_{ud}^*) \quad (2.10)$$

is unique among the CKM parameters, in that it can be measured in tree-level processes without significant theoretical uncertainty from lattice QCD calculations [?]. Because tree-level processes are less likely to be affected by Beyond-Standard-Model (BSM) effects, direct measurements of  $\gamma$  can be considered a SM benchmark, which can be compared to estimates based on measurements of other CKM elements that are measured in loop-level processes, and thus are more likely to be affected by BSM effects [?]. The current, worldwide combination of direct measurements, published by the CKMFitter group, is  $\gamma = (72.1^{+5.4}_{-5.7})^\circ$ , to be compared with the estimate from loop-level observables of  $\gamma = (65.66^{+0.90}_{-2.65})^\circ$  [?]. Other world averages exist [?, ?], but the overall picture is the same: the ability to constrain BSM physics is currently limited by the uncertainty of the direct measurements. Hence further precision measurements of  $\gamma$  are highly motivated. Presently, the precision is driven by time-integrated measurements of direct  $CP$ -violation in  $B^\pm \rightarrow DK^\pm$  decays;

Not sure if I should spend time explaining the non-gamma measurements entering?

<sup>2</sup>It is generally true that all phases of a single term in a given amplitude will be convention dependent, but that the phase differences between terms are not.

<sup>3</sup>Other variants of the Wolfenstein parameterisation do exist [?]. They all agree at the lowest orders of  $\lambda$ .

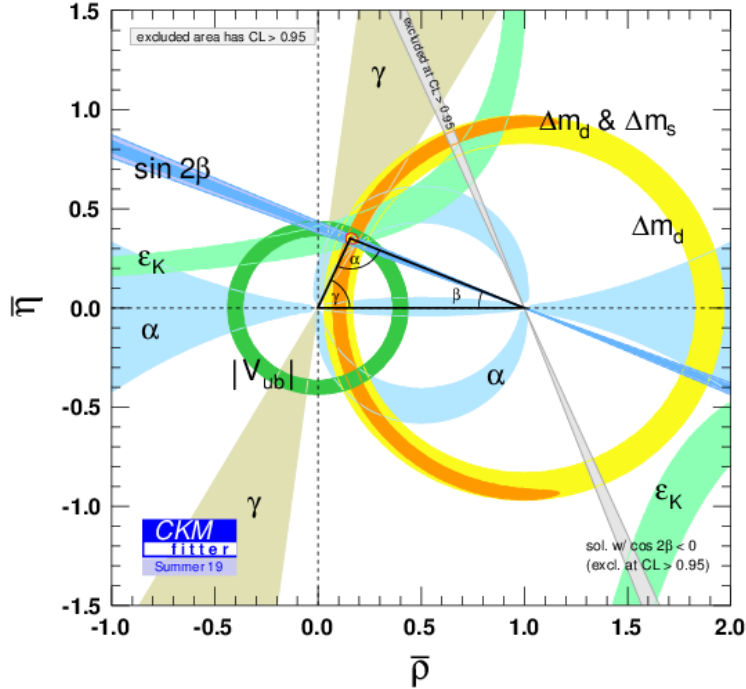


**Figure 2.2:** Current constraints on the Unitarity Triangle parameters as determined by the CKMFitter group for the EPS 2019 conference [?].

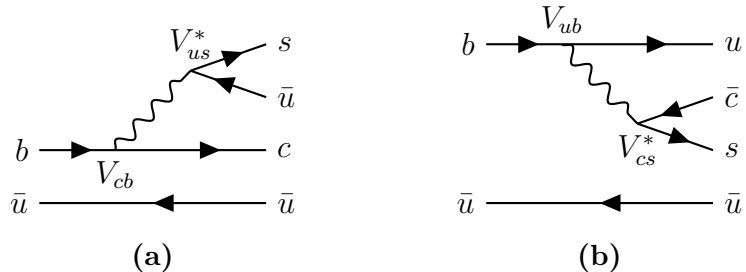


**Figure 2.3:** Tree level Feynman diagrams describing (a)  $B^- \rightarrow D^0 K^-$  and (b)  $B^- \rightarrow \bar{D}^0 K^-$  decays. The electro-weak phase difference between the two decays is  $\Delta\phi = \arg(V_{cb}V_{us}^*/V_{ub}V_{cs}^*) \simeq \gamma$ .

such a measurement is the topic of this thesis and the theory behind is treated in detail in the following section. It is also possible to measure  $\gamma$  in time-dependent mixing analyses of  $B_s^0 \rightarrow D_s^\mp K^\pm$ ,  $B^0 \rightarrow D^\mp \pi^\pm$  and related decays, by measuring  $CP$  violation in interference between mixing and decay. These modes are expected to provide competitive measurements in the future [?, ?].

### 301 2.2.2 Measuring $\gamma$ in tree level decays

302 The phase  $\gamma$  can be measured in tree-level processes with interference between  
 303  $b \rightarrow c\bar{s}u$  and  $b \rightarrow \bar{c}s u$  transitions. The canonical example, also the subject  
 304 of this thesis, is based on measurements sensitive to interference between the  
 305  $B^\pm \rightarrow D^0 K^\pm$  and  $B^\pm \rightarrow \bar{D}^0 K^\pm$  decay amplitudes. As illustrated in Fig. 2.3 for  
 306 the case of  $B^-$  decays, the electro-weak phase difference between the two decays  
 307 is  $\Delta\phi = \arg(V_{cb}V_{us}^*/V_{ub}V_{cs}^*)$ . While  $\Delta\phi$  is not identical to the definition of  $\gamma$  in  
 308 Eq. (2.10), the ratio of the involved CKM matrix elements is [?]

$$\begin{aligned} -\frac{V_{cd}^*/V_{ud}^*}{V_{us}^*/V_{cs}^*} &= -\frac{-\lambda[1 - \frac{\lambda^4}{2}A^2(1 - 2(\rho - i\eta))](1 - \frac{\lambda^2}{2} - \frac{\lambda^4}{8}(1 + 4A^2))}{\lambda(1 - \frac{\lambda^2}{2} - \frac{\lambda^4}{4})} \\ &= 1 - \lambda^4 A^2(1 - 2(\rho - i\eta)) + \mathcal{O}(\lambda^5). \end{aligned} \quad (2.11)$$

309 The ratio equals unity to  $\mathcal{O}(\lambda^4) \simeq 2.6 \times 10^{-3}$ , and thus  $\Delta\phi \simeq \gamma$  is a good  
 310 approximation within current experimental uncertainties. For the remainder of this  
 311 thesis the approximation will be used without further comment. The diagrams in  
 312 Fig. 2.3 describe the leading order contributions to the two amplitudes

$$\begin{aligned} A[B^- \rightarrow D^0 K^-] &\equiv A_B \\ A[B^- \rightarrow \bar{D}^0 K^-] &\equiv \bar{A}_B \equiv r_B A_B e^{i(\delta_B - \gamma)}, \end{aligned} \quad (2.12a)$$

313 where the last equality introduces two new parameters: the amplitude magnitude  
 314 ratio  $r_B \equiv |\bar{A}_B|/|A_B|$ , and  $\delta_B$ , the strong-phase difference between the decay  
 315 amplitudes. Since all  $CP$ -violation is attributed to the electro-weak phase in the  
 316 SM, the  $CP$ -conjugate decay amplitudes are [?]

$$\begin{aligned} A[B^+ \rightarrow \bar{D}^0 K^+] &= A_B \\ A[B^+ \rightarrow D^0 K^+] &= \bar{A}_B = r_B A_B e^{i(\delta_B + \gamma)}. \end{aligned} \quad (2.12b)$$

317 In an experimental setting, the  $D^0$  and  $\bar{D}^0$  mesons are reconstructed in some  
 318 final state,  $f$  or its  $CP$ -conjugate  $\bar{f}$ . In analogy with the  $B^\pm$  decays, the  $D$   
 319 decay amplitude can be related<sup>4</sup>

$$\begin{aligned} A[D^0 \rightarrow f] &= A[\bar{D}^0 \rightarrow \bar{f}] = A_D \\ A[\bar{D}^0 \rightarrow f] &= A[D^0 \rightarrow \bar{f}] = r_D A_D e^{i\delta_D}. \end{aligned} \quad (2.13)$$

320 where the assumption has been made that  $CP$  violation in the  $D$  decays is negligible,  
 321 and  $\delta_D$  denotes a  $CP$ -conserving strong-phase difference. While  $CP$ -violation in

---

<sup>4</sup>In this notation  $\delta_D$  is thus phase of the suppressed  $D$ -decay amplitude minus the phase of the favoured  $D$ -decay amplitude. This is the opposite convention to that used in the LHCb measurements with the ADS technique, but aligns with the notation used in the literature on  $\gamma$  measurements in  $D \rightarrow K_S^0 \pi^+ \pi^-$  decays.

<sup>322</sup>  $D$  decays has recently been measured [?], the size of the effect is small and it is  
<sup>323</sup> considered negligible in this thesis. Based on Eqs. 2.12 and (2.13), the decay rates  
<sup>324</sup> of  $B^+$  and  $B^-$  mesons into the possible final states can be seen to satisfy

$$\Gamma(B^- \rightarrow D(\rightarrow f)K^-) \propto 1 + r_D^2 r_B^2 + 2r_B r_D \cos [\delta_B + \delta_D - \gamma], \quad (2.14a)$$

$$\Gamma(B^+ \rightarrow D(\rightarrow \bar{f})K^+) \propto 1 + r_D^2 r_B^2 + 2r_B r_D \cos [\delta_B + \delta_D + \gamma], \quad (2.14b)$$

$$\Gamma(B^- \rightarrow D(\rightarrow \bar{f})K^-) \propto r_D^2 + r_B^2 + 2r_B r_D \cos [\delta_B - \delta_D - \gamma], \quad (2.14c)$$

$$\Gamma(B^+ \rightarrow D(\rightarrow f)K^+) \propto r_D^2 + r_B^2 + 2r_B r_D \cos [\delta_B - \delta_D + \gamma]. \quad (2.14d)$$

<sup>325</sup> The processes in Eqs. (2.14a) and (2.14b) are  $CP$ -conjugate and it is clear how, in the  
<sup>326</sup> general case where  $\delta_B + \delta_D \neq 0$ , a non-zero value of  $\gamma$  leads to  $CP$  violation in the form  
<sup>327</sup> of differing decay rates. The same is true for the processes in Eqs. (2.14c) and (2.14d).  
<sup>328</sup> Depending on the choice of  $D$  final state, these expressions can be used to relate  
<sup>329</sup>  $\gamma$  to various observables that are experimentally accessible. This thesis concerns  
<sup>330</sup> the choice  $f = K_S^0 \pi^+ \pi^-$  or  $f = K_S^0 K^+ K^-$ , where the terms related to the  $D$  decay  
<sup>331</sup> all have a non-trivial variation over the phase space of the decay. However, it is  
<sup>332</sup> useful to first analyse the simpler case where  $f$  is a two-body state.

<sup>333</sup> The simplest case is when  $f$  is chosen to be a  $CP$  eigenstate, so that  $f = \pm \bar{f}$   
<sup>334</sup> and the rate equations of (2.14a)–(2.14d) simplify, because  $r_D = 1$  and  $\delta_D \in \{0, \pi\}$ .  
<sup>335</sup> Measurements of  $\gamma$  in such decay modes are denoted GLW measurements, after  
<sup>336</sup> Gronau, London, and Wyler who described the approach in the early 90ies [?, ?].  
<sup>337</sup> Experimentally it is preferable to measure yield ratios rather than absolute rates,  
<sup>338</sup> and the observables of interest are thus the  $CP$  asymmetry

$$\begin{aligned} A_{CP=\pm 1} &= \frac{\Gamma[B^- \rightarrow D_{CP} K^-] - \Gamma[B^+ \rightarrow D_{CP} K^+]}{\Gamma[B^- \rightarrow D_{CP} K^-] + \Gamma[B^+ \rightarrow D_{CP} K^+]} \\ &= \frac{\pm r_B \sin \delta_B \sin \gamma}{1 + r_B^2 \pm 2r_B \cos \delta_B \cos \gamma}, \end{aligned} \quad (2.15a)$$

<sup>339</sup> as well as the ratio

$$\begin{aligned} R_{CP=\pm 1} &= 2 \frac{\Gamma[B^- \rightarrow D_{CP} K^-] + \Gamma[B^+ \rightarrow D_{CP} K^+]}{\Gamma[B^- \rightarrow D^0 K^-] + \Gamma[B^+ \rightarrow \bar{D}^0 K^+]} \\ &= 1 + r_B^2 \pm 2r_B \cos \delta_B \cos \gamma. \end{aligned} \quad (2.15b)$$

<sup>340</sup> In practice,  $A_{CP}$  and  $R_{CP}$  are obtained from measured yield ratios that are corrected  
<sup>341</sup> with appropriate branching fractions. A measurement of  $A_{CP}$  and  $R_{CP}$  alone is not  
<sup>342</sup> sufficient to determine the underlying physics parameters  $(\gamma, r_B, \delta_B)$ , and this is  
<sup>343</sup> not solely due to the number of parameters exceeding the number of constraints:  
<sup>344</sup> the equations also allow for multiple, ambiguous solutions for  $(\gamma, \delta_B)$ . One way  
<sup>345</sup> to break the ambiguity, first noted in the original paper [?], is to make further

346 measurements in additional  $B$  decays. These can be described with the formalism  
347 described above, but will not share the same ambiguous solutions because  $(r_B, \delta_B)$   
348 are unique to a given  $B$  decay. Another method is to analyse  $D$  decay final states  
349 that are not  $CP$  eigenstates.

350 A few years later, Atwood, Dunietz, and Sonis analysed an alternative choice of  
351  $D$  final states: a simultaneous analysis of a Cabibbo-favoured (CF) decay  $D^0 \rightarrow f$   
352 and the doubly-Cabibbo-suppressed (DCS) decay  $D^0 \rightarrow \bar{f}$  into the  $CP$  conjugate  
353 final state [?, ?]. Their suggested method is named the ADS method after the  
354 authors. The classical example is to take  $f = K^- \pi^+$  and  $\bar{f} = \pi^- K^+$ . The relative  
355 suppression means that the  $r_D$  of Eq. (2.14) is small, typically of the same order of  
356 magnitude as  $r_B$ , and thus the  $CP$  asymmetry of the suppressed decay is  $\mathcal{O}(1)$ :

$$\begin{aligned} A_{ADS(\bar{f})} &= \frac{\Gamma[B^- \rightarrow D(\rightarrow \bar{f})K^-] - \Gamma[B^+ \rightarrow D(\rightarrow f)K^+]}{\Gamma[B^- \rightarrow D(\rightarrow \bar{f})K^-] + \Gamma[B^+ \rightarrow D(\rightarrow f)K^+]} \\ &= \frac{r_D r_B \sin(\delta_B - \delta_D) \sin \gamma}{r_D^2 + r_B^2 + 2r_D r_B \cos(\delta_B - \delta_D) \cos \gamma}. \end{aligned} \quad (2.16a)$$

357 The large  $CP$  asymmetry is a prime feature of the ADS method. However, also the  
358 suppressed-to-favoured yield ratio is sensitive to the physics parameters of interest:

$$\begin{aligned} R_{ADS(\bar{f})} &= \frac{\Gamma[B^- \rightarrow D(\rightarrow \bar{f})K^-] + \Gamma[B^+ \rightarrow D(\rightarrow f)K^+]}{\Gamma[B^- \rightarrow D(\rightarrow f)K^-] + \Gamma[B^+ \rightarrow D(\rightarrow \bar{f})K^+]} \\ &= \frac{r_B^2 + r_D^2 + 2r_D r_B \cos(\delta_B - \delta_D) \cos \gamma}{1 + r_D^2 r_B^2 + 2r_D r_B \cos(\delta_B + \delta_D) \cos \gamma}. \end{aligned} \quad (2.16b)$$

359 The interpretation of  $A_{ADS}$  and  $R_{ADS}$  in terms of  $(\gamma, r_B, \delta_B)$  requires knowledge of  
360 the  $r_D$  and  $\delta_D$  parameters, but these can be measured independently. In general,  
361 the constraints from a single set of ADS observables suffer the same ambiguities as  
362 in the GLW case. However, unlike the GLW case, each  $D$  decay mode provides an  
363 independent set of constraints, because the parameters related to the  $D$  decay vary.

364 The discussion of this section has centred on the classical case of  $B^\pm \rightarrow DK^\pm$   
365 decays with a two-body  $D$  final state. With minor modifications the techniques  
366 have been used to make measurements of  $\gamma$  in  $B^0$  decays [?], with  $B$  decay final  
367 states including excited  $D$  mesons [?], excited kaons [?], or pions [?]. The decay  
368  $B^\pm \rightarrow D\pi^\pm$  also is also  $CP$ -violating, although the effect is much smaller than  
369 in the  $B^\pm \rightarrow DK^\pm$  decay, because it is expected that  $r_B^{D\pi^\pm} \simeq 0.005$  [?], whereas  
370  $r_B^{DK^\pm} \simeq 0.1$ . Furthermore, it is possible to use multi-body  $D$  final states. However,  
371 in some cases, a better precision can then be obtained by exploiting phase-space  
372 dependent decay rates. This is the topic of the next section.

## 373 2.3 Measuring $\gamma$ using multi-body D final states

374 In multi-body  $D$  decays, the  $r_D$  and  $\delta_D$  parameters of the fundamental rate equations  
 375 in Eq. (2.14) vary over the phase space of the  $D$  decay. This section describes  
 376 a model-independent approach to measure  $\gamma$  in  $B \rightarrow D(\rightarrow K_S^0\pi^+\pi^-)h^\pm$  decays  
 377 by exploiting this variation. The theory is identical for  $D \rightarrow K_S^0K^+K^-$  decays,  
 378 and similar ideas have been proposed for the  $D \rightarrow K_S^0\pi^+\pi^-\pi^0$  [?] and  $D \rightarrow$   
 379  $2\pi^+2\pi^-$  modes [?]. First, however, the formalism for describing amplitudes of  
 380 multi-body decays is briefly reviewed.

### 381 2.3.1 Dalitz plots and the phase space of multi-body decays

382 In general, the phase space of the  $n$ -body decay  $P \rightarrow p_1 + p_2 + \dots + p_n$  consists of  $n$   
 383 four momenta, with a total of  $4n$  components. The requirement that each of the final  
 384 state particles is on-shell provides  $n$  constraints on these components, and energy-  
 385 momentum conservation removes a further 4 degrees of freedom. If the original  
 386 particle  $P$  is a scalar, the decay is isotropic, which removes an additional 3 degrees  
 387 of freedom, leaving the total number of degrees of freedom at  $3n - 7$ . For the specific  
 388 case of three-body decays, the available phase space can thus be parameterised with  
 389 only two parameters. A practical and often used choice is the invariant masses

$$s_{12} = m^2(p_1 p_2) = (p_1^\mu + p_2^\mu)^2, \quad s_{13} = m^2(p_1 p_3) = (p_1^\mu + p_3^\mu)^2. \quad (2.17)$$

390 The choice of particle pairs is arbitrary, and the coordinates easily related

$$m_P^2 + m_{p_1}^2 + m_{p_2}^2 + m_{p_3}^2 = m^2(p_1 p_2) + m^2(p_1 p_3) + m^2(p_2 p_3). \quad (2.18)$$

391 A scatter plot of  $(s_{12}, s_{13})$  values for a sample of particle decays is denoted a Dalitz  
 392 plot [?]. It has the very useful feature that the presence of (narrow) resonances  
 393 in the decay leads to visible bands in the scatter plot. Figure 2.4 illustrates how  
 394 the limits of the Dalitz plot are defined by kinematic constraints, and shows an  
 395 example of a Dalitz plot for  $D \rightarrow K_S^0\pi^+\pi^-$  decays in which the  $K^*(892)^\pm$  and  $\rho(770)$   
 396 resonances are clearly visible. The plot shows the sample of  $B^+ \rightarrow D\pi^+$  decays  
 397 used to make the measurement described in Chapter 5 and thus the  $D$  meson is in  
 398 a superposition of  $D^0$  and  $\bar{D}^0$  states (as detailed in the following section).

399 In terms of the coordinates of Eq. (2.17) the differential decay rate is given by

$$d\Gamma = \frac{1}{32(2\pi)^3 m_P^3} |\mathcal{M}|^2 ds_{12} ds_{13}, \quad (2.19)$$

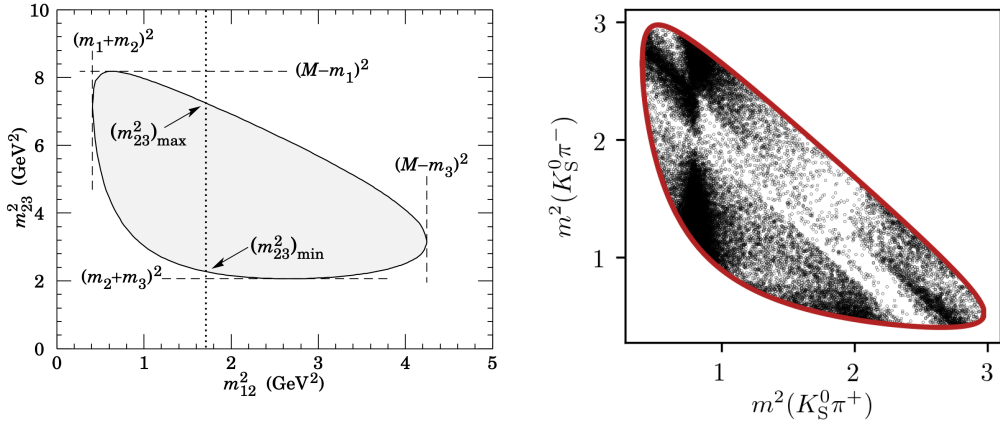


**Figure 2.4:** (Left) Schematic of a Dalitz plot and the limits of the kinematically allowed phase space limits. (Right) Example of a Dalitz plot for  $D \rightarrow K_S^0 \pi^+ \pi^-$  decays where the  $D$  meson originates in a  $B^+ \rightarrow D\pi^+$  decay; the decaying  $D$  meson is in a superposition of the  $D^0$  and  $\bar{D}^0$  states, but predominantly  $\bar{D}^0$ -like.

where  $\mathcal{M}$  is the QFT matrix element, or total decay amplitude, corresponding to the decay. In general, it is not possible to calculate  $\mathcal{M}$  from first principles. Instead, a model is defined with an empirically well motivated form, in which a number of free parameters must be determined experimentally. The simplest case is that of an *isobar* model, where it is assumed that the full decay can be decomposed into consecutive two-body decays of the form  $P \rightarrow R_{12}(\rightarrow p_1 + p_2)p_3$ . Thus,  $\mathcal{M}$  is expressed as a non-resonant constant amplitude term,  $k_{NR}$ , plus a sum of resonance terms

$$\mathcal{M}(s_{12}, s_{13}) = k_{NR} + \sum_r k_r \mathcal{M}^r(s_{12}, s_{13}). \quad (2.20)$$

The exact form of the  $\mathcal{M}^r$  function depends on the resonance in question. An overview is given in the PDG review on resonances and references therein [?]. The isobar formalism breaks down when resonances in the decay are not well separated. In this case, models of the form in Eq. (4.27) can still be employed, if the contribution from overlapping resonances are collected in a single term. An example of such a model, is the amplitude model for  $D^0 \rightarrow K_S^0 \pi^+ \pi^-$  decays developed by the Belle collaboration for a measurement of the CKM angle  $\beta$  in 2018 [?]. In this model, individual terms are included for  $D^0 \rightarrow K^*(\rightarrow K_S^0 \pi^\pm)\pi^\mp$  decays, whereas the  $\pi\pi$  and  $K\pi$   $S$ -wave contributions are modelled with the so-called  $K$ -matrix- and LASS formalisms [?, ?]. The amplitude and phase of  $\mathcal{M}$  as predicted by this model are shown in Fig. 2.5.

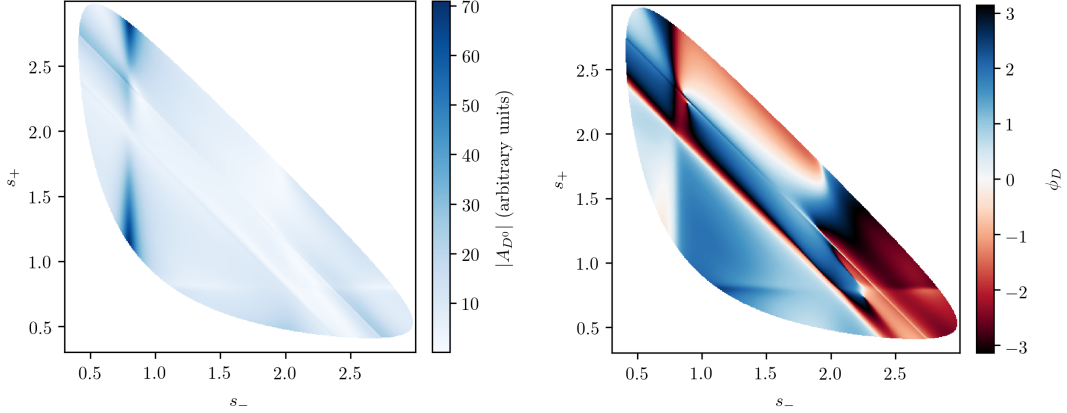


**Figure 2.5:** The (left) magnitude and (right) phase of the  $D \rightarrow K_S^0 \pi^+ \pi^-$  amplitude in the Belle 2018 model [?].

### 2.3.2 The GGSZ method to measure $\gamma$

The non-trivial phase-space dependence of the  $D \rightarrow K_S^0 \pi^+ \pi^-$  decay amplitude can be exploited to measure  $\gamma$  with  $B^\pm \rightarrow DK^\pm$  or  $B^\pm \rightarrow D\pi^\pm$  decays. This approach was proposed independently by Bondar [?], and by Giri, Grossman, Soffer, and Zupan [?] after whom it takes the commonly used acronym GGSZ. For this specific decay  $s_-$  and  $s_+$  are used to describe the Dalitz coordinates  $m^2(K_S^0 \pi^-)$  and  $m^2(K_S^0 \pi^+)$ , respectively, and the  $D$  decay amplitude is a function of these coordinates

$$A_S^{\bar{D}}(s_-, s_+) = A(\bar{D}^0 \rightarrow K_S^0 \pi^+ \pi^-). \quad (2.21)$$

To a good approximation the  $K_S^0$  meson is a  $CP$  eigenstate, meaning that the  $K_S^0 \pi^+ \pi^-$  state is self-conjugate. Assuming this approximation to be exact, and that  $CP$  violation in the  $D$  decay is negligible, the  $D$  decay amplitude satisfies the symmetry relation

$$A_S^{\bar{D}}(s_-, s_+) = A_S^D(s_+, s_-). \quad (2.22)$$

The impact of the  $K_S^0$  meson *not* being an exact  $CP$  eigenstate is treated in detail in Chapter 4. In order to simplify equations, the short-hand notation

$$(s_{-+}) = (s_-, s_+), \quad (s_{+-}) = (s_+, s_-), \quad (2.23)$$

will be employed for the remainder of the thesis, so that the relation in Eq. (2.22) can be expressed as  $A_S^{\bar{D}}(s_{-+}) = A_S^D(s_{+-})$ . Thus, the rate equations of Eq. (2.14)

433 for the  $D \rightarrow K_S^0\pi^+\pi^-$  decay mode are

$$\begin{aligned} d\Gamma^-(s_{-+}) &\propto |\mathcal{A}_S^-|^2 = |A_B|^2 |A_{K_S^0}|^2 \\ &\times [|A_S^D(s_{-+})|^2 + r_B^2 |A_S^D(s_{+-})|^2 + 2r_B |A_S^D(s_{-+})| |A_S^D(s_{+-})| \\ &\times (\cos[\delta_D(s_{-+})] \cos[\delta_B - \gamma] + \sin[\delta_D(s_{-+})] \sin[\delta_B - \gamma])], \end{aligned} \quad (2.24a)$$

$$\begin{aligned} d\Gamma^+(s_{-+}) &\propto |\mathcal{A}_S^+|^2 = |A_B|^2 |A_{K_S^0}|^2 \\ &\times [|A_S^D(s_{+-})|^2 + r_B^2 |A_S^D(s_{-+})|^2 + 2r_B |A_S^D(s_{-+})| |A_S^D(s_{+-})| \\ &\times (\cos[\delta_D(s_{-+})] \cos[\delta_B + \gamma] - \sin[\delta_D(s_{-+})] \sin[\delta_B + \gamma])]. \end{aligned} \quad (2.24b)$$

434 Here,  $\delta_D(s_{-+}) = \phi_D(s_{-+}) - \phi_D(s_{+-}) = -\delta_D(s_{+-})$ , where  $\phi_D(s_{-+})$  denotes the  
 435 complex phase of the  $A_S^D(s_{-+})$  amplitude, and a standard trigonometric relation  
 436 have been employed to factorise the terms depending on the complex phases of the  $B$   
 437 and  $D$  decays. It can be seen that in the case where  $\gamma = 0$  the  $B^+$  and  $B^-$  decay rates  
 438 are symmetric if the Dalitz coordinates are exchanged:  $\Gamma^+(s_-, s_+) = \Gamma^-(s_+, s_-)$ .  
 439 The presence of  $CP$  violation in the  $B$  decay breaks the symmetry. Therefore it is  
 440 possible to measure  $\gamma$  (and the nuisance parameters  $r_B$  and  $\delta_B$ ) from the phase-space  
 441 distribution of  $B^\pm \rightarrow D(\rightarrow K_S^0\pi^+\pi^-)K^\pm$  decays, given knowledge of  $A_S^D(s_{-+})$ .

442 A series of measurements of  $\gamma$  have been made that use amplitude models of  
 443 the  $D$  decay [?, ?, ?, ?, ?, ?, ?, ?, ?]. However, a model-independent approach has been  
 444 proposed by Bondar and Poluektov [?, ?] that relies on binning phase-space, in  
 445 which case the necessary information on the  $D$  decay amplitude can be summarised  
 446 in a small set of coefficients that can be measured in a separate experiment. That is  
 447 the approach followed in this thesis, and has been used previously by the Belle [?]  
 448 and LHCb collaborations [?]. It is described in detail in the following section.

449 Such a model-independent approach is favourable for two reasons. Firstly,  
 450 uncertainty estimates related to model inputs and the choice of parameterisation in  
 451 an amplitude model are non-trivial, yet would become the leading systematic with  
 452 the very high precision expected for  $\gamma$  measurements in the near future. Secondly,  
 453 amplitude models are notoriously hard to reproduce, and in a high-precision era it  
 454 is favourable that any experiment is easy to reinterpret in various extensions of the  
 455 SM. This is a lot easier for an experiment that measures a small set of well-defined  
 456 observables, than for an experiment that fits a complicated amplitude model.

457 An alternative model-independent approach has recently been proposed by  
 458 Poluektov [?] where the externally measured input on the  $D$ -decay phase are Fourier  
 459 expansion coefficients, and which therefore avoids binning phase space; this approach  
 460 may have the potential to improve the obtainable precision in the future.

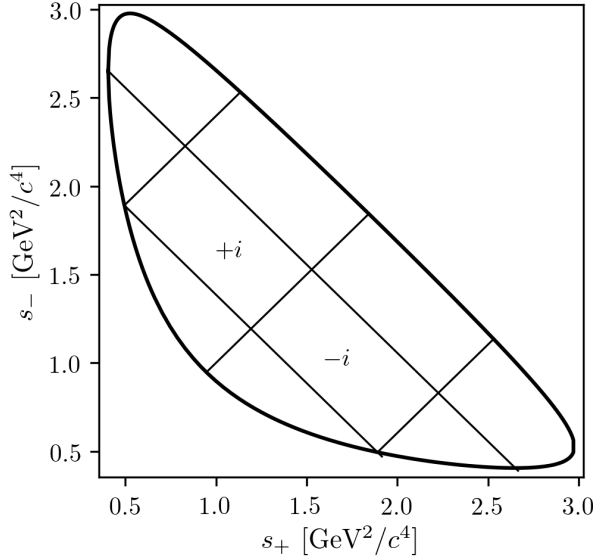


**Figure 2.6:** Illustration of the binning scheme used in GGSZ measurements: the bins are symmetric around the  $m^2(K_S^0\pi^+) = m^2(K_S^0\pi^-)$  diagonal, and numbered so that opposite bins have the same number, but with opposite sign.

### 2.3.3 A model-independent approach

The phase-space distribution can be analysed in a model-independent way, if the  $D$ -decay phase space is split into regions, or bins, and the  $B$  decay yield in each bin determined experimentally. A measurement of  $\gamma$  using this approach is the main topic of the thesis. This section describes the fundamental principle, whereas the details pertaining to the exact experimental approach are delegated to Section 2.4.

The amplitude symmetry of Eq. (2.22) is exploited by defining  $2N$  bins to be symmetric around the  $s_- = s_+$  diagonal of the Dalitz plot, numbered  $i = -N$  to  $N$  (omitting zero) such that if the point  $(s_-, s_+)$  is in bin  $i$ , then  $(s_+, s_-)$  is in bin  $-i$ , and by convention  $i > 0$  for bins where  $s_- > s_+$ . The principle is illustrated in Fig. 2.6, but the binning schemes used in actual measurements are more complicated. The decay rates in Eq. (2.24) can be integrated over such bins, and give the bin yields

$$\begin{aligned} N_i^- &\propto h^- \left[ K_i + r_B^2 K_{-i} + 2\sqrt{K_i K_{-i}} (c_i x_- + s_i y_-) \right], \\ N_i^+ &\propto h^+ \left[ K_{-i} + r_B^2 K_i + 2\sqrt{K_i K_{-i}} (c_i x_+ - s_i y_+) \right], \end{aligned} \quad (2.25)$$

where the parameters describing the  $B$  decay have been expressed in terms of the observables

$$x_\pm = r_B \cos(\delta_B \pm \gamma), \quad y_\pm = r_B \sin(\delta_B \pm \gamma), \quad (2.26)$$

<sup>476</sup> and a number of phase-space integrated quantities related to the  $D$ -decay have  
<sup>477</sup> been introduced. The  $K_i$  parameters denote fractional yield of a flavour-tagged  
<sup>478</sup>  $D^0$  decaying into bin  $i$ , defined as

$$K_i = \frac{1}{N_K} \int_i ds^2 |A_S^D(s_{-+})|^2, \quad N_K = \int ds^2 |A_S^D(s_{-+})|^2, \quad (2.27)$$

<sup>479</sup> where  $\int_i ds^2$  denotes integration over bin  $i$  of the Dalitz plot. The  $c_i$  and  $s_i$  denote  
<sup>480</sup> the amplitude-weighted average of  $\cos \delta_D(s_{-+})$  and  $\sin \delta_D(s_{-+})$  over bin  $i$

$$\begin{aligned} c_i &= \frac{\int_i ds^2 |A_S^D(s_{-+})| |A_S^D(s_{-+})| \cos[\delta_D(s_{-+})]}{\sqrt{\int_i ds^2 |A_S^D(s_{-+})|^2} \sqrt{\int_i ds^2 |A_S^D(s_{-+})|^2}}, \\ s_i &= \frac{\int_i ds^2 |A_S^D(s_{-+})| |A_S^D(s_{-+})| \sin[\delta_D(s_{-+})]}{\sqrt{\int_i ds^2 |A_S^D(s_{-+})|^2} \sqrt{\int_i ds^2 |A_S^D(s_{-+})|^2}}. \end{aligned} \quad (2.28)$$

<sup>481</sup> By the symmetry properties of  $\delta_D(s_{-+})$  these parameters satisfy  $c_i = c_{-i}$  and  
<sup>482</sup>  $s_i = -s_{-i}$ . The normalisation constants  $h^+$  and  $h^-$  are identical in the ideal case,  
<sup>483</sup> but it is convenient to define them separately for practical reasons: depending on  
<sup>484</sup> the experimental setup, there may be overall production and detection asymmetries  
<sup>485</sup> that affect the total signal yields. An experimental analysis can be made insensitive  
<sup>486</sup> to these effects because they can be absorbed into the normalisation constants, as  
<sup>487</sup> long as they are constant over the  $D$ -decay phase space. This comes at the cost  
<sup>488</sup> that the information on  $x_\pm$  and  $y_\pm$  from the overall  $CP$  asymmetry is lost, but  
<sup>489</sup> Section 2.3.5 will show the loss in precision to be minimal.

<sup>490</sup> Thus, for a set of  $2N$  bins, the bin yields of Eqs. (2.25) provide  $4N$  constraints  
<sup>491</sup> on a total of  $4N + 6$  parameters:  $(h^\pm, K_i, c_i, s_i, x_\pm, y_\pm)$ . However, the  $K_i$ ,  $c_i$ , and  
<sup>492</sup>  $s_i$  parameters relate only to the  $D$  decay, and can thus, in principle, be measured  
<sup>493</sup> in independent experiments. With such external inputs, a measurement of the  
<sup>494</sup>  $B^\pm \rightarrow D(\rightarrow K_S^0 \pi^+ \pi^-) K^\pm$  yields in a set of bins can be used to constrain  $x_\pm$  and  
<sup>495</sup>  $y_\pm$ , and thereby  $(\gamma, r_B, \delta_B)$ . The measurement presented in this thesis determines  
<sup>496</sup> the  $K_i$  parameters directly, but uses externally measured values of  $c_i$  and  $s_i$  as  
<sup>497</sup> input, as measured in quantum correlated  $D$  decays by the CLEO [?] and BESIII [?]  
<sup>498</sup> collaborations. Because these measurements are the foundation of the approach,  
<sup>499</sup> they are described in some detail in the following section. In the future, it is possible  
<sup>500</sup> that the  $c_i$  and  $s_i$  parameters may be measured in quantum-correlated  $D$  decays  
<sup>501</sup> in LHCb [?], and in charm-mixing measurements [?].

### 502 2.3.4 Measuring strong-phase inputs at charm factories

503 The strong-phase parameters  $c_i$  and  $s_i$  have been measured by the CLEO and  
 504 BESIII collaborations, using quantum correlated  $D^0\bar{D}^0$  pairs from decays of the  
 505  $\psi(3770)$  resonance state, itself produced in  $e^+e^-$  collisions at the resonance energy.  
 506 The  $\psi(3770)$  has quantum-number  $C = -1$ , which is conserved in the strong decay  
 507 into two  $D$  mesons, and thus the two  $D$  mesons are produced in an anti-symmetric  
 508 wave function. By observing the decay of one  $D$  meson into a specific final state,  
 509 say a  $CP$  eigenstate, the quantum state of the other  $D$  meson can be determined.  
 510 The measurement is based on decays where both  $D$  decays are reconstructed, one  
 511 in the  $K_S^0\pi^+\pi^-$  final state, the other in one of several different tag categories.  
 512 The main principles are outlined below, but most experimental considerations and  
 513 implementation details are left out for the sake of brevity.

514 The simplest case is when one  $D$  meson decays into a final state that uniquely  
 515 tags the flavour, such as  $\bar{D}^0 \rightarrow K^+e^-\bar{\nu}_e$ . In that case, the  $D$  meson decaying to  
 516  $K_S^0\pi^+\pi^-$  is known to be in the  $D^0$  state and the decay rate is simply determined by  
 517  $A_S^D : \Gamma(s_{-+}) \propto |A_S^D(s_{-+})|^2$ . This allows for a measurement of the  $K_i$  parameters.

518 If one  $D$  meson is reconstructed in a  $CP$ -even state, eg.  $K^+K^-$ , or a  $CP$ -odd  
 519 state, eg.  $K_S^0\pi^0$ , the  $D$  meson decaying to  $K_S^0\pi^+\pi^-$  is known to be in a state of  
 520 opposite  $CP$ . Thus, for a tag-decay of  $CP = \pm 1$  the decay rate has the form

$$\Gamma_{CP=\pm 1} \propto |A_S^D(s_{-+}) \mp A_S^D(s_{+-})|^2 \quad (2.29a)$$

521 and the bin yields will be given by

$$M_i^\pm \propto K_i + K_{-i} \mp 2\sqrt{K_i K_{-i}} c_i. \quad (2.29b)$$

522 Thus a simultaneous analysis of flavour and  $CP$  tagged decays allow for a deter-  
 523 mination of the  $K_i$  and  $c_i$  parameter sets.

524 Finally, the case where both  $D$  mesons, for now denoted  $D$  and  $D'$ , decay into  
 525 the  $K_S^0\pi\pi$  final state can be considered. The total amplitudes have contributions  
 526 from the case where  $D$  is in the  $D^0$  state and  $D'$  is in the  $\bar{D}^0$  state, as well as the  
 527 opposite flavour assignment. Thus the decay rate satisfies

$$\Gamma_{CP=\pm 1} \propto |A_S^D(s_{-+})A_S^D(s'_{+-}) + A_S^D(s_{+-})A_S^D(s'_{-+})|^2 \quad (2.30a)$$

528 where  $s_{-+}$  denotes the Dalitz-plot coordinates of the  $D$  meson, and  $s'_{-+}$  those of  
 529 the  $D'$  meson. Defining  $M_{ij}$  to be the yield of decays where the  $D$  decay is in  
 530 bin  $i$  and the  $D'$  in bin  $j$ , the bin yields satisfy

$$M_{ij} \propto K_i K_{-j} + K_j K_{-i} - 2\sqrt{K_i K_{-i} K_j K_{-j}} (c_i c_j + s_i s_j). \quad (2.30b)$$

531 Thus, analysing these decays in addition to the  $CP$  and flavour tagged decays provide  
 532 information on all of  $K_i$ ,  $c_i$ , and  $s_i$ . Note, however, that Eqs. (2.29) and (2.30) are  
 533 invariant under the transformation  $\delta_D \rightarrow -\delta_D$ . In practice, the analysis is extended  
 534 in a number of ways to enhance the statistics: using "flavour-tag" states that are not  
 535 exact flavour tags, such as  $K^-\pi^+$ , using self-conjugate multi-body  $D$ -decay final  
 536 states that are not exact  $CP$  eigenstates, such as  $\pi^+\pi^-\pi^0$ , and using the  $K_L^0\pi^+\pi^-$   
 537 final state as well. However, the main principles are the same as described above.

538 The measurements of  $c_i$  and  $s_i$  are made for a range of different binning schemes.  
 539 It was noted already in Ref. [?] that a rectangular binning scheme, such as the  
 540 example in Fig. 2.6, does not provide the optimal sensitivity to  $\gamma$ . A better sensitivity  
 541 can be obtained if the bins are defined such that  $\delta_D$  is approximately constant over  
 542 a given bin, by defining bin  $i$  out of  $N$  via the condition

$$\text{bin}_i = \{(s_-, s_+) \mid 2\pi(i - 3/2)/N < \delta_D(s_-, s_+) < 2\pi \times (i - 1/2)/N\}. \quad (2.31)$$

543 In practice, the binning scheme is defined by splitting the  $D$ -decay phase-space  
 544 into quadratic *micro bins* with a width of  $0.0054 (\text{GeV}/c^2)^2$  and assigning a bin  
 545 number to each micro bin via the condition in (2.31) as evaluated in an amplitude  
 546 model of choice. The obtained binning scheme when using an amplitude model  
 547 developed by the BaBar collaboration in 2008 [?] is shown in Fig. 2.7a. In Ref [?]  
 548 it was also shown that the binning can be even further optimised for sensitivity.  
 549 The suggested figure of merit is

$$Q^2 = \frac{\sum_i \left( \frac{1}{\sqrt{N_i^B}} \frac{dN_i^B}{dx} \right)^2 + \left( \frac{1}{\sqrt{N_i^B}} \frac{dN_i^B}{dy} \right)^2}{\int ds^2 \left[ \left( \frac{1}{|\Gamma^B(s_-)|} \frac{d|\Gamma^B(s_-)|^2}{dx} \right)^2 + \left( \frac{1}{|\Gamma^B(s_-)|} \frac{d|\Gamma^B(s_-)|^2}{dy} \right)^2 \right]} \quad (2.32)$$

550 which quantifies the statistical sensitivity for a given binning, relative to the one  
 551 achievable in an unbinned analysis. The CLEO collaboration defined an *optimal*  
 552 binning scheme by an iterative procedure where, starting from the equal binning  
 553 scheme, a micro-bin is randomly reassigned new bin numbers in each step, and a  
 554 step accepted if  $Q^2$  increases. The optimisation is done for the case where  $x = y = 0$   
 555 and thus  $Q^2$  simplifies to  $Q_{x=y=0}^2 = \sum_i N_i^{x=y=0} (c_i^2 + s_i^2) / N_{\text{total}}^{x=y=0}$ . The resulting  
 556 binning scheme is shown in Fig. 2.7b. An additional binning scheme is defined,  
 557 denoted the *modified optimal* scheme and shown in Fig. 2.7c, where the  $Q^2$  figure  
 558 of merit is modified to take into account the presence of backgrounds [?]. The  
 559 modified optimal binning scheme has proven beneficial to use in measurements with  
 560 small signal yields [], but is not employed in the present thesis.

Where exactly is this phase sign known from?  
Is the overall sign not arbitrary in amplitude models?

**Table 2.1:** The experimentally measured  $c_i$  and  $s_i$  values used in the thesis. The  $D \rightarrow K_S^0\pi^+\pi^-$  values are the combined values from the BESIII and CLEO measurements published by BESIII [?]. The  $D \rightarrow K_S^0K^+K^-$  values are measured by CLEO [?].

Optimal binning scheme: $D \rightarrow K_S^0\pi^+\pi^-$		
Bin $i$	$c_i$	$s_i$
1	$-0.037 \pm 0.049$	$0.829 \pm 0.097$
2	$0.837 \pm 0.067$	$0.286 \pm 0.152$
3	$0.147 \pm 0.066$	$0.786 \pm 0.154$
4	$-0.905 \pm 0.021$	$0.079 \pm 0.059$
5	$-0.291 \pm 0.041$	$-1.022 \pm 0.062$
6	$0.272 \pm 0.082$	$-0.977 \pm 0.176$
7	$0.918 \pm 0.017$	$-0.184 \pm 0.065$
8	$0.773 \pm 0.033$	$0.277 \pm 0.118$

2-bins binning scheme: $D \rightarrow K_S^0K^+K^-$		
Bin $i$	$c_i$	$s_i$
1	$0.818 \pm 0.107$	$-0.445 \pm 0.215$
2	$-0.746 \pm 0.083$	$-0.229 \pm 0.220$

Both the CLEO and BESIII collaborations have measured the values of  $c_i$  and  $s_i$  for the equal, optimal, and modified optimal binning schemes. The results are also shown in Fig. 2.7, where they are compared to the expectation from the latest amplitude model [?]. The measurements presented in this thesis are based on a combination of the BESIII and CLEO results for the optimal binning scheme, made by the BESIII collaboration [?] and tabulated in Table 2.1.

While the *definition* and *optimisation* of these binning schemes depend on knowledge of  $A_S^D(s_-, s_+)$  via an amplitude model, it is important to note that no model information is needed when the binning schemes are used in the subsequent measurements of strong-phases<sup>5</sup> or  $CP$ -observables. Therefore the measurements will not be biased by any modelling imperfections, although the obtained precision might be lower than expected.

The preceding discussion has been focusing on the  $D \rightarrow K_S^0\pi^+\pi^-$  channel, however the  $D \rightarrow K_S^0K^+K^-$  channel can be analysed completely analogously. The CLEO collaboration measure  $c_i$  and  $s_i$  values for this mode as well, in three binning schemes [?]. These are all equal-phase binning schemes, with 2, 3, and 4 bins,

<sup>5</sup>With the exception of minimal model-dependence introduced when the  $K_L^0\pi^+\pi^-$  final state is employed to constrain the  $s_i$  parameters by the  $D$ -factories [?, ?], the impact of which is well under control.

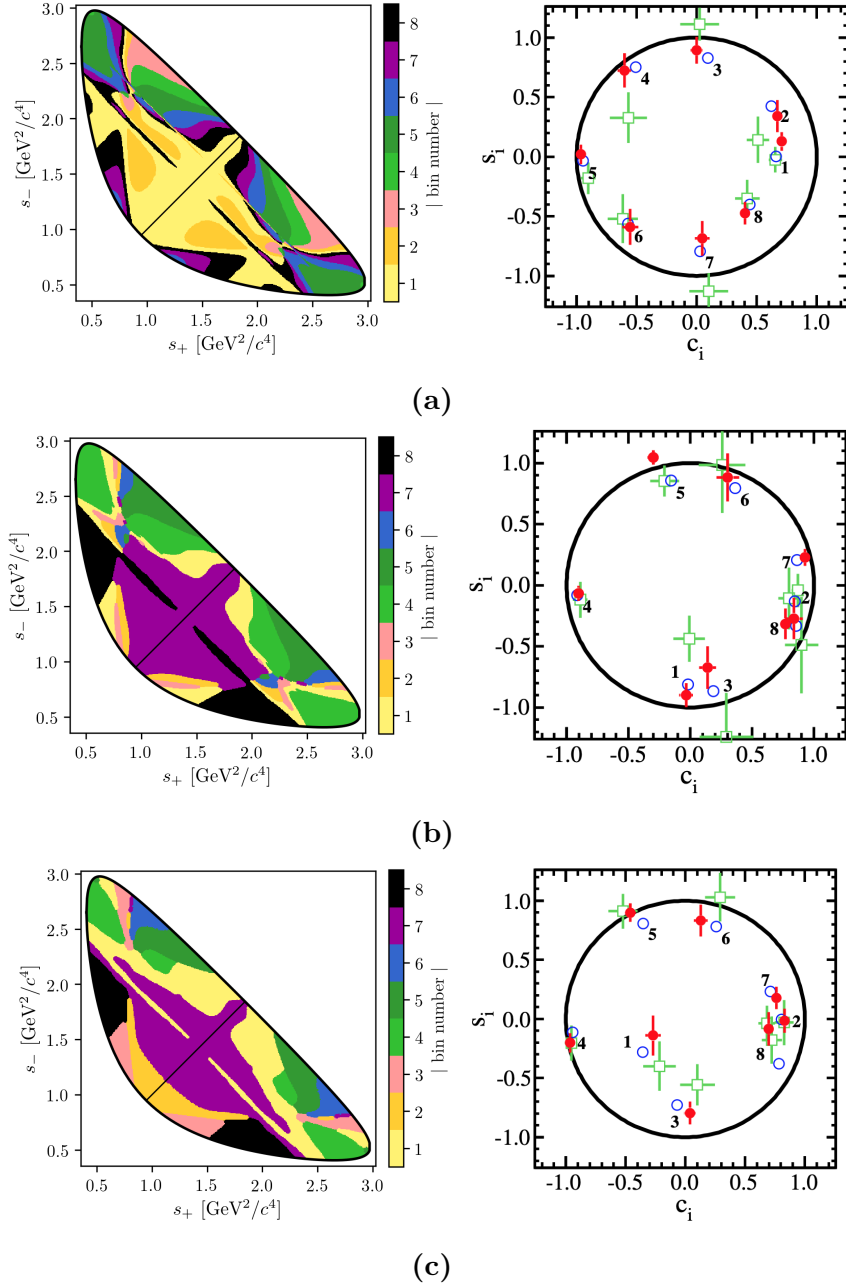


**Figure 2.7:** The (left) binning schemes and (right) measured values of  $(c_i, s_i)$  for (a) equal, (b) optimal, and (c) modified optimal binning schemes for  $D \rightarrow K_S^0 \pi^+ \pi^-$  decays. The plots of the measured values are taken from Ref. [?] and show the results obtained by (red) BESIII, (green) CLEO, and (blue) the model expectation using the model from Ref. [?]. The measurement featured in this thesis used the optimal binning scheme.

respectively, shown in Fig. 2.8. The  $D \rightarrow K_S^0 K^+ K^-$  decay amplitude is almost completely dominated by two  $K^+ K^-$  resonances, the  $CP$ -odd  $\phi(1020)$  and the  $CP$ -even  $a_0(980)$ , and this means that very little gain in sensitivity can be made by altering the equal-phase binning schemes. The measured  $c_i$  and  $s_i$  values are also shown in Fig. 2.8 and tabulated in Table 2.1 for the 2-bins scheme, which is used in this thesis. A BESIII measurement is in preparation, but has not been finished at the time of writing.

### 2.3.5 Global CP asymmetry and the relation to GLW and ADS measurements

The introduction of separate normalisation factors  $h^+$  and  $h^-$  in Eq. (2.25) hides the fact that information on  $\gamma$  (in principle) can be obtained from the asymmetry in phase-space-integrated  $B^+$  and  $B^-$  yields. In the ideal case where  $h^- = h^+$  the total yield asymmetry is

$$\begin{aligned} A_{GGSZ} &= \frac{\sum_i N_- - N_i^+}{\sum_{i=-N}^N N_i^- + N_i^+} = \frac{\sum_{i=-N}^N \sqrt{K_i K_{-i}} c_i (x_- - x_+)}{1 + r_B^2 + 2 \sum_{i=-N}^N \sqrt{K_i K_{-i}} c_i (x_- + x_+)} \\ &= \frac{2 \sum_{i=1}^N \sqrt{K_i K_{-i}} c_i (x_- - x_+)}{1 + r_B^2 + 4 \sum_{i=1}^N \sqrt{K_i K_{-i}} c_i (x_- + x_+)}, \end{aligned} \quad (2.33)$$

where it has been exploited that  $\sum_{i=-N}^N \sqrt{K_i K_{-i}} s_i = 0$  by definition. The size of the asymmetry is governed by the factor  $\sum_{i=1}^N \sqrt{K_i K_{-i}} c_i$ , which is small for  $D \rightarrow K_S^0 \pi^+ \pi^-$  and  $D \rightarrow K_S^0 K^+ K^-$  decays. The underlying reason is that  $\delta_D(s_-, s_+)$  varies significantly across phase-space for these decays, as evident by the spread in the values of  $c_i$  in Table 2.1, which reduces the *average* of the asymmetry-generating  $D^0 - \bar{D}^0$  interference term to being close to zero. The value of  $\sum_{i=-N}^N \sqrt{K_i K_{-i}} c_i$  is closely related to the  $CP$  content of the final state in question: for a self-conjugate  $CP$  even (odd) final state

$$A_{D^0}(s_-, s_+) = {}^{(+)}_{(-)} A_{\bar{D}^0}(s_-, s_+) = {}^{(+)}_{(-)} A_{D^0}(s_+, s_-) \quad (2.34)$$

and thus  $\sum_{i=1}^N \sqrt{K_i K_{-i}} c_i = {}^{(+)}_{(-)} 1$ . This motivates the definition of the  $CP$ -even fraction of the decay

$$\mathcal{F}_+ \equiv \frac{1}{2} \left( 1 + \sum_{i=1}^N \sqrt{K_i K_{-i}} c_i \right). \quad (2.35)$$

With  $\mathcal{F}_+$  in hand, the asymmetry in Eq. (2.33) can be rewritten

$$A_{GGSZ} = \frac{(2\mathcal{F}_+ - 1)r_B \sin \delta_B \sin \gamma}{1 + r_B^2(2\mathcal{F}_+ - 1)2r_B \cos \delta_B \cos \gamma}, \quad (2.36)$$

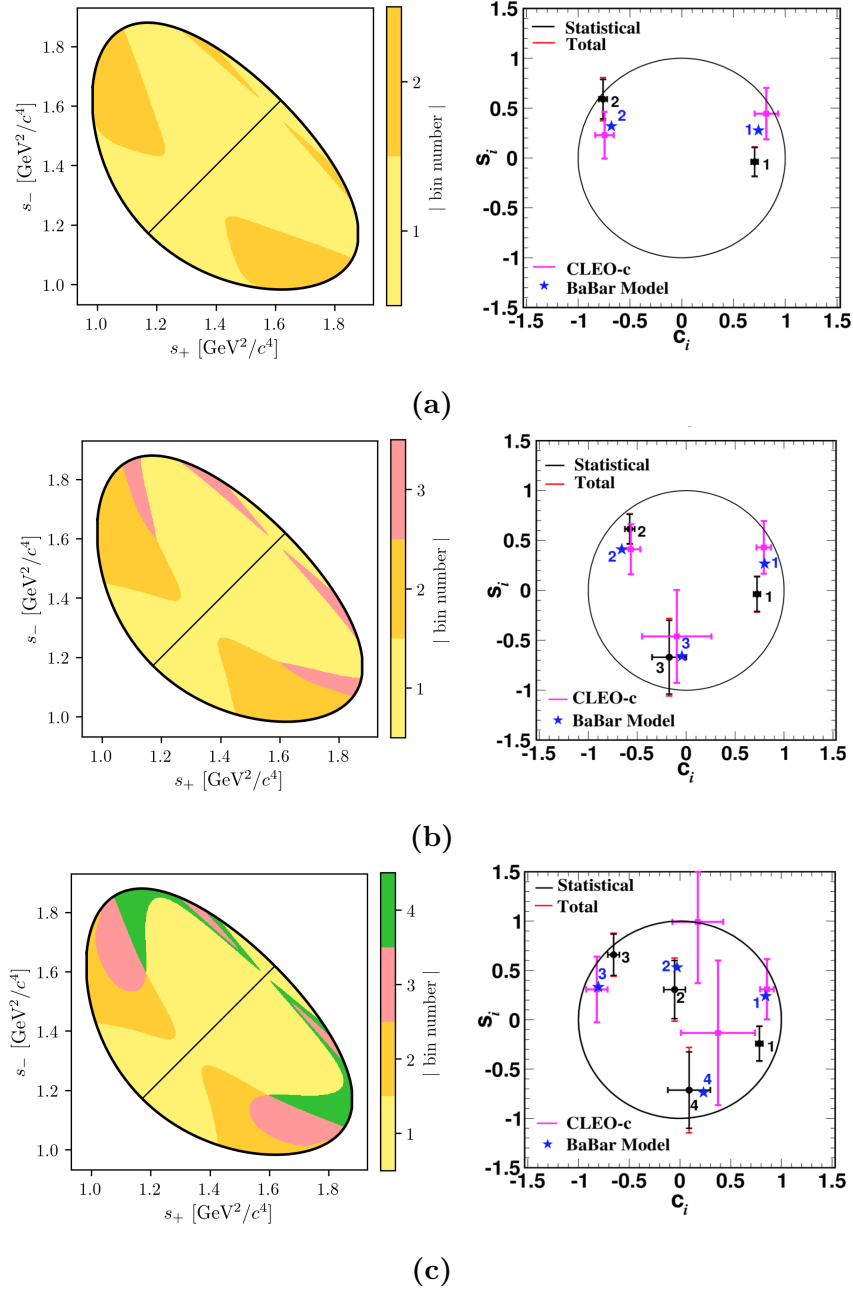


**Figure 2.8:** The (left) binning schemes and (right) measured values of  $(c_i, s_i)$  for the (a) 2-, (b) 3-, and (c) 4-bins binning schemes for  $D \rightarrow K_S^0 K^+ K^-$  decays. The plots of the measured values are taken from Ref. [?] and show the (error bars) results obtained by (black) BESIII, (pink) CLEO, and (blue) the model expectation using the model from Ref. [?]. The measurement featured in this thesis uses the 2-bins scheme.

which is the usual form used in quasi-GLW measurements []; for  $N = 1$  the definition in Eq. (2.35) is equivalent to  $\mathcal{F}_+$  as defined in Ref. []. The value of  $\mathcal{F}_+$  is independent of the number and shape of bins in a given binning scheme, as long as the bin definitions follow the symmetry principles outlined in Section 2.3.3. For  $D \rightarrow K_S^0\pi^+\pi^-$  and  $D \rightarrow K_S^0K^+K^-$  decays the values of  $\mathcal{F}_+$  are

$$\begin{aligned}\mathcal{F}_+(K_S^0\pi^+\pi^-) &= X? \\ \mathcal{F}_+(K_S^0K^+K^-) &= X?\end{aligned}\tag{2.37}$$

as evaluated with the Belle 2018 model for  $D \rightarrow K_S^0\pi^+\pi^-$  decays and the BaBar 2010 model for  $D \rightarrow K_S^0K^+K^-$  decays. Since  $r_B^{DK^\pm} \sim 0.1$  the predicted global asymmetries are thus approximately 1–2 %, which is not resolvable with the current experimental yields. As shown in Chapter 4,  $CP$  violation in the  $K_S^0$  sector leads to asymmetries of a similar size, further complicating the use of global asymmetries to constrain  $x_\pm$  and  $y_\pm$ . Thus these modes are ill-suited for quasi-GLW measurements, and ignoring global asymmetries leads to a negligible loss of information on  $\gamma$  in a GGSZ measurement. The reverse is true for a well-suited quasi-GLW mode, such as  $D \rightarrow \pi^+\pi^-\pi^0$ : if  $\mathcal{F}_+$  is close to either zero or unity, it means that  $(c_i, s_i)$  will be close to  $(\pm 1, 0)$  in all bins for *any* given binning scheme, and the set of bins will provide almost identical constraints on  $x_\pm$  and  $y_\pm$ . Thus, the binning of phase space leads to no significant gain in precision compared to a global analysis.

Indeed, a crucial quality of the GGSZ method, is that exactly because each bin-pair provides independent constraints on  $x_\pm$  and  $y_\pm$ , the method provides a single solution for  $(\gamma, r_B, \delta_B)$  that does not suffer the ambiguities of the ADS and GLW approaches. In order to illustrate this further, it is useful to make one more comparison of the model-independent GGSZ formalism to the ADS and GLW formalisms. If there was no  $CP$  symmetry the  $B^+$  yield in bin  $+i$  would equal the  $B^-$  yield in bin  $-i$ . Therefore the relevant  $CP$  asymmetry for a given Dalitz bin is

$$\begin{aligned}A_{GGSZ}^i &\equiv \frac{N_i^- - N_{-i}^+}{N_i^- + N_{-i}^+} \\ &= \frac{\sqrt{K_i K_{-i}}(c_i(x_- - x_+) + s_i(y_- - y_+))}{K_i + r_B^2 K_{-i} + 2\sqrt{K_i K_{-i}}(c_i(x_- + x_+) + s_i(y_- + y_+)})\end{aligned}\tag{2.38}$$

This expression is identical to the ADS asymmetry in Eq. (2.16a) if the effective  $D$ -decay parameters  $r_D^i$  and  $\delta_D^i$  are defined via

$$\kappa_i \cos \delta_D^i \equiv c_i \quad , \quad \kappa_i \sin \delta_D^i \equiv s_i \quad , \quad r_D^i \equiv \sqrt{K_i/K_{-i}},\tag{2.39}$$

and a coherence factor,  $\kappa$ , is included in the interference terms of the ADS expression, as is standard for multi-body  $D$  decays []. These parameters allow us to classify

**Table 2.2:** Classification of the bins used in model-independent GGSZ measurements, in terms of whether the interplay between the  $D^0$  and  $\bar{D}^0$  amplitudes in the bin resemble typical GLW or ADS behaviour. The parameters are calculated using the 2018 Belle model [1] for  $D \rightarrow K_S^0\pi^+\pi^-$  decays and the 2010 BaBar model [2] for  $D \rightarrow K_S^0K^+K^-$  decays.

Optimal binning scheme: $D \rightarrow K_S^0\pi^+\pi^-$					
Bin $i$	$\hat{r}_D$	$\hat{\delta}_D$	$\mathcal{F}_+$	$\kappa$	Bin type
1	0.473	91.9°	48.97 %	0.81	Mixed
2	0.164	11.1°	63.38 %	0.85	ADS-like
3	0.157	79.4°	52.50 %	0.89	ADS-like
4	0.768	175.3°	5.85 %	0.92	GLW-odd-like
5	0.759	-99.9°	42.84 %	0.87	Mixed
6	0.223	-64.5°	57.92 %	0.87	ADS-like
7	0.651	-13.3°	89.44 %	0.89	GLW-even-like
8	1.745	21.0°	87.08 %	0.92	GLW-even-like

2-bins binning scheme: $D \rightarrow K_S^0K^+K^-$					
Bin $i$	$\hat{r}_D$	$\hat{\delta}_D$	$\mathcal{F}_+$	$\kappa$	Bin type
1	0.816	19.8°	86.14 %	0.78	GLW-even-like
2	0.775	154.5°	16.23 %	0.77	GLW-odd-like

629 a given pair of bins with number  $\pm i$  as either *GLW-like*, if  $\delta_D^i$  is close to 0 or  $\pi$   
 630 and  $r_D^i$  is close to unity, or *ADS-like* if  $0 < r_D^i \ll 1$ . The  $CP$ -even fraction of the  
 631  $D$ -decay can also be defined for a given bin-pair:

$$\mathcal{F}_+^i = \mathcal{F}_+^{-i} \equiv \frac{1}{2} \left( 1 + 2c_i \frac{\sqrt{K_i K_{-i}}}{K_i + K_{-i}} \right) = \frac{1}{2} \left( 1 + 2c_i \frac{r_D^i}{1 + r_D^{i/2}} \right). \quad (2.40)$$

632 A GLW-even-like bin pair will have  $\mathcal{F}_+^i \simeq 1$  and a GLW-odd-like bin pair will  
 633 have  $\mathcal{F}_+^i \simeq 0$ .

634 Table 2.2 summarises a classification of the bins for the optimal  $D \rightarrow K_S^0\pi^+\pi^-$   
 635 binning scheme and the 2-bins  $D \rightarrow K_S^0K^+K^-$  binning scheme following these  
 636 principles. Two bins are classified as *mixed* because  $r_D^i$  is not particularly small,  
 637 but  $\mathcal{F}_+^i$  is close to 0.5. The fact that multiple bin types appear for both the  
 638  $D \rightarrow K_S^0\pi^+\pi^-$  and  $D \rightarrow K_S^0K^+K^-$  modes underline that each mode benefits from  
 639 being analysed in the GGSZ formalism, and that the bins provide independent  
 640 constraints, allowing for a non-ambiguous solution for  $(\gamma, r_B, \delta_B)$ .

## 2.4 Strategy for the LHCb measurement

The main topic of the thesis is a model-independent GGSZ measurement using  $B^\pm \rightarrow DK^\pm$  and  $B^\pm \rightarrow D\pi^\pm$  decays, and the two  $D$  final states  $K_S^0\pi^+\pi^-$  and  $K_S^0K^+K^-$ . The measurement uses the optimal binning scheme for the  $D \rightarrow K_S^0\pi^+\pi^-$  mode, with the combined strong-phase inputs from the BESIII [?] and CLEO [?] collaborations published in Ref. [?]. For the  $D \rightarrow K_S^0K^+K^-$  channel, the 2-bins scheme is used with the strong-phase parameters measured by the CLEO collaboration [?]. The details of the analysis are presented in Chapter (5), but the overall strategy and a few extensions of the formalism from the previous sections are given here.

Due to the geometry of the LHCb detector, the signal reconstruction efficiency for  $B^\pm \rightarrow D(\rightarrow K_S^0h^+h^-)h'^\pm$  decays varies significantly across the  $D$ -decay phase space. Denoting the efficiency profile as  $\eta(s_-, s_+)$ , the yield equations of Eq. (2.25) are therefore modified slightly

$$\begin{aligned} N_i^- &= h^{B^-} \left[ F_i + r_B^2 F_{-i} + 2\sqrt{F_i F_{-i}} (c'_i x_- + s'_i y_-) \right], \\ N_i^+ &= h^{B^+} \left[ F_{-i} + r_B^2 F_i + 2\sqrt{F_i F_{-i}} (c'_i x_+ - s'_i y_+) \right], \end{aligned} \quad (2.41)$$

where the phase-space integrated quantities now include the efficiency profile

$$F_i = \frac{1}{N_F} \int ds^2 \eta(s_{-+}) |A_S^D(s_{-+})|^2, \quad N_F = \int ds^2 \eta(s_{-+}) |A_S^D(s_{-+})|^2, \quad (2.42)$$

$$c'_i = \frac{\int_i ds^2 \eta(s_{-+}) |A_S^D(s_{-+})| |A_S^D(s_{-+})| \cos[\delta_D(s_{-+})]}{\sqrt{\int_i ds^2 \eta(s_{-+}) |A_S^D(s_{-+})|^2} \sqrt{\int_i ds^2 \eta(s_{-+}) |A_S^D(s_{-+})|^2}}, \quad (2.43)$$

with an analogous definition of  $s'_i$ . At leading order, the strong-phase parameters are unaffected by the non-uniform efficiency, and, in addition, the bin definitions favour bins for which  $c_i$  and  $s_i$  take on similar values across each bin. Therefore, the  $c_i$  and  $s_i$  values reported by the charm factories are used directly in the measurement. The impact on the obtained central values is negligible, as described in detail in Section 5.6 where a systematic uncertainty is assigned.

The  $F_i$  are significantly different to the  $K_i$  due to the experimental acceptance profile in LHCb. Given external inputs for the strong-phase parameters, it is possible to fit the  $F_i$  parameters and  $x_\pm$  and  $y_\pm$  simultaneously in a fit to the LHCb  $B^\pm \rightarrow DK^\pm$  data set, in which case the obtained  $F_i$  parameters incorporate the correct acceptance profile correction by construction. However, the obtainable precision for the  $CP$  observables measured by this procedure is suboptimal. As

an alternative, the first LHCb measurement [?] made a simultaneous analysis of  $B^\pm \rightarrow DK^\pm$  and a much larger sample of  $B^\pm \rightarrow D\pi^\pm$  decays; since the  $F_i$  parameters relate to the  $D$  decay, they can effectively be obtained in the  $D\pi^\pm$  sample and shared between the two  $B^\pm \rightarrow Dh^\pm$  channels. However, there is  $CP$  violation present in the  $B^\pm \rightarrow D\pi^\pm$  decays, which led to a dominant systematic uncertainty. Later LHCb measurements [?, ?] instead relied on flavour tagged  $D$  mesons from  $\bar{B}^0 \rightarrow D^{*+}(\rightarrow D^0\pi^+)\mu^-\bar{\nu}_\mu X$  decays to obtain  $F_i$ , where no  $CP$  violation is possible. However, due to necessarily different triggering paths and selections, the acceptance profile is not exactly identical between semi-leptonic decays and the  $B^\pm \rightarrow Dh^\pm$  decays of interest. An efficiency correction based on simulation was therefore applied to obtain the correct  $F_i$ , and in this case, the uncertainty related to the correction constituted the largest systematic uncertainty on the measurement.

Both sources of systematic uncertainty can be avoided by making a simultaneous analysis of  $B^\pm \rightarrow DK^\pm$  and  $B^\pm \rightarrow D\pi^\pm$  decays, where  $CP$ -violating observables are measured in *both* channels and the  $F_i$  parameters are shared. Effectively, the  $F_i$  are determined in the high statistics  $B^\pm \rightarrow D\pi^\pm$  channel, but with no systematic effect from  $CP$ -violation in that channel, since the  $CP$ -violation is incorporated in the yield description. At the start of the work that lead to this thesis, it was not clear to what degree the measured  $CP$ -violating observables in  $B^\pm \rightarrow D\pi^\pm$  decays were affected by  $CP$  violation in the neutral kaon sector. The impact had been shown to scale as  $\mathcal{O}(|\epsilon|/r_B)$  [?], which is negligible for the  $B^\pm \rightarrow DK^\pm$  channel but suggests potentially large biases in the  $B^\pm \rightarrow D\pi^\pm$  channel, where  $r_B$  is 20 times smaller. However, the dedicated analysis presented in Chapter 4 has proved the effect on GGSZ measurements to be in fact be *smaller* than  $\mathcal{O}(|\epsilon|/r_B)$  and the simultaneous measurement is indeed viable.

The measurement is performed by making extended maximum-likelihood fits to the  $m_B$  spectra of  $B \rightarrow D(\rightarrow K_S^0 h^+ h^-)h'^\pm$  candidates split by charge and Dalitz bin. The  $B^\pm \rightarrow DK^\pm$  signal yields are parameterised using the expressions in Eq. (2.41) directly, thus obtaining values for  $x_\pm^{DK}$  and  $y_\pm^{DK}$  directly. The Cartesian  $CP$ -violating observables  $x_\pm$  and  $y_\pm$  are employed because they lead to better statistical behaviour than fits to data where the underlying parameters  $(\gamma, r_B^{DK^\pm}, \delta_B^{DK^\pm})$  are determined [], at the cost of introducing a fourth degree of freedom. With the addition of the  $B^\pm \rightarrow D\pi^\pm$  mode as a true signal channel, two new underlying parameters are introduced,  $r_B^{D\pi^\pm}$  and  $\delta_B^{D\pi^\pm}$ . It is only necessary to introduce an additional two, not four, Cartesian parameters [?] by defining

$$\xi_{D\pi^\pm} = \left( \frac{r_B^{D\pi^\pm}}{r_B^{DK^\pm}} \right) \exp[i(\delta_B^{D\pi^\pm} - \delta_B^{DK^\pm})] \quad (2.44a)$$

704 and letting

$$x_\xi^{D\pi} = \text{Re}[\xi_{D\pi^\pm}] \quad y_\xi^{D\pi} = \text{Im}[\xi_{D\pi^\pm}]. \quad (2.44\text{b})$$

705 In terms of these parameters, the usual Cartesian  $x_\pm$  and  $y_\pm$  are given by

$$x_\pm^{D\pi} = x_\xi^{D\pi} x_\pm^{DK} - y_\xi^{D\pi} y_\pm^{DK}, \quad y_\pm^{D\pi} = x_\xi^{D\pi} y_\pm^{DK} + y_\xi^{D\pi} x_\pm^{DK}. \quad (2.45)$$

706 Using this expression, the  $B^\pm \rightarrow D\pi^\pm$  yields can also be defined via Eq. (2.41) in the  
707 maximum-likelihood fit. This allows for a stable fit for all six  $x$  and  $y$  parameters, as  
708 well as the shared  $F_i$ , as described in much greater detail in Chapter 5. Note that  $\xi$   
709 does not depend on  $\gamma$ : all information on  $CP$  asymmetries in both the  $B^\pm \rightarrow DK^\pm$   
710 and  $B^\pm \rightarrow D\pi^\pm$  channels is encoded in  $x_\pm^{DK}$  and  $y_\pm^{DK}$ .

711 The combined analysis of  $B^\pm \rightarrow DK^\pm$  and  $B^\pm \rightarrow D\pi^\pm$  decays presents a sig-  
712 nificant step forward, because it solves the problem of obtaining  $F_i$  parameters  
713 for the appropriate acceptance profile in a manner that avoids leading systematic  
714 uncertainties, and almost all reliance on simulation. This is of great importance,  
715 if the large data samples that will be collected by LHCb in the future are to be  
716 exploited to their full potential.

# 3

717

718

## The LHCb experiment

719 We have a detector? I thought ntuples were made of magic.

### 720 **3.1 Subdetectors**

#### 721 **3.1.1 The VELO**

#### 722 **3.1.2 Magnet and tracking stations**

#### 723 **3.1.3 The RICH**

#### 724 **3.1.4 Calorimeters**

#### 725 **3.1.5 Muon detectors**

### 726 **3.2 Track reconstruction**

### 727 **3.3 The LHCb triggering system**

#### 728 **3.3.1 The level-0 hardware trigger**

#### 729 **3.3.2 High-level triggers**

#### 730 **3.3.3 Offline data filtering: the LHCb stripping**

### 731 **3.4 Simulation**

732 A short description of truth matching: note that all simulation samples described

733 in the thesis have been truth matched appropriately.

<sup>734</sup> Include a short description of RapidSim.

# 4

735

736

737

## Neutral kaon $CP$ violation and material interaction in BPGGSZ measurements

738 The presence of a  $K_S^0$  meson in the  $D \rightarrow K_S^0 h^+ h^-$  final states introduces a small  
739 bias in BPGGSZ measurements due to  $CP$ -violation in the neutral kaon sector  
740 and asymmetries caused by the interaction between the neutral kaons and detector  
741 material. These fundamental physics effects are reviewed in Section 4.1, after which  
742 the chapter presents a detailed analysis of the impact on the LHCb measurement  
743 that is the subject of the thesis, as well as future  $\gamma$  measurements with the Belle II  
744 experiment. Prior to this analysis, the only existing work on the effect on  $\gamma$   
745 measurements suggested a small effect in  $B^\pm \rightarrow DK^\pm$  measurements but potentially  
746 very significant effects in measurements based on  $B^\pm \rightarrow D\pi^\pm$  decays [?]. However,  
747 as described in Section 4.1.1, the analysis in Ref. [?] does not take into account  
748 the fundamental aspect of the BPGGSZ method: that it relies on the phase-space  
749 distribution of signal decays, not phase-space integrated asymmetries. Furthermore,  
750 the study only considers the  $CP$ -violation effect, not material interaction. Therefore,  
751 a more detailed study was necessary before the  $B^\pm \rightarrow D\pi^\pm$  decay mode could  
752 reliably be promoted to a signal channel.

753

754

### 4.1 $CP$ violation and material interaction of neutral kaons

755

756

A brief review of the general phenomenology of mixing and  $CP$  violation in the neutral kaon system is useful, before analysing the impact on  $\gamma$  measurements.

757 The presentation in this section follows the PDG review of  *$CP$  violation in the  
758 quark section [?]*. The general theory considers any pair of neutral mesons  $|M^0\rangle$   
759 and  $|\bar{M}^0\rangle$  related by  $CP$  conjugation

$$CP|M^0\rangle = e^{i\phi_M}|\bar{M}^0\rangle \quad CP|\bar{M}^0\rangle = e^{-i\phi_M}|M^0\rangle, \quad (4.1a)$$

760 where  $\phi_M$  is an arbitrary phase. In this thesis, the convention  $\phi_M = 0$  is chosen  
761 to equal zero, so that

$$CP|M^0\rangle = |\bar{M}^0\rangle \quad CP|\bar{M}^0\rangle = |M^0\rangle. \quad (4.1b)$$

762 A meson state that starts as a general superposition of  $|M^0\rangle$  and  $|\bar{M}^0\rangle$  states

$$\begin{aligned} \psi_M^0 &\equiv \psi_M(0) = a(0)|M^0\rangle + b(0)|\bar{M}^0\rangle \\ &\equiv \psi_{M^0}^0 + \psi_{\bar{M}^0}^0 \end{aligned} \quad (4.2)$$

763 will, over time, involve into a state that consists of a different superposition of  
764  $|M^0\rangle$  and  $|\bar{M}^0\rangle$ , as well as components for all possible states the meson system  
765 can decay into

$$\begin{aligned} \psi_M(t) &= a(t)|M^0\rangle + b(t)|\bar{M}^0\rangle + \sum c_i(t)f_i \\ &\equiv \psi_{M^0}(t) + \psi_{\bar{M}^0}(t) + \sum c_i(t)f_i. \end{aligned} \quad (4.3)$$

766 For time scales that are longer than the typical strong-interaction, the time evolution  
767 of the  $M^0-\bar{M}^0$  superposition can be described by a  $2 \times 2$  Hamiltonian

$$\frac{d}{dt} \begin{pmatrix} \psi_{M^0}(t) \\ \psi_{\bar{M}^0}(t) \end{pmatrix} = -i\mathcal{H}_0 \begin{pmatrix} \psi_{M^0}(t) \\ \psi_{\bar{M}^0}(t) \end{pmatrix} \quad (4.4)$$

768 that is *non-Hermitian* (to allow for decay) but can be parameterised in terms  
769 of two Hermitian matrices  $\mathcal{M}$  and  $\Gamma_0$

$$\mathcal{H}_0 = \mathcal{M} - \frac{i}{2}\Gamma_0. \quad (4.5)$$

770 The quantum states with well-defined (real) masses,  $m_j$ , and (real) decay widths,  
771  $\Gamma_j$ , are the two eigenstates of  $\mathcal{H}_0$  with eigenvalues  $\lambda_j = m_j - \frac{i}{2}\Gamma_j$ . The eigenstates  
772 (of course) evolve independently in time, so that

$$\psi_j(t) = e^{-i\lambda_j t}\psi_j^0 = e^{-im_j t - \frac{\Gamma_j}{2}t}\psi_j^0. \quad (4.6)$$

773 The eigenstates are denoted  $H$  and  $L$  according to the size of  $m_j$ , the real part  
774 of the eigenvalues, such that  $m_H > m_L$ . Assuming that  $\mathcal{H}_0$  conserves  $CPT$  the  
775 eigenstates have the general form

$$\begin{aligned} |M_H\rangle &\equiv p|M^0\rangle - q|\bar{M}^0\rangle \\ |M_L\rangle &\equiv p|M^0\rangle + q|\bar{M}^0\rangle \end{aligned} \quad (4.7)$$

where  $p$  and  $q$  are complex numbers that satisfy  $|q|^2 + |p|^2 = 1$ . With the convention in Eq. (4.1b) it follows that if  $\mathcal{H}_0$  also conserves  $CP$ , so that  $|M_H\rangle$  and  $|M_L\rangle$  are  $CP$  eigenstates, then  $p = \pm q$ , where the sign depends on which of the heavy and the light meson states is  $CP$  even, and which is  $CP$  odd.

The eigenstates of the Hamiltonian governing the neutral kaon system are almost, but not exactly, equal to the  $CP$  eigenstates

$$|K_1\rangle = \frac{|K^0\rangle + |\bar{K}^0\rangle}{\sqrt{2}} \quad |K_2\rangle = \frac{|K^0\rangle - |\bar{K}^0\rangle}{\sqrt{2}}, \quad (4.8)$$

which are  $CP$  even and odd, respectively. This approximate equality leads to the most prominent feature of the neutral kaon system: the two eigenstates of  $\mathcal{H}_0$  have lifetimes that differ by orders of magnitude. This is best understood by assuming, for a moment, that the states in Eq. (4.8) *do* equal the eigenstates with definite life times. The  $K_1$  state can decay in the  $CP$  even  $\pi^+\pi^-$  and  $\pi^0\pi^0$  modes, and does so almost 100% of the time; these decay modes are not available to the  $K_2$  (in the absence of direct  $CP$  violation) which results in a much lower decay rate and much longer life time. Therefore, the eigenstates in the kaon system are labelled the *short-lived* kaon,  $K_S^0$ , which is almost  $CP$  even, and the *long-lived* kaon,  $K_L^0$ , which is almost  $CP$  odd. The life times are [?]

$$\tau_{K_S^0} = (8.954 \pm 0.004) \times 10^{-11} \text{s} \quad \tau_{K_L^0} = (5.116 \pm 0.021) \times 10^{-8} \text{s}. \quad (4.9)$$

Experimentally, it is found that the  $K_S^0$  corresponds to the light eigenstate, but that the mass splitting [?]

$$\begin{aligned} \Delta m = m_{K_L^0} - m_{K_S^0} &= (0.5289 \pm 0.0009) \times 10^{10} \hbar s^{-1} \\ &\simeq 3.5 \times 10^{-6} \text{ eV} \end{aligned} \quad (4.10)$$

is tiny compared to the neutral kaon masses of  $m_{K_S^0} = 497.6 \text{ MeV}/c^2$  [?].

However, the discovery of  $K_L^0 \rightarrow \pi\pi$  decays by Kronin and Fitch in 1964 established that the  $K_S^0$  and  $K_L^0$  are *not* exactly equal to the  $CP$  eigenstates in Eq. (4.8), because the  $\mathcal{H}_0$  relevant to the kaon system is  $CP$ -violating. The  $CP$  violation in the kaon sector is conventionally parameterised in terms of the complex parameters  $\epsilon$  and  $\epsilon'$ , in terms of which

$$\frac{A(K_L^0 \rightarrow \pi^+\pi^-)}{A(K_S^0 \rightarrow \pi^+\pi^-)} = \epsilon + \epsilon' \quad \frac{A(K_L^0 \rightarrow \pi^0\pi^0)}{A(K_S^0 \rightarrow \pi^0\pi^0)} = \epsilon - 2\epsilon'. \quad (4.11)$$

In these expressions  $\epsilon$  denotes the contribution from  $CP$  violation in mixing and  $\epsilon'$  the contribution due to direct  $CP$  violation in the decays. The  $\epsilon$  parameter has been measured to be [?]

$$|\epsilon| = (2.228 \pm 0.011) \times 10^{-3}, \quad \arg \epsilon = (43.52 \pm 0.05)^\circ. \quad (4.12)$$

803 Direct  $CP$  violation is ignored for the remainder of the thesis, because  $\epsilon'$  is measured  
804 to be three orders of magnitude smaller than  $\epsilon$ . In terms of the  $CP$  eigenstates  
805 of Eq. (4.8), the mass eigenstates  $K_S^0$  and  $K_L^0$  are given by

$$\begin{aligned} |K_S^0\rangle &= \frac{|K_1\rangle + \epsilon|K_2\rangle}{\sqrt{1+|\epsilon|^2}} &= \frac{(1+\epsilon)|K^0\rangle + (1-\epsilon)|\bar{K}^0\rangle}{\sqrt{2(1+|\epsilon|^2)}} \\ |K_L^0\rangle &= \frac{|K_2\rangle + \epsilon|K_1\rangle}{\sqrt{1+|\epsilon|^2}} &= \frac{(1+\epsilon)|K^0\rangle - (1-\epsilon)|\bar{K}^0\rangle}{\sqrt{2(1+|\epsilon|^2)}}, \end{aligned} \quad (4.13)$$

806 corresponding to the definition  $p = (1+\epsilon)/\sqrt{2(1+|\epsilon|^2)}$  and  $q = (1-\epsilon)/\sqrt{2(1+|\epsilon|^2)}$   
807 in Eq. (4.7).

808 In an experimental setting, the time evolution of a neutral kaon state is affected  
809 by nuclear interactions with the detector. The interaction is governed by the strong  
810 force, and therefore sensitive to the *flavour* of the kaon state; the interaction  
811 strength is thus different for  $K^0$  and  $\bar{K}^0$  mesons. This difference introduces a  
812 non-zero  $K_S^0 \leftrightarrow K_L^0$  transition amplitude for neutral kaons traversing a detector  
813 segment. This effect was predicted early in the history of kaon physics [?] and is  
814 commonly denoted *kaon regeneration*. The effect can be described by including a  
815 material-interaction term in the Hamiltonian that is diagonal in the  $(|K^0\rangle, |\bar{K}^0\rangle)$   
816 basis, so that the equation governing the time evolution is [?, ?]

$$\frac{d}{dt} \begin{pmatrix} \psi_{K^0}(t) \\ \psi_{\bar{K}^0}(t) \end{pmatrix} = -i \left[ \mathcal{H}_0 + \begin{pmatrix} \chi & 0 \\ 0 & \bar{\chi} \end{pmatrix} \right] \begin{pmatrix} \psi_{K^0}(t) \\ \psi_{\bar{K}^0}(t) \end{pmatrix}. \quad (4.14)$$

817 The complex parameters  $\chi$  and  $\bar{\chi}$  describe the material interaction of the  $K^0$   
818 and  $\bar{K}^0$  flavour eigenstates and are related to their scattering cross section, as  
819 described further in Section 4.3.4. The solution of Eq. (4.14) for the time evolution  
820 in the  $K_S^0$  and  $K_L^0$  states is [?]

$$\begin{aligned} \psi_S(t) &= e^{-i\Sigma t} \left( \psi_S^0 \cos \Omega t + \frac{i}{2\Omega} (\Delta\lambda\psi_S^0 - \Delta\chi\psi_L^0) \sin \Omega t \right), \\ \psi_L(t) &= e^{-i\Sigma t} \left( \psi_L^0 \cos \Omega t - \frac{i}{2\Omega} (\Delta\lambda\psi_L^0 + \Delta\chi\psi_S^0) \sin \Omega t \right), \end{aligned} \quad (4.15)$$

821 in terms of the parameters

$$\begin{aligned} \Delta\chi &= \chi - \bar{\chi}, \\ \Delta\lambda &= \lambda_L - \lambda_S = (m_L - m_S) - \frac{i}{2}(\Gamma_L - \Gamma_S), \\ \Sigma &= \frac{1}{2}(\lambda_S + \lambda_L + \chi + \bar{\chi}), \\ \Omega &= \frac{1}{2}\sqrt{\Delta\lambda^2 + \Delta\chi^2}. \end{aligned} \quad (4.16)$$

822 In the vacuum limit where  $\chi = \bar{\chi} = 0$ , the expressions in Eq. (4.6) and Eq. (4.15) are  
823 equal.

### 4.1.1 A first look at the impact on $\gamma$ measurements

The effects described above have an impact on measurements of  $CP$  asymmetries in modes with a neutral kaon in the final state. This was analysed for the first time in relation to  $\gamma$  measurements by Grossman and Savastio in 2014 [?]. The authors point out two sources of corrections to be included:

- the fact that  $K_S^0$  is not an exact  $CP$  eigenstate can break potential symmetry relations employed in an analysis, and
- that when the neutral kaon is reconstructed in a  $\pi\pi$  final state there will be contributions from both  $K_S^0$  and  $K_L^0$  decays.

The analysis in this chapter considers yet another effect, not treated by Grossman and Savastio, namely that

- material interaction can emulate the effect of neutral kaon  $CP$  violation, because it couples the almost- $CP$ -even  $K_S^0$  and the almost- $CP$ -odd  $K_L^0$  states.

Due to the presence of  $K_L^0 \rightarrow \pi\pi$  decays, Grossman and Savastio point out that the relevant decay rates to consider in an experimental setting are of the form

$$d\Gamma(t) \propto |\psi_S(t) + \epsilon\psi_L(t)|^2. \quad (4.17)$$

The time dependence of the decay rates considered in Chapter 2 was left out because all terms shared a common time dependence. That is not the case in Eq. (4.17), due to the very different decay rates of the  $K_S^0$  and  $K_L^0$  components of the kaon state. As a consequence, the time-integrated yields have the form

$$N \propto \int dt \eta(t) |\psi_S(t) + \epsilon\psi_L(t)|^2, \quad (4.18)$$

where  $\eta(t)$  is the time acceptance in a given experimental setting. Thus, the acceptance is crucial to model in order to correctly estimate the impact of kaon  $CP$ -violation effects on a given measurement.

Considering BPGBSZ measurements, the main effect of neutral kaon  $CP$  violation is a breakdown of the fundamental Dalitz-plot symmetry that is exploited in the derivation of the bin yield equations. Extending the amplitude definition of Eq. (2.21) to include  $K_L^0$  decays

$$A_{S(L)}^{(\overline{D})}(s_-, s_+) = A((\overline{D})^0 \rightarrow K_{S(L)}^0 \pi^+ \pi^-), \quad (4.19)$$

the authors point out that  $CP$ -violation in the  $K_S^0$  system means that the relation  $A_S^{(\overline{D})}(s_{-+}) = A_S^D(s_{+-})$  is not exactly true; and in addition, there is now a

dependence on  $A_L^D(s_{-+})$  which satisfies a different approximate symmetry, namely  $A_L^{\bar{D}}(s_{-+}) \simeq -A_L^D(s_{+-})$ . Grossman and Savastio describe these symmetry breaking effects in detail, but do not explicitly derive the corrections to the yield equations of Chapter 2, nor try to quantify the potential bias on  $\gamma$  in a measurement based on the binned yields. Instead, they derive expressions for the bias in a measurement obtained from phase-space integrated  $CP$  asymmetries. This is done for both GLW measurements that use  $D \rightarrow K_S^0 X$  final states and for the  $D \rightarrow K_S^0 h^+ h^-$  final states; however, for their quantitative estimate of  $\Delta\gamma$  the authors make an approximation that corresponds to assuming that the  $D \rightarrow K_S^0 h^+ h^-$  final state is a  $CP$  eigenstate, making the two results identical. The authors find that in this case, assuming a uniform experimental acceptance for all kaon decay times, the asymmetry has the form<sup>1</sup>

$$A = \frac{2r_B \sin \gamma \sin \delta_B + 2\text{Re}[\epsilon]}{1 + r_B^2 - 2r_B \cos \gamma \cos \delta_B}, \quad (4.20)$$

If a measured value of  $A$  is interpreted to obtain  $\gamma$  without taking the  $\epsilon$  term into account, it leads to a bias of

$$\Delta\gamma = -\frac{\text{Re}[\epsilon]}{r_B \cos \gamma \sin \delta_B} + O(|\epsilon|). \quad (4.21)$$

The scaling  $\Delta\gamma \sim \mathcal{O}(r_B/|\epsilon|)$  is the main result of the analysis by Grossman and Savastio. For  $B^\pm \rightarrow D K^\pm$  decays, where  $r_B^{DK^\pm} \simeq 0.1$  this suggests a bias at the percent level, which is negligible compared to current experimental uncertainties. However, in the  $B^\pm \rightarrow D \pi^\pm$  case, where  $r_B^{D\pi^\pm} \simeq 0.005$  [?], their result suggests relative biases that are potentially of  $\mathcal{O}(1)$ .

The conclusions are lacking on two accounts, however. Firstly, as made clear in Section 2.3.5, the  $K_S^0 \pi^+ \pi^-$  and  $K_S^0 K^+ K^-$  states are *far from*  $CP$  eigenstates. From the asymmetry expression in that section, it is clear that the bias in a determination of  $\gamma$  based on phase-space asymmetries will in fact scale as

$$\Delta\gamma \sim \mathcal{O}\left(\frac{|\epsilon|}{(2\mathcal{F}_+ - 1)r_B}\right), \quad (4.22)$$

which suggests that Grossman and Savastio severely *underestimates* the potential impact. This is described in detail in Section 4.2.3. More importantly, the analysis of the phase-space integrated asymmetry is in fact *irrelevant* to BPGGSZ measurements as they are currently performed: as described in Section 2.3.5 the information from

---

<sup>1</sup>In fact the expression in Eq. (4.20) is missing a term, as will be clear when an analogous expression is derived in detail in Section 4.2.3.

the global asymmetry is completely discarded. Therefore it is necessary to analyse the effects of kaon  $CP$ -violation on a full, binned analysis of  $D \rightarrow K_S^0 h^+ h^-$  decays, which is done in detail in the following sections. While the aim is to extend the analysis if Grossman and Savastio, the treatment in the following sections is completely independent of that in Ref. [?].

## 4.2 Impact on BPGBSZ measurements of $\gamma$ : principles

The analysis of the impact on BPGBSZ measurements is carried out in two stages. This section treats the leading order effects analytically, and derives the overall order of magnitude of the expected bias in a general setting. Then Section 4.3 presents a detailed numerical study of the expected effect in measurements with the LHCb and Belle II experiments specifically, because these will be crucial to constrain  $\gamma$  during the coming decade [?, ?].

### 4.2.1 Modified symmetry relations

In order to derive the corrections to the asymmetry relation  $A_S^D(s_{-+}) \simeq A_S^{\bar{D}}(s_{+-})$ , it is beneficial to express  $A_{S(L)}^D$  in terms of the amplitudes

$$A_{1/2}^{\bar{D}} = A(\overline{D}^0 \rightarrow K_{1/2}^0 \pi^+ \pi^-), \quad (4.23)$$

because these amplitude satisfy the exact symmetries  $A_1^D(s_{-+}) = A_1^{\bar{D}}(s_{+-})$  and  $A_2^D(s_{-+}) = -A_2^{\bar{D}}(s_{+-})$ . This approach is different to that of Grossman and Savastio, but the final results are equivalent. After the decay of a  $D^0$  meson to a neutral kaon, the kaon state is

$$\begin{aligned} \psi^0 &= A_1^D |K_1\rangle + A_2^D |K_2\rangle \\ &= N \left[ (A_1^D - \epsilon A_2^D) |K_S^0\rangle + (A_2^D - \epsilon A_1^D) |K_L^0\rangle \right], \end{aligned} \quad (4.24)$$

with the normalisation constant  $N = \sqrt{1 + |\epsilon|^2}/(1 - \epsilon^2)$ . Thus it can be seen that

$$\begin{aligned} A_S^D(s_{-+}) &= N \left[ (A_1^D(s_{-+}) - \epsilon A_2^D(s_{-+})) \right], \\ A_L^D(s_{-+}) &= N \left[ (A_2^D(s_{-+}) - \epsilon A_1^D(s_{-+})) \right], \end{aligned} \quad (4.25)$$

900 with an analogous expression for the  $\bar{D}^0$  decay amplitudes. Therefore, the generalised  
901 relations between the  $D^0$  and  $\bar{D}^0$  amplitudes are

$$\begin{aligned} A_S^{\bar{D}}(s_{+-}) &= N[A_1^{\bar{D}}(s_{+-}) - \epsilon A_2^{\bar{D}}(s_{+-})] \\ &= N[A_1^D(s_{-+}) + \epsilon A_2^D(s_{-+})] = A_S^D(s_{-+}) + 2N\epsilon A_2^D(s_{-+}), \\ A_L^{\bar{D}}(s_{+-}) &= N[A_2^{\bar{D}}(s_{+-}) - \epsilon A_1^{\bar{D}}(s_{+-})] \\ &= -N[A_2^D(s_{-+}) + \epsilon A_1^D(s_{-+})] = -A_L^D(s_{-+}) - 2N\epsilon A_1^D(s_{-+}). \end{aligned} \quad (4.26)$$

#### 902 4.2.2 Relationship between the $K_S^0$ and $K_L^0$ amplitudes

903 The decay amplitude  $A(D^0 \rightarrow K_S^0 \pi^+ \pi^-)$  has been carefully studied, and a number  
904 of amplitude models have been published [?, ?, ?, ?, ?]. No models have been  
905 published for  $D^0 \rightarrow K_L^0 \pi^+ \pi^-$  decays. However, following an approach laid out by  
906 the CLEO collaboration [?], the two amplitudes can be related. Again, this is  
907 most easily done by relating the  $A_1^D(s_{+-})$  and  $A_2^D(s_{+-})$  amplitudes. In the isobar  
908 formalism, the decay amplitude  $A(D^0 \rightarrow K_1 \pi^+ \pi^-)$  is expressed as a non-resonant  
909 constant amplitude plus a sum of resonances

$$A(D^0 \rightarrow K_1 \pi^+ \pi^-) = k_{NR} + \sum_{CF} k_i R^i(s_{K\pi^-}) + \sum_{DCS} k_j R^j(s_{K\pi^+}) + \sum_{R_{\pi\pi}} k_k R^k(s_{\pi^+\pi^-}). \quad (4.27)$$

910 The resonances are split into Cabibbo-favoured (CF)  $K^{*-}$  resonances, doubly  
911 Cabibbo-suppressed (DCS)  $K^{*+}$  resonances and  $\pi\pi$  resonances.<sup>2</sup> The CF resonances  
912 couple to the  $\bar{K}^0$  component of  $K_1 (\propto K^0 + \bar{K}^0)$ , and therefore the corresponding  
913  $k_i$  in the  $K_2 (\propto K^0 - \bar{K}^0)$  amplitude will have a relative minus sign. The DCS  
914 resonances couple to the  $K^0$  component of  $K_1$ , and so the corresponding  $k_j$  in the  
915  $K_2$  amplitude will have a relative plus sign. For the  $h^+ h^-$  resonances, there will be  
916 a coupling to both the  $K^0$  and  $\bar{K}^0$  components, however the coupling to the  $K^0$   
917 component is expected to be suppressed with a Cabibbo suppression factor  $r_k e^{i\delta_k}$ ,  
918 where  $r_k \simeq \tan^2 \theta_C \simeq 0.05$  is determined by the Cabibbo angle  $\theta_C$  and  $\delta_k$  can take  
919 any value. Therefore, the  $k_k$  for these resonances have a relative  $-(1 - 2r_k e^{i\delta_k})$   
920 factor in the  $K_2$  amplitude. The same effect leads to the differences in decay rates  
921 between  $D^0 \rightarrow K_S^0 \pi^0$  and  $D^0 \rightarrow K_L^0 \pi^0$  decays [?, ?]. Thus, given a model of the

---

<sup>2</sup>In modern models, the  $\pi\pi$  and  $K\pi$   $S$ -wave components are modelled via the  $K$ -matrix formalism and LASS parametrisations, respectively, instead of sums of individual resonances [?]. This does not alter the arguments below, as the  $R$  functions of Eq. (4.27) can equally well represent such terms.

922 form in Eq. (4.27), a model for the  $A(D^0 \rightarrow K_2\pi^+\pi^-)$  amplitude will have the form

$$A(D^0 \rightarrow K_2\pi^+\pi^-) = k_{NR} + \sum_{CF} (-k_i) R^i(s_{K\pi^-}) + \sum_{DCS} (+k_j) R^j(s_{K\pi^+}) \\ + \sum_{R_{\pi\pi}} (-(1 - 2r_k e^{i\delta_k}) k_k) R^k(s_{\pi^+\pi^-}). \quad (4.28)$$

923 An important consequence of these substitution rules is that

$$A_2^D(s_{+-}) = -A_1^D(s_{+-}) + r_A \Delta A(s_{+-}), \quad (4.29)$$

924 where  $r_A \simeq \tan^2 \theta_C$  and  $\Delta A(s_{+-}) \sim A_1^D(s_{+-})$  are of the same order of magnitude  
925 (at least when averaged over the bins used in  $\gamma$  measurements). This relation is  
926 sufficient to make the qualitative arguments of this section, while the full set of  
927 substitution rules above are used in the quantitative studies of Section 4.3.

### 928 4.2.3 Modification of the BPGBSZ yield equations

929 With suitable models to calculate  $A_{S(L)}^{\bar{D}}$  (or  $A_{1/2}^{\bar{D}}$ ) and knowledge of  $\Delta\chi$  for the  
930 materials relevant to an experimental setting, the relations derived in the preceding  
931 sections can be employed to calculate the expected phase-space bin yields,  $N_i^\pm$ ,  
932 including the effects of kaon  $CP$  violation and material interaction. The decay  
933 rates have additional terms compared to those in Eq. (2.24), because the  $K_L^0$   
934 contribution must be taken into account

$$d\Gamma(t, s_{+-}) \propto |\psi_S(t, s_{+-}) + \epsilon\psi_L(t, s_{+-})|^2, \quad (4.30)$$

935 where the time-dependence of  $\psi_{S/L}(t, s_{+-})$  is governed by Eq. (4.15), and the phase-  
936 space dependence is included in the state component, by defining  $\psi_{S/L}^0$  in terms of  
937  $A_{S(L)}^{\bar{D}}(s_{+-})$ . For example, for the case of a  $B^- \rightarrow DK^-$  decay, the definition is

$$\begin{aligned} \psi_{S/L}^{0,B^-}(s_{+-}) &= A_S^D(s_{+-}) + r_B e^{i(\delta_B - \gamma)} A_S^{\bar{D}}(s_{+-}) \\ &= A_1^D(s_{+-}) - \epsilon A_2^D(s_{+-}) + r_B e^{i(\delta_B - \gamma)} (A_1^{\bar{D}}(s_{+-}) - \epsilon A_2^{\bar{D}}(s_{+-})) \\ &= A_1^D(s_{+-}) - \epsilon A_2^D(s_{+-}) + r_B e^{i(\delta_B - \gamma)} (A_1^D(s_{+-}) + \epsilon A_2^D(s_{+-})). \end{aligned} \quad (4.31)$$

938 It is useful to look at the corrections to the BPGBSZ yield expressions in Eq. (2.25)  
939 to lowest order in  $\epsilon$  and  $r_\chi = \frac{1}{2} \frac{\Delta\chi}{\Delta\lambda}$ , the dimensionless parameter governing material  
940 interactions. For LHCb and Belle II the average  $|r_\chi| \simeq 10^{-3}$ , as detailed in the  
941 Section 4.3. To first order in  $r_\chi$ , the time-dependent kaon states within a material,  
942 given in Eq. (4.15), simplify to [?]

$$\begin{aligned} \psi_S(t, s_{+-}) &= e^{-\frac{i}{2}(x+\bar{x})t} e^{-i\lambda_S t} (\psi_S^0(s_{+-}) - r_\chi (1 - e^{-i\Delta\lambda t}) \psi_L^0(s_{+-})), \\ \psi_L(t, s_{+-}) &= e^{-\frac{i}{2}(x+\bar{x})t} e^{-i\lambda_L t} (\psi_L^0(s_{+-}) + r_\chi (1 - e^{+i\Delta\lambda t}) \psi_S^0(s_{+-})). \end{aligned} \quad (4.32)$$

943 By inserting these expressions into Eq. (4.30) and employing the definition in  
944 Eq. (4.31) (and a similar definition for  $B^+$  decays), the binned yields can be  
945 calculated by an integration over time and phase space. In the remainder of this  
946 section, it is assumed that the experimental time acceptance is  $\eta(t) = 1$  for all times  
947 and that  $r_\chi$  is constant at all times; more realistic assumptions are introduced in  
948 Section 4.3. In this case, the binned yields are given by the expression

$$N_i^- = h_B^{-'} \left( \hat{K}_{+i} + r_B^2 \hat{K}_{-i} + 2\sqrt{\hat{K}_{+i} \hat{K}_{-i}} (x_- \hat{c}_i + y_- \hat{s}_i) + O(r\epsilon) \right), \\ N_i^+ = h_B^{+'} \left( \hat{K}_{-i} + r_B^2 \hat{K}_{+i} + 2\sqrt{\hat{K}_{+i} \hat{K}_{-i}} (x_+ \hat{c}_i - y_+ \hat{s}_i) + O(r\epsilon) \right), \quad (4.33)$$

949 where a number of new parameters have been defined, and where  $O(r\epsilon)$  denotes terms  
950 of  $O(r_A\epsilon)$ ,  $O(r_B\epsilon)$ ,  $O(r_A r_\chi)$ , and  $O(r_B r_\chi)$ . Since  $r_B \sim r_A \sim 10^{-1}$  (in  $B^\pm \rightarrow D K^\pm$   
951 decays) and  $r_\chi \sim \epsilon \sim 10^{-3}$ , these terms are all of the same order of magnitude.

952 The new normalisation constants  $h_B^{\pm'} = h_B^\pm (1 + |\epsilon + r_\chi|^2 \frac{\Gamma_S}{\Gamma_L} \mp \Delta h)$  are de-  
953 fined in terms of

$$\Delta h = 2\text{Re}[\epsilon + r_\chi] - 4 \frac{\Gamma_S}{\Gamma_L + \Gamma_S} \frac{\text{Re}[\epsilon + r_\chi] + \mu \text{Im}[\epsilon + r_\chi]}{1 + \mu^2}, \quad \mu = 2 \frac{m_L - m_S}{\Gamma_L + \Gamma_S}. \quad (4.34)$$

954 The  $\hat{K}_i$  parameters are defined to be

$$\hat{K}_i = \frac{1}{1 + |\epsilon + r_\chi|^2 \frac{\Gamma_S}{\Gamma_L}} \left( K_i^{(1)} + |\epsilon + r_\chi|^2 \frac{\Gamma_S}{\Gamma_L} K_i^{(2)} \right), \quad (4.35)$$

955 in which the  $K_i^{(1/2)}$  parameters are phase-space integrals, defined as in Eq. (2.27)  
956 but for  $A_{1/2}^D$ . To lowest order, the  $\hat{K}_i$  correspond to the fractional  $D^0$  decay yield  
957 in each bin, as obtained in a measurement that averages  $D^0$  and  $\bar{D}^0$  decays, and  
958 assumes the  $A_S^D(s_{-+}) = A_S^D(s_{+-})$  symmetry to be exact:

$$K_i^{\text{meas}} \equiv \frac{N_i^D + N_{-i}^{\bar{D}}}{\sum_j N_j^D + N_{-j}^{\bar{D}}} = \hat{K}_i + \mathcal{O}(r\epsilon). \quad (4.36)$$

959 Here,  $N_i^D$  ( $N_i^{\bar{D}}$ ) is the expected yield of flavour tagged  $D^0$  ( $\bar{D}^0$ ) mesons into bin  
960  $i$  of the  $D$  decay phase-space.

961 In similar fashion, the parameters  $(\hat{c}_i, \hat{s}_i)$  have been introduced to denote the  
962 *measured* average strong-phases, which are expected to differ from  $(c_i, s_i)$  at  $O(\epsilon)$ ,  
963 since neutral kaon  $CP$  violation is not taken into account in the measurements  
964 by CLEO. Thus, any corrections arising if  $(\hat{c}_i, \hat{s}_i)$  and  $(c_i, s_i)$  are substituted in  
965 Eq. (4.33) will appear in the  $O(r_B\epsilon)$  terms.

966 Two observations can be made from the expression in (4.33). The first is that  
967 the phase-space *distribution* is only changed at  $O(r\epsilon)$  compared to the expression in

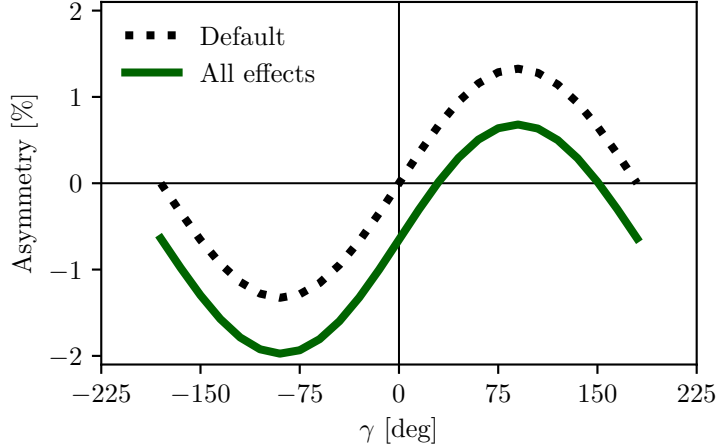


**Figure 4.1:** The asymmetry  $A_{\text{total}}$  as a function of  $\gamma$  calculated to  $O(\epsilon)$  using Eq. (4.37). The calculation is made using for (black dotted line) the default case where  $\Delta h = 0$  and (green) including neutral kaon  $CP$ -violation and material interaction with  $r_\chi = \epsilon$ .

Eq. (2.25), if the measured  $\hat{K}_i$  are used in the experimental analysis. This equally true whether the  $K_i$  are fitted in the signal channel along with  $x_\pm$  and  $y_\pm$ , as is the case in the measurement presented in the thesis, or if they are obtained in a control channel with flavour tagged  $D$  decays, according to Eq. (4.36). As the  $D^0 - \bar{D}^0$  interference term that provides sensitivity to  $\gamma$  enters at order  $O(r_B)$ , the impact on  $\gamma$  measurements can be expected to be  $\Delta\gamma/\gamma \sim O(r\epsilon/r_B)$ . For  $B \rightarrow DK$  analyses, where  $r_B \simeq 0.1$ , this is at the permille level, so the induced  $\Delta\gamma$  bias can be expected to be smaller than  $1^\circ$ . Even in the case of  $B^\pm \rightarrow D\pi^\pm$  decays, this suggests biases that are maximally a few percent. This is the main result of the chapter, because it means that the effect of neutral kaon  $CP$  violation and material interaction is small compared to the precision of the measurement that is the main subject of the thesis.

The second observation relates to potential future measurements of  $\gamma$ , which may also include sensitivity from the total, phase-space-integrated yield asymmetry

$$A_{\text{total}} = \frac{N^- - N^+}{N^- + N^+} = \frac{2(2\mathcal{F}_+ - 1)r_B \sin \delta_B \sin \gamma + \Delta h}{1 + r_B^2 + 2(2\mathcal{F}_+ - 1)r_B \cos \delta_B \cos \gamma} + O(r\epsilon), \quad (4.37)$$

where the definition of  $\mathcal{F}_+$  from Section 2.3.5 has been employed. In the limit  $r_B \rightarrow 0$  the expression agrees with the result for the analogous asymmetry in  $D^\pm \rightarrow \pi^\pm K_S^0$  decays in Ref. [?], evaluated to  $O(\epsilon)$  for an infinite and uniform time-acceptance. As hinted at above, the fact that  $\mathcal{F}_+ \simeq 0.5$  means that the asymmetry due to  $\gamma$  being non-zero is not  $\mathcal{O}(r_B)$ , but of approximately the same order of magnitude as the asymmetry due to  $CP$  violation in the neutral kaon sector, governed by  $\Delta h$ . This is illustrated in Fig. 4.1, where the expression in Eq. (4.37) is plotted in the default

988 case where  $\Delta h = 0$ , using the model in Ref. [?] to calculate  $K_i$  and  $c_i$ , as well as  
989 including neutral kaon  $CP$  violation and material interaction effects, calculated using  
990  $r_\chi = \epsilon$ , with  $\epsilon$  taking the value in Eq. (4.12). The asymmetry changes significantly  
991 when including the latter effects. Therefore, measurements based only on the global  
992 asymmetry will suffer relative biases of tens of degrees, not a few degrees, if neutral  
993 kaon  $CP$  violation and material interaction is not taken into account.

994 **4.3 Impact on BPGBSZ measurements of  $\gamma$ :**  
995 **LHCb and Belle II measurements**

996 The previous section has established that the bias due to neutral kaon  $CP$  violation  
997 and material interaction is at the sub-percent level for measurements based on  
998  $B^\pm \rightarrow DK^\pm$  decays, and just a few percent in  $B^\pm \rightarrow D\pi^\pm$  decays. Thus, the effects  
999 only contribute a manageable systematic uncertainty in the measurement that is  
1000 the subject of the thesis. However, the expected precision on  $\gamma$  measurements  
1001 will increase significantly in the coming decade, as both the LHCb [?] and Belle  
1002 II [?] collaborations expect to make BPGBSZ measurements that measure  $\gamma$  with  
1003 a precision of 1–3°. Therefore a deeper understanding of the expected bias for  
1004 these specific experiments is important.

1005 This section details a study, where the equations of the previous section are  
1006 evaluated numerically to all orders, and care is taken to realistically model the  
1007 experiment specific conditions. The scope of the original analysis, published in  
1008 Ref. [?], was a stand-alone paper that covers both LHCb and Belle II, and which  
1009 therefore does not rely on full detector simulation. Instead the following approaches  
1010 are taken to model the necessary input

- 1011 • the experimental time-acceptance is modelled based on the detector geometry  
1012 and typical neutral kaon momentum spectrum
- 1013 • the material interaction is included, using the material budget information  
1014 available in the technical design reports on each experiment
- 1015 • both the time-acceptance and material interaction depends on the neutral  
1016 kaon momentum, for which realistic distributions are estimated using the  
1017 `RapidSim` simulation package [?].

1018 Each input is described in detail in the following sections. The study has been  
1019 repeated to assign a systematic uncertainty to the LHCb measurement in Chapter 5,  
1020 with slight adjustments to match the exact fit setup and with the inputs above  
1021 extracted from full LHCb simulation. This is described further in Section 4.3.7.

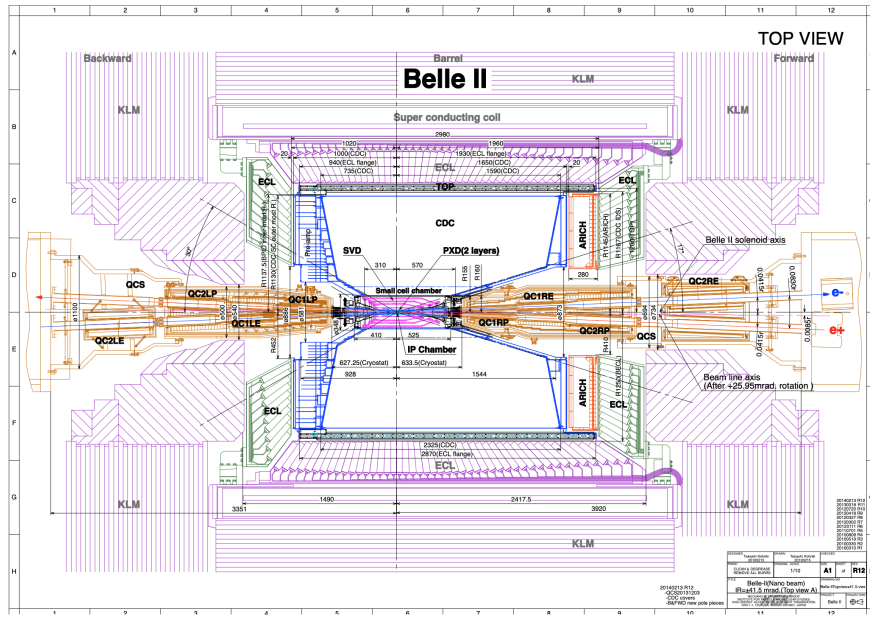


**Figure 4.2:** Schematic of the Belle II detector, reproduced from Ref. [?].

### 1022 4.3.1 Detector geometries

1023 The LHCb geometry and sub detectors are described in details in Chapter 3. In the  
 1024 LHCb measurement discussed in Chapter 5, the  $K_S^0$  mesons are reconstructed in  
 1025 the  $\pi^+\pi^-$  final state and two distinct categories of decay are considered, depending  
 1026 on where in the detector the  $K_S^0$  decay occurs. The categories have very different  
 1027 decay-time acceptance, and therefore two scenarios are considered for LHCb: one  
 1028 in which the decay products of the  $K_S^0$  leave reconstructed tracks in both the silicon  
 1029 vertex detector and downstream tracking detectors (denoted *long-long* or LL), and  
 1030 one in which the decay products of the  $K_S^0$  only leave tracks in the downstream  
 1031 tracking detectors (denoted *down-down* or DD).

1032 The Belle II detector is a general purpose spectrometer, built to collect data  
 1033 from asymmetric  $e^+e^-$  collisions made by the SuperKEKB accelerator in Japan [?].  
 1034 A schematic of the detector is shown in Fig. 4.2. The relevant sub detectors for  
 1035 the present study are the tracking detectors: a central silicon vertex detector,  
 1036 comprised of a total of six layers within 140 mm of the beam, and a large volume  
 1037 drift chamber with 56 wire layers, extending to a radius of 1130 mm [?]. A single  
 1038 scenario is considered for Belle II, because essentially all the  $K_S^0$  mesons produced  
 1039 in signal decays in Belle II decay within the tracking volume, with more than 90 %  
 1040 decaying in the vertex detector according to the studies described below. Thus,  
 1041 three scenarios are considered in total: LL LHCb, DD LHCb, and Belle II.

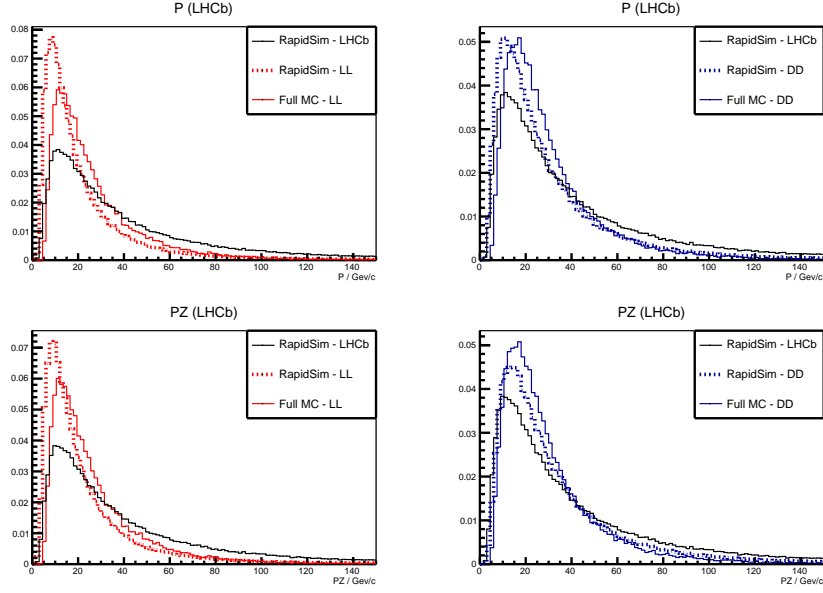


**Figure 4.3:** Momentum spectra for the  $K_S^0$  meson in LHCb, as generated using **RapidSim** (black lines) directly, as well as reweighted to match decay time acceptance in the (red) LL and (blue) DD data categories of LHCb. The LHCb spectra are compared with the spectra in fully simulated signal decays, for both (dotted red lines) LL and (dotted blue lines) DD data categories.

### 1042 4.3.2 Kaon momentum distributions

1043 The neutral kaon momentum distributions are obtained using **RapidSim** [?], a simple  
1044 tool to generate MC samples. **RapidSim** has an inbuilt capability to generate decays  
1045 of  $B$  mesons with the kinematic distribution found in LHCb collisions and falling in  
1046 the LHCb acceptance. However, the distributions need to be reweighted to take the  
1047 kaon-decay-time acceptance into account. After being reweighted, the **RapidSim**  
1048 momentum spectra are reasonably close to those found in full LHCb simulation  
1049 samples of  $B^\pm \rightarrow D(\rightarrow K_S^0\pi^+\pi^-)K^\pm$  decays, as seen in Fig. 4.3

1050 At Belle II, the signal  $B$  mesons stem from decays of  $\Upsilon(4S)$  mesons produced in  
1051 asymmetric electron-positron collisions. This leads to substantially different decay  
1052 kinematics in comparison to those found at LHCb. The momentum distribution in  
1053 Belle II is estimated by letting **RapidSim** decay  $B$  mesons with a momentum of 1.50  
1054 GeV/ $c$  along the  $z$ -axis using **RapidSim**, corresponding to the  $\gamma\beta = 0.28$  boost of  
1055 the centre-of-mass system in Belle II when operated at the  $\Upsilon(4S)$  resonance [?]. A  
1056 perfect  $4\pi$  angular acceptance is assumed. It is not necessary to reweigh the Belle II  
1057 momentum spectrum to account for the kaon-decay-time acceptance because all  
1058 produced  $K_S^0$  mesons decay in the tracking volume.

1059 The resulting momentum distributions for the three types of sample are shown in  
1060 Fig. 4.4.

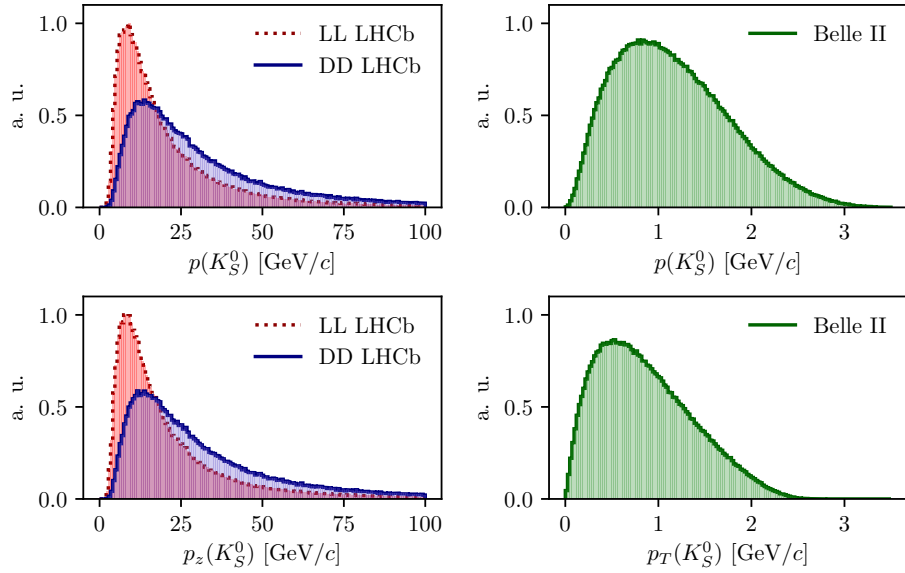


**Figure 4.4:** Momentum distributions for the LHCb (red dotted line) LL and (blue) DD categories, as well as (green) Belle II, obtained using `RapidSim`.

### 4.3.3 Experimental time acceptance

In order to model the experimental time acceptance, the time-dependent decay rates are only integrated over a finite time interval  $(\tau_1, \tau_2)$ . The intervals are defined for each of the three experimental categories, by requiring that a neutral kaon, if produced at  $x = y = z = 0$  with momentum  $p = (p_T, p_z)$ , decays within the relevant part of the corresponding detector. For the LL LHCb category, it is required that the kaon decays before reaching  $z_{max} = 280$  mm, corresponding to a decay where the decay products traverse at least 3 VELO segments (ignoring a number of widely spaced VELO segments placed at a distance of up to  $z = 750$  mm from the interaction point) [?]. For the DD LHCb category a decay at  $z \in [280, 2350]$  mm is required, corresponding to decay between the LL cut-off and the first downstream tracking station [?]. The time acceptance has a significant impact for the LHCb categories, where some 20 % of the kaons escape the tracking stations completely before decaying.

For Belle II, it is assumed that the  $K_S^0$  reconstruction is similar to the Belle  $K_S^0$  reconstruction, which is based on a neural network and reconstructs  $K_S^0$  decays for which the decay product leave tracks in both the drift chamber and silicon vertex detectors, as well as decays that leave tracks in the drift chamber only [?, ?]. Therefore, the  $K_S^0$  decay is required to be within  $r_{max} = 1130$  mm of the beam axis, corresponding to a decay within the outer radius of the drift-chamber. In practice,

1081 most of the kaons decay inside the silicon vertex detector, and requiring a decay  
1082 before 1130 mm is essentially equivalent to having no time cut-off.

#### 1083 4.3.4 Detector material budget

1084 The effect of the material interaction is governed by parameter  $\Delta\chi$  of Eq. (4.16). The  
1085 parameter varies along a given kaon path, as the kaon intersects detector components  
1086 made of different materials. In these studies, the calculations are simplified by  
1087 using a single average material parameter for each experimental scenario. The  
1088 average material parameters can be estimated for a given experimental scenario  
1089 by considering the type and length of material traversed by a kaon in the relevant  
1090 sub-detector(s). The average value is estimated, by exploiting that  $\Delta\chi$  is related to  
1091 the forward scattering amplitude  $f$  ( $\bar{f}$ ) of  $K^0$  ( $\bar{K}^0$ ) mesons in a given material [?, ?]

$$\Delta\chi = -\frac{2\pi\mathcal{N}}{m_K}(f - \bar{f}) = -\frac{2\pi(N_A\rho/A)}{m_K}(f - \bar{f}), \quad (4.38)$$

1092 where  $\mathcal{N} = N_A\rho/A$  is the scattering centre density of the material,  $m_K$  is the mass  
1093 of the kaon state,  $A$  and  $\rho$  are the nucleon number and density of the material,  
1094 and  $N_A$  is Avogadro's number. Measurements made for a range of nuclei [?] show  
1095 that in the momentum range  $p_K \in [20, 140] \text{ GeV}/c$

$$\left| \frac{f - \bar{f}}{p_K} \right| = 2.23 \frac{A^{0.758}}{p_K^{0.614}(\text{GeV}/c)} \text{ mb}, \quad \arg[f - \bar{f}] = -\frac{\pi}{2}(2 - 0.614), \quad (4.39)$$

1096 where the phase of  $\Delta f$  is determined via a phase-power relation [?]. In the numerical  
1097 studies presented here, Eq. (4.39) is also used for the low momentum neutral kaons  
1098 in the Belle II calculations, as a more detailed modelling of the low momentum  $\Delta\chi$   
1099 based on Ref. [?] is found to yield very similar results. The scattering centre density  
1100  $\mathcal{N}$  is approximated as being constant, equal to the average density along a neutral  
1101 kaon path due to its intersection with different detector segments. This average  
1102 is estimated using the simplifying assumption that the total detector material  
1103 budget is due to silicon. In practice,  $\mathcal{N} = N_A\rho/A$  is calculated using  $A = 28$  and  
1104  $\rho = f^{\text{Si}}\rho^{\text{Si}}$ , where  $f^{\text{Si}} < 1$  is the average fraction of a neutral kaon path length that  
1105 is inside detector material, estimated via the known dimensions of the detector, the  
1106 average nuclear interaction length seen by a track traversing it cf. the technical  
1107 design reports [?, ?], and the nuclear interaction length of silicon  $\lambda_I^{\text{Si}} = 465.2 \text{ mm}$  [?].  
1108 The average value of  $r_\chi = \frac{1}{2}\frac{\Delta\chi}{\Delta\lambda}$ , which governs the size of the matter regeneration  
1109 effect, can be calculated for the three considered experimental scenarios and satisfy  
1110  $|r_\chi^{\text{LL}}| = 2.7 \times 10^{-3}$ ,  $|r_\chi^{\text{DD}}| = 2.2 \times 10^{-3}$ , and  $|r_\chi^{\text{Belle II}}| = 1.0 \times 10^{-3}$ .

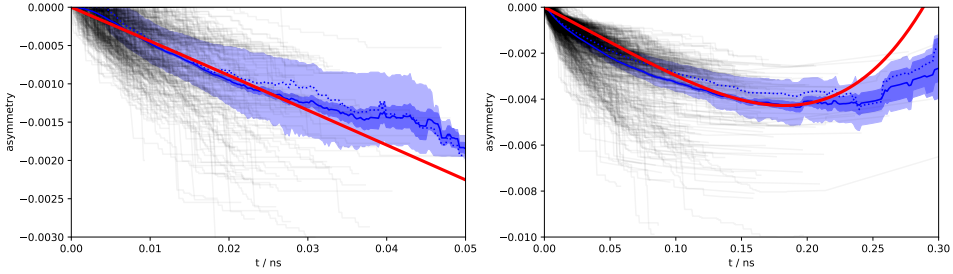


**Figure 4.5:** The asymmetry in Eq. (4.40) as a function of time for (left) LL and (right) DD  $K_S^0$  tracks in a simulated LHCb sample. The black lines show individual tracks. The light blue area is the central 50 % quantile, the dark blue area is the  $1\sigma$  uncertainty band on the mean. The red lines are calculated using the average  $\Delta\chi$  values that are also used in the calculation of biases in BPGGSZ measurements.

The neutral kaon tracks in LHCb generally pass through somewhere between zero (for a significant amount of the LL tracks) and a hundred (for some DD tracks) distinct detector segments. Therefore it is worth examining the degree to which using a single average  $\Delta\chi$  value, obtained following the procedure outlined above, provides a reasonable description of the average material interaction. This can be done using full LHCb simulation, where the kaon state for a simulated track can be evaluated at all times, by applying Eq. (4.15) iteratively for each detector segment the track traverses, using a  $\Delta\chi$  value appropriate for that segment. This is done in Fig. 4.5 for a simple observable: the yield asymmetry

$$A_{K^0} = \frac{|\psi_K^0(t)|^2 - |\psi_{\bar{K}^0}(t)|^2}{|\psi_K^0(t)|^2 + |\psi_{\bar{K}^0}(t)|^2}, \quad (4.40)$$

where  $\psi_K^0(t)$  ( $\psi_{\bar{K}^0}(t)$ ) is the amplitude for an initial  $K^0$  ( $\bar{K}^0$ ) to decay to two pions at time  $t$ . In this calculation, it is assumed that  $\epsilon = 0$  to isolate the material effect with no asymmetry contribution from the inherent  $CP$ -violation in the neutral kaon sector. While the track-by-track asymmetries are found to differ significantly depending on the exact detector segments a track intersects, the average asymmetry is seen to evolve smoothly as a function of decay time, and in reasonable agreement with the asymmetry value that is calculated using the average  $\Delta\chi$  values estimated above.

The LHCb detector is undergoing a significant upgrade prior to the start of the LHC Run 3. However, the material budget and geometry of the relevant sub-detectors will be similar to the sub-detectors used during Run 1 and 2 [?, ?]. Hence the results of this study will be valid for measurements during the upgrade phases of LHCb, even though the detector parameters presented in this section relate to the original LHCb detector.

### 1133 4.3.5 Calculation procedure

1134 The main idea in the bias study is to calculate the BPGBSZ bin yields including  
1135 the full effect of neutral kaon  $CP$  violation and material, fit them using the default  
1136 equations of Chapter 2, and obtain the bias  $\Delta\gamma = \gamma - \gamma^0$  due to the kaon effects not  
1137 being considered in the parameter extraction. For the purpose of Ref. [?], a simple  
1138 fit setup of a single  $B^\pm \rightarrow Dh^\pm$  mode is investigated, where the  $K_i$  parameters are  
1139 determined in a control channel with the relevant experimental acceptance. This  
1140 setup is modified in the study used to assign a systematic uncertainty on the LHCb  
1141 measurement of Chapter 5, as described in Section 4.3.7 below.

1142 In practice, the amplitude model for  $D^0 \rightarrow K_S^0 \pi^+ \pi^-$  decays in Ref. [?] is taken  
1143 to represent the  $A_1(s_{+-})$  amplitude. Then  $A_2(s_{+-})$  is obtained as described in  
1144 Section 4.2.2. In terms of  $A_1$  and  $A_2$ , the amplitudes  $A_{S(L)}^{(\bar{D})}(s_{+-})$  can be expressed  
1145 and related via Eqs. (4.25) and (4.26), and the full signal decay amplitudes as a  
1146 function of phase-space coordinates, time, and the material interaction parameter  
1147  $\Delta\chi$  can be calculated for a given set of input parameters  $(\gamma^0, r_B^0, \delta_B^0)$ . The squared  
1148 decay amplitudes are then integrated over phase space and the kaon decay times  
1149 to obtain the binned signal yield.

1150 The signal yields depend on the momentum via the time-acceptance parameters  
1151  $\tau_1$  and  $\tau_2$ , and because the material interaction parameter  $\Delta\chi$  is momentum  
1152 dependent. Therefore, the yields are averaged over the  $K_S^0$  momentum distributions  
1153 of LHCb and Belle II.

1154 The parameters  $x_\pm$  and  $y_\pm$  are determined by a maximum likelihood fit to the  
1155 calculated yields, after which the fit result and covariance matrix are interpreted in  
1156 terms of the physics parameters  $(\gamma, r_B, \delta_B)$  using another maximum likelihood  
1157 fit [?]. In the fits, the  $K_i$  are obtained using the definition  $K_i = K_i^{\text{meas}} =$   
1158  $(N_i^D + N_{-i}^{\bar{D}})/(\sum_j N_j^D + N_{-j}^{\bar{D}})$ , in terms of the expected yields  $N_i^D$  ( $N_i^{\bar{D}}$ ) of a flavour-  
1159 tagged  $D^0$  ( $\bar{D}^0$ ) decays in bin  $i$  of the  $D$  decay phase space, calculated as described  
1160 above for  $r_B^0 = 0$ . This corresponds to experimentally measuring the  $K_i$  in a control  
1161 channel, and takes the effect of neutral kaon  $CP$  violation and material interaction  
1162 on  $K_i$  measurements into account, as well the experimental time acceptance. The  
1163  $(c_i, s_i)$  are calculated using  $A_1(s_{+-})$  and the experimental time acceptance is taken  
1164 into account in this calculation as well.

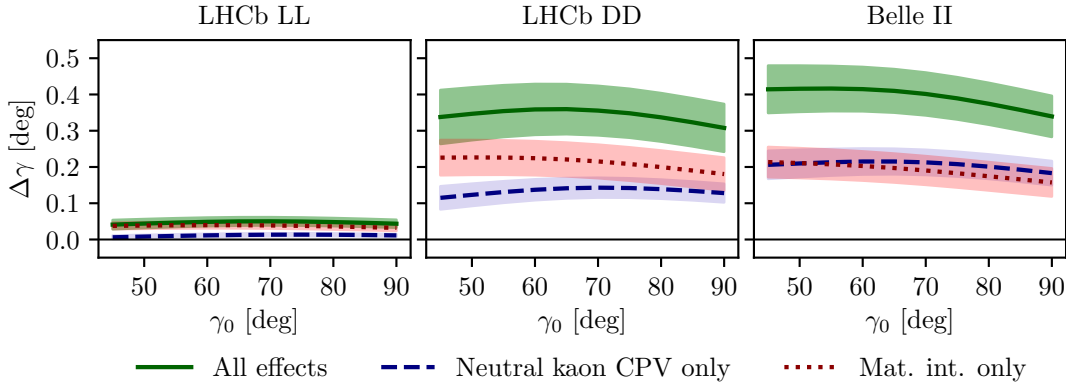


**Figure 4.6:** The bias  $\Delta\gamma$  as a function of input  $\gamma_0$  for (left) the LL LHCb category, (centre) the DD LHCb category, and (right) Belle II. The bias is calculated due to (blue, dashed line) neutral kaon  $CP$  violation alone, (red, dotted line) material interaction alone, and (green line) both effects. The shaded region shows the estimated  $1\sigma$  uncertainty band.

### 4.3.6 Results

The obtained bias  $\Delta\gamma$  is shown as a function of input  $\gamma^0$  for the various experimental conditions in Fig. 4.6. The calculations are made using  $(r_B^0, \delta_B^0) = (0.1, 130^\circ)$ , approximately equal to the physics parameters relevant for  $B^\pm \rightarrow DK^\pm$  decays [?, ?]. The bias does not vary significantly with  $\gamma^0$  in the plotted range, which includes the world average value of direct  $\gamma$  measurements as well as the values obtained in full unitarity-triangle fits [?, ?, ?], and for all cases, the bias is found to be below  $0.5^\circ$ , corresponding to relative biases of about half a percent. Thus the biases are of  $O(r\epsilon/r_B)$  as expected, given the arguments of Section 4.2.3. The contributions from the individual  $K_S^0$  CPV and material interaction effects are also shown. It is seen that the neutral kaon  $CP$  violation and material interaction effects leads to approximately equal biases in all three cases.

Given the decay-time acceptance and momentum distribution for each experimental category, the mean life time,  $\langle\tau\rangle$ , of the reconstructed kaons can be calculated. In terms of the  $K_S^0$  lifetime  $\tau_{K_S^0} = (0.895 \pm 0.004) \times 10^{-11}$  s [?],  $\langle\tau_{LL}\rangle \simeq 0.1\tau_{K_S^0}$  for the LHCb LL category,  $\langle\tau_{DD}\rangle \simeq 0.8\tau_{K_S^0}$  for the LHCb DD category, and at Belle II  $\langle\tau_{Belle\,II}\rangle \simeq \tau_{K_S^0}$ . The difference in average kaon lifetime is reflected in the observed biases, which are found to be larger in the samples with longer lived kaons. The very small effect in the LL category is to be expected because the  $CP$ -violation effect due to  $K_S^0$  not being  $CP$ -even is approximately cancelled by the  $CP$ -violation effect arising from  $K_S^0 - K_L^0$  interference for kaons with decay times much smaller than  $\tau_{K_S^0}$  [?].

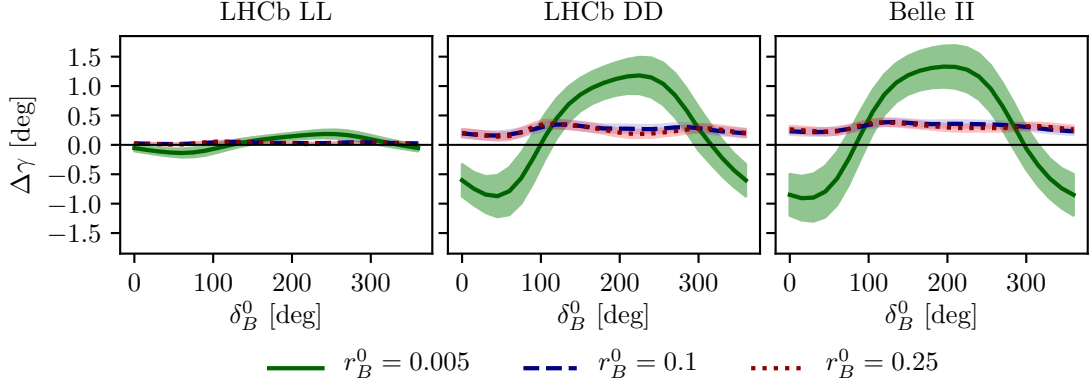


**Figure 4.7:** The bias  $\Delta\gamma$  as a function of input  $\delta_B$  for (left) the LL LHCb category, (centre) the DD LHCb category, and (right) Belle II. The bias is calculated for  $\gamma = 75^\circ$  and (green line)  $r_B = 0.005$ , (blue, dashed line)  $r_B = 0.1$ , and (red, dotted line)  $r_B = 0.25$ . The shaded region shows the estimated  $1\sigma$  uncertainty band.

1187 The uncertainty bands in Fig. 4.6 are calculated by repeating the study while  
1188 varying some of the inputs. The model dependence of the predicted biases is  
1189 probed by repeating the study using two other amplitude models as input for  
1190  $A_1(s_{+-})$  and  $A_2(s_{+-})$ : the model published in Ref. [?] and the model included in  
1191 EVTGEN [?]. hen defining  $A_2(s_{+-})$  in terms of  $A_1(s_{+-})$ , there is an uncertainty  
1192 due to the unknown  $(r_k, \delta_k)$  parameters used to describe the  $\pi\pi$  resonance terms.  
1193 This uncertainty is assessed by making the study with several different random  
1194 realisations of the parameter set. The studies are repeated while varying the time  
1195 acceptances and material densities with  $\pm 10\%$ . There is an additional uncertainty  
1196 due to the use of simulation samples generated with `RapidSim` to describe the kaon  
1197 momentum distribution, in lieu of full detector simulations.

1198 There is also an uncertainty from the use of  $(c_i, s_i)$  as calculated using  $A_1(s_{+-})$ .  
1199 It is to be expected that the measured values  $(\hat{c}_i, \hat{s}_i)$  from the CLEO collaboration  
1200 differ by those calculated using  $A_1^D(s_-, s_+)$  by terms of  $O(\epsilon)$  due to neutral kaon  
1201  $CP$  violation, which is not taken into account in the measurement [?]. These  
1202 corrections can be calculated via a procedure analogous to the one used to estimate  
1203 the corrections on measurements of  $\gamma$  in this paper. However, as these corrections  
1204 are much smaller than the experimental uncertainties in the measurement, they  
1205 have not been studied further.

1206 For the purpose of this thesis, it is important to consider the bias in measurements  
1207 that use  $B^\pm \rightarrow D\pi^\pm$  decays as well, and other  $B$  decay modes can also be used in  
1208 BPFGSZ measurements, such as  $B^\pm \rightarrow D^*K^\pm$ ,  $B^\pm \rightarrow DK^{*\pm}$ , and  $B^0 \rightarrow DK^{*0}$ .  
1209 For the purpose of the study presented here, the main difference between the decay

channels is that they have different values of  $r_B$  and  $\delta_B$ . Figure 4.7 shows  $\Delta\gamma$  as a function of input  $\delta_B^0$ , for  $\gamma^0 = 75^\circ$  and three different values of  $r_B^0$ . Aside from  $r_B^0 = 0.1$ , the results are shown for  $r_B^0 = 0.005$ , which corresponds to the expectation in  $B^\pm \rightarrow D\pi^\pm$  decays [?] and  $r_B^0 = 0.25$ , which corresponds to  $B^0 \rightarrow DK^{*0}$  decays [?, ?]. The most notable feature is that the biases are significantly larger in the  $B^\pm \rightarrow D\pi^\pm$  case. This is expected: the  $r_B^0$  dependent behaviour is governed by the relative importance of different  $O(r\epsilon)$  correction terms to the phase-space distribution. There are terms of both  $O(r_A\epsilon)$  and  $O(r_B\epsilon)^3$ , which lead to expected biases of size  $O(r_A\epsilon/r_B)$  and  $O(r_B\epsilon/r_B) = O(\epsilon)$ , respectively, cf. the discussion of Section 4.2.3. In the  $B^\pm \rightarrow D\pi^\pm$  case, the  $O(r_A\epsilon)$  correction terms dominate because  $r_A/r_B \simeq (0.05/0.005) = 10$ . This explains the relatively large bias, as  $|r_A\epsilon/r_B^{D\pi}| \simeq 4\%$ . The bias is seen to be up to  $\pm 1.5^\circ$ , but only about  $+0.2^\circ$  with the expected value of  $\delta_B^{D\pi} \simeq 300^\circ$  [?, ?]. These biases are *much smaller* than the precision on  $\gamma$  that is obtainable in a  $B^\pm \rightarrow D\pi^\pm$  analysis with current experimental yields, and do thus not pose a problem. In the  $r_B^0 = 0.1$  and  $r_B^0 = 0.25$  cases the  $O(r_B\epsilon)$  correction terms dominate, and the biases are of  $O(\epsilon)$ , independent of the  $r_B^0$  value. Therefore both cases have biases of similar size.

Further, it is clear that the biases depend on  $\delta_B^0$  and that the oscillation period of the  $\delta_B$  dependence is different between the  $r_B^0 = 0.005$  case and the  $r_B^0 \in \{0.1, 0.25\}$  cases. It is to be expected that  $\Delta\gamma$  oscillates as a function of  $\delta_B^0$ , because  $\delta_B^0$  enters the yield equations via  $\cos(\delta_B^0 \pm \gamma)$  and  $\sin(\delta_B^0 \pm \gamma)$  terms. As explained above, the  $O(r_A\epsilon)$  terms dominate the  $B^\pm \rightarrow D\pi^\pm$  bias, and these are independent of  $\delta_B^0$ . The  $O(r_B\epsilon)$  terms, however, are important for the bias corrections for larger  $r_B$  values, and the terms include factors of  $\cos(\delta_B^0 \pm \gamma)$  and  $\sin(\delta_B^0 \pm \gamma)$ . This explains the different bias dependence on  $\delta_B^0$ .

While the input value of  $\gamma^0 = 75^\circ$  was chosen for these studies, there is minimal variation in the results if another value of  $\gamma^0$  in the range  $[60^\circ, 85^\circ]$  is used.

### 4.3.7 Coupled $B^\pm \rightarrow DK^\pm$ and $B^\pm \rightarrow D\pi^\pm$ measurements

The studies presented above have been extended on two accounts in order to assign a systematic uncertainty to the LHCb measurement presented in Chapter 5. Firstly, full LHCb simulation has been used to obtain the momentum distributions, as well as to fit a better description of the time acceptance and the reconstruction efficiency profile over the  $D$ -decay phase space. Secondly, the fit setup is modified

---

<sup>3</sup>There are similar terms of  $O(r_A r_\chi)$  and  $O(r_B r_\chi)$ , but as  $\epsilon$  and  $r_\chi$  are of the same order of magnitude, these terms can be treated completely analogously to the  $O(r_A\epsilon)$  and  $O(r_B\epsilon)$  terms, and have been left out of the discussion for brevity.

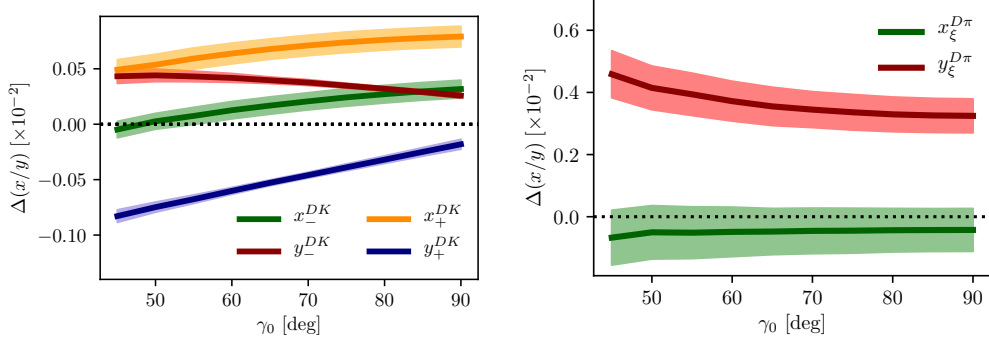


**Figure 4.8:** The bias on (left) the  $B^\pm \rightarrow DK^\pm$  and (right)  $B^\pm \rightarrow D\pi^\pm$   $CP$ -violation observables in the LHCb DD category, evaluated in bias studies with inputs based on full LHCb simulation, calculated as a function of input  $\gamma_0$ .

to correspond to the experimental approach described in Section 2.4 and Chapter 5: the signal yields are calculated for both the  $B^\pm \rightarrow DK^\pm$  and  $B^\pm \rightarrow D\pi^\pm$  channels, and fitted in a combined fit to obtain  $(x_{\pm}^{DK}, y_{\pm}^{DK}, x_{\xi}^{D\pi}, y_{\xi}^{D\pi})$ , where the  $F_i$  parameters are allowed to float in the fit. The biases obtained for each observable are shown in Fig. 4.8, evaluated using the time-acceptance, momentum distribution, and material budget relevant for the DD category (since the effect in the LL category is much smaller). As will be clear in Chapter 5, these biases are all significantly smaller than the corresponding statistical uncertainties. Thus, the effects of neutral kaon  $CP$  violation and material interactions contribute a manageable systematic uncertainty in current BPGGSZ measurements, even if the  $B^\pm \rightarrow D\pi^\pm$  channel is promoted to a signal channel.

As the statistical uncertainty becomes comparable with the bias effects described in this chapter, the systematic uncertainty should be assigned by a more accurate study, incorporating the traversed material on a track-by-track basis in full detector simulation. Such a detailed calculations can also be used to apply a bias correction if desired.

## 4.4 Concluding remarks

The analysis presented in this chapter has shown the expected impact of neutral kaon  $CP$  violation and material interaction on current BPGGSZ measurements to be small compared to the statistical uncertainties; first by simple order-of-magnitude estimates and then by a detailed calculation of the expected effect in LHCb and Belle II.

While the calculations were made for the case of  $D \rightarrow K_S^0 \pi^+ \pi^-$  decays, the BPGGSZ approach can of course also be applied in other  $D$ -decay final states,

such as  $D \rightarrow K_S^0 K^+ K^-$  and  $D \rightarrow K_S^0 \pi^+ \pi^- \pi^0$ . The biases on measurements of  $\gamma$  based the  $D$  decay phase-space distributions should be of similar size in these decay channels. The impact on  $\gamma$  measurements based on the phase-space-integrated yield asymmetry can be expected to be tens of degrees for the  $D \rightarrow K_S^0 K^+ K^-$  channel, where the yield asymmetry is expected to be around 2 %, for the reasons explained in Section 4.2.3. The  $D \rightarrow K_S^0 \pi^+ \pi^- \pi^0$  decay, however, is dominantly  $CP$ -odd [?], and the bias in measurements based on the total asymmetry is therefore expected to be  $O(\epsilon/r_B)$ , ie. a few degrees [?]. More precise calculations of the biases would require a repeat of the study included here, with relevant amplitude models and binning schemes in place.

The chapter focuses on the model-independent, binned approach that is the subject of the thesis. However, the underlying mechanism that determines the scale of the bias, namely that the phase-space *distribution* of signal decays is unaffected at  $\mathcal{O}(\epsilon)$  and  $\mathcal{O}(r_\chi)$ , is independent on the exact measurement approach. Therefore it is expected that amplitude-model-based measurements and measurements made with new unbinned methods such as those in Ref [?] will be similarly biased if kaon  $CP$  violation and regeneration are not accounted for.

# 5

1284

1285

1286

## A BPGBGSZ measurement of $\gamma$ with $B^\pm \rightarrow Dh^\pm$ decays

1287 This chapter describes a model-independent BPGBGSZ measurement of  $\gamma$  with  
1288  $B^\pm \rightarrow DK^\pm$  and  $B^\pm \rightarrow D\pi^\pm$  decays where  $D \rightarrow K_S^0\pi^+\pi^-$  and  $D \rightarrow K_S^0K^+K^-$ ,  
1289 commonly denoted  $B^\pm \rightarrow D(\rightarrow K_S^0h^+h^-)h'^\pm$  decays. The measurement is made  
1290 with the full LHCb data set collected during Run 1 and 2 of the LHC, corresponding  
1291 to an integrated luminosity of about  $9\text{ fb}^{-1}$ . The analysis is under review for  
1292 publication in the Journal of High Energy Physics at the time of writing [?]  
1293 (one can hope).

### 1294 5.1 Candidate reconstruction and selection

1295 The  $B^\pm \rightarrow D(\rightarrow K_S^0h^+h^-)h'^\pm$  candidates are constructed during the offline *stripping*  
1296 stage described in Section 3.3.3. The candidates are defined by first combining  
1297 tracks to form a  $K_S^0 \rightarrow \pi^+\pi^-$  vertex, then a  $D \rightarrow K_S^0h^+h^-$  vertex, and finally  
1298 the  $B^\pm \rightarrow Dh'^\pm$  candidate. Each final state track is required to satisfy certain  
1299 momentum thresholds and track-quality requirements, and to be separated from all  
1300 primary interaction vertices. Each decay vertex is required to satisfy a fit-quality  
1301 threshold and to be separated from the primary vertex. Momentum thresholds  
1302 are applied to the composite particles and they are required to have reconstructed  
1303 invariant masses close to their known masses<sup>1</sup> except that the  $B$  candidate is  
1304 required to have a reconstructed invariant mass in the interval  $4750\text{--}7000\text{ MeV}/c^2$ .

---

<sup>1</sup>The exact mass window depends on the particle type and reconstruction category; narrower mass windows are applied at a later stage, as described below.

1305 The  $B$  candidate is required to satisfy  $\chi^2_{\text{IP}} < 25$ , where  $\chi^2_{\text{IP}}$  is the difference in  $\chi^2$   
 1306 value of the primary vertex fit, when the vertex is formed with- and without the  $B$   
 1307 candidate. As the final *stripping* stage, a multivariate algorithm is applied to the  
 1308 formed  $B$  candidate to reduce the amount of random track combinations, denoted  
 1309 combinatorial background, even further than the aforementioned requirements.

1310 Two data categories are defined, depending the tracks used to form the  $K_S^0$   
 1311 candidate: the LL category where both pions are long tracks, and DD category where  
 1312 both pions are downstream tracks, using the track classifications of Section 3.2.

1313 Each candidate is re-analysed with the `DecayTreeFitter` (DTF) frame work [?],  
 1314 where a simultaneous fit of the full decay chain is made with a number of constraints  
 1315 applied: the momenta of the composite  $D$  and  $K_S^0$  particles are required to form  
 1316 invariant masses exactly equal to the known particle masses [?], and the momentum  
 1317 of the  $B$  candidate is required to point in the direction defined by the  $B$  decay  
 1318 vertex and the primary vertex. This refit results in improved resolution of the  
 1319 invariant masses of the composite particles and, very importantly, of the Dalitz  
 1320 coordinates in the  $D$ -decay phase space. It also ensures that all candidates fall in the  
 1321 kinematically allowed region of the  $D$ -decay phase space. Unless otherwise specified,  
 1322 all results in this chapter are based on the refitted track momenta; for reasons  
 1323 explained below, some studies have to be based on parameters that are obtained  
 1324 without the constraints described above, or with only a subset of them applied.

1325 Following the stripping stage, the further selection of signal candidates is  
 1326 performed in three steps: an initial set of requirements that remove a large fraction  
 1327 of candidates that are very likely to be background and veto a number of specific  
 1328 backgrounds, the application of a multivariate analysis algorithm designed to allow  
 1329 for filtering combinatorial background, and finally a set of particle-identification  
 1330 requirements. The requirements are summarised in Table 5.1, and each step is  
 1331 described in detail in the following sections.

### 1332 5.1.1 Initial requirements

1333 At the hardware trigger level, it is required that a particle associated with the signal  
 1334 decay triggered the hadronic level-0 trigger (Trigger on Signal, or TOS), or that  
 1335 the level-0 trigger decision was caused by a particle that is not associated with the  
 1336 signal decay (Trigger Independent of Signal, or TIS). The inclusion of the latter  
 1337 category increases the data sample about 50 %. At the software trigger level,

1338 Before any processing of the data, a loose preselection is applied to remove  
 1339 obvious background candidates. The reconstructed  $D$  ( $K_S^0$ ) mass is required to  
 1340 be within 25 (15) MeV/ $c^2$  of the known values [?]. The *companion* particle, the

**Table 5.1:** Summary of requirements applied to data. The base requirements are applied to all data samples before training or applying the BDT.

Base requirements		
Variable	Cut	Comment
Bachelor momentum, $p$	$< 100 \text{ GeV}/c$	
Bachelor has RICH	<i>true</i>	
$K^\pm$ in $D$ decay: momentum, $p$	$< 100 \text{ GeV}/c$	In $D \rightarrow K_S^0 K^+ K^-$
$K^\pm$ in $D$ decay: have RICH	<i>true</i>	In $D \rightarrow K_S^0 K^+ K^-$
DecayTreeFit converged	<i>true</i>	
$D$ mass	$m_{D^0} \in m_{D^0}^{PDG} \pm 25 \text{ MeV}/c^2$	From DTF with constrained $K_S^0$ mass
$K_S^0$ mass	$m_{K_S^0} \in m_{K_S^0}^{PDG} \pm 15 \text{ MeV}/c^2$	From DTF with constrained $D^0$ mass

Background suppressing requirements		
Variable	Cut	Comment
$K_S^0$ flight distance $\chi^2$	$> 49$	for LL only
$\Delta z_{\text{significance}}^{DB}$	$> 0.5$	for all candidates

PID requirements		
Channel	Cut	Comment
$B^\pm \rightarrow DK^\pm$	PIDK > 4	for bachelor
$B^\pm \rightarrow D\pi^\pm$	PIDK < 4	for bachelor
$B^\pm \rightarrow Dh^\pm$	IsMuon = 0	for bachelor
$B^\pm \rightarrow D(\rightarrow K_S^0 \pi^+ \pi^-)h^\pm$	PIDe < 0 & IsMuon = 0	for charged $D$ decay products
$B^\pm \rightarrow D(\rightarrow K_S^0 K^+ K^-)h^\pm$	PIDK > -5 & IsMuon = 0	for charged $D$ decay products

BDT requirements		
Channel	Cut	Comment
Run 1, DD	$> 0.6$	
Others	$> 0.8$	

1341 pion or kaon produced in the  $B^\pm \rightarrow Dh^\pm$  decay, is required to have associated  
 1342 RICH information and a momentum less than  $100 \text{ GeV}/c$ ; this ensures good particle-  
 1343 identification performance. Finally, all of the DTF fits of the full decay chain  
 1344 are required to have converged properly.

1345 Two additional requirements are made at this stage in order to suppress specific  
 1346 backgrounds. In order to suppress decays of the type  $B^\pm \rightarrow K_S^0 h^+ h^- h'^\pm$  with  
 1347 no intermediate  $D$  meson, so called *charmless* decays, it is required that the  
 1348 significance of the  $z$ -separation of the  $D^0$  decay vertex and the  $B^\pm$  decay vertex  
 1349 is above 0.5. The significance of the  $z$ -separation of the  $D^0$  decay vertex and  
 1350 the  $B^\pm$  decay vertex is defined as

$$\Delta z_{\text{significance}}^{D-B} = \frac{z_{vtx}^D - z_{vtx}^B}{\sqrt{\sigma^2(z_{vtx}^D) + \sigma^2(z_{vtx}^B)}}. \quad (5.1)$$

1351 This source of background described further in section 5.3.1. In order to suppress  
 1352 a background from  $D \rightarrow 4\pi$  and  $D \rightarrow \pi\pi KK$  decays, it is required that the  $K_S^0$

1353 flight distance  $\chi_{\text{FD}}^2$  is greater than 49, where

$$\chi_{\text{FD}}^2 = \left( \frac{\Delta r}{\sigma(\Delta r)} \right)^2, \quad (5.2)$$

1354 and  $\Delta r$  is the measured flight distance of the  $K_S^0$  meson. This background is  
1355 described in further detail in section 5.3.2.

### 1356 5.1.2 Boosted decision tree

1357 A Gradient Boosted Decision Tree [?] (abbreviated BDT in the following) is  
1358 applied to classify each candidate on a scale from  $-1$  to  $+1$  as signal-like ( $+1$ )  
1359 or combinatorial-background-like ( $-1$ ), based on the values of a number of input  
1360 parameters for candidate in question. The BDT is implemented in the TMVA  
1361 frame work [?, ?].

1362 A boosted decision tree classifier consists of a number of sequentially trained  
1363 decision trees, each of which classify events as either signal or background. Each tree  
1364 bases the decision on an individual subset of variables, out of an overall set of input  
1365 variables. At each training step, the input events are weighted when training a new  
1366 tree, so that events that the already-trained trees classify incorrectly are given a  
1367 higher weight; this is denoted boosting. The term *gradient boosting* denotes a specific  
1368 weight calculation scheme [?]. The final score is the average over all decision trees.

1369 The full set of input variables are given in Table 5.2. It includes the momenta  
1370 of particles in the decay; a number of geometric parameters such a absolute and  
1371 relative vertex positions, and distances of closest approach between tracks;  $\chi_{\text{IP}}^2$   
1372 values for a number of particles in the decay chain; the  $\chi^2$  per degree of freedom  
1373 of the DTF refit; DIRA values, which denote the angle between the fitted particle  
1374 momenta and the vector spanned by it's production ad decay vertices; and finally  
1375 an isolation variable, defined as

$$A_{pt} = \frac{p_T(B) - \sum p_T(\text{other})}{p_T(B) + \sum p_T(\text{other})} \quad (5.3)$$

1376 where the sum is over all other tracks in a cone around the  $B$ -candidate. The cone  
1377 is defined as being within a circle with a radius of 1.5 units around the  $B$  candidate  
1378 in the  $(\eta, \phi_{\text{azim}})$ -plane. This variable is highly efficient in rejecting combinatorial  
1379 background. Two algorithms are trained, one for the LL category of  $K_S^0$  mesons and  
1380 one for the DD category, because some input parameters relate to the  $K_S^0$  meson  
1381 and have very different distributions between the two categories.

**Table 5.2:** Input parameter set used in BDTG trained to separate signal and combinatorial background, sorted according to importance in LL BDT.

Variable name	Importance LL/DD (Rank in DD)	Description
$\log(1-Ks_{\text{DIRA}}_{\text{BPV}})$	7.2 % / 3.5 % (16)	$\log \cos \theta_{\text{DIRA}}$ for $K_S^0$
$\log(Bu_{\text{RHO}}_{\text{BPV}})$	5.7 % / 5.5 % (5)	Radial distance of $B$ vertex to beam line
$\log(Bach_{\text{PT}})$	5.2 % / 6.9 % (1)	$p_T$ of the bachelor particle
$\log(1-D0_{\text{DIRA}}_{\text{BPV}})$	4.9 % / 5.8 % (4)	$\log \cos \theta_{\text{DIRA}}$ for $D$
$\log(1-Bu_{\text{DIRA}}_{\text{BPV}})$	4.9 % / 6.4 % (3)	$\log \cos \theta_{\text{DIRA}}$ for $B^\pm$
$\log(D0_{\text{RHO}}_{\text{BPV}})$	4.8 % / 5.3 % (6)	Radial distance of $D$ vertex to beam line
$Bu_{\text{PTASY\_1.5}}$	4.7 % / 4.9 % (7)	Asymmetry parameters of $B^\pm$
$\log(D0_{\text{PT}})$	4.7 % / 6.6 % (2)	$p_T$ of the $D$ meson
$\log(Bu_{\text{constDOKSPV\_CHI2NDOF}})$	4.2 % / 4.5 % (9)	$\chi^2/\text{d.o.f}$ of kinematical refit with DecayTreeFitter
$\log(Bu_{\text{FDCHI2\_OWNPV}})$	3.9 % / 4.1 % (11)	Flight distance $\chi^2$ of the $B^\pm$
$\log(\max_{\text{Ksh1h2\_IPCHI2\_OWNPV}})$	3.9 % / 3.0 % (20)	Largest $\chi^2_{\text{IP}}$ of the $K_S^0$ decay products
$\log(D0_{\text{IPCHI2\_OWNPV}})$	3.8 % / 3.3 % (17)	$\chi^2_{\text{IP}}$ of the $D$
$\log(\min_{\text{Ksh1h2\_IPCHI2\_OWNPV}})$	3.7 % / 0.9 % (26)	Smallest $\chi^2_{\text{IP}}$ of the $K_S^0$ decay products
$\log(Bu_{\text{P}})$	3.7 % / 3.9 % (12)	$p$ of the $B^\pm$ meson
$\log(Bu_{\text{IPCHI2\_OWNPV}})$	3.6 % / 4.6 % (8)	$\chi^2_{\text{IP}}$ of the $B^\pm$
$Bu_{\text{MAXDOCA}}$	3.6 % / 3.3 % (18)	"Distance of closest approach" for $B^\pm$ vertex
$\log(Bach_{\text{IPCHI2\_OWNPV}})$	3.3 % / 4.3 % (10)	$\chi^2_{\text{IP}}$ of the bachelor particle
$\log(Bu_{\text{PT}})$	3.3 % / 3.7 % (14)	$p_T$ of the $B^\pm$ meson
$\log(\max_{\text{h1h2\_IPCHI2\_OWNPV}})$	3.1 % / 3.8 % (13)	Largest $\chi^2_{\text{IP}}$ of the $D$ decay products
$\log(\min_{\text{h1h2\_IPCHI2\_OWNPV}})$	3.0 % / 3.4 % (19)	Smallest $\chi^2_{\text{IP}}$ of the $D$ decay products
$\log(Ks_{\text{VTXCHI2DOF}})$	2.9 % / 2.3 % (21)	$\chi^2$ of vertex fit for $K_S^0$
$D0_{\text{MAXDOCA}}$	2.9 % / 1.0 % (25)	"Distance of closest approach" for $D$ vertex
$\log(D0_{\text{VTXCHI2DOF}})$	2.7 % / 1.6 % (24)	$\chi^2$ of vertex fit for $D$
$\log(D0_{\text{P}})$	2.7 % / 1.8 % (22)	$p$ of the $D$ meson
$\log(Bach_{\text{P}})$	2.2 % / 3.6 % (15)	$p$ of the bachelor particle
$\log(Bu_{\text{VTXCHI2DOF}})$	1.8 % / 1.7 % (23)	$\chi^2$ of vertex fit for $B^\pm$

The BDTs are trained and tested with input samples representing typical signal and background decay candidates: a signal sample that consists of simulated  $B^\pm \rightarrow D(\rightarrow K_S^0\pi^+\pi^-)\pi^\pm$  decays corresponding to the LHCb running conditions for the years 2012–2018, and a sample of combinatorial background candidates from real data, where the reconstructed invariant mass of the  $B$  meson is larger than 5800 MeV/ $c^2$ . The candidates in both samples were required to have passed the initial requirements described in the preceding section. The input-parameter distributions in the signal and background training samples are shown in Figs. 5.1 and 5.2. The signal and background samples are each split into two before the training stage: one sub sample, the training sample, is used to train the BDT, after which the trained algorithm is applied to the other sub sample, the test sample. The classifier is found to perform well on the test sample, not just the training sample, which ensures that it does not suffer significant overtraining. The BDT output distribution are shown for both test and training samples in Fig. 5.3, where it is clear that the classifier very effectively separates signal and background candidates.

Each candidate in data is classified using the BDT, and candidates that are assigned a score below some threshold value are discarded. The threshold values are chosen in a set of pseudo experiments, such that the expected sensitivity to  $\gamma$  is maximised. This is done by performing preliminary fits to the data set for a range of different BDT threshold values, then generating many pseudo data sets with the obtained yields, and applying the full fit and interpretation procedure described in Sections 5.4–5.7 to each data set. Thus, the expected uncertainty on  $\gamma$  is obtained for a range of threshold values. The procedure is applied independently for the LL and DD categories, as well as for the Run 1 and Run 2 data sets, because some parameter distributions differ slightly between the two runs. The optimal threshold values are found to be 0.8 in all situations, except for LL candidates in Run 1 where it is 0.6. This is illustrated in Fig. 5.4 where the results of the threshold scans are shown. The same classifier is applied to both  $B^\pm \rightarrow D\pi^\pm$  and  $B^\pm \rightarrow DK^\pm$  candidates, and both  $D$  final state categories. While the classifiers were trained using samples of  $B^\pm \rightarrow D(\rightarrow K_S^0\pi^+\pi^-)\pi^\pm$  simulation and data, the decays are similar enough that no significant improvement in performance was obtained when considering a more elaborate setup. Across all categories, the requirement on the BDT output is found to remove approximately 98 % of the combinatorial background, while being approximately 93 % efficient on signal.

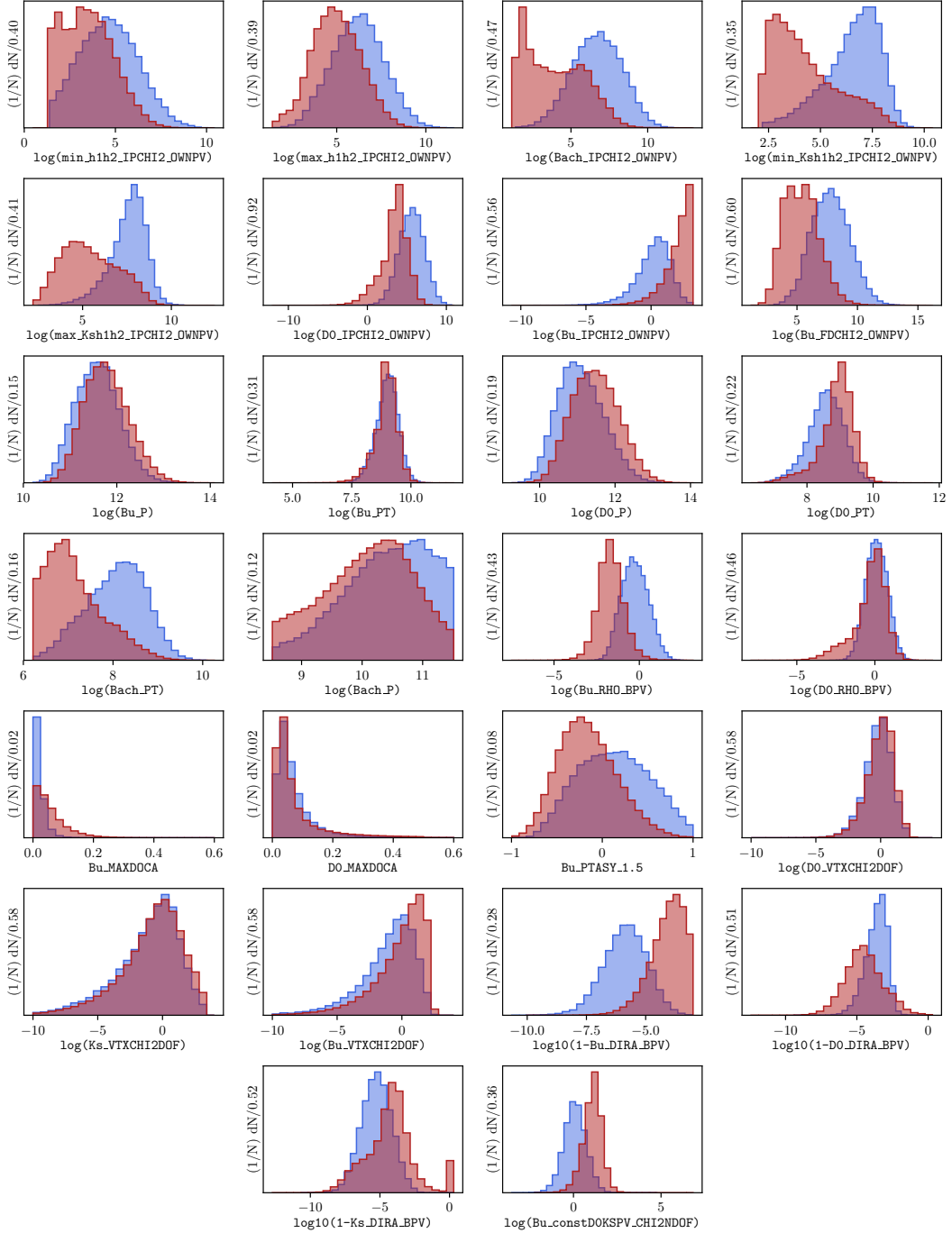


**Figure 5.1:** Distribution of input parameters in the LL training samples of (blue) signal decays from simulation and (red) background decays from the upper  $B$  sideband. The variable names described further in Table 5.2.

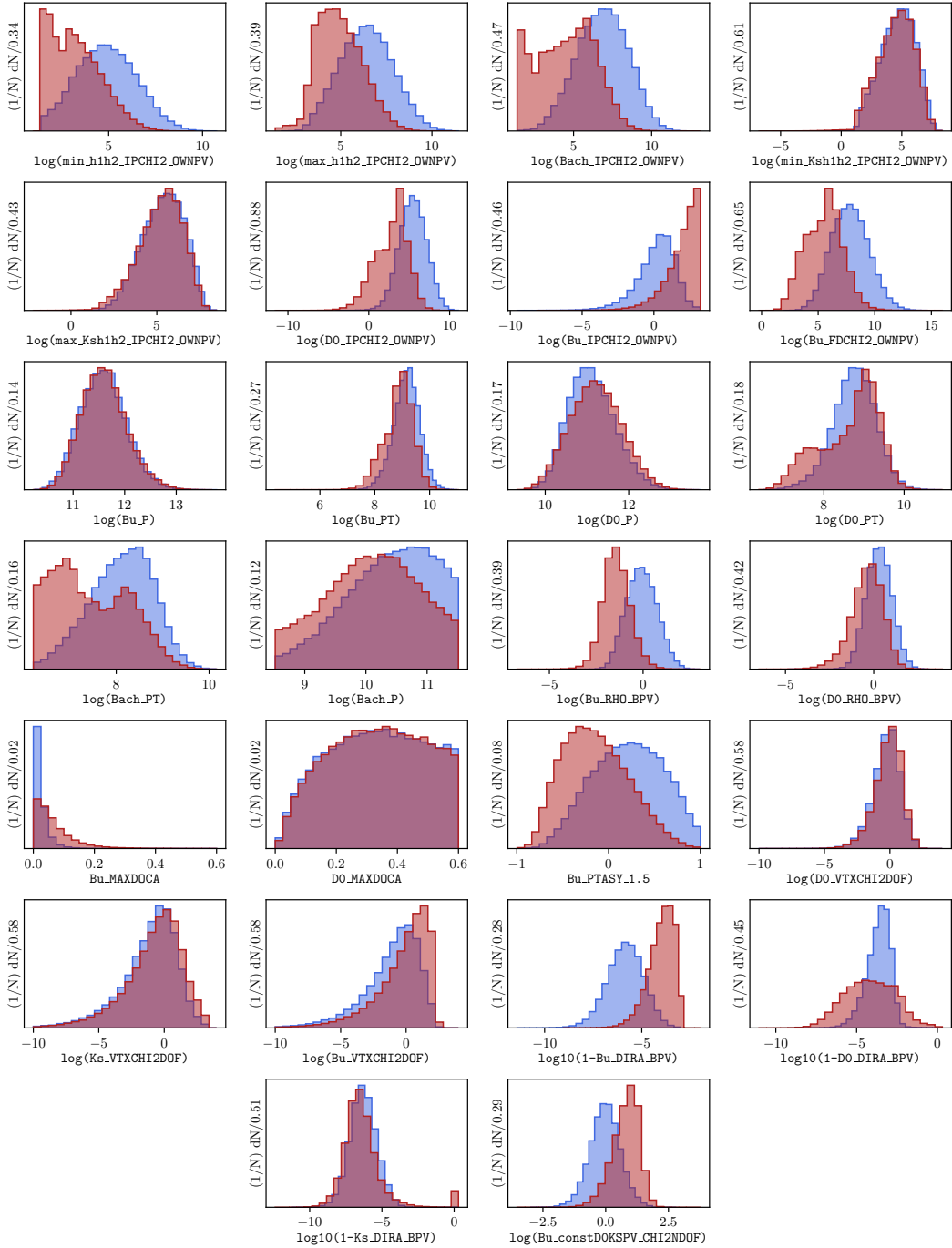


**Figure 5.2:** Distribution of input parameters in the DD training samples of (blue) signal decays from simulation and (red) background decays from the upper  $B$  sideband. The variable names described further in Table 5.2.

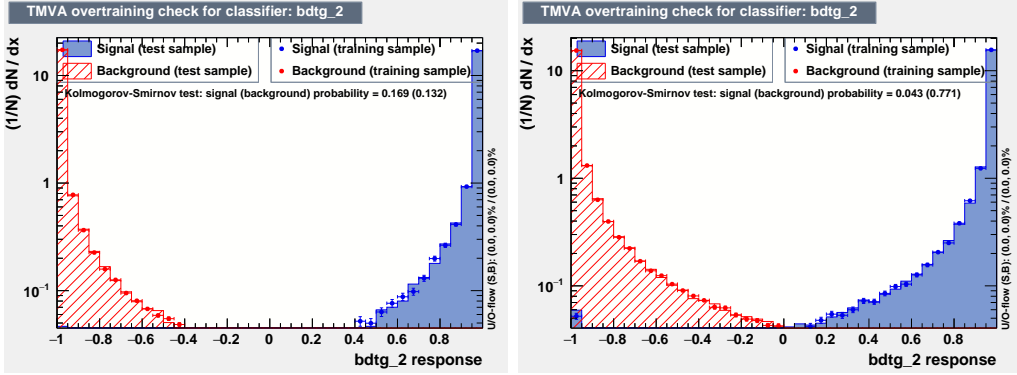


**Figure 5.3:** Distribution of BDT variable on test and training samples for (left) the LL and (right) the DD category, with logarithmic  $y$ -scale.

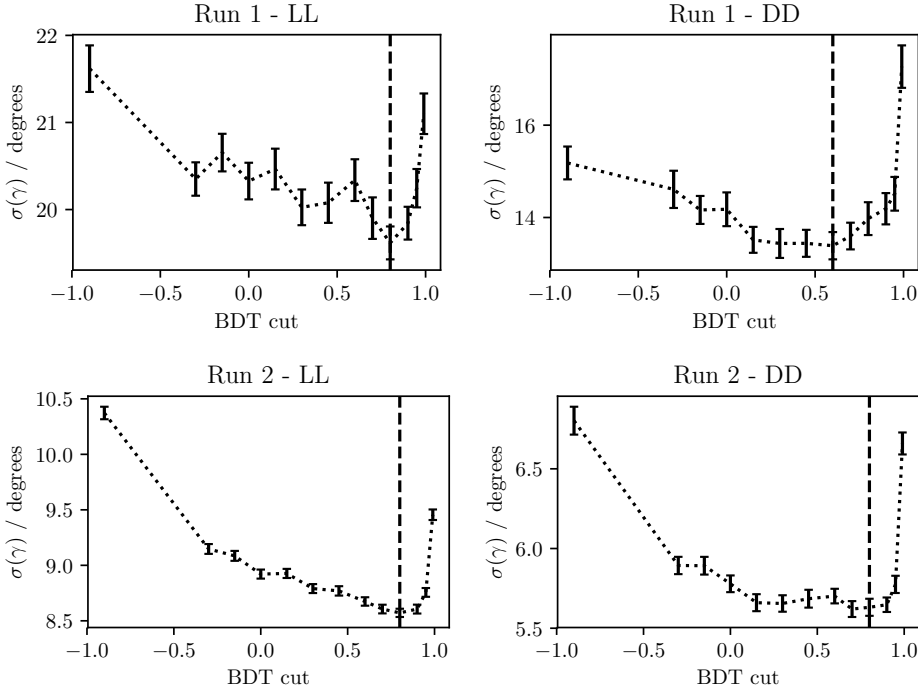


**Figure 5.4:** The mean uncertainty on  $\gamma$  in toy studies, performed with the signal and background yields corresponding to a given BDT requirement, using (top) the Run 1 and (bottom) Run 2 datasets, using only candidates in (left) the LL category and (right) the DD category. The dashed line shows the threshold value employed to discard background-like candidates in the selection.

### 1416 5.1.3 Particle-identification requirements

- 1417 A PID requirement is made to separate  $B^\pm \rightarrow DK^\pm$  and  $B^\pm \rightarrow D\pi^\pm$  candidates in  
 1418 the data sample, by requiring that the PIDK of the companion particle satisfies  
 1419  $\text{PIDK} < 4$  for  $B^\pm \rightarrow D\pi^\pm$  candidates and  $\text{PIDK} > 4$  for  $B^\pm \rightarrow DK^\pm$  candidates.  
 1420 The PIDK variable was defined in Section 3.1.3. This ensures that any given  
 1421 candidates is selected into only one of these samples.

1422 Further to the requirement on the companion, PID requirements are made to  
1423 suppress semi-leptonic backgrounds as well as decays where a final state particle  
1424 decays in flight, and a loose PID requirement is made in the  $D \rightarrow K_S^0 K^+ K^-$   
1425 channels where it leads to a higher signal purity:

- 1426 • the companion particle is required to satisfy `IsMuon` = 0.
- 1427 • For the  $B \rightarrow D(\rightarrow K_S^0 \pi^+ \pi^-) h^\pm$  samples it is require that the charged pion  
1428 track from the  $D$  decay with opposite charge to the companion satisfies  
1429  $\text{PIDe} < 0 \& \text{IsMuon} = 0$ , and for the other charged pion that `IsMuon` = 0.
- 1430 • For the  $B \rightarrow D(\rightarrow K_S^0 K^+ K^-) h^\pm$  samples it is required that the charged kaon  
1431 tracks from the  $D$  decay have RICH information, a momentum less than 100  
1432  $\text{GeV}/c$  and  $\text{PIDK} > -5 \& \text{IsMuon} = 0$ .

1433 These backgrounds are described in Section 5.3.3.

#### 1434 5.1.4 Final requirements

1435 For a small fraction of candidates in the final sample, it is the case that two  
1436 or more candidates originate in the same  $pp$  collision. In order to make sure  
1437 that all candidates are completely independent, a single, arbitrary candidate from  
1438 each  $pp$  collision is kept for these collisions, and the other candidates discarded.  
1439 This requirements results in the removal of less than 0.7% of candidates in  
1440 each data category.

1441 Furthermore, the  $D$  mass used to define the binning schemes described in Ref. [?]  
1442 differs slightly from the mass used in the DTF refit. Therefore a few of the decays are  
1443 reconstructed with Dalitz coordinates outside the allowed kinematic region. Because  
1444 this problem only concerns a handful of candidates, they are simply discarded.

#### 1445 5.1.5 Selected candidates

1446 In total, about 47,000  $B^\pm \rightarrow DK^\pm$  candidates and 400,000  $B^\pm \rightarrow D\pi^\pm$  candidates  
1447 are selected, as summarised in Table 5.3. An example of the  $B$  mass distribution in  
1448 one of the data categories is shown in Fig. 5.5; it is clear that a significant number  
1449 of these candidates are background decays. The Dalitz plots for candidates in the  
1450 signal region where  $m_B \in [5249, 5309] \text{ MeV}/c^2$  are shown in Fig. 5.6 and 5.7. Due to  
1451 the large yields in the full Run 1 and 2 LHCb data set, the asymmetries between  
1452 the  $B^+$  and  $B^-$  distributions are visible to the eye in the  $B^\pm \rightarrow DK^\pm$  plots.

**Table 5.3:** Final candidate yield in each data category after the full selection has been applied, including removing candidates outside the region  $m_B \in [5080, 5800] \text{ MeV}/c^2$ .

$B$ Decay	$D$ final state	$K_S^0$ type	Run 1	Run 2	Total
$B^\pm \rightarrow DK^\pm$	$K_S^0\pi^+\pi^-$	LL	2275	10525	12800
		DD	5097	23508	28605
	$K_S^0K^+K^-$	LL	383	1610	1993
		DD	772	3397	4169
$B^\pm \rightarrow D\pi^\pm$	$K_S^0\pi^+\pi^-$	LL	18209	90509	108718
		DD	40167	205807	245974
	$K_S^0K^+K^-$	LL	2879	13757	16636
		DD	6033	29790	35823

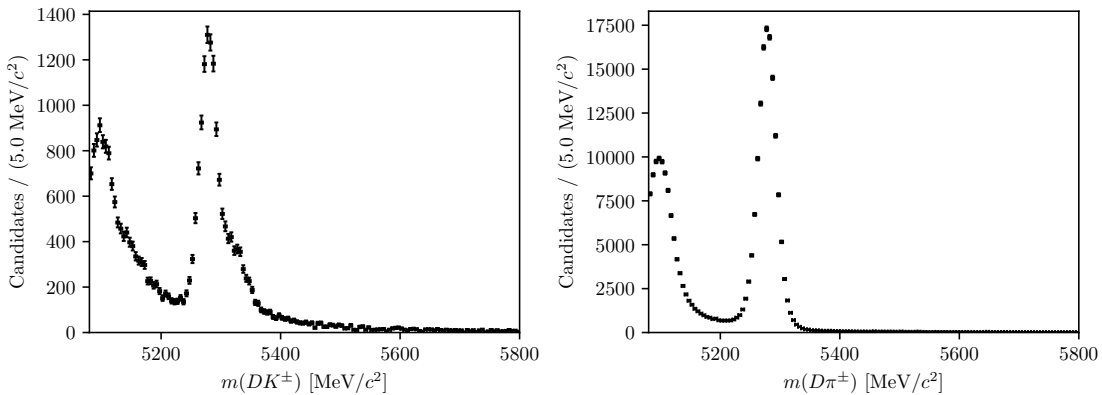


**Figure 5.5:** The spectrum of  $m_B$  in the (left)  $B^\pm \rightarrow DK^\pm$  and (right)  $B^\pm \rightarrow D\pi^\pm$  samples where  $D \rightarrow K_S^0\pi^+\pi^-$  and the  $K_S^0$  meson is reconstructed in the DD category, after the full selection has been applied.

## 5.2 Signal selection efficiencies

The efficiency of each step of the selection on signal decays can be investigated using simulated  $B \rightarrow D(\rightarrow K_S^0\pi^+\pi^-)\pi$  decays. Only decays that were placed in the "test" sample when training the BDT are used, in order to avoid overestimating the efficiency. The yields after each requirement, relative to those right after the centralised selection stage, are shown in Fig. ???. The PID requirements are treated separately below, because the efficiency of those is obtained using calibration data. The efficiencies of each individual selection step are shown in Fig. ???. The main reason that some signal decays do not survive the base requirement is the  $p_{\text{companion}} < 100 \text{ GeV}/c$  requirement, which is in place to ensure that the PID performance for the companion is good. For decays with  $p_{\text{companion}} > 100 \text{ GeV}/c$ , only about 60 % of  $B^\pm \rightarrow DK^\pm$  decays survive the subsequent  $PIDK > 4$  requirement and the cross-feed from misidentified  $B^\pm \rightarrow D\pi^\pm$  decays is 50 % larger than in the

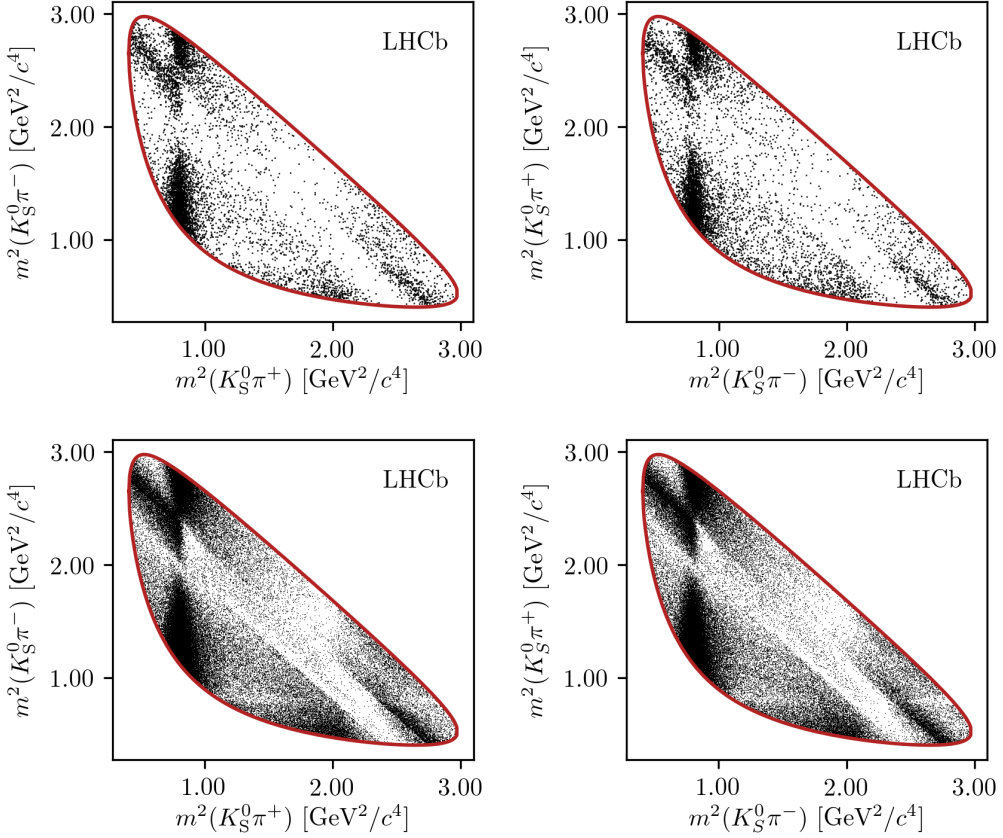


**Figure 5.6:** Dalitz plots of (left)  $B^+ \rightarrow Dh^+$  and (right)  $B^- \rightarrow Dh^-$  candidates in the signal region, in the (top)  $B^\pm \rightarrow DK^\pm$  and (bottom)  $B^\pm \rightarrow D\pi^\pm$  channels where  $D \rightarrow K_S^0\pi^+\pi^-$ . The LL and DD categories have been combined.

current selection. Thus, loosening this requirement leads to little statistical gain, while leading to larger systematic effects from the crossfeed background.

Equivalent plots are made for combinatorial background in Figs. ?? and ??, using  $B \rightarrow D(\rightarrow K_S^0\pi^+\pi^-)\pi$  candidates in data with a reconstructed  $B$  mass above 5600 MeV/ $c^2$ ; it can be seen that the BDT is extremely efficient at rejection of combinatorial background, but that the base requirements and requirement on the  $K_S^0$  flight distance also remove a decent amount of background.

In general, the total selection efficiency of all stages up until the PID requirements, including the offline stage and the effect of the geometrical LHCb acceptance, is about 1 permille, slightly higher for  $B^\pm \rightarrow DK^\pm$  than  $B^\pm \rightarrow D\pi^\pm$  decays, and slightly higher for  $D \rightarrow K_S^0 K^+ K^-$  than  $D \rightarrow K_S^0\pi^+\pi^-$  decays. However, the overall selection efficiency does not impact the measurement at all, because the observables of interest are sensitive *only* to the distribution of decays over the Dalitz plot (except, of course, a higher signal efficiency is desirable because it leads to larger signal yields). Likewise, it makes no difference that the overall selection efficiencies

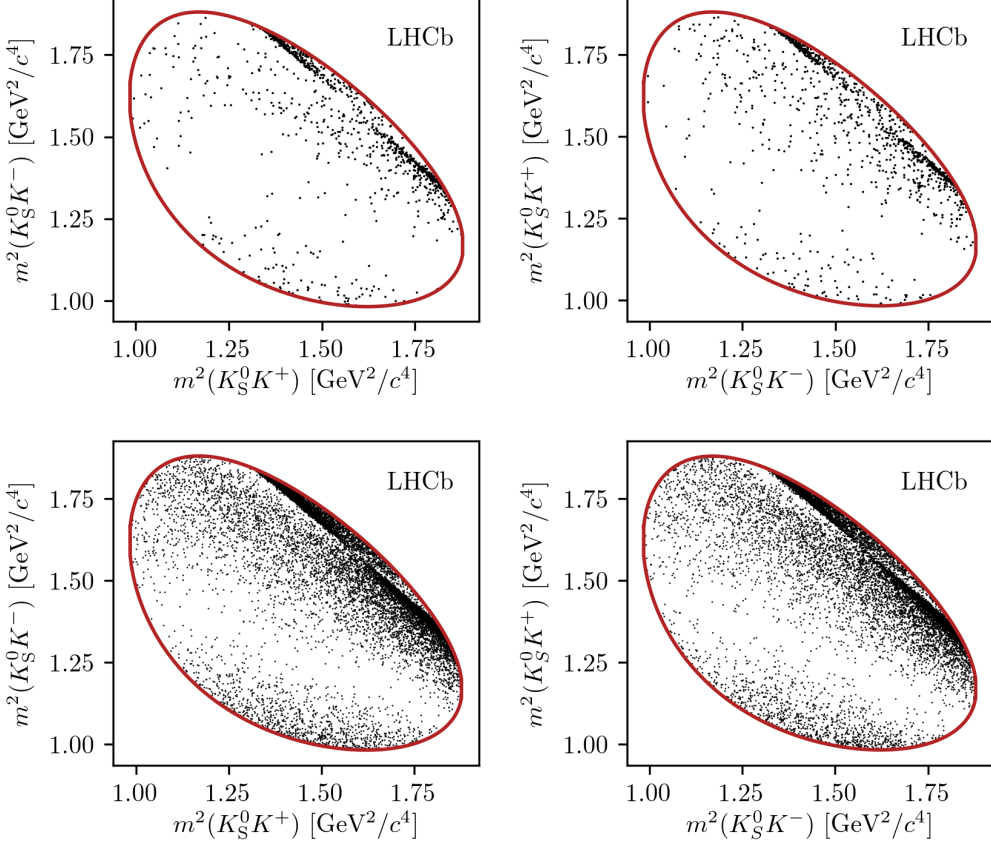


**Figure 5.7:** Dalitz plots of (left)  $B^+ \rightarrow Dh^+$  and (right)  $B^- \rightarrow Dh^-$  candidates in the signal region, in the (top)  $B^\pm \rightarrow DK^\pm$  and (bottom)  $B^\pm \rightarrow D\pi^\pm$  channels where  $D \rightarrow K_S^0 K^+ K^-$ . The LL and DD categories have been combined.

differ slightly between  $B^\pm \rightarrow DK^\pm$  and  $B^\pm \rightarrow D\pi^\pm$  decays, as long as the efficiency profile over the Dalitz plot is identical between the two decay channels. This is confirmed separately in Section ?? below.

### 5.2.1 Efficiency of the PID requirements

The efficiencies of the PID requirements on the companion enter the yield parameterisations of the mass fits in Section 5.4 and 5.5 and must therefore be known. They are determined using samples of calibration data selected without relying on PID variables, as implemented in the PIDCalib frame work [?]. Reasonably pure samples of pion and kaon tracks are obtained from  $D^0 \rightarrow K^-\pi^+$  decays, where the  $D$  meson originates in a  $D^{*+} \rightarrow D^0\pi^+$  decay and can therefore be flavour tagged. The remaining background is subtracted via the *sPlot* [?] procedure, based on a two-dimensional fit of the  $m(K^-\pi^+)$  and  $m(D^0\pi^+) - m(D^0)$  distributions. The obtained weights are employed to calculate the average efficiency of the requirement

**Table 5.4:** PID efficiencies obtained with the `PIDCalib` tool. The uncertainty incorporates statistical uncertainty due to the size of the reference sample, the systematic uncertainty due to the choice of binning scheme in `PIDCalib`, and a systematic uncertainty due to the `sWeight` calculation in `PIDCalib` of 0.1 %.

Efficiency	Particle	$D$ final state	$\varepsilon_{\text{PID}} (\%)$	
			LL	DD
Run I and II				
Correct ID	Kaon	$D \rightarrow K_S^0 \pi^+ \pi^-$	$86.74 \pm 0.13$	$86.90 \pm 0.22$
		$D \rightarrow K_S^0 K^+ K^-$	$86.22 \pm 0.26$	$86.56 \pm 0.30$
Pion		$D \rightarrow K_S^0 \pi^+ \pi^-$	$97.11 \pm 0.11$	$97.17 \pm 0.13$
		$D \rightarrow K_S^0 K^+ K^-$	$97.07 \pm 0.11$	$97.16 \pm 0.14$

on `PIDK` for a number of bins in the momentum and pseudorapidity of the calibration tracks, and the number of charged tracks in the detector, thus constructing a three-dimensional efficiency lookup table. The procedure is carried out for each PID requirement, companion species, data-taking year, track charge, and magnet polarity. Based on these tables, expected PID efficiencies for the  $B^\pm \rightarrow D\pi^\pm$  and  $B^\pm \rightarrow DK^\pm$  signal decays are calculated that take the kinematical distribution and detector occupancy in the BPGBGSZ data samples into account, by using the high-purity sample of  $B^\pm \rightarrow D\pi^\pm$  candidates in the signal region as a reference. The dominating uncertainty on the efficiencies is statistical in nature, due to the finite size of the reference sample. In addition, systematic uncertainties are included due to the `sPlot` procedure, estimated at 0.1 % [?], and due to the choice of binning scheme, estimated by repeating the procedure using a number of alternative binning schemes. The final efficiency estimates are shown in Table 5.4, including all sources of uncertainty.

### 5.2.2 Efficiency profile over the Dalitz plot

The studies above share the  $F_i$  parameters between the  $B \rightarrow D\pi$  and  $B \rightarrow DK$  channels. This is reasonable, since the phase-space dependence of the reconstruction efficiency is expected to be very similar between the two decays, given the similar kinematics. This assumption is verified in large simulation samples that were generated for the 2015+16 analysis [?] (described in detail in section ??). The full selection is applied to the samples. The  $B \rightarrow D\pi$  sample LL (DD) sample has about 50,000 (130,000) decays, and the  $B \rightarrow DK$  samples LL (DD)<sup>2</sup> sample has 44,000 (112,000) decays. For  $B \rightarrow D\pi$  this is about 80 % of the number of decays in the full Run 1+2 data sample, and for  $B \rightarrow DK$  this is a factor of

<sup>2</sup>LL and DD denote two data categories, split by the track types for the pion candidates used to form the  $K_S^0$  candidate. See Section ??.

**Figure 5.8:** The  $(m^2(K_S^0\pi^+), m^2(K_S^0\pi^-))$  distribution in simulated samples of (left)  $B \rightarrow DK$  decays and (center)  $B \rightarrow D\pi$  decays, as well as (right) the ratio between the two histograms (corrected for differences in sample sizes). The  $p$  values are the results of  $\chi^2$  compatibility tests between the two histograms.

**Figure 5.9:** One-dimensional distributions of  $m^2(K_S^0\pi^+)$ ,  $m^2(K_S^0\pi^-)$ ,  $m^2(\pi^+\pi^-)$ , and  $m^2(K_S^0\pi^+) - m^2(K_S^0\pi^-)$  in (blue)  $B^\pm \rightarrow D(\rightarrow K_S^0\pi^+\pi^-)K^\pm$  and (red)  $B^\pm \rightarrow D(\rightarrow K_S^0\pi^+\pi^-)\pi^\pm$  decays in the (top) LL and (bottom) DD categories. The  $p$  values are the results of Kolmogorov-Smirnov compatibility tests between the distributions.

about 9 more decays than in the data sample. The decays were simulated with an equal decay probability across the  $D$ -decay phase space, so that any non-uniform distribution of reconstructed decays is completely determined by a phase-space dependent reconstruction and selection efficiency. Therefore the assumption that the phase-space dependence is identical between the  $B \rightarrow D\pi$  and  $B \rightarrow DK$  channels is verified by seeing if the Dalitz coordinates are distributed differently between the  $B \rightarrow D\pi$  and  $B \rightarrow DK$  MC samples.

This is investigated with two statistical tests. The first is a  $\chi^2$  comparison of 2D histograms of the distribution of  $m^2(K_S^0\pi^+)$  and  $m^2(K_S^0\pi^-)$  in the different  $B \rightarrow D\pi$  and  $B \rightarrow DK$  channels. These histograms, and the ratio between them, is shown in Fig. 5.8, along with the  $p$ -values from the  $\chi^2$  tests. It can be seen that in all cases the probability of obtaining the two histograms assuming that they share the same underlying distribution has a reasonable value, and there is no clear trend in the ratio plots. The second test is a Kolmogorov-Smirnov test of the compatibility of the one-dimensional distributions of  $m^2(K_S^0\pi^+)$ ,  $m^2(K_S^0\pi^-)$ ,  $m^2(\pi^+\pi^-)$ , and  $m^2(K_S^0\pi^+) - m^2(K_S^0\pi^-)$ . These distributions and the corresponding  $p$ -values are shown in Fig. 5.9 and 5.10. Again, all the  $p$  values are reasonable. Therefore it is concluded that there are no statistically significant differences between the phase-space dependence of the reconstruction and selection efficiency between the  $B \rightarrow D\pi$  and  $B \rightarrow DK$  channels with these statistics. Because the simulation samples have approximately the same amount of decays as data (or significantly more in the  $B \rightarrow DK$  case), any potential differences will be negligible with current statistics. Thus sharing the  $F_i$  parameters between the  $B \rightarrow D\pi$  and  $B \rightarrow DK$  channels is viable, and no efficiency correction is necessary.

**Figure 5.10:** One-dimensional distributions of  $m^2(K_S^0\pi^+)$ ,  $m^2(K_S^0\pi^-)$ ,  $m^2(\pi^+\pi^-)$ , and  $m^2(K_S^0\pi^+) - m^2(K_S^0\pi^-)$  in (blue)  $B^\pm \rightarrow D(\rightarrow K_S^0K^+K^-)K^\pm$  and (red)  $B^\pm \rightarrow D(\rightarrow K_S^0K^+K^-)\pi^\pm$  decays in the (top) LL and (bottom) DD categories. The  $p$  values are the results of Kolmogorov-Smirnov compatibility tests between the distributions.

## 1541 5.3 Background studies

1542 A wide range of backgrounds can potentially pollute the sample of signal candidates.

1543 The backgrounds group into three categories depending on how they are treated

1544 in the analysis:

- 1545 • Backgrounds that can be effectively removed in the selection
- 1546 • Backgrounds that are only present at a level where the impact on the
- 1547 measurement result is small, and which do therefore not have to be modelled
- 1548 • Backgrounds that are present at a level where they have to be modelled in
- 1549 the fit to data, and cannot effectively be rejected further in the selection

1550 The latter category comprises of combinatorial background, which remains present

1551 at a non-negligible level after the application of the BDT described in Section 5.1.2;

1552 contributions from a number of partly reconstructed  $B \rightarrow Dh^\pm X$  decays, where

1553  $X$  denotes a pion or photon that is not included in the reconstructed decay, and

1554 which can only be separated from signal decays by their  $m(Dh)$  distribution; and

1555 finally  $B^\pm \rightarrow D\pi^\pm$  decays that are categorised as  $B^\pm \rightarrow DK^\pm$  decays in the particle-

1556 identification step and vice-versa. These background sources are described in detail

1557 in Section 5.4. This section focuses on backgrounds that led to specific requirements

1558 in the selection or proved to be small enough to not merit special treatment.

### 1559 5.3.1 Charmless decays

1560 There is potentially a so-called *charmless* background present in data, consisting

1561 of  $B^\pm \rightarrow K_S^0h^+h^-h^\pm$  decays. These have the same final state as the signal decay,

1562 but no intermediate  $D$  meson. Because all final state particles are reconstructed,

1563 this background peaks in the  $B$  mass spectrum. This background is suppressed

1564 by requiring the reconstructed  $B$  and  $D$  decay vertices to be separated in the

1565  $z$  direction; specifically by requiring that  $\Delta z_{\text{significance}}^{D-B} > 0.5$ , where  $\Delta z_{\text{significance}}^{D-B}$

1566 was defined in Eq. (5.1). The remaining background level can be investigated

1567 by investigating the  $D$  mass sidebands.

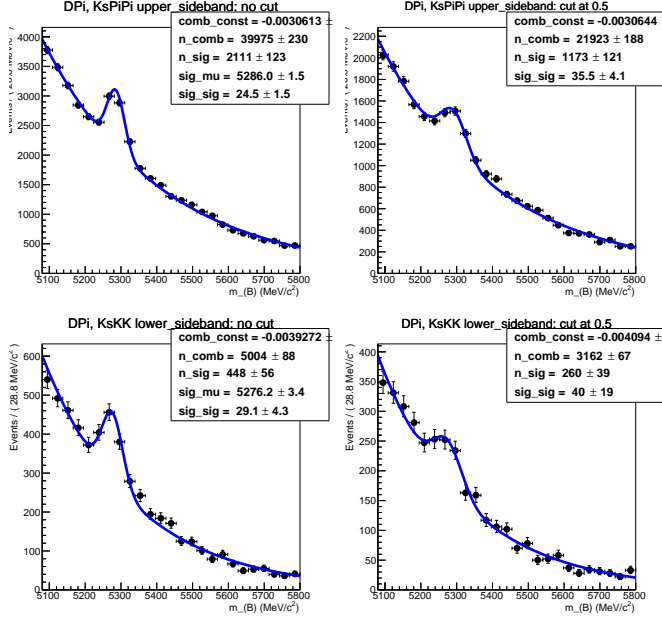


**Figure 5.11:** The  $B$  mass distribution of (top)  $B^\pm \rightarrow D(\rightarrow K_S^0\pi^+\pi^-)\pi^\pm$  and (bottom)  $B^\pm \rightarrow D(\rightarrow K_S^0K^+K^-)\pi^\pm$  candidates reconstructed in both the LL and DD categories, residing in the upper  $D$  mass sideband  $m_D \in [1910, 1960] \text{ MeV}/c^2$  for  $D \rightarrow K_S^0\pi^+\pi^-$  and in the lower sideband  $m_D \in [1910, 1960] \text{ MeV}/c^2$  for  $D \rightarrow K_S^0K^+K^-$ , with (left) no requirement on  $\Delta z_{\text{significance}}^{BD}$  and (right) after a requirement of  $\Delta z_{\text{significance}}^{BD} > 0.5$ .

1568 However, the use of the DecayTreeFitter  $\chi^2$  as an input variable in the BDT  
 1569 removes essentially all of the  $D$  (and  $K_S^0$ ) sideband, due to the mass constraints  
 1570 in the decay chain fit. Therefore separate BDT's are trained for LL and DD  
 1571 candidates without the  $\chi^2$  as an input variable, and used when selecting candidates  
 1572 for the background studies presented in this section, and the following. In a similar  
 1573 manner, all mass window requirements are made on the *default* reconstructed  
 1574 masses, obtained with no use of DecayTreeFitter. The overlap of the two sets of  
 1575 selected candidates in the signal  $B$ -mass window is above 95 %.

1576 The reconstructed  $B$  mass spectrum is shown for  $B^\pm \rightarrow D\pi^\pm$  candidates in the  
 1577  $D$  sidebands in Fig. 5.11, both before and after making a requirement on  $\Delta z_{\text{significance}}^{D-B}$ .  
 1578 A peak is clearly visible, the size of which is reduced by the requirement. This peak  
 1579 is partly due to a contribution from  $B^\pm \rightarrow K_S^0\pi^+\pi^-\pi^\pm$  decays ( $B^\pm \rightarrow K_S^0K^+K^-\pi^\pm$   
 1580 decays) in the  $D \rightarrow K_S^0\pi^+\pi^-$  ( $D \rightarrow K_S^0K^+K^-$ ) channel, and partly due to real  
 1581 signal decays that leak into the  $D$  sidebands. The number of real signal decays can  
 1582 be calculated from the yield obtained in the fit of Section 5.4, and the reconstructed  
 1583  $m_D$  distribution in simulated signal decays. Subtracting this contribution, it is  
 1584 estimated that approximately 450 (200) charmless decays are present in the  $K_S^0\pi^+\pi^-$   
 1585 ( $K_S^0K^+K^-$ ) data samples. In similar fashion, Fig. 5.12 shows the  $m_B$  spectra for

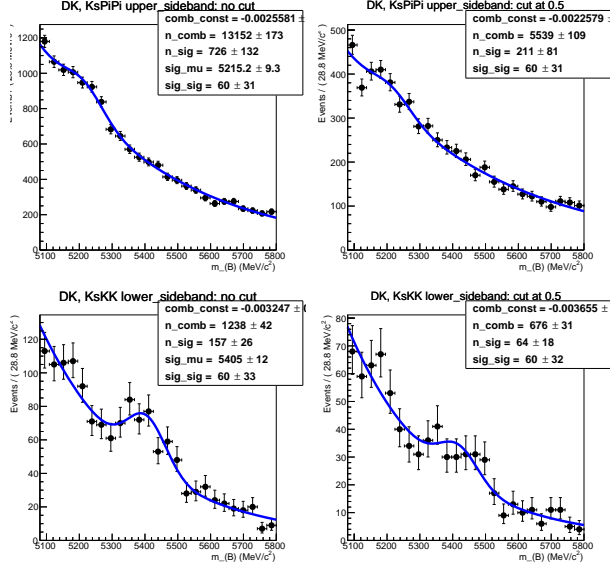


**Figure 5.12:** The  $B$  mass distribution of (top)  $B^\pm \rightarrow D(\rightarrow K_S^0\pi^+\pi^-)K^\pm$  and (bottom)  $B^\pm \rightarrow D(\rightarrow K_S^0K^+K^-)K^\pm$  candidates reconstructed in both the LL and DD categories, residing in the upper  $D$  mass sideband  $m_D \in [1910, 1960] \text{ MeV}/c^2$  for  $D \rightarrow K_S^0\pi^+\pi^-$  and in the lower sideband  $m_D \in [1910, 1960] \text{ MeV}/c^2$  for  $D \rightarrow K_S^0K^+K^-$ , with (left) no requirement on  $\Delta z_{\text{significance}}^{BD}$  and (right) after a requirement of  $\Delta z_{\text{significance}}^{BD} > 0.5$ .

1586  $B^\pm \rightarrow DK^\pm$  candidates in the  $D$  sidebands. In these plots, the peaks are at  
 1587  $m_B$  values that are lower (higher) than the  $B$  mass in the  $K_S^0\pi^+\pi^-$  ( $K_S^0K^+K^-$ )  
 1588 categories, because they stem from real  $B^\pm \rightarrow K_S^0K^+K^-\pi^\pm$  decays where a kaon is  
 1589 mis-reconstructed as a pion or a pion is misreconstructed as a kaon, respectively.  
 1590 The total contribution of charmless decays in the  $B^\pm \rightarrow DK^\pm$  data samples is  
 1591 estimated to be about 200 decays. As described further in Section 5.6.11, the  
 1592 presence of a charmless background at these levels has a negligible impact on  
 1593 the measurement results.

### 1594 5.3.2 Background from four-body $D$ decays

1595 A similar potential background is from real  $B^\pm \rightarrow Dh^\pm$  decays where the  $D$  meson  
 1596 decays directly to the  $\pi^+\pi^-h^+h^-$  final state, without an intermediate  $K_S^0$  meson.  
 1597 This background can be investigated by looking for a peak in the  $B$  mass spectrum  
 1598 for candidates in the  $K_S^0$  sideband, as illustrated in Fig. 5.13. The figure shows  
 1599 the spectrum in the final data sample, illustrating the significant effect of making  
 1600 the requirement on the  $K_S^0$  flight distance that was discussed in Section 5.1.1. The  
 1601 BDT that does *not* rely on the DTF  $\chi^2$  has been used to suppress combinatorial  
 1602 background. The remaining peak after requiring  $\chi_{\text{FD}}^2 > 49$  is completely accounted  
 1603 for by real signal decays that leak into the  $K_S^0$  sideband.

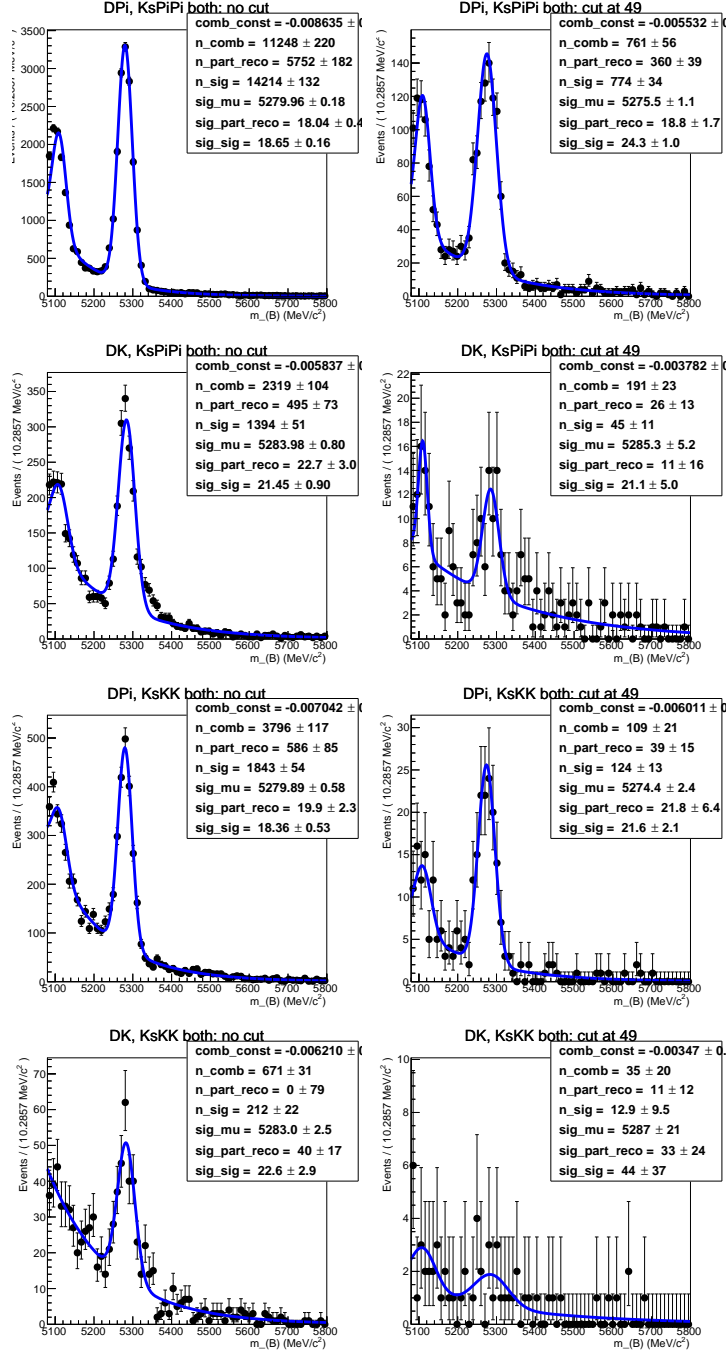


**Figure 5.13:** The  $B$  mass spectrum in the  $K_S^0$  sideband where  $m_{K_S^0} \in [467, 482] \text{ MeV}/c^2$  or  $m_{K_S^0} \in [512, 527] \text{ MeV}/c^2$  (left) without a requirement on the  $K_S^0$  flight distance significance, and (right) after the requirement implemented in the analysis.

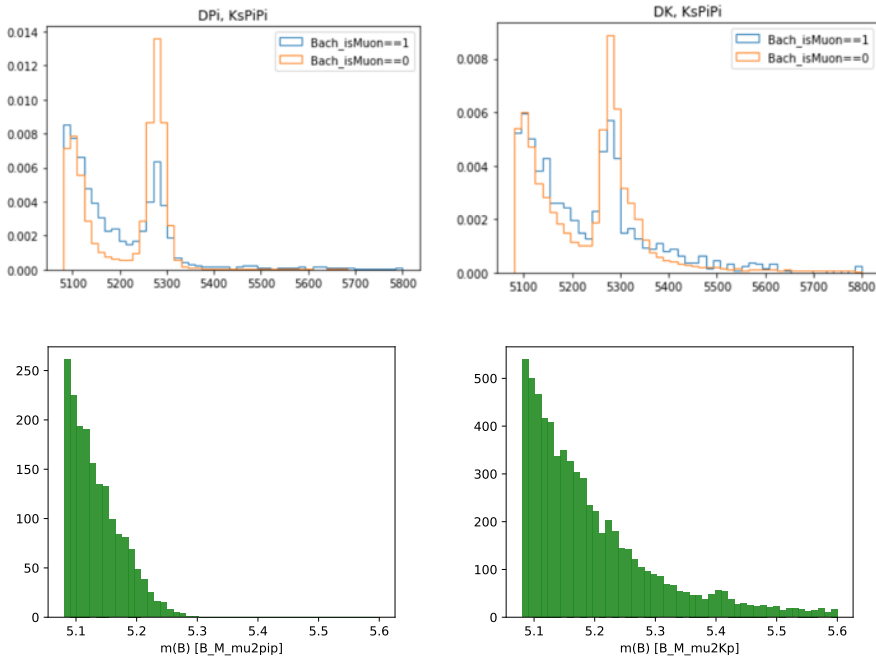


**Figure 5.14:** (Top) The  $m_B$  spectra in data split by the value of `Bach_isMuon` for (left) the  $D\pi^\pm$  and (right) the  $DK^\pm$  samples where  $D \rightarrow K_S^0\pi^+\pi^-$ . The two histograms are normalised independently, so that the distributions can be compared. The fractions candidates in data (with  $m_B \in [5080, 5800]$  MeV/c<sup>2</sup>) that satisfy `Bach_isMuon=1` are 1.6 % and 1.8 % for the  $D\pi^\pm$  and  $DK^\pm$  channels respectively. (Bottom) the RapidSim mass spectra for  $B^\pm \rightarrow D^0\mu^\pm\nu_\mu$  decays reconstructed in the (left)  $D\pi^\pm$  and (right)  $DK^\pm$  categories.

### 1604 5.3.3 Semi-leptonic backgrounds

1605 The data sample has a minor background from  $B \rightarrow D\mu\nu_\mu X$  decays, visible  
 1606 in the  $B$  mass spectrum when the companion is required to satisfy `isMuon=1`.  
 1607 This is shown in Fig. 5.14 for both the  $B^\pm \rightarrow DK^\pm$  and  $B^\pm \rightarrow D\pi^\pm$  channels  
 1608 where  $D \rightarrow K_S^0\pi^+\pi^-$ . The  $B$  mass spectra for simulated  $B^\pm \rightarrow D\mu^\pm\nu_\mu$  decays  
 1609 reconstructed in each category are also shown, from simulation samples produced via  
 1610 RapidSim. The background is very efficiently vetoed by requiring `IsMuon=0` on the  
 1611 companion. This requirement removes approximately 85 % of the background decays,  
 1612 as estimated using the `PIDCalib` calibration samples and the ( $p, p_T$ ) distribution  
 1613 for the muon in the RapidSim samples. The fraction of signal candidates for  
 1614 which the companion satisfies `IsMuon=1` in simulated signal samples is  $\leq 0.9$  %  
 1615 so the impact on signal yield is small.

1616 The analogous  $B \rightarrow Dev_eX$  background is investigated by inspecting the  $B$   
 1617 mass spectra after making requirements on `PIDe` for the companion candidate, but  
 1618 a presence of the semi-leptonic background in data is not visible and no electron  
 1619 veto is applied to the companion.

1620 **Background from semi-leptonic D decays**

1621 There is a potential background from real  $B^\pm \rightarrow Dh^\pm$  decays where the  $D$   
1622 meson decays semi-leptonically:  $D^0 \rightarrow K_S^0\pi^-\ell^+\nu_\ell$ . This background is particularly  
1623 dangerous because it peaks at the  $B$  mass, when the  $D$ -mass requirement is applied  
1624 and it is reconstructed in the  $D \rightarrow K_S^0\pi^+\pi^-$  category. This is illustrated in Fig. 5.15  
1625 using RapidSim samples of  $B^\pm \rightarrow D(\rightarrow K^{*-}(X)(\rightarrow K_S^0\pi^-)\ell^+\nu_\ell)h^\pm$  decays for  
1626  $X = 892, 1430, 1680$ . The expected background yields relative to signal can be  
1627 estimated by applying the  $B$  and  $D$  mass cuts to decays in the RapidSim samples,  
1628 and using the relative branching ratios. Only the  $D^0 \rightarrow K^{*-}(892)\ell\nu_\ell$  branching  
1629 fractions have been measured [?], but there is no reason to expect that higher  
1630  $K^*$  resonances should not contribute. To estimate their potential contribution,  
1631 the branching ratios are approximated by

$$\text{BR}[D^0 \rightarrow K^{*-}(X)(\rightarrow K_S^0\pi^-)\ell\nu_\ell] \simeq \frac{\text{BR}[D^0 \rightarrow K^{*-}(X)(\rightarrow K_S^0\pi^-)\pi^+]}{\text{BR}[D^0 \rightarrow K^{*-}(892)(\rightarrow K_S^0\pi^-)\pi^+]} \text{BR}[D^0 \rightarrow K^{*-}(892)(\rightarrow K_S^0\pi^-)\ell\nu_\ell]$$

1632 because all the relevant  $D^0 \rightarrow K^{*-}(\rightarrow K_S^0\pi^-)\pi^+$  branching fractions are known [?].  
1633 The efficiencies and branching ratios relative to the signal channel are given in  
1634 Table 5.5. It is clear that the higher  $K^*$  resonances are important: the smaller  
1635 branching ratios are compensated for by a higher selection efficiency, due to the  
1636 smaller phase-space of the missed neutrino. The total background yield is 1.1 %  
1637 of the signal yield in both the  $B^\pm \rightarrow D\pi^\pm$  and  $B^\pm \rightarrow DK^\pm$  channels. However,  
1638 there will be an additional contribution in the  $B^\pm \rightarrow DK^\pm$  channel from real  
1639  $B^\pm \rightarrow D\pi^\pm$  decays with semi-leptonic  $D$  decays and a mis-identification of the  
1640 companion. This background also peaks, and the yield is approximately 0.4 %  
1641 of the  $B^\pm \rightarrow DK^\pm$  signal yield.

1642 The potential impact from the presence of the background is estimated by

- 1643 1. calculating the expected  $B^\pm \rightarrow D\pi^\pm$  and  $B^\pm \rightarrow DK^\pm$  yields in each bin for  
1644 physics parameters similar to the world average values
- 1645 2. then calculating the background bin yields in each bin, using the relative  
1646 branching fractions and efficiencies described above and taking the bin-  
1647 distribution from the RapidSim samples. The RapidSim samples are produced  
1648 using the ISGW2 model in EvtGen [?], yielding the Dalitz distributions in  
1649 Fig. 5.16.

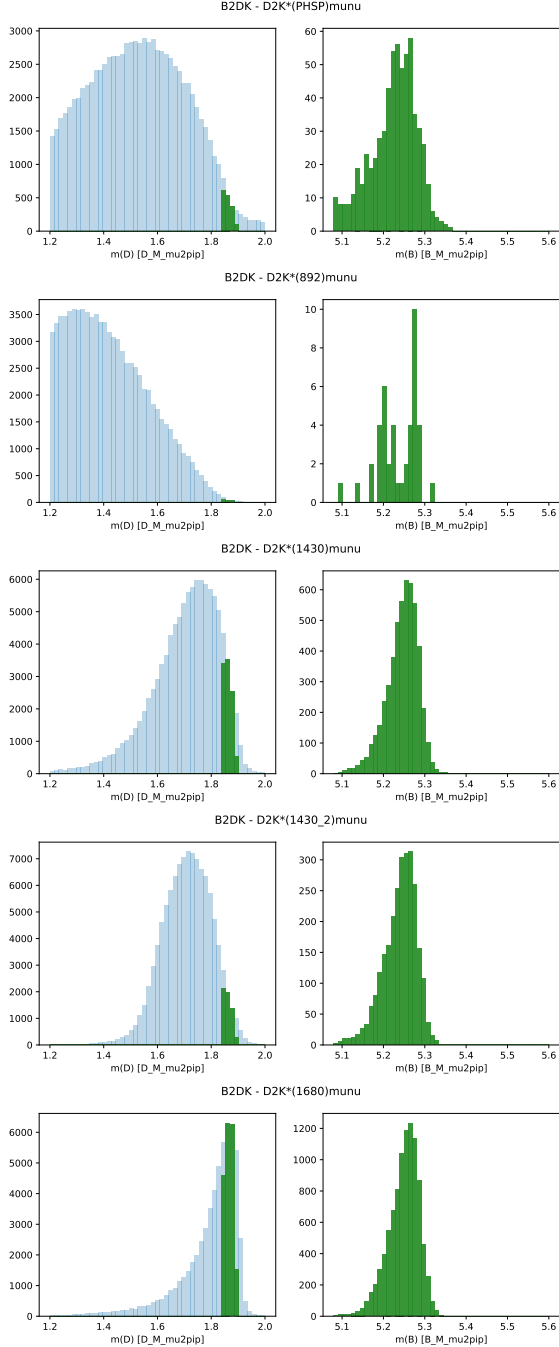


**Figure 5.15:** The reconstructed (left)  $m(K_S^0 \pi^+ \pi^-)$  and (right)  $m(Dh)$  distributions in RapidSim samples of  $B^\pm \rightarrow DK^\pm$  decays where  $D^0 \rightarrow K_S^0 \pi^- \mu^+ \nu_\mu$ . The top plot is for PHSP decays, and the following plots show the distribution where the  $K_S^0 \pi^-$  originate in the resonances  $K^{*-}(892)$ ,  $K^{*-}_0(1430)$ ,  $K^{*-}_2(1430)$ , and  $K^{*-}(1680)$ . The shapes for the  $D^0 \rightarrow K_S^0 \pi^- e^+ \nu_e$  case are almost identical.

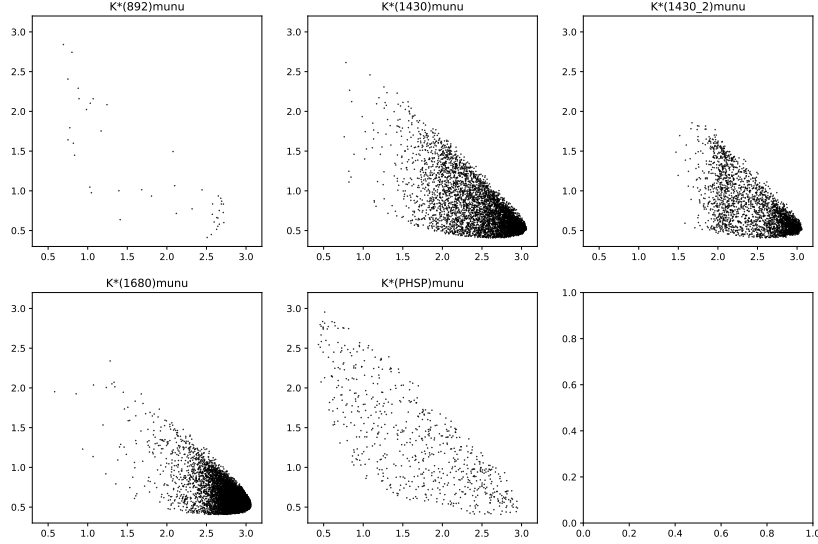


**Figure 5.16:** Dalitz distribution for  $D \rightarrow K_S^0 \pi \mu \nu_\mu$  decays in RapidSim, where the  $K_S^0 \pi^-$  originate in the resonances  $K^{*-}(892)$ ,  $K^{*-}_0(1430)$ ,  $K^{*-}_2(1430)$ , and  $K^{*-}(1680)$ , as well as for a flat PHSP distribution.

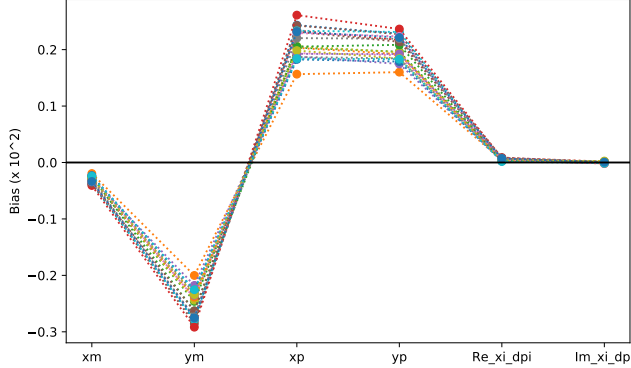


**Figure 5.17:** Estimated biases on the measured observables due to the presence of  $D \rightarrow K_S^0 \pi \ell \nu_\ell$  backgrounds, calculated while varying efficiencies and branching ratios within uncertainties.

- 1650     3. adding the signal and background yields, and fitting the new  $B^\pm \rightarrow D\pi^\pm$  and  
 1651      $B^\pm \rightarrow DK^\pm$  yields back with the default signal-yield expressions (including a  
 1652     fit of the  $F_i$  parameters)

1653     The obtained biases are shown in Fig. 5.17, where they are calculated a number  
 1654     of times, each time varying the efficiencies within statistical uncertainties and the  
 1655     relevant branching fractions within the measurement uncertainties. The systematic

**Table 5.5:** The selection efficiencies of  $B^\pm \rightarrow DK^\pm$  decays where  $D^0 \rightarrow K_S^0\pi^-\ell^+\nu_\ell$  when reconstructed in the  $D \rightarrow K_S^0\pi^+\pi^-$  mode in RapidSim relative to the signal selection efficiencies, for a number of decay modes: PHSP as well as resonant production where the  $K_S^0\pi^-$  pair originates in one of several  $K^*$  resonances. The relative branching ratios are also shown, calculated as explained in the main text, as well as the predicted relative yields.

Mode	$\epsilon_{bkg}/\epsilon_{signal}$ (%)	$\Gamma_{bkg}/\Gamma_{signal}$ (%)	$N_{bkg}/N_{signal}$ (%)
$D \rightarrow K_S^0\pi^-\mu^+\nu_\mu$ (PHSP)	$0.92 \pm 0.05$	$18.3 \pm 14.8$	$0.17 \pm 0.14$
$D \rightarrow (K_S^0\pi^-)_{K^{*-}(892)}\mu^+\nu_\mu$	$0.06 \pm 0.01$	$22.3 \pm 3.2$	$0.013 \pm 0.003$
$D \rightarrow (K_S^0\pi^-)_{K_0^{*-}(1430)}\mu^+\nu_\mu$	$7.3 \pm 0.1$	$3.7 \pm 0.8$	$0.27 \pm 0.06$
$D \rightarrow (K_S^0\pi^-)_{K_2^{*-}(1430)}\mu^+\nu_\mu$	$3.7 \pm 0.1$	$0.5 \pm 0.3$	$0.02 \pm 0.01$
$D \rightarrow (K_S^0\pi^-)_{K^{*-}(1680)}\mu^+\nu_\mu$	$24.4 \pm 0.3$	$0.6 \pm 0.5$	$0.15 \pm 0.12$
$D \rightarrow K_S^0\pi^-e^+\nu_e$ (PHSP)	$0.53 \pm 0.02$	$20.8 \pm 16.3$	$0.11 \pm 0.09$
$D \rightarrow (K_S^0\pi^-)_{K^{*-}(892)}e^+\nu_e$	$0.15 \pm 0.02$	$25.6 \pm 2.5$	$0.04 \pm 0.01$
$D \rightarrow (K_S^0\pi^-)_{K_0^{*-}(1430)}e^+\nu_e$	$6.3 \pm 0.1$	$4.2 \pm 0.8$	$0.26 \pm 0.05$
$D \rightarrow (K_S^0\pi^-)_{K_2^{*-}(1430)}e^+\nu_e$	$4.12 \pm 0.08$	$0.5 \pm 0.3$	$0.02 \pm 0.01$
$D \rightarrow (K_S^0\pi^-)_{K^{*-}(1680)}e^+\nu_e$	$10.0 \pm 0.2$	$0.7 \pm 0.5$	$0.07 \pm 0.05$
Total	-	-	$1.1 \pm 0.4$

uncertainty due to the unknown branching fractions and the use of RapidSim in lieu of full simulation is not included, but is of course significant. Nevertheless it is clear that the potential biases are significant compared to the size of the systematic uncertainties of the analysis presented in Section 5.6. Therefore the backgrounds are vetoed by requiring `IsMuon=0` and `PIDe < 0` on the pions from the  $D$ -decay with opposite charge to the bachelor in the  $D \rightarrow K_S^0\pi^+\pi^-$  channel. This requirement removes 88 % of the muonic background and 99 % of the electron background, according to PID efficiencies obtained via the `PIDCalib` package, using the  $(p, p_T)$  distribution for the muon/electron in the RapidSim samples. The survival rate for signal decays in full simulation is 94 %, so the impact on the obtainable precision is only about 3 %. A systematic uncertainty is assigned to account for the potential remaining background.

In the  $D \rightarrow K_S^0K^+K^-$  channel an analogous study shows the relative yields to be similar. The selection efficiencies are higher, as are the relative branching ratios due to the lower  $D \rightarrow K_S^0K^+K^-$  branching fraction, but in this mode the `PIDK > -5` requirement placed on the pion and lepton remove approximately 90 % of the background, leaving the relative rate similar to in  $D \rightarrow K_S^0\pi^+\pi^-$ . However, importantly, *the background is not peaking*, as shown in Fig. 5.18. The presence of a percent-level, *non-peaking* background in the  $D \rightarrow K_S^0K^+K^-$  channel is safe to ignore and thus no veto is applied in the  $D \rightarrow K_S^0K^+K^-$  channel.

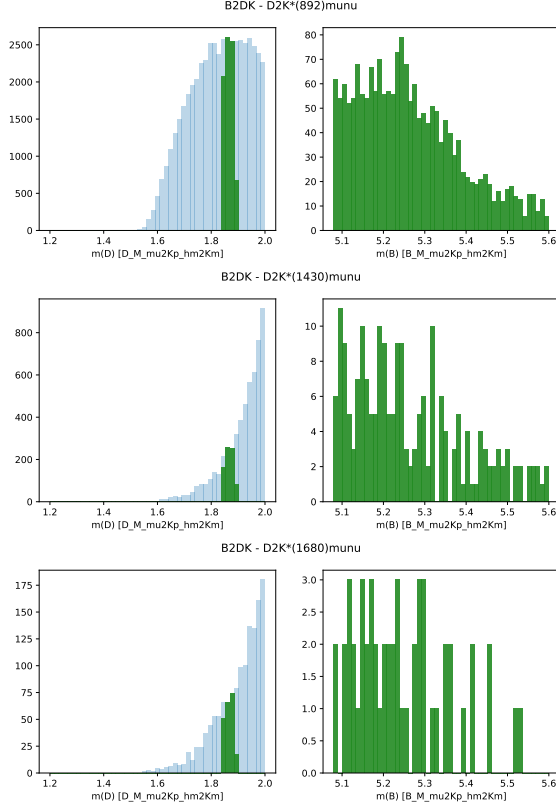


**Figure 5.18:** The reconstructed (left)  $m(K_S^0 K^+ K^-)$  and (right)  $m(Dh)$  distributions in RapidSim samples of  $B^\pm \rightarrow DK^\pm$  decays where  $D^0 \rightarrow K_S^0 \pi^- \mu^+ \nu_\mu$ , where the  $K_S^0 \pi^-$  originate in (top to bottom) the resonances  $K^{*-}(892)$ ,  $K^{*-}_0(1430)$ , and  $K^{*-}(1680)$ . The shapes for the  $D^0 \rightarrow K_S^0 \pi^- e^+ \nu_e$  case are almost identical.

1676     The muon-veto for the semi-leptonic background does remove some signal  
 1677     decays, where an original pion or kaon results in hits in the muon detectors. A  
 1678     significant contribution is from particles that decay in flight. The track quality  
 1679     of these decays is worse than for nominal decays, which affects the resolution on  
 1680     the reconstructed Dalitz coordinates. In simulated signal decays the standard  
 1681     deviation of  $\Delta m_\pm^2 = m_{reco}^2(K_S^0 \pi^\pm) - m_{TRUE}^2(K_S^0 \pi^\pm)$  is 50 % larger for decays where  
 1682     one of the  $D$ -decay products has `IsMuon=1` than in decays where this is not the  
 1683     case. This can lead to systematic biases on the observables, as described further in  
 1684     Section ???. The overall effect is small, as evidenced by the systematic uncertainty  
 1685     described in that section; nevertheless this fact motivates removing decay-in-flight  
 1686     decays of the  $D$ -decay products. Therefore it is also required that `IsMuon=0` for  
 1687     the  $D$ -decay pion with the same charge as the companion in the  $D \rightarrow K_S^0 \pi^+ \pi^-$   
 1688     channels, and on the  $D$ -decay kaons in the  $D \rightarrow K_S^0 K^+ K^-$  channels. This veto  
 1689     removes about 2 % of signal candidates in simulation that survive the lepton vetoes  
 1690     described in the previous sections.

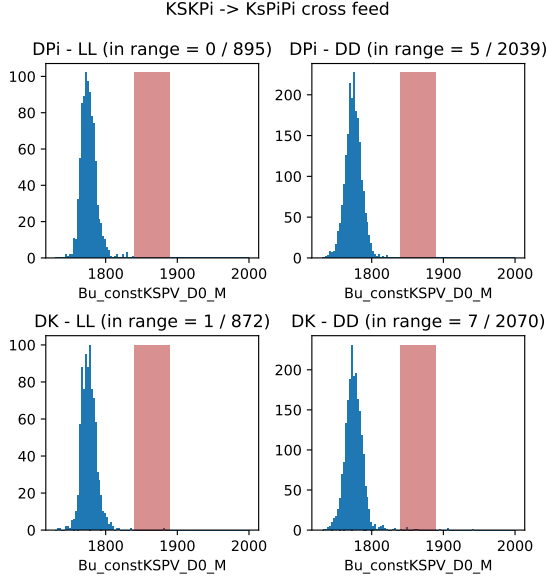


**Figure 5.19:** Simulated samples of (top)  $B^\pm \rightarrow D(\rightarrow K_S^0 K\pi)\pi^\pm$  and (bottom)  $B^\pm \rightarrow D(\rightarrow K_S^0 K\pi)K^\pm$  decays, reconstructed in the corresponding  $B^\pm \rightarrow D(\rightarrow K_S^0 \pi^+\pi^-)h^\pm$  channel, for (left) the LL and (right) DD track-type categories. The  $D$ -mass region included in the selection of signal decays is illustrated with the red band.

### 1691 5.3.4 Cross-feed from other $D \rightarrow K_S^0 h^+ h^-$ decays

1692 Misidentification of a  $D$  decay product can lead to background from cross-feed  
 1693 between the  $B^\pm \rightarrow D(\rightarrow K_S^0 \pi^+\pi^-)h^\pm$  and  $B^\pm \rightarrow D(\rightarrow K_S^0 K^+ K^-)h^\pm$  signal chan-  
 1694 nels, or cross-feed from  $B^\pm \rightarrow D(\rightarrow K_S^0 K\pi)h^\pm$  decays into either of the signal  
 1695 channels. However, this background is very highly suppressed by the employed  
 1696 requirement on the  $D$  mass. This is illustrated in Figs. 5.19 and 5.20, where  
 1697 the  $D$  mass distribution in samples of simulated  $B^\pm \rightarrow D(\rightarrow K_S^0 K\pi)K^\pm$  and  
 1698  $B^\pm \rightarrow D(\rightarrow K_S^0 K\pi)\pi^\pm$  decays are shown, when reconstructed as  $D \rightarrow K_S^0 \pi^+\pi^-$  and  
 1699  $D \rightarrow K_S^0 K^+ K^-$ , respectively. Essentially no decays that fall in the selected  $D$  mass  
 1700 window survive the full selection. Therefore this background is not considered further.  
 1701 Neither is the background due to cross-feed between  $B^\pm \rightarrow D(\rightarrow K_S^0 \pi^+\pi^-)h^\pm$   
 1702 and  $B^\pm \rightarrow D(\rightarrow K_S^0 K^+ K^-)h^\pm$ , since it involves two misidentified particles, and  
 1703 therefore will result in reconstructed  $D$  masses even further away from the selected  
 1704 mass window. A very loose PID requirement on the charged  $D$  decay products  
 1705 is nonetheless included in the  $D \rightarrow K_S^0 K^+ K^-$  channel, because it helps reduce  
 1706 the level of combinatorial background.

### 1707 5.3.5 Swapped-track backgrounds

1708 A possible peaking background stems from real  $B \rightarrow DhX$  decays with the same  
 1709 final state tracks as in the signal case, but where some tracks are mis-assigned in the

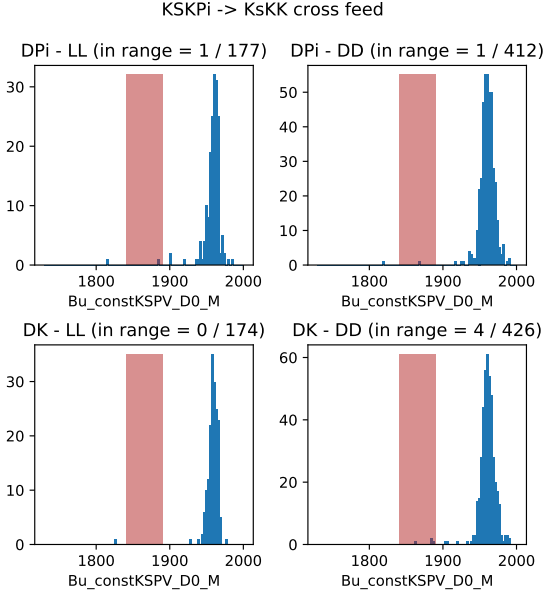


**Figure 5.20:** Simulated samples of (top)  $B^\pm \rightarrow D(\rightarrow K_S^0 K \pi^\pm)$  and (bottom)  $B^\pm \rightarrow D(\rightarrow K_S^0 K \pi^\pm)K^\pm$  decays, reconstructed in the corresponding  $B^\pm \rightarrow D(\rightarrow K_S^0 K^+ K^-)h^\pm$  channel, for (left) the LL and (right) DD track-type categories. The  $D$ -mass region included in the selection of signal decays is illustrated with the red band.

reconstruction. Examples are  $B^\pm \rightarrow (K_S^0 h'^+ h''^-)_D h^\pm$  decays where the companion and a  $D$ -decay product track are swapped, or  $B^\pm \rightarrow (K^- \pi^+)_D K_S^0 h^\pm$  decays, where the  $K_S^0$  is assigned to the  $D$  decay and the real companion is swapped with the  $D$ -decay product of the same charge. The signature of this background type is a peak at the  $D$  mass, when the invariant mass corresponding to the companion track and some subset of the  $D$ -decay tracks is formed. The presence of the background has been investigated by forming all such combinations, for all data categories, after the full selection has been applied. Only in a single channel is a peak visible: the  $B^\pm \rightarrow (K_S^0 \pi^+ \pi^-)K^\pm$  channel, where  $m(K^\pm \pi^\pm)$  has a peak, as shown in Fig. 5.21. Thus, a background is present from the favoured two-body  $D$  decay  $B^\pm \rightarrow (K^\pm \pi^\mp)_D K_S^0 \pi^\pm$ , where the  $K^\mp$  is reconstructed as the companion, and the pions assigned to the  $D$  decay.

Is is not favourable to veto this background, because a requirement on the invariant mass of a track combination that includes the companion track would impact the Dalitz-plot acceptance differently in the  $DK^\pm$  and  $D\pi^\pm$  channels. Thus it would break a fundamental underlying feature of the measurement: the identical selection efficiency profile between these modes. However, the yield excess in the  $m(K^\pm_{Bach} \pi^\mp_D)$  range around  $m_D$ , attributed to the background, corresponds to only about 0.5 % of the signal yield. A background at this level does not lead to a limiting systematic uncertainty on the measurement, as described in Section ??.

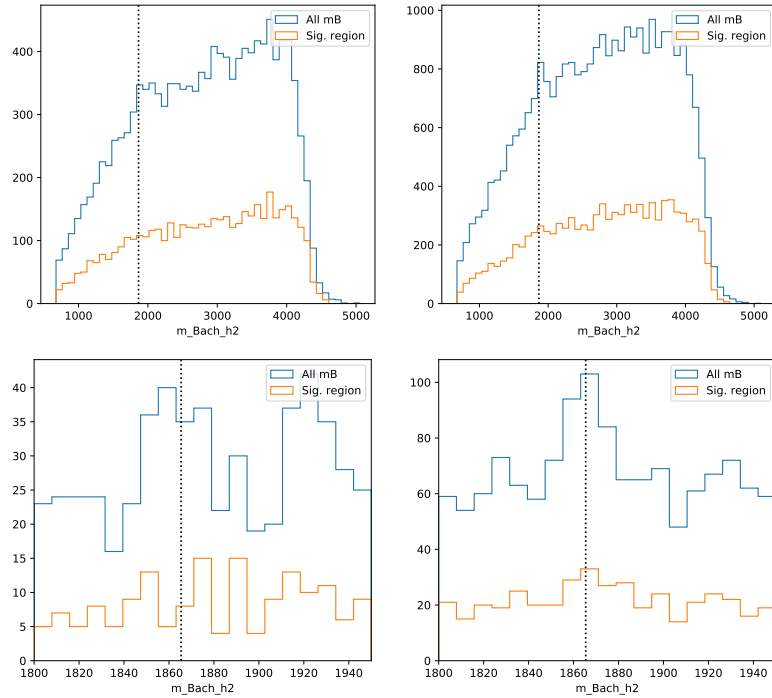


**Figure 5.21:** Invariant mass spectrum of the  $m^2(K^\pm\pi^\mp)$  combination in the  $B \rightarrow (K_S^0\pi^+\pi^-)K^\pm$  category for (blue) all candidate and (orange) candidates for which  $m_B \in m_B^{PDG} \pm 30 \text{ MeV}/c^2$ . The candidates are split into (left) the LL and (right) the DD candidates. The only difference between the top and bottom plots is the  $m(K\pi)$  mass range on the horizontal axis.

## 1730 5.4 Signal and background mass shapes

1731 The measurement employs *extended maximum-likelihood fits* [?] to the  $m(Dh^\pm)$   
 1732 distribution of signal candidates to determine the observables of interest. The  
 1733 analysis implements a two-step fit procedure: first the data samples are analysed  
 1734 without separating the candidates by  $B$  charge or Dalitz bin, in order to determine  
 1735 appropriate parametrisations of the  $m(Dh^\pm)$  distribution of the signal and relevant  
 1736 background components. The parameterisations are then kept fixed in a subsequent  
 1737 fit of the observables of interest, where the candidates are split by  $B$  charge  
 1738 and Dalitz bin. This section describes the first step, whereas the latter fit is  
 1739 the subject of Section 5.5.

1740 In both steps, the candidates are split in 8 categories depending on whether  
 1741 the companion is categorised as a kaon or pion, whether the  $K_S^0$  meson is in the  
 1742 LL or DD category, and by whether the  $D$  meson is reconstructed in the  $K_S^0\pi^+\pi^-$   
 1743 or  $K_S^0K^+K^-$  final state. In the remained of this text, these categories are indexed  
 1744 with the letter  $c$ . For each category,  $c$ , the expected number of observed decays

1745 at a given  $B$  mass,  $F^c(m)$ , is given by the sum of a signal contribution and a  
1746 number of background distributions

$$F^c(m|\theta) = N_s^c(\theta)f_s^c(m|\theta) + \sum_b N_b^c(\theta)f_b^c(m|\theta), \quad (5.4)$$

1747 where  $\theta$  denotes a set of parameters that describe the mass shapes and expected  
1748 yields, in which some parameters are shared between categories. The distributions  
1749  $f_{s/b}^c$  are normalised to integrate to unity, and the expected signal (background)  
1750 yields are denoted  $N_s^c$  ( $N_b^c$ ). A total, normalised distribution can then be defined

$$f^c(m|\theta) = \frac{1}{N_{\text{tot}}^c(\theta)} F^c(m|\theta), \quad N_{\text{tot}}^c(\theta) = N_s^c(\theta) + \sum_b N_b^c(\theta). \quad (5.5)$$

1751 Given a set of  $N_{\text{observed}}^c$  measured  $B$  masses,  $\{m_i^c\}$ , in a given category, the extended  
1752 log-likelihood function is defined

$$\ln \mathcal{L}_c(\theta|\{m_i^c\}) \equiv \sum_i \ln f^c(m_i^c|\theta) + \ln \text{Poisson}(N_{\text{tot}}^c(\theta), N_{\text{observed}}^c) \quad (5.6)$$

1753 In a simultaneous fit the total, negative log-likelihood is  $-\ln \mathcal{L} = -\sum_c \mathcal{L}_c$ , and  
1754 this function can be minimised to find the maximum-likelihood estimates of the  
1755 parameters in  $\theta$ , as well as their confidence regions and correlation coefficients.  
1756 This is handled with the `RooFit` package [?].

1757 Apart from signal decays, the fit includes components that describe combinatorial  
1758 background, backgrounds from decays where a companion pion is misidentified  
1759 as a kaon or vice versa, and partially reconstructed backgrounds. Each of these  
1760 components are described in detail in the following, before the results of the  
1761 first-stage fit are presented in Section 5.4.5.

### 5.4.1 Signal decays

1763 The signal component is modelled with a sum of a Gaussian density function,  
1764  $f_G(m|m_B, \sigma)$ , and a modified Gaussian distribution with the parameterisation

$$f_C(m|m_B, \sigma, \alpha_L, \alpha_R, \beta) \propto \begin{cases} \exp\left[\frac{-\Delta m^2(1+\beta\Delta m^2)}{2\sigma^2+\alpha_L\Delta m^2}\right], & \Delta m = m - m_B < 0 \\ \exp\left[\frac{-\Delta m^2(1+\beta\Delta m^2)}{2\sigma^2+\alpha_R\Delta m^2}\right], & \Delta m = m - m_B > 0, \end{cases} \quad (5.7)$$

1765 which is Gaussian when  $\Delta m^2 \ll \sigma^2/\alpha_{L/R}$  or  $\Delta m^2 \gg \beta^{-1}$  (with widths of  $\sigma$  and  
1766  $\sqrt{\alpha_{L/R}/\beta}$  respectively), with an exponential-like transition that is able to model the  
1767 effect of the experimental resolution of LHCb very well. For the case  $\beta = 0$  the shape  
1768 is denoted the *Cruijff* shape; however, in this case it tends to a uniform distribution

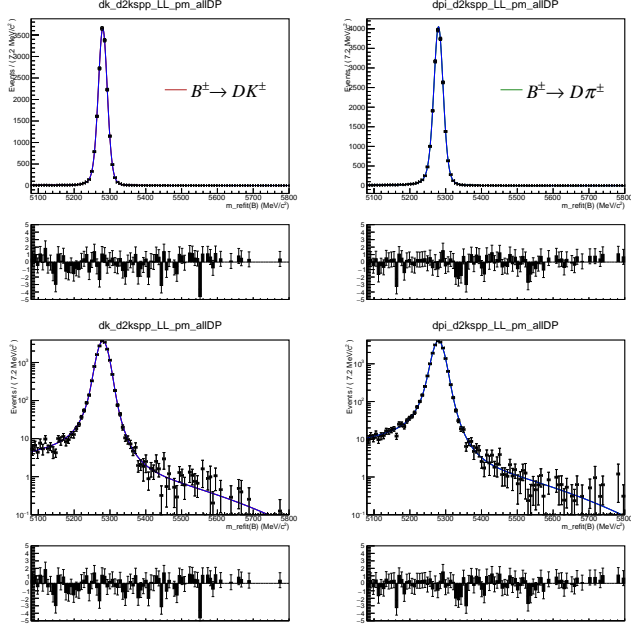


**Figure 5.22:** Fit projection of the signal shape to simulated  $B^\pm \rightarrow D(\rightarrow K_S^0 \pi^+ \pi^-) h^\pm$  samples reconstructed in the LL category. (Left) shows  $DK$  shapes, and (right) shows  $D\pi$  shapes. The shapes are shown with both linear and logarithmic  $y$ -axis scales.

for large  $\Delta m^2$  values, and cannot model the tails of the signal distribution well.  
Thus, the full density function is

$$f_s(m|m_B, \sigma, \alpha_L, \alpha_R, \beta) = k_C f_C(m|m_B, \sigma, \alpha_L, \alpha_R, \beta) + (1 - k_C) f_G(m|m_B, \sigma). \quad (5.8)$$

The tail parameters ( $\alpha_{L/R}, \beta$ ) and the constant  $k_C$  are determined in fits to simulated signal decays that have passed the full selection. The parameters are shared between the  $K_S^0 \pi^+ \pi^-$  and  $K_S^0 K^+ K^-$  channels, but otherwise independent in the fit categories. An example of a fit to simulated  $B^\pm \rightarrow D(\rightarrow K_S^0 \pi^+ \pi^-) h^\pm$  decays is given in Fig. 5.22. The resolution parameters  $\sigma$  are determined in the fit to actual data. Separate parameters are determined in the LL and DD categories, because the LL category has a better resolution on the  $K_S^0$  momentum, and therefore a narrow peak in reconstructed  $B$  mass. Likewise, separate resolution parameters are used for  $B^\pm \rightarrow D\pi^\pm$  and  $B^\pm \rightarrow DK^\pm$  decays, because the smaller  $Q$  value in the latter case leads to smaller momenta of the decay products, and a correspondingly better resolution.

The signal yields are determined independently in each  $B^\pm \rightarrow D\pi^\pm$  category. The yields in the  $B^\pm \rightarrow DK^\pm$  categories are then parameterised in terms of a single yield-ratio  $\mathcal{R}$ , and  $\epsilon^c$ , the corresponding selection efficiency for a given category

$$N_{DK^\pm}^c = \mathcal{R} \times N_{D\pi^\pm}^c \times \frac{\epsilon_{DK^\pm}^c}{\epsilon_{D\pi^\pm}^c}. \quad (5.9)$$

1785 The selection efficiency is obtained in simulation, except for the PID efficiencies  
 1786 which are obtained in calibration data as described in Section 5.1.3. The param-  
 1787 eter  $\mathcal{R}$  is shared between all categories, and corresponds to the branching ratio  
 1788 between  $B^\pm \rightarrow DK^\pm$  and  $B^\pm \rightarrow D\pi^\pm$  decays. Therefore, it can be compared to  
 1789 the branching ratio ratio measured in dedication measurements, which serves as  
 1790 an important cross check of the efficiency determination.

### 1791 5.4.2 Cross-feed between $B^\pm \rightarrow Dh^\pm$ channels

1792 There is a cross-feed between the  $B^\pm \rightarrow D\pi^\pm$  and  $B^\pm \rightarrow DK^\pm$  channels, where real  
 1793  $B^\pm \rightarrow D\pi^\pm$  decays are reconstructed as  $B^\pm \rightarrow DK^\pm$  decays, or where  $B^\pm \rightarrow DK^\pm$   
 1794 decays are reconstructed as  $B^\pm \rightarrow D\pi^\pm$  decays. Due to relative branching fractions  
 1795 the former contribution is by far the most important, but both are modelled.

1796 The cross-feed shapes are obtained in a data-driven manner using the sPlot  
 1797 method [?], and fixed in the fit to data. Separate shapes are determined for each  
 1798 category, using the following steps:

- 1799 • The procedure is based on the reasonably pure  $B^\pm \rightarrow D\pi^\pm$  sample obtained  
 1800 when the full selection is applied. A simple mass fit is performed to the  
 1801 invariant mass spectrum and the sPlot method [?] is used to obtain the  
 1802 sWeights,  $w_s$ , for the signal component. The mass fit uses the same components  
 1803 for signal, low mass shape, and combinatorial background as described in this  
 1804 section.
- 1805 • A set of weights are defined, based on the candidate-by-candidate PID  
 1806 efficiencies obtained as described in Section 5.1.3:
  - 1807 – The extracted PID efficiencies of the  $\text{PIDK} < 4$  cut  $\epsilon_{D\pi \rightarrow D\pi}(p, \eta, n_{\text{tracks}})$   
 1808 are used to reverse-weight the  $B^\pm \rightarrow D\pi^\pm$  sample, in order to obtain the  
 1809 bachelor kinematic distributions before the  $\text{PIDK} < 4$  cut is applied.
  - 1810 – The extracted PID efficiencies of the  $\text{PIDK} > 4$  cut  $\epsilon_{D\pi \rightarrow DK}(p, \eta, n_{\text{tracks}})$   
 1811 are used to obtain the bachelor kinematic distribution of the  $B^\pm \rightarrow D\pi^\pm$   
 1812 candidates mis-identified as  $B^\pm \rightarrow DK^\pm$ .
  - 1813 • The raw distribution of the invariant mass of  $B^\pm$  particles with a misidentified  
 1814 bachelor,  $m_B^{mis-ID}$ , is produced by also doing the DecayTreeFit kinematic refit  
 1815 while swapping the companion mass hypothesis of each  $B^\pm \rightarrow D\pi^\pm$  candidate  
 1816 to a kaon hypothesis.

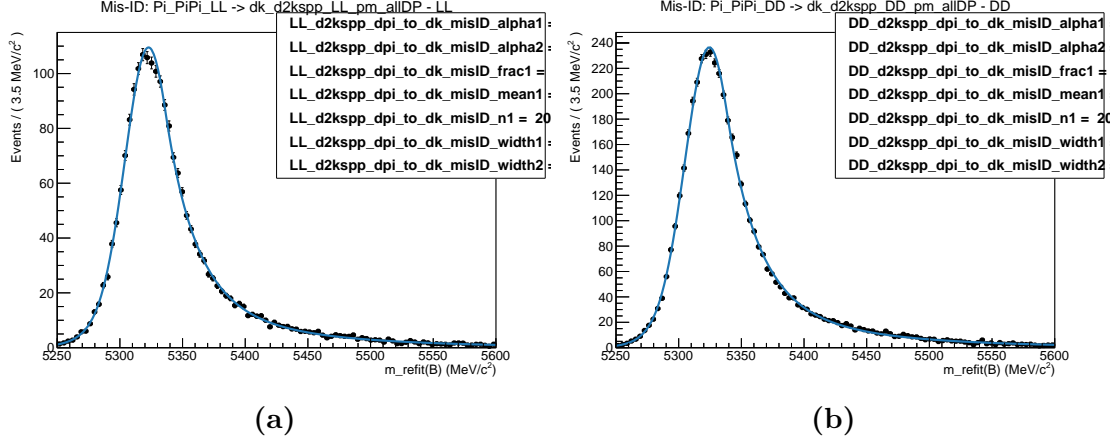


**Figure 5.23:** Fitted shape of  $B^\pm$  invariant mass spectrum for  $B^\pm \rightarrow D\pi^\pm$  events misidentified as  $B^\pm \rightarrow DK^\pm$  events for (a) LL and (b) DD candidates in the  $D \rightarrow K_S^0\pi^+\pi^-$  mode.

- 1817     • Each candidate is reweighted by the overall weight  $w = w_s^{\text{cand.}}/\epsilon_{D\pi \rightarrow D\pi}^{\text{cand.}}$  ·  
 1818         $\epsilon_{D\pi \rightarrow DK}^{\text{cand.}}$ , and the reweighed  $m_B^{\text{mis-ID}}$  distribution is fitted to obtain the cross-  
 1819        feed mass distribution function.

1820     The distributions are modelled with a sum of two Crystal Ball density functions,  
 1821     each defined by the parameterisation [?]

$$f_{\text{CB}}(m, \mu, \sigma, \alpha, n) \propto \begin{cases} \exp \left[ -\frac{1}{2} \left( \frac{m-\mu}{\sigma} \right)^2 \right] & \text{if } (m-\mu)/\sigma > -\alpha \\ A \left( B - \frac{m-\mu}{\sigma} \right)^{-n} & \text{otherwise,} \end{cases} \quad (5.10)$$

1822     where  $\alpha > 0$ , and

$$A = \left( \frac{n}{\alpha} \right)^n \exp[-\alpha^2/2], \quad B = \frac{n}{\alpha} - \alpha. \quad (5.11)$$

1823     The obtained  $m_B^{\text{mis-ID}}$  spectrum and obtained mass shape is given in Fig. 5.23  
 1824     for the  $D \rightarrow K_S^0\pi^+\pi^-$  category; the  $D \rightarrow K_S^0K^+K^-$  shapes are very similar. An  
 1825     analogous procedure is used to obtain the mass distribution of  $B^\pm \rightarrow DK^\pm$  decays  
 1826     reconstructed in the  $B^\pm \rightarrow D\pi^\pm$  category. In the first stage where sPlots are  
 1827     extracted by a fit to the  $B^\pm \rightarrow DK^\pm$  mass spectrum, the cross-feed component  
 1828     determined as described above is included. An example of one of the resulting  
 1829     shapes is given in Fig. 5.24

1830     The yield of cross-feed from  $B^\pm \rightarrow D\pi^\pm$  decays in a given  $B^\pm \rightarrow DK^\pm$  category  
 1831     is parameterised in terms of the yield of correctly identified  $B^\pm \rightarrow D\pi^\pm$  decays and  
 1832     the mis-identification probability extracted from calibration samples as described

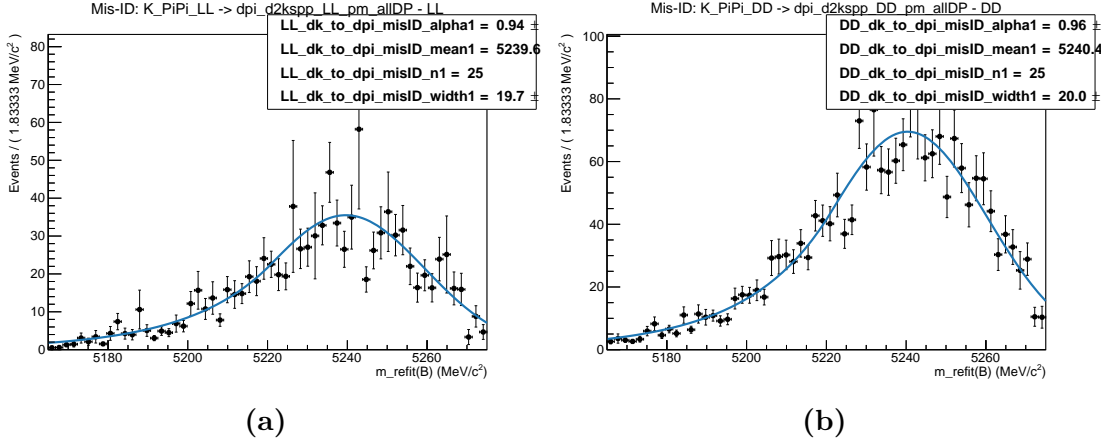


**Figure 5.24:** Fitted shape of  $B^\pm$  invariant mass spectrum for  $B^\pm \rightarrow DK^\pm$  events misidentified as  $B^\pm \rightarrow D\pi^\pm$  events for (a) LL and (b) DD candidates. The shape is obtained using  $D \rightarrow K_S^0 \pi^+ \pi^-$  decays, and used in the  $D \rightarrow K_S^0 K^+ K^-$  mode as well.

in Section 5.1.3. Denoting the rate at which a pion is reconstructed as a kaon by  $\epsilon_{\pi \rightarrow K}^c$  in a given category,  $c$ , the yield is

$$N_{\pi \rightarrow K}^c = N_{D\pi^\pm}^c \frac{\epsilon_{\pi \rightarrow K}^c}{1 - \epsilon_{\pi \rightarrow K}^c}, \quad (5.12)$$

with an analogous definition of the yield of the cross-feed component from  $B^\pm \rightarrow DK^\pm$  decays in the  $B^\pm \rightarrow D\pi^\pm$  spectrum.

### 5.4.3 Partially reconstructed backgrounds

A number of background candidates stem from partly reconstructed  $B$  decays of the type  $B \rightarrow DhX$ , where  $X$  denotes a photon or a pion that is not reconstructed. It is not possible to reject these decays in the selection, due to the similarity to signal decays. However, the missing momentum results in reconstructed  $B$  masses below the actual  $B$  mass, and the backgrounds are also denoted *lowmass* backgrounds. These mass distributions are modelled with analytic shapes, derived based on two principles. Firstly, the kinematic endpoints of the distributions are fully defined by the particle masses in the decay. Secondly, the angular distribution of the missing particle has a one-to-one relation to the missing momentum, and therefore to the reconstructed  $B$  mass. Depending on the spin-parity of the particles and resonances involved in the decay, two different mass distributions arise.

In  $B$  decays where the missing particle is a scalar that is produced in the decay of a vector resonance (eg.  $B^\pm \rightarrow D^{*0}(\rightarrow D^0 \pi^0)\pi^\pm$  decays where the  $\pi^0$  is not reconstructed), the  $m(D^0 \pi^\pm)$  distribution has a double-peak structure. The  $D^{*0}$  helicity angle  $\theta$  is defined as the angle between the  $\pi^0$  momentum vector in the  $D^{*0}$

rest frame and the  $D^{*0}$  boost vector in the  $B$  rest frame. The helicity of  $D^{*0}$  means that the  $\pi^0$  will travel predominantly in the direction where  $\theta = 0$  or  $\theta = \pi$ . When  $\theta = 0$  the fraction of momentum carried by the missing  $\pi^0$  is lower, leading to a higher reconstructed  $m(D^0\pi^\pm)$ . When  $\theta = \pi$  the converse occurs. The resulting  $B$  mass distribution is a parabola  $f_{\text{HORNS}}^0(m)$  peaking near both kinematic endpoints  $a$  and  $b$

$$f_{\text{HORNS}}^0(m) = \begin{cases} (m - \frac{a+b}{2})^2, & \text{if } a < m < b \\ 0, & \text{otherwise.} \end{cases} \quad (5.13)$$

Due to the double-peaking structure, and the fact that was developed by Paolo Gandini for the two-body ADS/GLW analyses [], this shape is denoted a *HORNSdini* shape when convolved with a resolution function as described below.

The second relevant decay situation is where the missing particle is a vector, again produced via the intermediate decay of a vector resonance (eg.  $B^\pm \rightarrow D^{*0}(\rightarrow D^0\gamma)\pi^\pm$  decays where the photon is not reconstructed). In this case, the spin-parity of the photon ( $1^-$ ) means that it will decay preferentially in the  $\theta = \frac{\pi}{2}$  or  $\theta = \frac{3\pi}{2}$  directions, and so a double-peak structure is not seen. In this case the parabolic distribution  $f_{\text{HILL}}^0(m)$  with kinematic endpoints  $a, b$  has negative curvature and can be described by

$$f_{\text{HILL}}^0(m) = \begin{cases} -(m - a)(m - b), & \text{if } a < m < b \\ 0, & \text{otherwise.} \end{cases} \quad (5.14)$$

Resolution effects mean that the parabolic shapes must be convolved with a resolution function, chosen to be a sum of two Gaussians. For a single Gaussian shape  $f_G(x|\mu, \sigma)$  with mean  $\mu$  and width  $\sigma$ , the double Gaussian is expressed as

$$f_{DG}(x) = f_G(x|\mu, \sigma) + k_G f_G(x|\mu, R_\sigma \sigma). \quad (5.15)$$

where  $\sigma$  is the width of the first Gaussian, and  $k_G$  is the relative fractions between the two Gaussians and  $R_\sigma$  is their relative widths. Further, selection effects can distort the horns shape such that one of the peaks is higher than the other. This is taken into account by introducing a linear polynomial with slope parameter  $\xi$ . As  $\xi \rightarrow 0$ , the left hand peak decreases in size relative to the right hand peak. The resulting *HORNSdini* and *HILLdini* distributions are therefore

$$f_{\text{HORNS/HILL}}(m) = \int_a^b dx f_{\text{HORNS/HILL}}^0(x) f_{DG}(m|x, \sigma, k_G, R_\sigma) \left( \frac{1-\xi}{b-a}x + \frac{b\xi - a}{b-a} \right). \quad (5.16)$$

Examples of the shapes are given in Fig. 5.25. A further term  $\delta m$  can be added to allow a translation of the full shape. These shapes are used to fit all partially reconstructed backgrounds, as described in the following section.

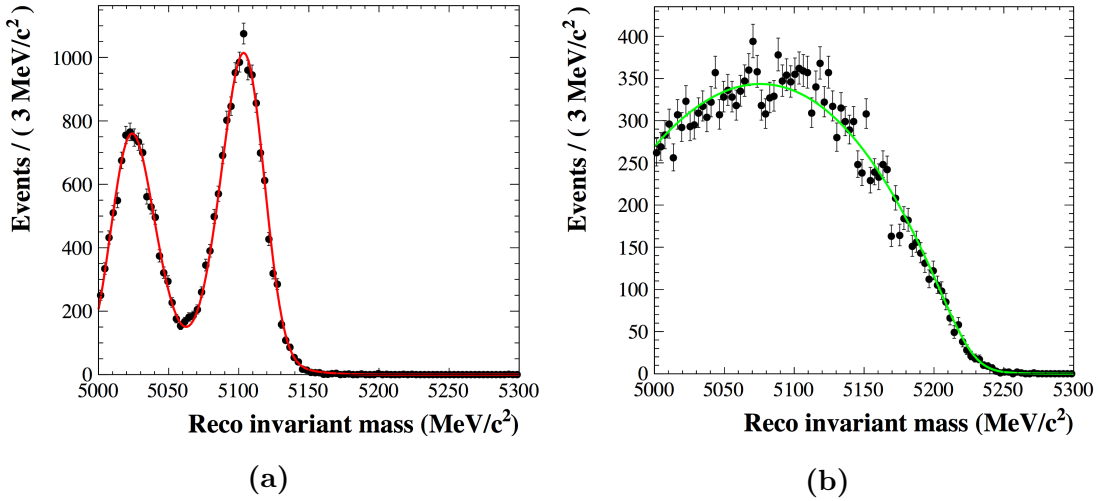


**Figure 5.25:** (a) The *HORNsdini* distribution (red) fit to  $B^\pm \rightarrow (D^{*0} \rightarrow D^0[\pi^0])\pi^\pm$  MC (black) after full event selection. (b) The *HILLsdini* distribution (green) fit to  $B^\pm \rightarrow (D^{*0} \rightarrow D^0[\gamma])\pi^\pm$  MC (black) after full event selection.

#### 1880 Determination of the partially reconstructed background distributions

1881 In both the  $B^\pm \rightarrow DK^\pm$  and  $B^\pm \rightarrow D\pi^\pm$  categories, components are included to  
 1882 describe contributions from the partially reconstructed decays (where the particle  
 1883 in square brackets is not reconstructed)

- 1884 •  $B^\pm \rightarrow (D^{*0} \rightarrow D^0[\pi^0])h^\pm$ , described using a *HORNsdini* distribution
- 1885 •  $B^\pm \rightarrow (D^{*0} \rightarrow D^0[\gamma])h^\pm$ : described using a *HILLdini* distribution
- 1886 •  $B^0 \rightarrow (D^{*\pm} \rightarrow D^0[\pi^\pm])h^\mp$ : described using a *HORNsdini* distribution
- 1887 •  $B^{\pm(0)} \rightarrow D^0 h^\pm [\pi^{0(\mp)}]$ : described using a *HORNsdini* distribution

1888 The mass distributions of all the  $B \rightarrow D^*h^\pm$  contributions are obtained from  
 1889 fits to samples of full LHCb simulation. Examples of these fits are shown in  
 1890 Fig. 5.26. All shape parameters are kept fixed in the fit to data, except for the  
 1891 parameter  $\sigma$  of the resolution function in Eq. (5.15) which is allowed to obtain  
 1892 the value preferred by data.

1893 The mass distribution of  $B^{\pm(0)} \rightarrow D^0 h^\pm [\pi^{0(\mp)}]$  decays reconstructed in the  
 1894  $B^\pm \rightarrow D\pi^\pm$  categories is obtained from full LHCb simulation samples of  $B^\pm \rightarrow D^0\rho^\pm$   
 1895 and  $B^0 \rightarrow D^0\rho^0$  decays. The shapes were compared to those predicted by an  
 1896 amplitude model for  $B^0 \rightarrow D^0 \rightarrow \pi^\pm\pi^\mp$  decays developed by LHCb [?], but found  
 1897 to be very similar for the  $m(D\pi^\pm)$  range relevant to this analysis. The obtained  
 1898 shapes are shown in Fig. 5.27.

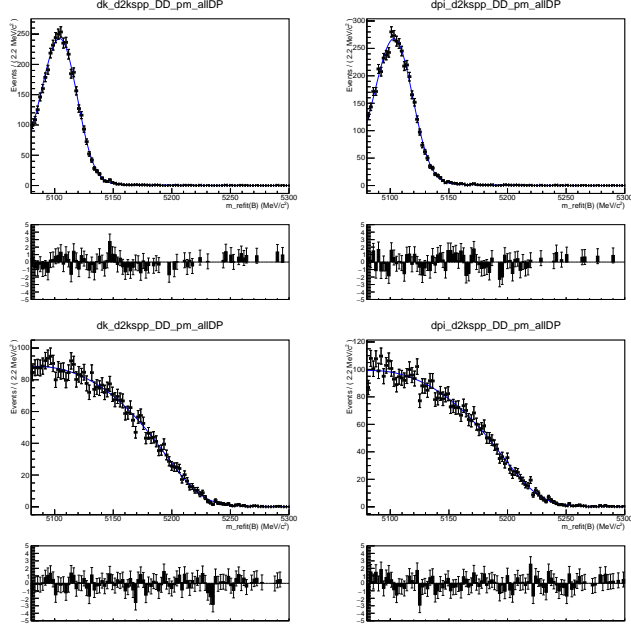


**Figure 5.26:** Fit projection of the fit to (top) simulated  $B^+ \rightarrow D^{*0}(\rightarrow D^0[\pi^0])h^\pm$  decays and (bottom) simulated  $B^+ \rightarrow D^{*0}(\rightarrow D^0[\gamma])h^\pm$  decays, all reconstructed in the DD category. Both the (left)  $DK$  shapes and (right) shows  $D\pi$  shapes are shown.

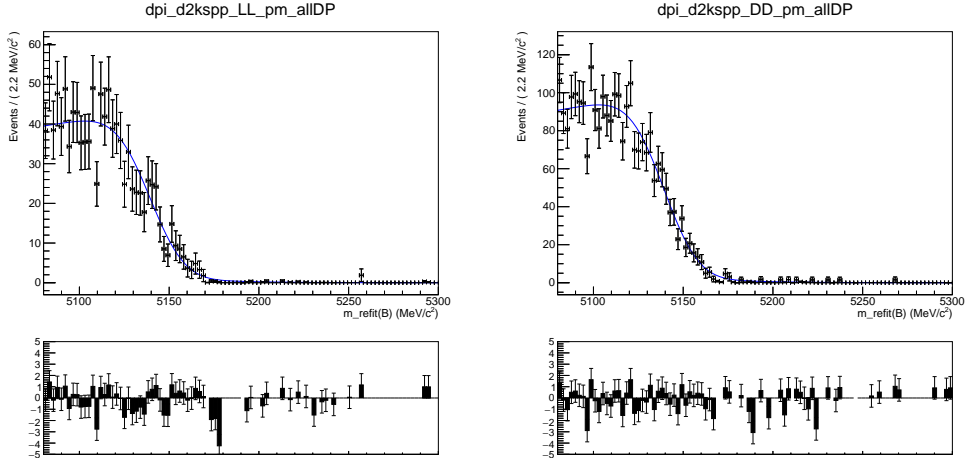


**Figure 5.27:** Projections of the fit to simulated  $B^\pm \rightarrow D\rho^\pm$  and  $B^0 \rightarrow D\rho^0$  samples reconstructed as  $B^\pm \rightarrow D\pi^\pm$  decays for (left) the LL and (right) the DD categories.

1899      The mass distribution of  $B^{\pm(0)} \rightarrow D^0 K^\pm [\pi^{0(\mp)}]$  decays reconstructed in the  
 1900  $B^\pm \rightarrow DK^\pm$  categories, on the other hand, is obtained from a sample of signal  
 1901 decays, generated via a amplitude model for  $B^0 \rightarrow D^0 \rightarrow K^\pm \pi^\mp$  decays developed  
 1902 by LHCb [?] and smeared to take the LHCb resolution into account. This follows  
 1903 an approach developed in the context of a GLW analysis based on partially recon-  
 1904 structed decays made within LHCb [?]. The obtained shape is shown in Fig. 5.28.  
 1905      The background yields of these backgrounds are parameterised in terms of

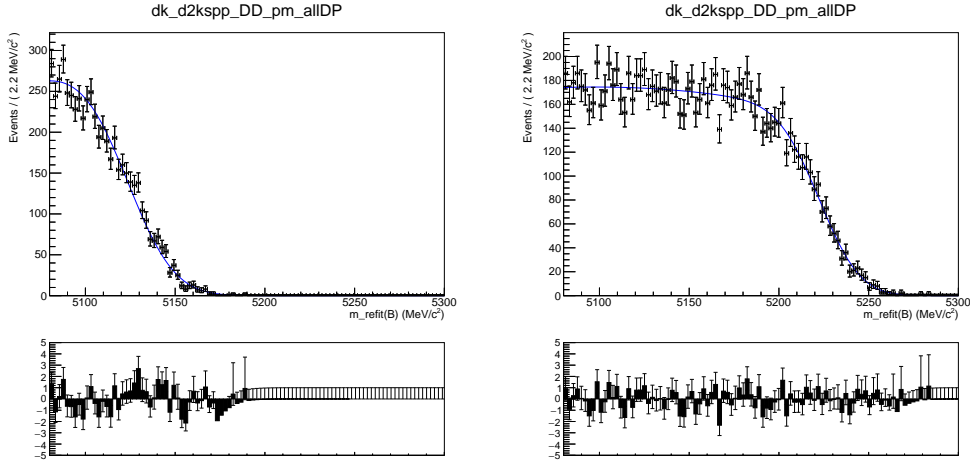


**Figure 5.28:** Fit projection for the fit used to obtain a shape for the partly reconstructed background from (left)  $B \rightarrow DK\pi$  decays and (right)  $B_s^0 \rightarrow D K^+ \pi^-$  decays where a pion is not reconstructed.

one total yield parameter, accounting for all partially reconstructed  $B^\pm$  and  $B^0$  decays, and a number of parameters that describe the relative rates of the different contributions. In the  $B^\pm \rightarrow D\pi^\pm$  channels, the relative rates of the  $B^\pm \rightarrow (D^{*0} \rightarrow D^0[\pi^0])h^\pm$  and  $B^0 \rightarrow (D^{*\pm} \rightarrow D^0[\pi^\pm])h^\mp$  backgrounds are fixed from the known branching fractions, and relative selection efficiencies in simulation. These backgrounds have almost identical mass distributions and it is not possible to determine the ratio in the fit to data. The relative yield of  $B^\pm \rightarrow D^*(\rightarrow D^0[\gamma])\pi^\pm$  compared to the  $B \rightarrow D^*(\rightarrow D^0[\pi])\pi^\pm$  is denoted  $f_{D^*\gamma}^{D\pi}$  and is floated in the fit to data, as is the relative yield of  $B \rightarrow D^0\pi^\pm[\pi]$  decays compared to the  $B \rightarrow D^*\pi$  modes, denoted  $f_{D\pi\pi}^{D\pi}$ . In the  $B^\pm \rightarrow DK^\pm$  channels, all the relative background rates are fixed via known branching fractions and relative selection efficiencies; this is necessary to obtain a stable fit, due to the lower yields.

In the  $B^\pm \rightarrow DK^\pm$  categories, an additional partially reconstructed background is considered from  $B_s^0 \rightarrow \bar{D}^0[\pi^+]K^-$  (an conjugate) decays. The mass shape is obtained from simulated decays, generated using an amplitude model published by LHCb [?] and smeared to account for the experimental resolution. The obtained shape is shown in Fig. 5.28. The yield of this background component is fixed relative to the signal yields in the corresponding  $B^\pm \rightarrow D\pi^\pm$  category, taking the relative branching ratios and hadronisation factors into account.

In the  $B^\pm \rightarrow DK^\pm$  channels there is a contribution from partially reconstructed  $B \rightarrow D^*\pi^\pm X$  decays where the companion pion is misidentified as a kaon. The reverse contribution is negligible due to the relative branching fractions, and the fact that it is mostly shifted below the mass range of the fit. These are modelled

1929 using analytic, empirical mass distributions (essentially sums of a number of regular  
1930 *HORNs/HILLdini* distributions), with parameters that are determined in fits to  
1931 simulated  $B \rightarrow D^*\pi^\pm$  and  $B \rightarrow D\rho$  decays where the pion is reconstructed with  
1932 the kaon mass hypothesis. The shapes are fixed in the fit to data.

1933

### 1934 **Partially reconstructed backgrounds that are not modelled**

1935 It was considered whether a background from  $\Lambda_b^0 \rightarrow D^0 p\pi^-$  decays where a pion  
1936 is not reconstructed, and the proton is misidentified as the companion, can be  
1937 expected to contribute significantly. The has been investigated in full LHCb  
1938 simulation samples, for the  $D$  final state  $K_S^0\pi^+\pi^-$ . Taking into account the selection  
1939 efficiencies, branching fractions, and hadronisation fraction of this background, the  
1940 expected relative yield of the  $\Lambda_b^0$  background compared to signal of 0.03 % in the  
1941  $B^\pm \rightarrow D\pi^\pm$  channel, which is completely negligible. In the  $B^\pm \rightarrow DK^\pm$  channel,  
1942 total of about 200 decays are expected, combined for the LL and DD categories.  
1943 However, most of these lie at  $B$  masses smaller than the signal peak, and their impact  
1944 is small. Therefore it is not necessary to model the background in the nominal fit;  
1945 a systematic uncertainty is assigned that accounts for the small potential impact.

1946 In the analogous case of  $\Lambda_b^0 \rightarrow D^0 pK^-$  decays, the missing energy of the non-  
1947 reconstructed kaon results in a reconstructed  $B$  mass below the fit range.

1948 It has also been investigated whether a background from  $\Lambda_b^0 \rightarrow \Lambda_c^+ \pi^-$  or  $\Lambda_b^0 \rightarrow$   
1949  $\Lambda_c^+ K^-$  decays can be expected, where  $\Lambda_c^+ \rightarrow p K_S^0 \pi^+ \pi^-$ , a pion is missed and the  
1950 proton is misidentified as a pion or kaon from the  $D$  decay. Since no PID requirement  
1951 is made on the  $D$  decay products in the  $D \rightarrow K_S^0 \pi^+ \pi^-$  channels, and only a loose  
1952 one for  $D \rightarrow K_S^0 K^+ K^-$ , this is possible in principle. In practice, the background is  
1953 sufficiently suppressed from the applied  $D$  mass requirement to have no significant  
1954 impact, and is therefore not modelled. A systematic uncertainty is assigned that  
1955 accounts for any potential impact on the measurement due to this choice.

#### 1956 **5.4.4 Combinatorial background**

1957 The combinatorial background is modelled with an exponentially falling density  
1958 function, where both the yield and exponential slope are determined independently  
1959 for each category. This shape is found to model the combinatorial well in all  
1960 categories, most evident in the high- $m_B$  regions where this background dominates.

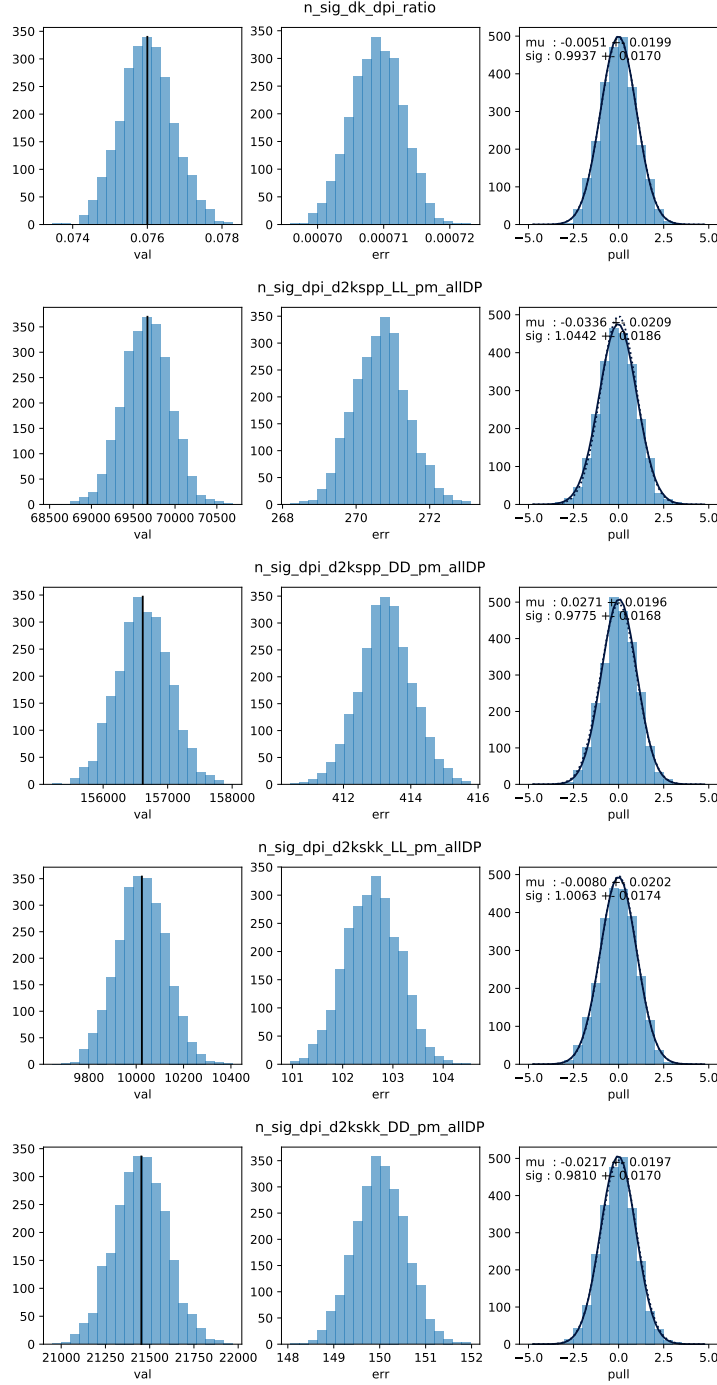


**Figure 5.29:** Pull plots for the signal yield parameters in global fits to toy datasets for (top) the  $D\pi^\pm$ - $DK^\pm$  yield ratio, and then the  $D\pi^\pm$  yield in the LL and DD  $D \rightarrow K_S^0\pi^+\pi^-$  modes, and the LL and DD  $D \rightarrow K_S^0K^+K^-$  modes.

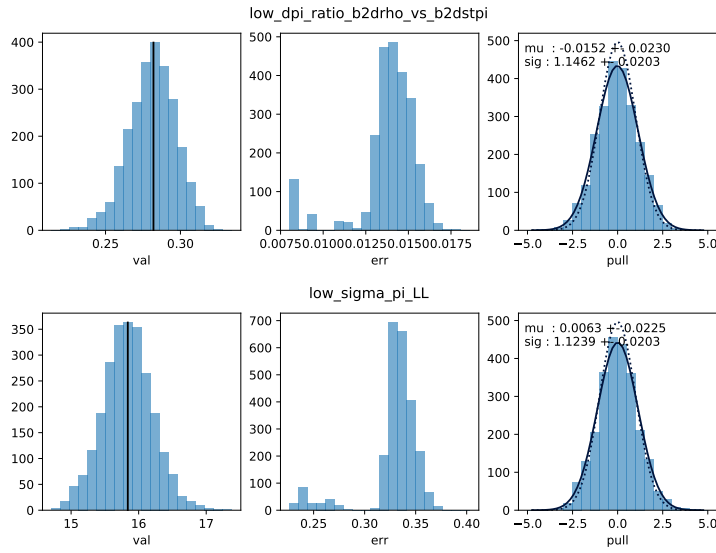


**Figure 5.30:** Examples of lowmass related parameters where the uncertainties are underestimated in some toy fits. This is taken into account when propagating the fit uncertainties to the systematic uncertainties on the final results.

#### 5.4.5 Fit results

The fit range is chosen to be  $m_B \in [5080, 5800] \text{ MeV}/c^2$ . The low end of this interval includes the high-mass peak of the double-peak structure in the partially reconstructed background, which helps the fit constrain the relative contributions of backgrounds in the lowmass regions. A number of additional backgrounds exist at even lower  $m_B$  values, thus extending the fit range to lower masses would necessitates an extended model, but not benefit the description of the signal region. The high end of the interval includes enough combinatorial background to allow the fit to determine the exponential slope parameter accurately.

A large number of pseudoexperiments are carried out to verify that the fit procedure is self-consistent, in which toy data sets are generated according to the expected  $B$  mass distributions, and then fitted. None of the parameters obtained in the fit exhibit a mean bias different from zero, and for most parameters the uncertainties are well estimated. This is the case for the signal yields, and the  $DK^\pm-D\pi^\pm$  yield ratio  $\mathcal{R}$ , as evidenced by the pull plots in Fig. 5.29. The fit underestimates the uncertainty by 10-20 % for some of the parameters related to the partly reconstructed backgrounds, as shown in Fig. 5.30, but this is taken into account when the uncertainties are propagated to the observables in the second-stage fit, as described in Section 5.6.3.

The projections of the fit to data are shown in Figs. 5.31 and 5.32, for the  $D \rightarrow K_S^0\pi^+\pi^-$  and  $D \rightarrow K_S^0K^+K^-$  data sets, respectively. The obtained yields for

**Table 5.6:** Fitted total candidate yields. The quoted signal yields are for the number of candidates that survive the respective PID cut, whereas the  $DK^\pm$ - $D\pi^\pm$  ratio is corrected for PID and selection efficiencies so that it corresponds to the branching ratio.

Component	LL	DD
Signal		
$B^\pm \rightarrow D(\rightarrow K_S^0\pi^+\pi^-)\pi^\pm$	$61,573 \pm 254$	$139,080 \pm 389$
$B^\pm \rightarrow D(\rightarrow K_S^0K^+K^-)\pi^\pm$	$9,160 \pm 98$	$19,910 \pm 144$
$R_{DK/D\pi} = n(DK)/n(D\pi)$ (%)		$7.72 \pm 0.08$
Combinatorial		
$B^\pm \rightarrow D(\rightarrow K_S^0\pi^+\pi^-)\pi^\pm$	$3,479 \pm 198$	$9,928 \pm 376$
$B^\pm \rightarrow D(\rightarrow K_S^0K^+K^-)\pi^\pm$	$1,103 \pm 94$	$2,545 \pm 155$
$B^\pm \rightarrow D(\rightarrow K_S^0\pi^+\pi^-)K^\pm$	$1,826 \pm 107$	$3,987 \pm 177$
$B^\pm \rightarrow D(\rightarrow K_S^0K^+K^-)K^\pm$	$380 \pm 39$	$655 \pm 58$
Part. Reco.		
$B^\pm \rightarrow D(\rightarrow K_S^0\pi^+\pi^-)\pi^\pm$	$43,004 \pm 242$	$95,452 \pm 403$
$B^\pm \rightarrow D(\rightarrow K_S^0K^+K^-)\pi^\pm$	$6,247 \pm 99$	$13,241 \pm 157$
$R_{DK/D\pi}^{low} = n_{low}(DK)/n_{low}(D\pi)$ (%)		$6.65 \pm 0.12$

1982 each fit component are given in Table 5.6. The total yield of  $B^\pm \rightarrow D\pi^\pm$  decays is  
 1983 approximately 230,000 across all channels. The obtained value of the yield ratio is  
 1984  $\mathcal{R} = (7.7 \pm 0.1)\%$ , corresponding to a total  $B^\pm \rightarrow DK^\pm$  yield of 16,500, of which  
 1985 about 14,300 pass the PID requirement and are reconstructed in the  $B^\pm \rightarrow DK^\pm$   
 1986 category. This value of  $\mathcal{R}$  is in excellent agreement with expectation from the  
 1987 known branching fractions [?], which predict  $\mathcal{R}_{PDG} = (7.8 \pm 0.3)\%$ . The shape  
 1988 parameters determined in the fit to data are summarised in Table 5.7.

## 1989 5.5 Measurement of the CP-violation observables

1990 The section describes the second fit stage, in which the *CP*-violation observables  
 1991 of interest are determined. Compared to the first fit stage, the candidates are  
 1992 further split by  $B$  charge, and by the assigned Dalitz bin number, making for a  
 1993 total of 160 categories. Another extended maximum-likelihood fit is carried out,  
 1994 in which shape parameters of all signal and background components are fixed to  
 1995 those determined in the first fit stage, and thus all floating parameters relate to  
 1996 the signal and background yields. The signal yields are expressed in terms of the

**Table 5.7:** Fitted parameter values.

	LL	DD
$\sigma_{D\pi}$ (MeV/ $c^2$ )	$14.27 \pm 0.05$	$14.58 \pm 0.04$
$\sigma_{DK}$ (MeV/ $c^2$ )	$13.61 \pm 0.24$	$14.19 \pm 0.17$
$\mu$ (MeV/ $c^2$ )		$5278.60 \pm 0.04$
Combinatorial Slopes		
Decay mode	Slope ( $10 \times 10^{-3} GeV^{-1}c^2$ )	
$B^\pm \rightarrow D(\rightarrow K_S^0\pi^+\pi^-)\pi^\pm$	$-3.1 \pm 0.2$	$-4.0 \pm 0.1$
$B^\pm \rightarrow D(\rightarrow K_S^0K^+K^-)\pi^\pm$	$-4.1 \pm 0.4$	$-5.5 \pm 0.3$
$B^\pm \rightarrow D(\rightarrow K_S^0\pi^+\pi^-)K^\pm$	$-3.2 \pm 0.2$	$-3.9 \pm 0.2$
$B^\pm \rightarrow D(\rightarrow K_S^0K^+K^-)K^\pm$	$-4.2 \pm 0.4$	$-4.3 \pm 0.4$
Part. Reco.		
$\sigma_{D\pi}^{low}$ (MeV/ $c^2$ )	$13.73 \pm 0.33$	$13.78 \pm 0.28$
$f_{D\pi\pi}^{D\pi}$		$0.268 \pm 0.013$
$f_{D^*\gamma}^{D\pi}$		$0.317 \pm 0.005$

1997 observables of interest,  $(x_\pm^{DK}, y_\pm^{DK}, x_\xi^{D\pi}, y_\xi^{D\pi})$ , allowing the fit to determine their  
 1998 optimal values. The details of the fit setup are summarised in the following section,  
 1999 before the results are presented in Section 5.5.2, and a wide range of consistency  
 2000 checks are described in Section 5.5.3.

### 2001 5.5.1 Fit setup

2002 The signal yields in each bin (in a given category) are defined using the equations  
 2003 of Chapter 2, in order to allow for the determination of the  $(x_\pm^{DK}, y_\pm^{DK}, x_\xi^{D\pi}, y_\xi^{D\pi})$   
 2004 observables. In practice, a set of variables are defined

$$Y_{c,i}^- = F_{c,-i} + [(x_-^c)^2 + (y_-^c)^2]F_{c,-i} + 2\sqrt{F_{c,i}F_{c,-i}}(c_i^cx_-^c + s_i^cy_-^c), \quad (5.17)$$

$$Y_{c,i}^+ = F_{c,-i} + [(x_+^c)^2 + (y_+^c)^2]F_{c,-i} + 2\sqrt{F_{c,i}F_{c,-i}}(c_i^cx_+^c - s_i^cy_+^c), \quad (5.18)$$

2005 for each data category,  $c$ , in terms of which the bin yields that enter the like-  
 2006 lihood are given by

$$N_{c,i}^\pm = \frac{Y_{c,i}^\pm}{\sum_j Y_{c,j}^\pm} \times N_{c,\text{total}}^\pm. \quad (5.19)$$

2007 This parameterisation is essentially identical to the expressions in Section 2.4,  
 2008 slightly modified so that the phase-space-integrated yields of  $B^+$  and  $B^-$  decays

in a given category are determined directly, in lieu of the normalisation constants  $h^\pm$  of that section. A single set of four parameters,  $(x_-^{DK}, y_-^{DK}, x_+^{DK}, y_+^{DK})$ , are shared between *all*  $B^\pm \rightarrow DK^\pm$  categories; they enter the expressions of Eq. (5.17) directly, and are thus determined in the fit. In the  $B^\pm \rightarrow D\pi^\pm$  categories, the four corresponding parameters,  $(x_-^{D\pi}, y_-^{D\pi}, x_+^{D\pi}, y_+^{D\pi})$ , are parameterised in terms of  $(x_\pm^{DK}, y_\pm^{DK})$  and the addition two observables  $(x_\xi^{D\pi}, y_\xi^{D\pi})$ , as detailed in Section 2.4.

The strong-phase parameters  $(c_i, s_i)$  are fixed in the fit to data. In the  $D \rightarrow K_S^0 \pi^+ \pi^-$  categories, the combined CLEO [?] and BESIII [?] measurement results are used, as reported in Ref. [?]. In the  $D \rightarrow K_S^0 K^+ K^-$  categories, the results reported by the CLEO collaboration in Ref. [?] are used. The experimental uncertainty on these measurements is propagated to the measured  $CP$ -violation observables as part of the systematic uncertainties in Section ??.

The  $F_i$  parameters are determined in the fit. Separate parameter sets are determined for the LL and DD categories because the acceptance profile over the Dalitz plot differs between them. The  $F_i$  are, however, shared between the  $B^\pm \rightarrow DK^\pm$  and  $B^\pm \rightarrow D\pi^\pm$  categories; the small difference in the  $D$  momentum spectrum between the channels does not lead to a detectable difference in the acceptance profiles. This is a crucial assumption of the method, shown to be true using large samples of simulated decays in Section ???. Because the  $F_i$  are subject to the constraint that  $\sum_{i=-N}^N F_i^c = 1$ , it is beneficial to introduce a reparameterisation in the likelihood function. The  $F_i$  are re-expressed in terms of a set of recursive fractions

$$\mathcal{R}_i = \begin{cases} F_i & , \quad i = -N \\ F_i / (\sum_{j \geq i} F_j) & , \quad -N < i < +N \end{cases} , \quad (5.20)$$

for which the constraint is much simpler, namely that each  $\mathcal{R}_i$  lies in the interval  $[0, 1]$ . This results in much better convergence behaviour in the minimisation of the negative log likelihood.

The yield of combinatorial background decays is determined independently in each bin. A single, overall bin yield of partially reconstructed background from  $B^\pm$  and  $B^0$  decays is determined in each of the 160 categories; the relative contribution from each individual background is fixed from the results of the first-stage fit, corrected for the different fit region (a systematic uncertainty is assigned due to this choice). In the  $B^\pm \rightarrow DK^\pm$  channels, the bin yields of the partially reconstructed background from  $B_s^0 \rightarrow \bar{D}^0[\pi^+]K^-$  decays are expressed via the  $F_i$ , exploiting that a positive companion particle is always produced along with a  $\bar{D}^0$  meson (and vice versa). The overall yield is fixed from the results of the first stage fit. Finally,

**Table 5.8:** Mean biases and pulls for the observables of interest in the final, binned fit, obtained in a large number of pseudoexperiments.

Parameter	Name in code	Mean bias ( $\times 10^{-2}$ )	Mean pull	Pull width
$x_-^{DK}$	A_xm_dk	$-0.018 \pm 0.022$	$-0.01 \pm 0.02$	$1.01 \pm 0.02$
$y_-^{DK}$	A_ym_dk	$-0.014 \pm 0.026$	$-0.00 \pm 0.02$	$0.99 \pm 0.02$
$x_+^{DK}$	A_xp_dk	$-0.018 \pm 0.022$	$-0.01 \pm 0.02$	$1.00 \pm 0.02$
$y_+^{DK}$	A_yp_dk	$-0.016 \pm 0.028$	$0.01 \pm 0.02$	$1.00 \pm 0.02$
$x_\xi^{D\pi}$	A_Re_xi_dpi	$0.029 \pm 0.052$	$0.06 \pm 0.02$	$1.00 \pm 0.02$
$y_\xi^{D\pi}$	A_Im_xi_dpi	$0.000 \pm 0.060$	$0.01 \pm 0.02$	$1.00 \pm 0.02$

2043 the yield of the  $D\pi^\pm \leftrightarrow DK^\pm$  cross-feed components in each bin are determined  
 2044 via the obtained yield of correctly identified decays in the corresponding bin, and  
 2045 the known PID efficiencies. This is true for both fully and partially reconstructed  
 2046 decays, although only a  $D\pi^\pm \rightarrow DK^\pm$  component is included in the latter case.

2047 The fit range is decreased to  $m_B \in [5150, 5800] \text{ MeV}/c^2$ . The information from  
 2048 candidates with lower reconstructed  $B$  masses was useful in determining the relative  
 2049 rates and free mass shape parameters of the partially reconstructed background  
 2050 components in the first-stage fit; however, with these fixed in the second-stage  
 2051 fit, this is no longer the case. Furthermore, the setup assumes that the shape of  
 2052 the partially reconstructed background is identical across the Dalitz bins. This  
 2053 assumption is not perfectly true, but the impact is minimal when the lower limit  
 2054 of the fit range is taken to be  $5150 \text{ MeV}/c^2$ .

### 2055 Self-consistency check

2056 In order to establish the fit stability and investigate a potential bias, a series of  
 2057 pseudoexperiments are run, in which toy datasets are generated using the model,  
 2058 and then fitted back. The total yields are taken from the first-stage fit. The signal  
 2059 yields are distributed between Dalitz bins using input physics parameters that  
 2060 approximately equal the values obtained in Section 5.5.2 from the results of the fit  
 2061 to data. The  $F_i$  parameters are taken from a fit to data. The partly reconstructed  
 2062 background is distributed as "D<sup>0</sup>-like", ie. in the  $B^\pm$  channels  $N_i^\pm \propto F_{\mp i}$ , except for  
 2063 the  $B_s^0$  background, which is " $\bar{D}^0$ -like" ( $N_i^\pm \propto F_{\pm i}$ ). The combinatorial background  
 2064 includes real  $D$  mesons paired with a random bachelor, as well as fake  $D$  mesons  
 2065 that are themselves made up of random tracks. The former is distributed as 50/50  
 2066  $D^0$ -like and  $\bar{D}^0$ -like in the toy generation, whereas the latter is assumed to be evenly  
 2067 distributed over the Dalitz plot (ie. the bin yield is proportional to the bin area).

**Table 5.9:** Statistical uncertainties and correlation matrix for the fit to data.

Uncertainty ( $\times 10^{-2}$ )						
	$x_-^{DK^\pm}$	$y_-^{DK^\pm}$	$x_+^{DK^\pm}$	$y_+^{DK^\pm}$	$x_\xi^{D\pi^\pm}$	$y_\xi^{D\pi^\pm}$
$\sigma$	0.96	1.14	0.96	1.20	1.99	2.34

Correlations						
	$x_-^{DK^\pm}$	$y_-^{DK^\pm}$	$x_+^{DK^\pm}$	$y_+^{DK^\pm}$	$x_\xi^{D\pi^\pm}$	$y_\xi^{D\pi^\pm}$
$x_-^{DK^\pm}$	1.000	-0.125	-0.013	0.019	0.028	-0.165
$y_-^{DK^\pm}$		1.000	-0.011	-0.009	0.105	0.030
$x_+^{DK^\pm}$			1.000	0.088	-0.099	0.038
$y_+^{DK^\pm}$				1.000	-0.076	-0.141
$x_\xi^{D\pi^\pm}$					1.000	0.146
$y_\xi^{D\pi^\pm}$						1.000

2068 A set of 2000 pseudoexperiments has been run, out of which 98.8 % converged  
 2069 properly. The pull plots for the observables of interest are shown in Fig. 5.33 and  
 2070 the mean biases and pulls are summarised in Table 5.8. No biases are statistically  
 2071 significant, and the uncertainties are seen to be well estimated.

### 2072 5.5.2 Main results

2073 The values and statistical uncertainties of observables obtained in the fit are

$$\begin{aligned} x_-^{DK} &= (-5.68 \pm 0.96) \times 10^{-2}, & y_-^{DK} &= (-6.55 \pm 1.14) \times 10^{-2}, \\ x_+^{DK} &= (-9.30 \pm 0.98) \times 10^{-2}, & y_+^{DK} &= (-1.25 \pm 1.23) \times 10^{-2}, \\ x_\xi^{D\pi} &= (-5.47 \pm 1.99) \times 10^{-2}, & y_\xi^{D\pi} &= (0.71 \pm 2.33) \times 10^{-2}. \end{aligned} \quad (5.21)$$

2074 The statistical correlation matrix for the observables is given in Table 5.9. The  
 2075 2D log-likelihood profile for the observables is shown in Fig. 5.34.

2076 The full set of fit projections in all 160 categories is included in Appendix A.  
 2077 While the  $CP$  asymmetry of the phase-space integrated yield is small, this is not the  
 2078 case for all individual bin-pairs. This is shown in Fig. 5.35 where, as an example,  
 2079 the fit projections for the  $B^+ \rightarrow DK^+$  decays in bin +2 and the  $B^- \rightarrow DK^-$   
 2080 decays in bin -2 of the  $D \rightarrow K_S^0 \pi^+ \pi^-$  Dalitz plot are compared. The presence  
 2081 of  $CP$  violation is clearly visible.

2082 The obtained  $F_i$  parameter values are shown in Table 5.10. These parameters can  
 2083 be useful in other BPFGGSZ measurements made within the LHCb collaboration:  
 2084 it is expected that the systematic uncertainty due to differences between the

**Table 5.10:** The fitted  $F_i$  values including statistical uncertainties. The underlying  $\mathcal{R}_i$  values are given with both statistical and systematic uncertainties in Section ??.

$F_i$ values: $D \rightarrow K_S^0 \pi^+ \pi^-$		
bin	LL	DD
-8	$0.024 \pm 0.001$	$0.024 \pm 0.000$
-7	$0.127 \pm 0.001$	$0.133 \pm 0.001$
-6	$0.062 \pm 0.001$	$0.056 \pm 0.001$
-5	$0.046 \pm 0.001$	$0.042 \pm 0.001$
-4	$0.095 \pm 0.001$	$0.095 \pm 0.001$
-3	$0.160 \pm 0.001$	$0.160 \pm 0.001$
-2	$0.153 \pm 0.001$	$0.153 \pm 0.001$
-1	$0.095 \pm 0.001$	$0.097 \pm 0.001$
1	$0.022 \pm 0.001$	$0.020 \pm 0.000$
2	$0.005 \pm 0.000$	$0.005 \pm 0.000$
3	$0.004 \pm 0.000$	$0.004 \pm 0.000$
4	$0.055 \pm 0.001$	$0.056 \pm 0.001$
5	$0.027 \pm 0.001$	$0.022 \pm 0.000$
6	$0.004 \pm 0.000$	$0.003 \pm 0.000$
7	$0.055 \pm 0.001$	$0.057 \pm 0.001$
8	$0.067 \pm 0.001$	$0.072 \pm 0.001$

$F_i$ values: $D \rightarrow K_S^0 K^+ K^-$		
bin	LL	DD
-2	$0.207 \pm 0.004$	$0.202 \pm 0.003$
-1	$0.222 \pm 0.004$	$0.230 \pm 0.003$
1	$0.290 \pm 0.005$	$0.296 \pm 0.003$
2	$0.281 \pm 0.005$	$0.271 \pm 0.003$

2085 Dalitz-plot acceptance profile in  $B^\pm \rightarrow Dh^\pm$  decays and, say,  $B \rightarrow D^* K$  or  
 2086  $B \rightarrow D K^*$  decays is smaller than the systematic arising from extracting the  
 2087 efficiency profile from simulated decays. Therefore, the obtain central values and  
 2088 uncertainties have been made public [?], including a set of systematic uncertainties  
 2089 discussed in Section 5.6.12.<sup>3</sup>

### 2090 5.5.3 Cross checks

2091 A series of cross checks are performed to verify that the fit to data is behav-  
 2092 ing as expected.

---

<sup>3</sup>In practice, it is the obtained  $\mathcal{R}_i$  values that are made public, related to the  $F_i$  parameters via Eq. (5.20).

2093 **Comparison to results of earlier analyses**

2094 It is confirmed that the results obtained in fits of the Run 1 or 2015+16 data  
 2095 sets in isolation are compatible with the results obtained in the original LHCb  
 2096 analyses of those data sets [?, ?]. In order to do so, the whole analysis procedure  
 2097 is carried out using only the relevant subset of data, and the strong-phase inputs  
 2098 from the CLEO collaboration are used in the fit. Two effects need to be taken  
 2099 into account when comparing the central values.

2100 The overlap between the samples need to be taken into account. The overlap  
 2101 is not 100 % due to changes in the candidate selection. The overlap between the  
 2102 new selection and the data set of the original analysis of Run 1 data is about  
 2103 70 %, whereas is it about 90 % for the 2015+16 data set. In order to determine the  
 2104 expected difference between the observables fitted from data sets with significant  
 2105 overlap, a large number of toy data sets were generated in sets of two, where  
 2106 70 (90) % of decays were shared between the data sets. Both data sets were  
 2107 fitted and the difference between the obtained central values for each observable  
 2108 tabulated; the standard deviation of these distributions are used to calculate the  
 2109 pulls between the old analysis results and the new fits to data. This check does  
 2110 not take into account that the semi-leptonic PID cuts were introduced to remove a  
 2111 potential peaking background, which may have had a small systematic effect on  
 2112 the earlier measurement results. Thus the expected differences are likely to be  
 2113 slightly underestimated and the check conservative.

2114 Furthermore, the  $F_i$  parameters were determined in a semi-leptonic control  
 2115 channel in the earlier analyses. Therefore, the expected difference obtained above is  
 2116 adjusted by adding the  $F_i$ -related systematic uncertainty of the original analysis  
 2117 in quadrature, when comparing the old results to those in new fits to the Run 1  
 2118 and 15+16 data sets. No further corrections have been made to the expected  
 2119 differences, which effectively assumes all other systematic uncertainties to be 100 %  
 2120 correlated. Also for this reason can the check be considered conservative. As can  
 2121 be seen in Tables 5.11 and 5.12, neither the Run 1 and 2015+16 comparisons show  
 2122 unreasonable differences in central values.

2123 **Directly fitting the signal yields**

2124 As a cross-check, the fit is run in an alternative mode, in which the signal yields of  
 2125 each bin are independent parameters. The obtained yields are compared to those  
 2126 predicted from the results of the default fit in Fig. 5.36. The yields are shown for  
 2127 each "effective bin", where effective bin  $i$  is defined as bin  $+i$  for  $B^+$  decays and bin

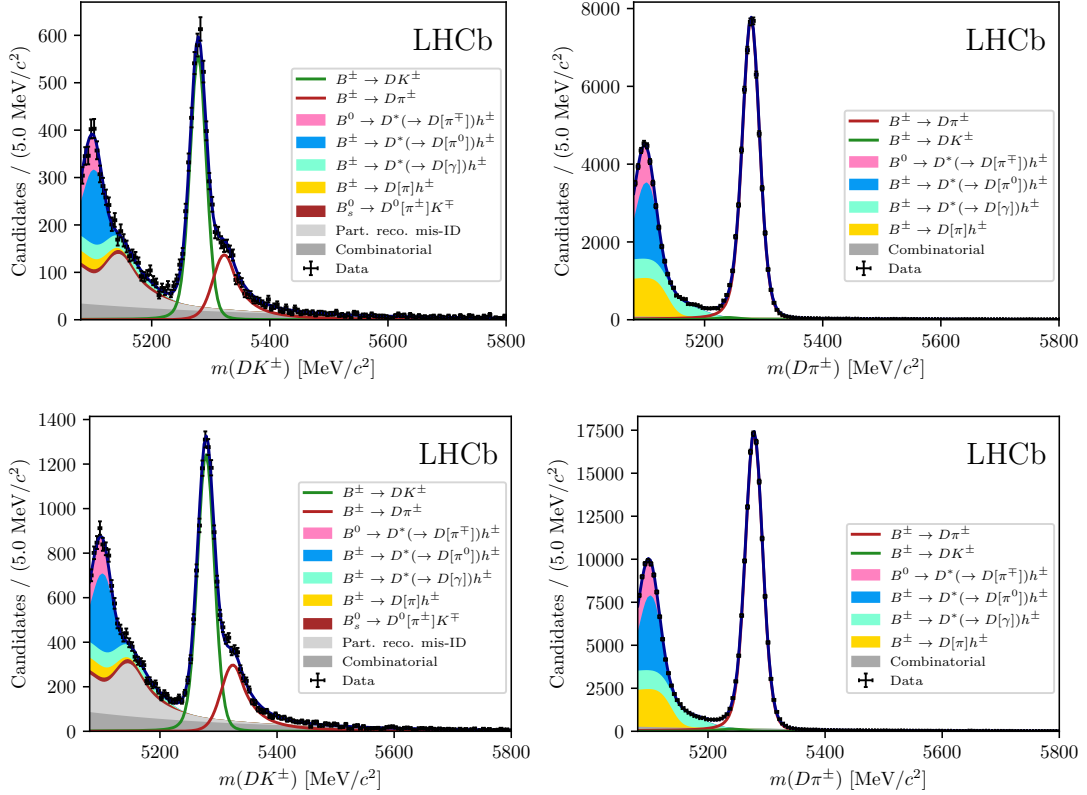


**Figure 5.31:** The invariant mass distribution for the (left)  $B^\pm \rightarrow DK^\pm$  channel and (right)  $B^\pm \rightarrow D\pi^\pm$  channel, where  $D \rightarrow K_S^0\pi^+\pi^-$  and the  $K_S^0$  is in the (top) LL and (bottom) the DD categories. The particle within square brackets in the legend denotes the particle that has not been reconstructed.

**Table 5.11:** Comparison between the results on the Run 1 analysis [?] and the central values obtained when fitting the Run 1 dataset with the selection and fit setup described in this note. The pull is calculated using the  $1\sigma$  expected difference, which takes the sample overlap and the systematic uncertainty on the  $F_i$  parameters in the previous analysis into account, but assumes all other systematic uncertainties to be perfectly correlated. The new fits are performed using the CLEO strong-phase inputs.

Observable	Run 1 result [?]	New Fit (central value $\times 10^{-2}$ )	Pull
$x_-^{DK}$	2.50	4.04	0.85
$y_-^{DK}$	7.50	9.14	1.02
$x_+^{DK}$	-7.70	-9.40	-0.91
$y_+^{DK}$	-2.20	0.80	1.77
<i>p</i> -value: 0.057			

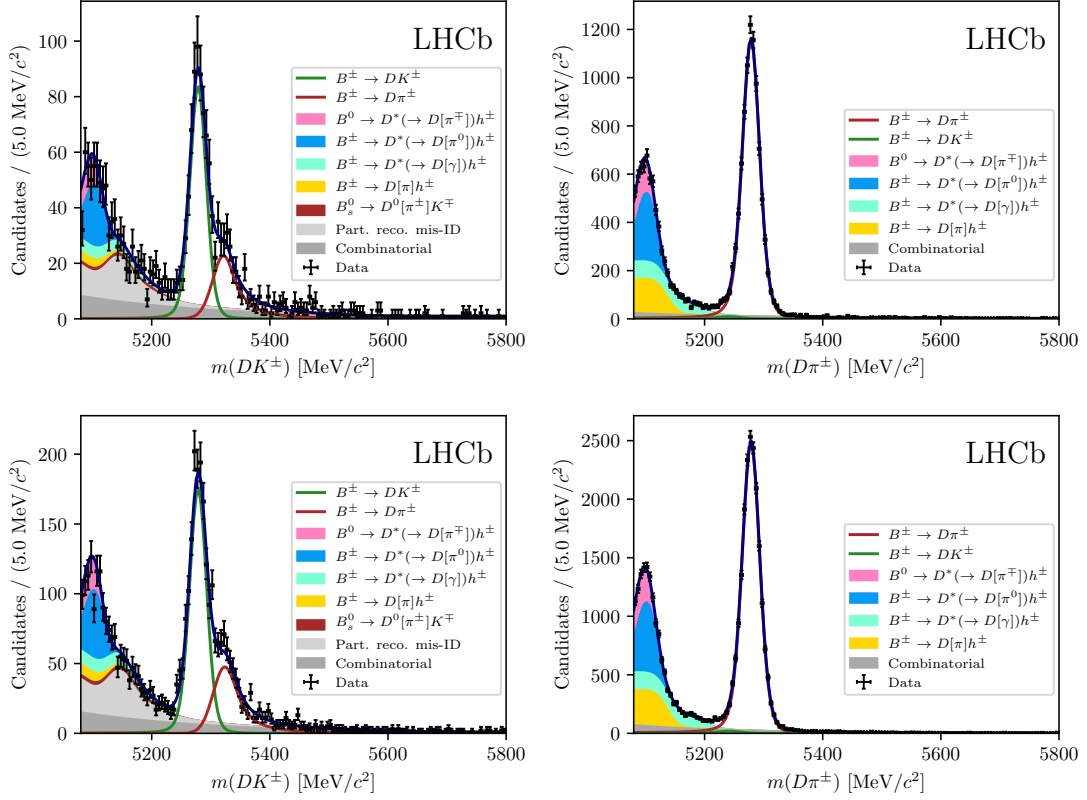


**Figure 5.32:** The invariant mass distribution for the (left)  $B^\pm \rightarrow DK^\pm$  channel and (right)  $B^\pm \rightarrow D\pi^\pm$  channel, where  $D \rightarrow K_S^0 K^+ K^-$  and the  $K_S^0$  is in the (top) LL and (bottom) the DD categories. The particle within square brackets in the legend denotes the particle that has not been reconstructed.

**Table 5.12:** Comparison between the results on the 2015+16 analysis [?] and the central values obtained when fitting the 2015+16 dataset with the selection and fit setup described in this note. The pull is calculated using the  $1\sigma$  expected difference, which takes the sample overlap and the systematic uncertainty on the  $F_i$  parameters in the previous analysis into account, but assumes all other systematic uncertainties to be perfectly correlated. The new fits are performed using the CLEO strong-phase inputs.

Observable	15+16 result [?]	New Fit	Pull
	(central value $\times 10^{-2}$ )		
$x_-^{DK}$	9.00	8.36	-0.50
$y_-^{DK}$	2.10	1.16	-0.62
$x_+^{DK}$	-7.70	-8.58	-0.56
$y_+^{DK}$	-1.00	-2.82	-1.39
<i>p</i> -value: 0.239			

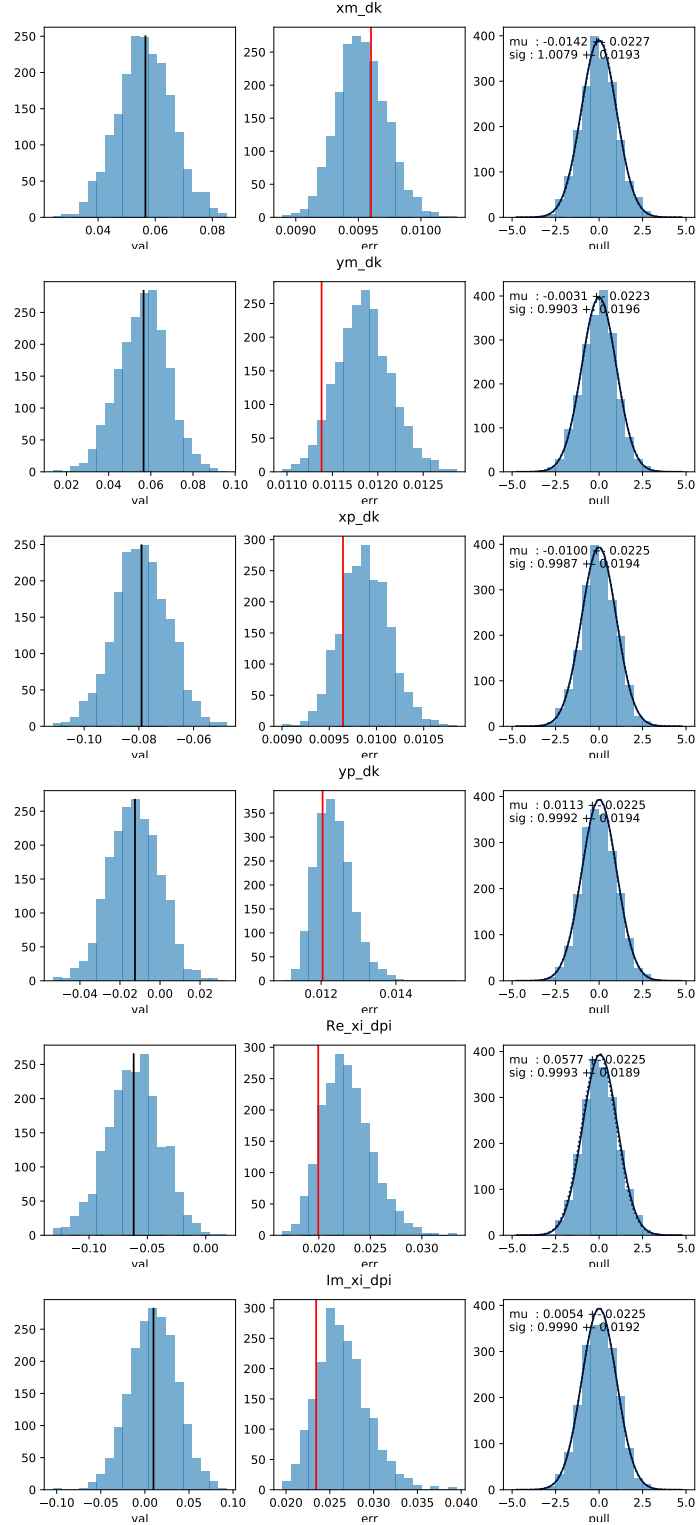


**Figure 5.33:** Pull plots for (from the top)  $x_{-}^{DK}$ ,  $y_{-}^{DK}$ ,  $x_{+}^{DK}$ ,  $y_{+}^{DK}$ ,  $x_{\xi}^{D\pi}$ , and  $y_{\xi}^{D\pi}$  from pseudoexperiments. The input values are shown with black lines in the left column. The uncertainty estimates in the fit to real data are shown with red lines in the central column.

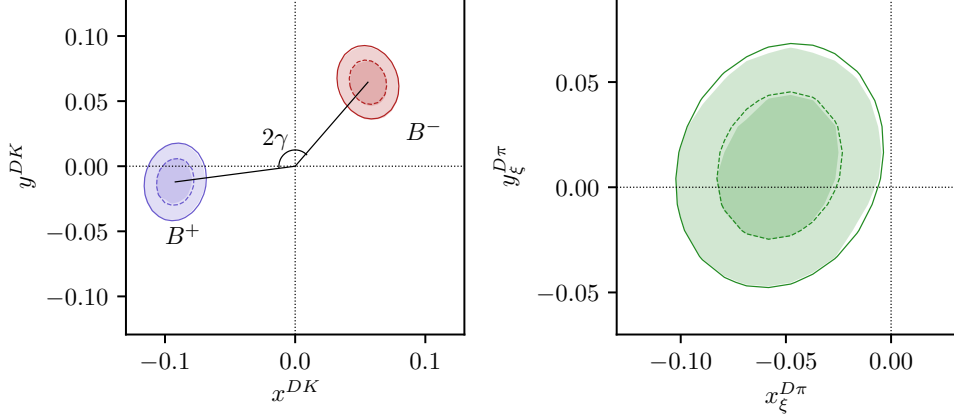


**Figure 5.34:** The 68 % and 95 % confidence regions for the fitted observables. The lines show the regions estimated from the covariance matrix returned by the default fit. The shaded areas are obtained in a likelihood scan, where the binned fit is run many times with all observables held at fixed values, scanning pairs of observables over the relevant ranges. The scan is made separately for the three pairs  $(x_{-}^{DK}, y_{-}^{DK})$ ,  $(x_{+}^{DK}, y_{+}^{DK})$ , and  $(x_{\xi}^{D\pi}, y_{\xi}^{D\pi})$ , holding the four other parameters fixed at their default-fit central values during a given scan. Then the minimum log-likelihood is related to a  $\chi^2$  via  $\mathcal{L}_{\min} = \frac{1}{2}\chi^2$  (discarding an irrelevant constant), and the confidence region limits placed at  $\chi^2 = 2.30$  and  $\chi^2 = 6.18$ , yielding the relevant percentiles for a  $\chi^2$  distribution with 2 degrees of freedom.

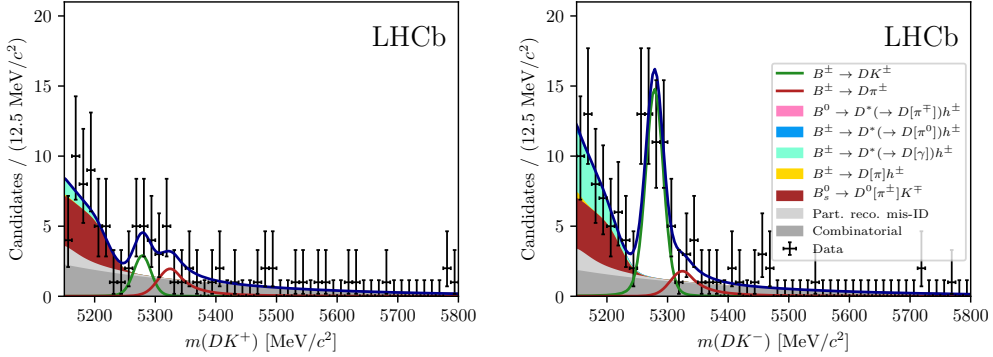


**Figure 5.35:** The invariant mass distribution for the (left)  $B^+ \rightarrow DK^+$  candidates in bin -2 and (right) the  $B^- \rightarrow DK^-$  candidates in bin +2, where  $D \rightarrow K_S^0\pi^+\pi^-$  and the  $K_S^0$  is reconstructed in the DD category.

2128     $-i$  for  $B^-$  decays; in the  $CP$  symmetric case, these bins are expected to have equal  
 2129    yields (modulo production and detection asymmetries). The agreement between the  
 2130    two fit set-ups is seen to be excellent. The normalised yield asymmetries, defined as

$$A^i \equiv \frac{N_{-i}^- - N_i^+}{N_{-i}^- + N_i^+} \quad (5.22)$$

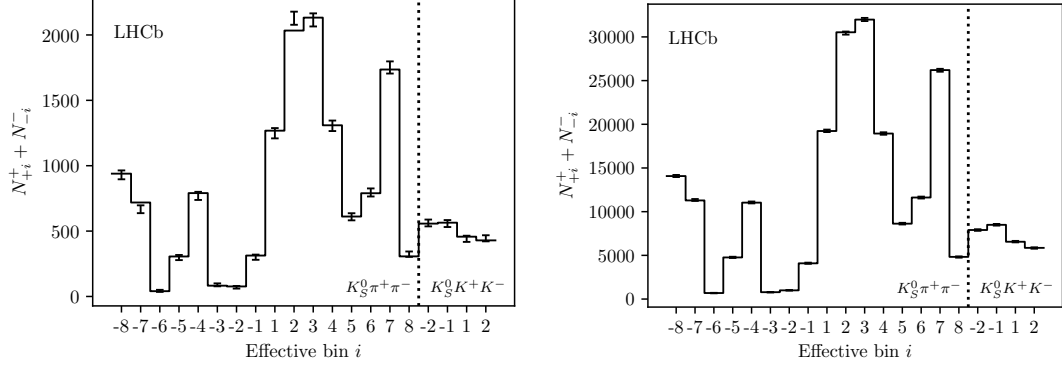


**Figure 5.36:** Comparison of (lines) the predicted yield given the determined  $CP$  observables and (error bars) the yield obtained in fits to data where each yield is an independent parameter. The yields are shown for (left)  $B^\pm \rightarrow DK^\pm$  decays and (right)  $B^\pm \rightarrow D\pi^\pm$  decays. The LL and DD categories have been combined, as has the  $B^+$  and  $B^-$  yields for each effective Dalitz bin, defined as bin  $+i$  for  $B^+$  decays and bin  $-i$  for  $B^-$  decays.

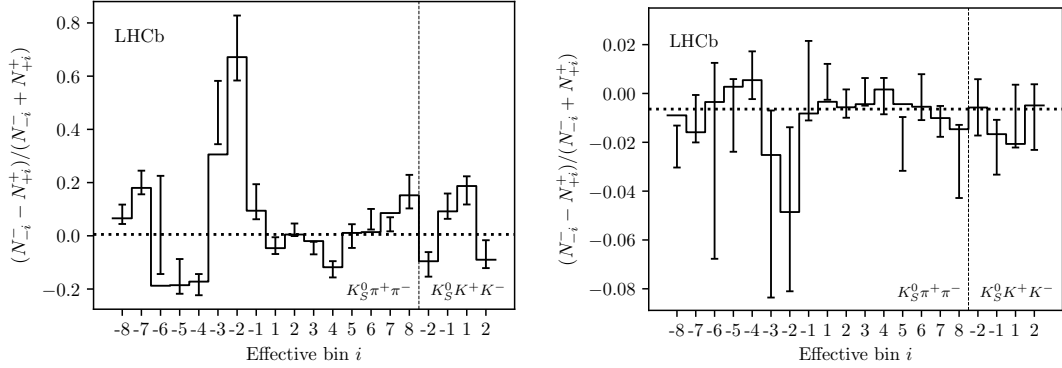


**Figure 5.37:** The bin-by-bin asymmetries  $(N_{-i} - N_{+i}) / (N_{-i} + N_{+i})$  for each Dalitz-plot bin number for (left)  $B^\pm \rightarrow DK^\pm$  decays and (right)  $B^\pm \rightarrow D\pi^\pm$  decays. The prediction from the central values of the  $CP$ -violation observables is shown with a solid line and the asymmetries obtained in fits with independent bin yields are shown with the error bars. The predicted asymmetries in a fit that does not allow for  $CP$  violation are shown with a dotted line.

are shown in Fig. 5.37 for all decay channels. Again, the agreement between the nominal fit, and the alternative fit with independent yields is found to be excellent. It is also clear how, in the case of  $B^\pm \rightarrow DK^\pm$  decays, the asymmetry is significantly different from zero for a number of bin pairs.

### 2135 Fitting subsets of the data separately

One cross check is carrying out, by determining the  $CP$  observables using a number of independent sub samples of the data set separately. This is done for the

2138 following following data splits

- 2139 • Fig. 5.38a shows the two dimensional log likelihood contours for the observables
- 2140 for fits to the Run 1, 2015+16, 2017 and 2018 datasets separately
- 2141 • Fig. 5.38b shows the same plots, comparing the fits to the data set split by
- 2142  $K_S^0$  track type.
- 2143 • Fig. 5.38c shows the same plots, comparing the fits to the data set split by
- 2144 whether the candidate event was triggered by one of the signal particles at the
- 2145 hardware level (TOS), or by another particle in the underlying event (TIS).
- 2146 • Fig. 5.38d shows the same plots, comparing the fits to the data set split the
- 2147 magnet polarity during data taking.
- 2148 • Fig. 5.38e shows the same plots, comparing the fits to the data set split by
- 2149 whether the  $D$  meson decays to the  $K_S^0\pi^+\pi^-$  or  $K_S^0K^+K^-$  final state.

2150 All figures show the Gaussian likelihood contours corresponding to the statistical  
2151 uncertainties. There is good agreement between the results in all cases, given  
2152 that in each cases the sub datasets are independent and therefore the statistical  
2153 errors are uncorrelated.

#### 2154 Significantly tightening the companion PID requirement

2155 One of the dominant backgrounds in the signal region of the  $B^\pm \rightarrow DK^\pm$  channel is  
2156 from partly reconstructed  $B \rightarrow D\pi X$  decays where the bachelor pion is misidentified  
2157 as a kaon. The background mode is well described by the included shape component,  
2158 and included in all relevant systematic studies. Nevertheless, an additional cross  
2159 check is carried out to ensure that it is not having a significant effect on the fit: the  
2160 analysis is repeated with PID requirement of  $\text{PID}_K > 12$  required to place a candidate  
2161 in the  $B^\pm \rightarrow DK^\pm$  category, instead of  $\text{PID}_K > 4$ . With this requirement 99.7 %  
2162 of  $B^\pm \rightarrow D\pi^\pm$  decays are correctly identified, making the cross-feed component  
2163 in the  $B^\pm \rightarrow DK^\pm$  channels significantly smaller than in the default fit. This  
2164 is clearly visible in Fig. 5.39, where the fit projections for the global fit of the  
2165  $D \rightarrow K_S^0\pi^+\pi^-$  modes are shown. In return, the probability of correctly identifying a  
2166 kaon companion drops to about 68–69 %, resulting in a smaller effective signal yield.

2167 The measurement results are compared in Table 5.13, where the differences  
2168 in central value are seen to be reasonably small. It is not trivial to determine  
2169 whether the difference is statistically significant or not: the same candidates are

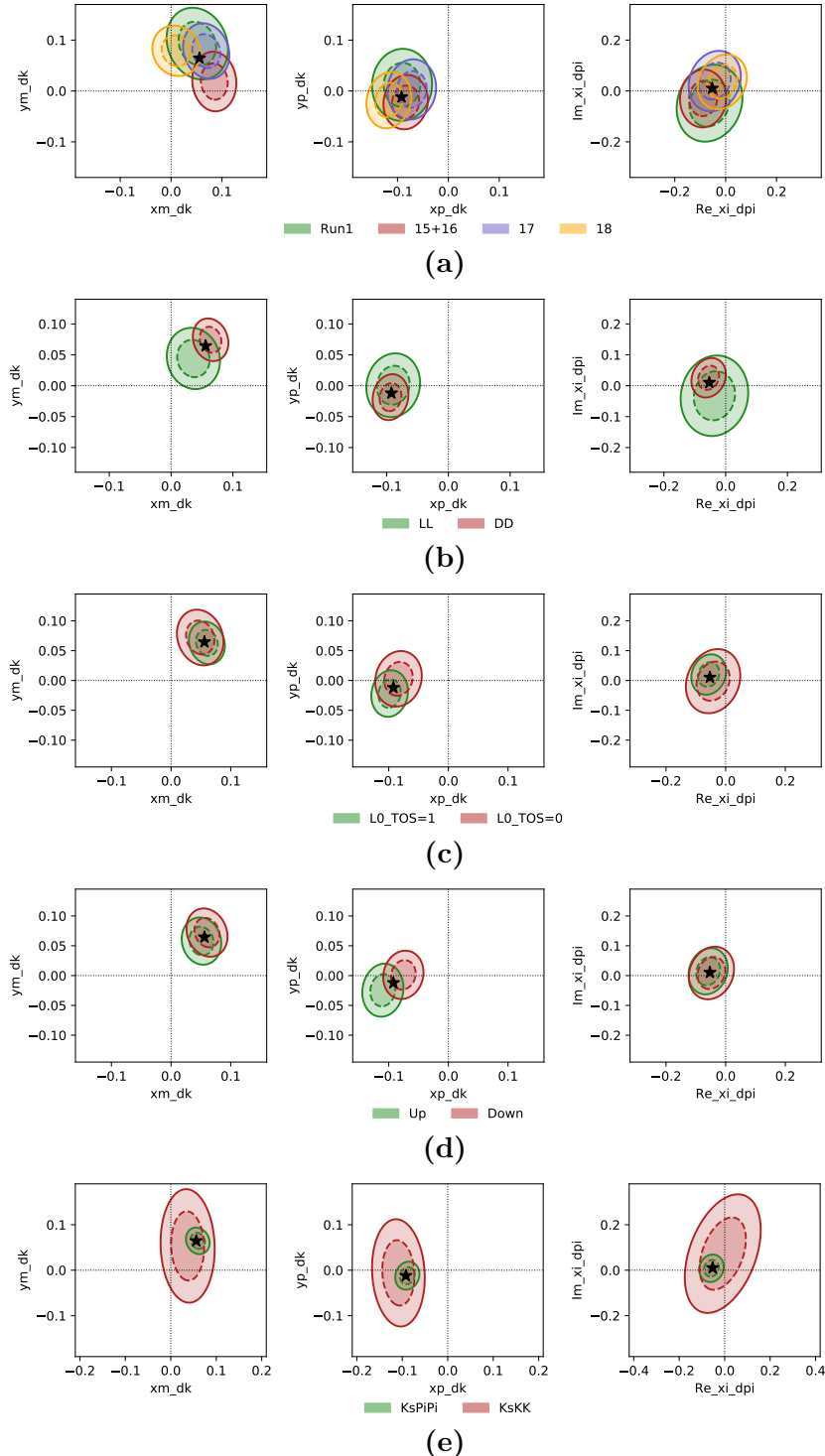


**Figure 5.38:** Comparison of the 68 % and 95 % confidence regions for (left)  $(x_{-}^{DK}, y_{-}^{DK})$ , (centre)  $(x_{+}^{DK}, y_{+}^{DK})$ , and (right)  $(x_{\xi}^{D\pi}, y_{\xi}^{D\pi})$  obtained from fits to sub sets of the data set. The uncertainties are statistical only. The central values of the default fit are shown with a black star. The dataset is split by (a) data taking year, (b) LL and DD  $K_S^0$  types, (c) trigger category, (d) magnet polarity, and (e)  $D$  decay mode.

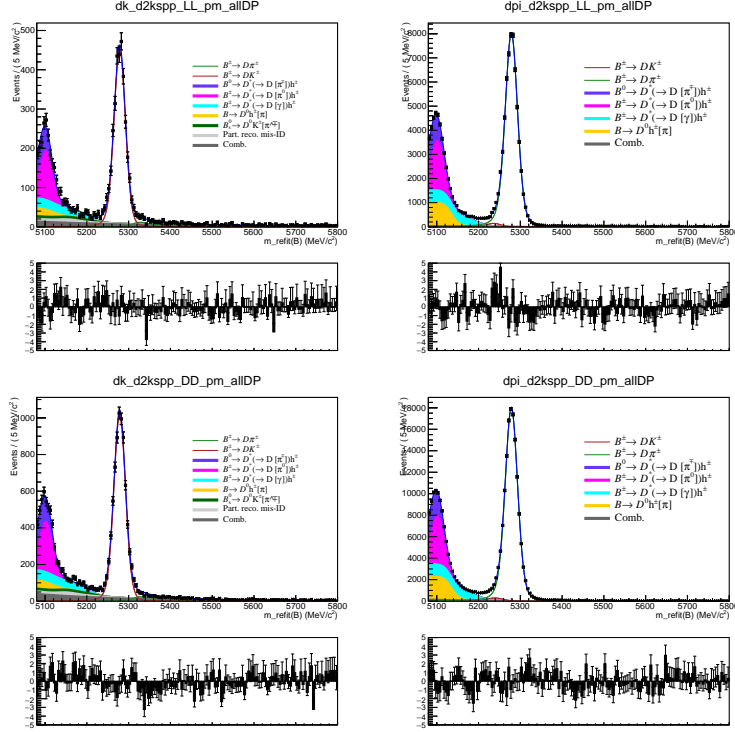


**Figure 5.39:** Fit projections for fits to the  $D \rightarrow K_S^0 \pi^+ \pi^-$  candidates with a bachelor PIDK cut at 12 instead of 4 used to split into (left)  $B^\pm \rightarrow DK^\pm$  and (right)  $B^\pm \rightarrow D\pi^\pm$  candidates, for (top) the LL and (bottom) DD categories.

analysed in both cases, the difference being that a number of candidates that are placed in the  $B^\pm \rightarrow DK^\pm$  category in the nominal fit are placed in the  $B^\pm \rightarrow D\pi^\pm$  category in the alternative fit. The uncertainty will not be 100 % correlated because signal events that move from the  $DK$  to  $D\pi$  category are placed in a region with high background; however, this is somewhat compensated for by candidates that remain in the  $DK$  category gaining statistical power due to the increased purity. An estimate of the expected statistical fluctuation can be determined by taking the difference of the statistical uncertainties in quadrature. Using this estimate, the observed shifts are found to be consistent with statistical fluctuation, and thus there is no sign of the background from  $D\pi^\pm \rightarrow DK^\pm$  cross-feed causing issues.

## 2180 Compare results obtained with different strong-phase inputs

2181 It is interesting to compare the results obtained with different strong-phase inputs.  
 2182 This is done in Fig. 5.40, where the default fit results are compared to those  
 2183 obtained if the  $CP$  fit is done with the CLEO-only inputs [?], and with the model  
 2184 predictions from the 2018 Belle model [?] and the 2008 BaBar model [?]. For the  
 2185 measurements, only the strong-phase-related uncertainties are included in the plot,  
 2186 since the statistical uncertainties are correlated. All results are found to agree well.

**Table 5.13:** Results of running the measurement with the default PIDK cut at 4 used to separate  $B^\pm \rightarrow DK^\pm$  and  $B^\pm \rightarrow D\pi^\pm$  candidates, as well as with an alternative PIK cut at 12, resulting in much lower cross-feed from misidentified  $B^\pm \rightarrow D\pi^\pm$  decays. We also show the pulls, defined as  $\Delta x / \sqrt{|\sigma_{PIDK>12}^2 - \sigma_{PIDK>4}^2|}$  as described in the main text body. The comparison was made before the BESIII measurement of the  $D \rightarrow K_S^0 K^+ K^-$  strong-phase inputs became available; therefore the fits use the CLEO-only results [?] for this mode, which explains why the results quoted for  $PIDK > 4$  differ slightly from the nominal fit results.

Parameter	PIDK > 4	PIDK > 12	$\sigma = \sqrt{\sigma_{PIDK>12}^2 - \sigma_{PIDK>4}^2}$	Pull
$x_-^{DK}$	$5.59 \pm 0.96$	$5.82 \pm 1.01$	0.30	0.77
$y_-^{DK}$	$6.45 \pm 1.14$	$6.86 \pm 1.19$	0.36	1.13
$x_+^{DK}$	$-9.21 \pm 0.96$	$-8.94 \pm 1.01$	0.30	0.93
$y_+^{DK}$	$-1.21 \pm 1.20$	$-0.94 \pm 1.26$	0.37	0.71
$x_\xi^{D\pi}$	$-5.30 \pm 1.99$	$-5.13 \pm 2.02$	0.32	0.52
$y_\xi^{D\pi}$	$1.03 \pm 2.34$	$1.71 \pm 2.33$	0.28	2.40

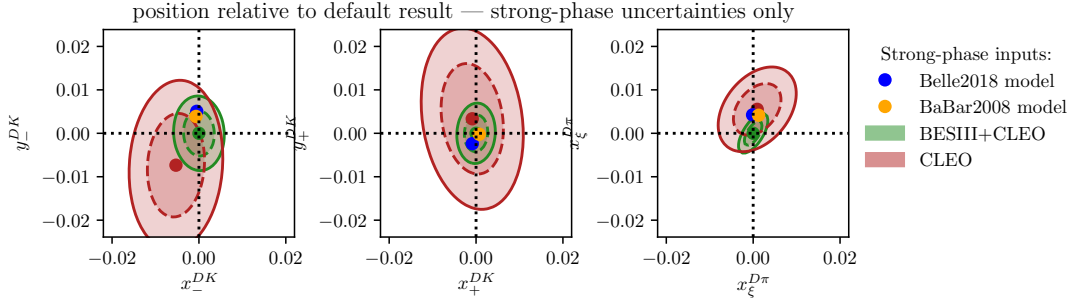


**Figure 5.40:** Fit results for (left)  $(x_-^{DK}, y_-^{DK})$ , (centre)  $(x_+^{DK}, y_+^{DK})$ , and (right)  $(x_\xi^{D\pi}, y_\xi^{D\pi})$  depending on strong-phase inputs, shown relative to the default fit results. The included results are based on (green) the BESIII-CLEO combination, which is the default, (red) the CLEO-only results, (blue dot) the 2018 Belle model [?] and (orange dot) the 2008 BaBar model [?]. For the measurements, only strong-phase related uncertainties are included in the plotted confidence regions.

## 5.6 Systematic uncertainties

The following sections cover the suite of systematic uncertainties on the measurement that has been considered. All uncertainties are summarised in Section 5.6.12.

### 5.6.1 Strong phase uncertainties

The observables  $x_\pm^{DK}$ ,  $y_\pm^{DK}$ ,  $x_\xi^{D\pi}$  and  $y_\xi^{D\pi}$  are extracted using the central values of  $c_i$  and  $s_i$  from the BESIII–CLEO combinations [?, ?, ?]. Subsequently, the measurement uncertainty on these inputs is propagated to the observables by performing a large set of fits to data, using alternative values of  $c_i$  and  $s_i$ . The new  $c_i$  and  $s_i$  values are

**Table 5.14:** Systematic uncertainties and correlation matrix due to strong-phase inputs.

Uncertainty ( $\times 10^{-2}$ )						
	$x_-^{DK\pm}$	$y_-^{DK\pm}$	$x_+^{DK\pm}$	$y_+^{DK\pm}$	$x_\xi^{D\pi\pm}$	$y_\xi^{D\pi\pm}$
$\sigma$	0.23	0.35	0.18	0.28	0.14	0.18

Correlations						
	$x_-^{DK\pm}$	$y_-^{DK\pm}$	$x_+^{DK\pm}$	$y_+^{DK\pm}$	$x_\xi^{D\pi\pm}$	$y_\xi^{D\pi\pm}$
$x_-^{DK\pm}$	1.000	-0.047	-0.490	0.322	0.189	0.144
$y_-^{DK\pm}$		1.000	0.059	-0.237	-0.116	-0.117
$x_+^{DK\pm}$			1.000	0.061	0.004	-0.139
$y_+^{DK\pm}$				1.000	0.127	-0.199
$x_\xi^{D\pi\pm}$					1.000	0.638
$y_\xi^{D\pi\pm}$						1.000

obtained by smearing the central values by their measured statistical and systematic uncertainties while taking into account their correlations. The use of different  $c_i$  and  $s_i$  values changes the extracted  $x_\pm^{DK}$ ,  $y_\pm^{DK}$ ,  $x_\xi^{D\pi}$  and  $y_\xi^{D\pi}$  values. The width of the distributions of central values extracted from 1000 data fits are assigned as a systematic uncertainty. The distributions are shown in Fig. 5.41 and the assigned uncertainties are summarised in Table 5.14. The correlation matrix related to the strong-phase uncertainty can be obtained from the correlations observed between observables in the fits, and is also given in the table.

The set of  $(c_i, s_i)$  that was employed in this analysis will be used in a series of future BPFGGSZ measurements, both with additional  $B$  decay modes within the LHCb collaboration and by the Belle II collaboration. This introduces some correlation between the measurement results. In order to allow for an estimate of the degree of correlation by future analysts, the 1000 samples  $(c_i, s_i)$  values and the corresponding fit results for  $(x_\pm^{DK}, y_\pm^{DK}, x_\xi^{D\pi}, y_\xi^{D\pi})$  have been made public as supplementary material to Ref. ??.

## 5.6.2 Efficiency-profile-related systematic uncertainties

The non-trivial efficiency profile over the Dalitz plot can have a range of effects, considered in the sections below.

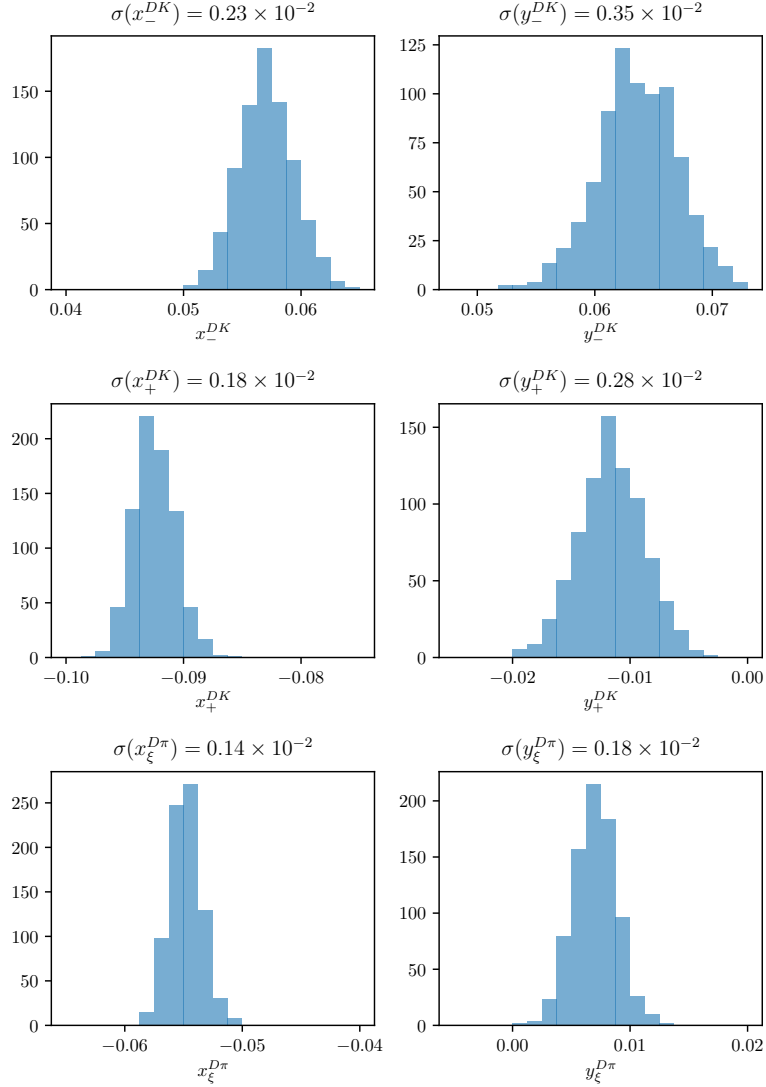


**Figure 5.41:** Spread of central values for the fitted observables when the input  $c_i$  and  $s_i$  from the BESIII+CLEO combination are varied according to their uncertainties and correlations.

2213    **The assumption that**  $\eta^{DK}(s_-, s_+) = \eta^{D\pi}(s_-, s_+)$

2214    The assumption that  $\eta^{DK}(s_-, s_+) = \eta^{D\pi}(s_-, s_+)$  as examined in detail in Section ??.  
 2215    It was found that with signal yields similar to those in the data set, no statistically  
 2216    significant difference between the efficiency profiles  $\eta^{DK}(s_-, s_+)$  and  $\eta^{D\pi}(s_-, s_+)$   
 2217    was discernible, and no additional uncertainty due to this assumption is assigned.

2218    **The assumption that**  $\eta(s_-, s_+) = \eta(s_+, s_-)$

2219    The measurement is sensitive to effects that break the assumption  $\eta(s_-, s_+) =$   
 2220     $\eta(s_+, s_-)$ . Such a breakdown would mean that opposite points on the Dalitz plot

have different efficiencies and can only arise through a charge detection asymmetry (e.g that it is more likely to detect a  $K^+$  in the detector rather than a  $K^-$ ).<sup>4</sup>

The potential size of such an asymmetry can be studied in simulation where the  $D$  decay has a uniform distribution over the allowed phase space; in such simulated samples, it would manifest itself as an observation different fractional yields of  $B^-$  decays in bin  $i$  and  $B^+$  decays in bin  $-i$ . This effect has been looked for using the large samples of  $B^\pm \rightarrow D\pi^\pm$  decays that were generated for the analysis of 2015 and 2016 data. The study is performed using the rectangular binning schemes shown in Fig. 5.42, because this scheme results in bin yields that are more sensitive to effects that vary smoothly over phase space. The comparison plots are shown in Fig. 5.43, where it can be seen that the  $p$  values for the hypothesis that there is no asymmetry all take on reasonable values. Hence no further systematic uncertainty is considered.

#### Effect of phase-space efficiency profile on $c_i$ and $s_i$

As discussed in Section 2.4 there is a small bias, because the  $c_i$  and  $s_i$  values that are used correspond to the definition

$$c_i = \frac{\int_i ds^2 |A_S^D(s_{-+})| |A_S^D(s_{+-})| \cos[\Delta\delta_D(s_{-+})]}{\sqrt{\int_i ds^2 |A_S^D(s_{-+})|^2} \sqrt{\int_i ds^2 |A_S^D(s_{+-})|^2}}, \quad (\text{and equivalent for } s_i,) \quad (5.23)$$

whereas the non-flat efficiency profile in LHCb,  $\eta(s_-, s_+) \equiv \eta(s_{-+})$ , means that the appropriate  $c_i'$  and  $s_i'$  entering the exact yield expressions are

$$c_i^{\text{eff}} = \frac{\int_i ds^2 \eta(s_{-+}) |A_S^D(s_{-+})| |A_S^D(s_{+-})| \cos[\Delta\delta_D(s_{-+})]}{\sqrt{\int_i ds^2 |A_S^D(s_{-+})|^2} \sqrt{\int_i ds^2 |A_S^D(s_{+-})|^2}}, \quad (\text{and equivalent for } s_i^{\text{eff}}.) \quad (5.24)$$

The shifts  $\Delta c_i = c_i^{\text{eff}} - c_i$ ,  $\Delta s_i = s_i^{\text{eff}} - s_i$  can be estimated using the efficiency profile in simulation and the latest amplitude models: the 2018 Belle model [?] for  $D \rightarrow K_S^0 \pi^+ \pi^-$  and the 2010 BaBar model [?] for  $D \rightarrow K_S^0 K^+ K^-$ . The strong-phase parameters are first calculated assuming a uniform reconstruction efficiency over phase space according to Eq. (5.23), obtaining a set of values  $\{c_i^{\text{model}}, s_i^{\text{model}}\}$ . Then, an alternative set is calculated,  $\{c_i^{\text{eff}}, s_i^{\text{eff}}\}$ , using the same model, and the reconstruction efficiency profile found in full LHCb simulation. The results, as well as their differences, are tabulated in Tables 5.15 and 5.16. The LHCb reconstruction

---

<sup>4</sup>Note that the measurement is insensitive to any asymmetry in the reconstruction of the companion track.

**Table 5.15:** The  $c_i$  and  $s_i$  values for  $D \rightarrow K_S^0 \pi^+ \pi^-$  decays calculated via the 2018 Belle model [?] in two cases: assuming a uniform reconstruction efficiency over phase space, denoted  $(c/s)_i^{\text{model}}$ , and including the LHCb efficiency profile as obtained in simulation, averaged for LL and DD, denoted  $(c/s)_i^{\text{eff}}$ . The change due to including the efficiency is also tabulated.

Bin	$c_i^{\text{model}}$	$c_i^{\text{eff}}$	$\Delta c_i$	$s_i^{\text{model}}$	$s_i^{\text{eff}}$	$\Delta s_i$
1	-0.027	-0.007	0.019	0.812	0.794	-0.018
2	0.837	0.859	0.022	0.164	0.152	-0.012
3	0.163	0.163	-0.000	0.872	0.880	0.008
4	-0.914	-0.915	-0.001	0.076	0.082	0.006
5	-0.149	-0.170	-0.021	-0.856	-0.854	0.002
6	0.373	0.362	-0.011	-0.782	-0.805	-0.023
7	0.863	0.862	-0.000	-0.203	-0.202	0.002
8	0.860	0.862	0.002	0.330	0.336	0.006

**Table 5.16:** The  $c_i$  and  $s_i$  values for  $D \rightarrow K_S^0 K^+ K^-$  decays calculated via the 2010 BaBar model [?] in two cases: assuming a uniform reconstruction efficiency over phase space, denoted  $(c/s)_i^{\text{model}}$ , and including the LHCb efficiency profile as obtained in simulation, averaged for LL and DD, denoted  $(c/s)_i^{\text{eff}}$ . The change due to including the efficiency is also tabulated.

Bin	$c_i^{\text{model}}$	$c_i^{\text{eff}}$	$\Delta c_i$	$s_i^{\text{model}}$	$s_i^{\text{eff}}$	$\Delta s_i$
1	0.738	0.735	-0.002	0.266	0.263	-0.003
2	-0.697	-0.744	-0.046	0.332	0.329	-0.003

efficiency at a given point in phase-space is taken to be proportional to the yield in simulation, as the simulated decays were generated with a uniform distribution over phase space. The efficiency is averaged over the LL and DD categories in the calculation.

A systematic uncertainty due to employing the measured  $c_i$  and  $s_i$  directly in the fit is assigned by generating a large number of toy data sets where the signal yields are calculated using  $(c_i^{\text{eff}}, s_i^{\text{eff}})$ , and then fitting the data sets using  $(c_i^{\text{model}}, s_i^{\text{model}})$ . The mean bias of each observable in these toys is assigned as the systematic uncertainty, and is determined to be  $0.1 \times 10^{-2}$  or less for all observables. The smallness of the effect is the reason no effort is made to correct the  $c_i$  and  $s_i$  values in the nominal measurement.

### 5.6.3 Mass shapes

A number of uncertainties relate to the mass distributions that enter the fit model. Each is described in detail the sections below.

2261 **Determination of shape parameters**

2262 The statistical uncertainties on the shape parameters that are obtained in fits  
 2263 to simulated decays and in the first stage fit to data need to be propagated to  
 2264 the uncertainty on the obtained parameters. This is done via a bootstrapping  
 2265 procedure, repeating these steps many times:

- 2266     • Each of the data sets used determine parameters of the signal, crossfeed, and  
 2267 lowmass shapes that are fixed in the first-stage fit to data of Section 5.4 are  
 2268 re-sampled with replacement, drawing a number of events equal to the original  
 2269 data-set size. These are from simulation for signal and lowmass shapes, and  
 2270 real data for the crossfeed shapes. All of the shapes are fit again, on the  
 2271 re-sampled data sets.
- 2272     • The real dataset is re-sampled with replacement, drawing a number of events  
 2273 equal to the original data-set size. Then, the first-stage fit of Section 5.4 is  
 2274 repeated with the shapes obtained as described above, obtaining values for  
 2275 the remaining shape parameters.
- 2276     • Finally, the  $CP$  fit is repeated using the shape parameters determined in the  
 2277 preceding steps, but *without* re-sampling the dataset (to avoid a statistical  
 2278 spread in the obtained central values that is independent of the shape  
 2279 parameters).

2280 The uncertainty on each observable is taken to be the standard deviation of the  
 2281 set of central values obtained as described above. This procedure propagates  
 2282 the statistical uncertainty on the fixed parameters to the observables, in a way  
 2283 that takes correlations into account, and which does not rely on the uncertainty  
 2284 estimates in the preliminary fits being accurate. The uncertainties are less than  
 2285  $0.1 \times 10^{-2}$  for all  $DK^\pm$  observables, in line with earlier analyses, and less than  
 2286  $0.2 \times 10^{-2}$  for all  $D\pi^\pm$  observables.

2287 A potential bias arises due the use of sWeights when obtaining the mass  
 2288 distribution of decays where a  $\pi \leftrightarrow K$  misidentification has taken place. This  
 2289 is because the  $m_{\text{swap}}(Dh^\pm)$  mass that is calculated while assuming a swapped  
 2290 companion hypothesis and the nominal  $m_{\text{default}}(Dh^\pm)$  mass are correlated (it  
 2291 is always the case that  $m_{\text{swap}} > m_{\text{default}}$  for a  $\pi \rightarrow K$  misidentification ,for  
 2292 example). Thus, the assumptions of the sPlot method are not satisfied [?]. The  
 2293 correlation coefficient in the signal region is about 20% for simulated signal  
 2294 decays. In order to assess the potential impact, an alternative mass distribution

for  $(B^\pm \rightarrow D\pi^\pm) \rightarrow (B^\pm \rightarrow DK^\pm)$  cross-feed is derived that does not rely on sWeights. Instead of fitting  $B^\pm \rightarrow D\pi^\pm$  sample in the whole fit range and assigning sWeights before recalculating the  $B$  mass under the kaon companion hypothesis, the shape is obtained using  $B^\pm \rightarrow D\pi^\pm$  candidates in the signal region. This is possible because the  $B^\pm \rightarrow D\pi^\pm$  sample is very pure. The shapes are compared in Fig. 5.44 and are seen to be almost identical. Thus the sWeights do successfully subtract the contribution of combinatorial and partially reconstructed backgrounds in the default setup. The impact on the obtained  $CP$ -violation observables of using one or the other shape in the fits is negligible, and no further systematic uncertainty is assigned due to this effect.

### Using the same mass shapes in all Dalitz bins

The mass shapes obtained the first-stage fit where all Dalitz bins are combined, are used in each individual bin of the subsequent binned fit. However, there could be some variation in the shape over the  $D$ -decay phase space, due to correlations between the phase-space coordinates and particle kinematics. The potential effect is investigated in pseudoexperiments, where toy data sets are generated with alternative signal, crossfeed, and combinatorial-background shapes that are allowed to differ between bins, and fitted with the default shapes. The partially reconstructed background is treated in a separate study, because further physics effects contribute to bin-by-bin variation, as described in the following section.

The alternative signal and cross-feed mass shapes are fitted independently in each bin, following identical procedures to those outlined in Sections 5.4.1 and 5.4.2. Examples of the obtained shapes are compared in Figs. 5.45 and 5.46.

The shape of the combinatorial background can also vary over the  $D$  decay phase-space; for example will the relative amount of fake  $D$  candidates versus real  $D$  decays paired with a random bachelor certainly depend on the real  $D$  decay amplitude for a given phase-space region. The effect is investigated in the high  $B$ -mass sideband  $m_B \in [5600, 6500] \text{ MeV}/c^2$ , in which the  $m(Dh^\pm)$  distribution is fitted with a single exponential distribution, in bins of the Dalitz plot. The fits combine  $B^+$  and  $B^-$  candidates and merge bins  $+i$  and  $-i$ , and are carried out for both the *optimal* binning scheme of Fig. 2.7 (on page 21) and a *rectangular* binning scheme, shown in Fig. 5.42, which better captures continuous trends over the Dalitz plot. The study is done for  $D \rightarrow K_S^0 \pi^+ \pi^-$  only due to available statistics. The DD category of  $B^\pm \rightarrow D\pi^\pm$  decays has the largest statistics and shows the largest variation, and the fitted slopes for this channel are shown in Fig. 5.47. Two effects are visible: 1) there is some variation in the slope as a function of the Dalitz

bin, especially visible for the rectangular scheme, and 2) the exponential slope is larger in general in the high  $B$ -mass sideband. The latter effect does not pose a problem, since the employed exponential is found to provide an excellent fit in the default fit region. It does however need to be taken into account when deriving alternative, bin-dependent combinatorial slopes relevant for the default fit region. In order to do so, the alternative slope for bin  $i$  is defined

$$\alpha_{\text{default-range}}^i = \frac{\alpha_{\text{high-}m_B}^i}{\alpha_{\text{high-}m_B}^{\text{all-DP}}} \times \alpha_{\text{default-range}}^{\text{all-DP}}, \quad (5.25)$$

and used when generating the combinatorial-background component of the toy data sets for the study.

The average bias obtained for each observable in the ensemble of pseudo-experiments is assigned as a systematic uncertainty, found to be about  $0.1 \times 10^{-2}$  for each observable.

### Ignoring physics effects in the lowmass background

In the  $CP$  fit, the same relative fractions of partly reconstructed  $B^\pm$  and  $B^0$  backgrounds are used in each bin, as determined in the first-stage fit described in Section 5.4 (whereas the partly reconstructed  $B_s^0 \rightarrow \bar{D}^0[\pi^+]K^-$  background is treated separately). However the distribution over the Dalitz plot depends on whether the partly reconstructed decays occur via an intermediate  $D^0$  meson, a  $\bar{D}^0$  meson, or and admixture of both. Consider a decay reconstructed as  $B^- \rightarrow DK^-$  but which is actually a partially-reconstructed background. There are then four types of background that should be considered:

- Decays in which the  $D$ -meson in the true decay is a  $D^0$ -meson. An example of this is  $B^- \rightarrow D^{*0}(D^0\pi^0)\pi^-$  for which the  $\pi^0$  from the  $D^{*0}$  decay is missed and the  $\pi^-$  is misidentified as the companion  $K^-$ . These are denoted ' $D^0$ -like'<sup>5</sup>.
- Decays in which the  $D$ -meson in the true decay is a  $\bar{D}^0$ -meson. An example of this is  $B_s^0 \rightarrow \bar{D}^0\pi^+K^-$  for which the  $\pi^+$  is missed and the  $K^-$  is reconstructed as the companion  $K^-$ . These are denoted ' $\bar{D}^0$ -like'.
- Decays in which the  $D$  meson in the true decay can be either flavour, and both  $D$  flavours contribute to the decay amplitude. An example of this is  $B^- \rightarrow D^*K^-$  for which the total decay amplitude into a  $D$  final state has

---

<sup>5</sup>The naming convention is defined in terms of the  $D$  present in candidates reconstructed as  $B^-$  decays. For the charge conjugate case this decay would of course happen via a  $\bar{D}^0$ , but is still denoted  $D^0$ -like.

2360 contributions from both  $D^{*0}$  (decaying to  $D^0$ ) and  $\bar{D}^{*0}$  (decaying to  $\bar{D}^0$ ). The  
 2361 relative amplitude magnitude and phase between the two possible  $B$  decays  
 2362 are denoted  $r_B^{D^*}$  and  $\delta_B^{D^*}$  respectively. These are denoted ‘ $r_B$ -like’.

- 2363 • Decays that can be reconstructed as both  $D^0$ - and  $\bar{D}^0$ -like but where there is  
 2364 no quantum-mechanical interference. An example is  $\bar{B}^0 \rightarrow D^0\pi^+\pi^-$  decays  
 2365 where either the  $\pi^+$  or  $\pi^-$  can be reconstructed as the bachelor. These are  
 2366 denoted 50/50  $D^0$ -like and  $\bar{D}^0$ -like.

2367 For  $B^+ \rightarrow DK^+$  decays everything is CP conjugated. The Dalitz-plot distribution  
 2368 for each of these cases is:

- 2369 •  $D^0$  decays (‘ $D^0$ -like’)

$$\begin{aligned} N_{\pm i}(B^-) &\propto F_{\pm i} \\ N_{\pm i}(B^+) &\propto F_{\mp i} \end{aligned} \quad (5.26)$$

- 2370 •  $\bar{D}^0$  decays (‘ $\bar{D}^0$ -like’):

$$\begin{aligned} N_{\pm i}(B^-) &\propto F_{\mp i} \\ N_{\pm i}(B^+) &\propto F_{\pm i} \end{aligned} \quad (5.27)$$

- 2371 • Decays with a quantum-mechanical admixture of  $D^0$  and  $\bar{D}^0$  (‘ $r_B$ -like’):

$$\begin{aligned} N_{\pm i}(B^-) &\propto F_{\pm i} + (r_B^*)^2 F_{\mp i} + 2\sqrt{F_{+i}F_{-i}}[x_{\pm i}^*c_{\pm i} + y_{\pm i}^*s_{\pm i}] \\ N_{\pm i}(B^+) &\propto F_{\mp i} + (r_B^*)^2 F_{\pm i} + 2\sqrt{F_{+i}F_{-i}}[x_{\pm i}^*c_{\pm i} - y_{\pm i}^*s_{\pm i}] \end{aligned} \quad (5.28)$$

2372 where  $(x_{\pm i}^*, y_{\pm i}^*)$  are defined analogously to the standard  $B^\pm \rightarrow DK^\pm$  case.

- 2373 • 50/50  $D^0$ -like and  $\bar{D}^0$ -like:

$$\begin{aligned} N_{\pm i}(B^-) &\propto F_{\pm i} + F_{\mp i} \\ N_{\pm i}(B^+) &\propto F_{\pm i} + F_{\mp i} \end{aligned} \quad (5.29)$$

2374 The use of a single background shape across all bins may therefore introduce biases  
 2375 because, if an admixture of these backgrounds is present, such a shape has no  
 2376 sensitivity to bin-to-bin variations.

2377 In the  $D\pi$  channel, the dominant backgrounds are all  $D^0$ -like ( $\bar{B}^0 \rightarrow D^{*-}\pi^0$ ,  
 2378  $B^- \rightarrow D^0\rho^-$ ,  $B^- \rightarrow D^{*0}\pi^-$ ). There is a small contribution from  $\bar{B}^0 \rightarrow D^0\rho(\rightarrow$   
 2379  $\pi^+\pi^-)$  decays where either the  $\pi^+$  or  $\pi^-$  from the  $\rho^0$  decay can be assigned as the  
 2380 bachelor, and thus this background is 50/50  $D^0$ -like and  $\bar{D}^0$ -like. The background

only corresponds to about 0.5 % of the total partially reconstructed background and thus the impact is small. Nevertheless it is considered in the study described below.

In the  $DK$  channel all categories of background appear. In the mass region of the  $CP$  fit approximately 75.5% of backgrounds are  $D^0$ -like ( $\bar{B}^0 \rightarrow D^{*-} K^-$ , mis-identified  $B^- \rightarrow D^{*0} \pi^-$ , and mis-identified  $B^- \rightarrow D^0 \rho^-$ ), 7.5 % are  $\bar{D}^0$ -like ( $B_s^0 \rightarrow \bar{D}^0 \pi^+ K^-$ ), 1 % is 50/50  $D^0$ - $\bar{D}^0$ -like (mis-identified  $B^0 \rightarrow D \rho^0$ ), and 16% are  $r_B$ -like ( $B^- \rightarrow D^* K^-$ ,  $B^0 \rightarrow DK^{*0}$ , and  $B^- \rightarrow DK^{*-}$ ).

In order to estimate the bias due to ignoring this effect, a large number of toy data sets are generated using the default low mass shapes and total yields from the first-stage fit in Section 5.4, but distributing each of them individually over the Dalitz-bins according to Eqs. (5.26)-(5.28). When calculating the distribution of  $B^+ \rightarrow D^{*0} K^+$  decays over the Dalitz plot, the values [?]

$$r_B^{D^*} = 0.191 \quad \delta_B^{D^*} = 331.6^\circ \quad (5.30)$$

are used. When calculating the distribution of  $B^+ \rightarrow D^0 K^{*+}$  decays over the Dalitz plot the values [?]

$$r_B^{K^*} = 0.092 \quad \delta_B^{K^*} = 40^\circ. \quad (5.31)$$

are used. The toy data sets are then fit with the default set up, and the observed mean bias assigned as the corresponding uncertainty. The corresponding uncertainties were found to be about  $0.1 \times 10^{-2}$  for all uncertainties. The variation in the shapes is rather small in the mass range included in the fit, which explains the small impact.

If the  $B_s^0$  background is *not* treated separately in the default fit, but instead included in a single lowmass background shape along with the  $B^0$  and  $B^\pm$  contributions, the systematic uncertainty is an order of magnitude larger when evaluated as described above, and would be a dominating systematic. This motivates the separate treatment of the  $B_s^0$  background.

#### 5.6.4 $CP$ violation and material interaction of the $K_S^0$

A systematic uncertainty due to  $CP$ -violation effects and material interaction of the  $K_S^0$  is assigned using the results obtained in Section 4.3.7. In that section, the expected bias on all observables in a combined  $B^\pm \rightarrow Dh^\pm$  measurement was evaluated for the detector geometry and particle kinematics of the LHCb experiment. The calculation was made for  $(r_B^{DK^\pm/D\pi^\pm}, \delta_B^{DK^\pm/D\pi^\pm})$  values close to the world averages, and a number of  $\gamma$  values; the results were summarised in Fig. 4.8. The systematic uncertainty is taken to be the largest absolute bias observed for each parameter in the study. The largest uncertainty (on  $y_\xi^{D\pi}$  where it is  $0.46 \times 10^{-2}$ ) is still an order of magnitude smaller than the statistical uncertainty.

2415 **5.6.5 Impact of  $D$  mixing**

2416 The effect of  $D$ -mixing is not accounted for in the measurement, which leads to  
2417 a small bias. Earlier studies have shown this to lead to a sub-degree bias on  
2418 measurements of  $\gamma$  in  $B^\pm \rightarrow DK^\pm$  decays, in the case where the  $F_i$  parameters  
2419 are determined experimentally under the same experimental conditions as the  $\gamma$   
2420 measurement [?]. A number of pseudoexperiments are carried out to verify that this  
2421 is also the case for the combined  $DK^\pm$ – $D\pi^\pm$  setup employed in the thesis. They  
2422 are performed following the same procedure described in Section 5.6.4 for the case  
2423 of  $K_S^0$   $CP$  violation. The yields are calculated while taking  $D$  mixing into account,  
2424 using the mixing parameter values  $x = (0.39^{+0.11}_{-0.12})\%$  and  $y = (0.65^{+0.06}_{-0.07})\%$  [?],  
2425 and then fitted back assuming no  $D$  mixing. The biases are found to be small, as  
2426 expected, all of them smaller than  $0.05 \times 10^{-2}$ . The largest relative biases are on  
2427 the  $B^\pm \rightarrow D\pi^\pm$  parameters, but even for those the relative effect is less than 2%.  
2428 In agreement with Ref. [?], it is found that the biases increase with an order of  
2429 magnitude if the  $F_i$  parameters are fixed to the expected values with no  $D$ -mixing,  
2430 instead of being determined as part of the fit.

2431 **5.6.6 PID efficiencies**

2432 The uncertainty related to PID efficiencies is assessed by repeating the full two-stage  
2433 fit procedure a number of times, each time varying the PID efficiencies within  
2434 the uncertainties. The used uncertainty includes both a statistical and systematic  
2435 component, as described in detail in Section 5.1.3. The standard deviations of  
2436 the central values obtained for each observable are assigned as the systematic  
2437 uncertainty. The uncertainties come out below  $0.1 \times 10^{-2}$  for all observables.

2438 **5.6.7 Dalitz-coordinate resolution**

2439 There is a small systematic uncertainty related to Dalitz-plot-bin migration, where  
2440 the non-perfect resolution on the momentum measurement means that a candidate  
2441 is assigned to a different bin that it truly belongs to. This leads to non-negligible  
2442 net migration between bins that share a border in a region of phase space where  
2443 the amplitude varies rapidly. However, since the  $F_i$  are measured in the data  
2444 set, all leading order effects of migration are inherently taken into account. The  
2445 measurement is only sensitive to differences in migration between the  $DK^\pm$  and  
2446  $D\pi^\pm$  channels and the effect is small.

2447 The systematic uncertainty due to this effect is assigned using pseudoexperiments.  
2448 The study is made for the  $D \rightarrow K_S^0\pi^+\pi^-$  mode only, which is sufficient since it  
2449 completely dominates the overall sensitivity.

- 2450     1. Signal  $B^\pm \rightarrow DK^\pm$  and  $B^\pm \rightarrow D\pi^\pm$  decays are generated continuously over  
 2451     phase space, according to the expected distribution obtained with the latest  
 2452     amplitude model from the Belle collaboration [], assuming values of  $\gamma$  and  
 2453      $(r_B^{DK^\pm/D\pi^\pm}, \delta_B^{DK^\pm/D\pi^\pm})$  close to the current world averages.
- 2454     2. The Dalitz coordinates of each candidate are then smeared using the experi-  
 2455     ment resolution obtained in simulation. This is described further below.
- 2456     3. Finally, the generated candidates are binned and fitted back using the default  
 2457     setup.

2458     The resolution is obtained via simulation, by comparing the reconstructed  
 2459     phase-space coordinates with those calculated from the true momenta in samples of  
 2460     simulated  $D \rightarrow K_S^0\pi^+\pi^-$  decays. As can be seen in Fig. 5.48, the resolution is found  
 2461     to vary over phase space and the distribution of shifts has significant exponential  
 2462     tails. In order to take both effects into account, the smearing is done by shifting each  
 2463     generated decay with a realised coordinate shift in full simulation, for a simulated  
 2464     decay that took place at approximately the same place in the Dalitz plot. The  
 2465     shift is multiplied with 120 % to take into account that the resolution is generally  
 2466     better in simulation than data. If the shift results in Dalitz coordinates outside the  
 2467     kinematically allowed region, a different shift is applied randomly instead.

2468     The average bias seen in the pseudoexperiments is assigned as the systematic  
 2469     uncertainty. The uncertainties come out at about  $(0.1 - 0.2) \times 10^{-2}$  for all parameters.  
 2470     It is noted that for all four  $DK^\pm$  parameters the bias is towards a smaller value  
 2471     of  $r_B^{DK}$ ; this is to be expected, as bin migration washes out the asymmetries in  
 2472     different areas of the Dalitz plot.

### 2473     5.6.8 The fixed yield fractions

2474     A number of relative yields are fixed from efficiencies in simulation and branching  
 2475     fractions. In the  $DK^\pm$  modes, this is the case for all the relative yields of the  
 2476     partially reconstructed backgrounds, including partially reconstructed  $B \rightarrow D\pi[X]$   
 2477     decays where the pion is misidentified as a kaon, and the yield of the  $B_s^0 \rightarrow DK\pi$   
 2478     background relative to the  $B \rightarrow D\pi$  yield. In the  $B^\pm \rightarrow D\pi^\pm$  channel, the only fixed  
 2479     yield ratio is that of the partially reconstructed  $B^\pm \rightarrow D^{*0}(\rightarrow D\pi^0)\pi^\pm$  and  $B^0 \rightarrow$   
 2480      $D^{*\mp}(\rightarrow D\pi^\mp)\pi^\pm$  modes. The uncertainty on the observables due to uncertainties  
 2481     on these fixed fractions is assessed by repeating the two-stage fit procedure many  
 2482     times, each time shifting the yield ratios randomly within their uncertainties. The  
 2483     uncertainty on each observable is taken to be the standard deviation of the set of  
 2484     central values obtained in these fits. These are all smaller than  $0.1 \times 10^{-2}$ .

**Table 5.17:** Summary of systematic uncertainties due to backgrounds that are potentially present with a small yield, but not included in the mass fit.

All uncertainties are quoted with implicit: $\times 10^{-2}$						
Mode	$\sigma(x_-^{DK^\pm})$	$\sigma(y_-^{DK^\pm})$	$\sigma(x_+^{DK^\pm})$	$\sigma(y_+^{DK^\pm})$	$\sigma(x_\xi^{D\pi^\pm})$	$\sigma(y_\xi^{D\pi^\pm})$
$A_b^0$ backgrounds	0.04	0.05	0.04	0.06	0.08	0.13
$B \rightarrow D\mu\nu X$	0.04	0.07	0.04	0.05	0.10	0.11
$B^\pm \rightarrow D(\rightarrow K_S^0\pi\mu\nu)h^\pm$	0.00	0.03	0.02	0.02	0.00	0.00
Swapped tracks	0.10	0.13	0.12	0.08	0.00	0.01
Total	0.11	0.16	0.13	0.12	0.08	0.13

### 5.6.9 Systematic uncertainty due to backgrounds that are not modelled in fit

2487 There are a number of backgrounds that are expected to be present at a small  
2488 level, but which are not modelled in the fits to data because their impact on the fit  
2489 results is minimal. Instead, a systematic uncertainty is assigned. Each contribution  
2490 is described in the following sections and the related systematic uncertainties  
2491 are summarised in Table 5.17.

## 2492 Background from $\Lambda_b$ decays

This section considers the possible impact of the two potential backgrounds from  $\Lambda_b^0$  decays described in Section 5.4.3:  $\Lambda_b^0 \rightarrow D^0 p \pi^-$  decays where the pion is not included in the candidate reconstruction and the proton assigned as the companion, and  $\Lambda_b^0 \rightarrow \Lambda_c^+ (\rightarrow p K_S^0 \pi^+ \pi^-) \pi^-$  decays where a pion in the  $\Lambda_c^+$  decay is not reconstructed and the proton reconstructed as one of the  $D$  decay products. The impact of not including these in the default fit is assessed by generating toy data sets where the backgrounds are included in the generation step, which are then fitted back with the default model. The former background is distributed over the Dalitz plot as  $\bar{D}^0$ -like, cf. the terminology of Section 5.6.3, since a positive bachelor is produced along with a  $D^0$  meson. The latter is also distributed as  $\bar{D}^0$ -like in the study; the exact distribution is unknown, but a  $\bar{D}^0$ -like background is likely to have the largest effect and thus this is a conservative choice. The total yields are taken relative to the signal yields, using the yield ratios discussed in Section 5.4.3. The  $m(D h^\pm)$  distributions are obtained using simulated samples, produced with `RapidSim`. The mean biases come out to be less than  $0.1 \times 10^{-2}$  for each  $CP$ -violation observable, which is assigned as a systematic uncertainty.

2509 **Semi-leptonic backgrounds**

2510 The impact of remnant  $B \rightarrow D\mu\nu_\mu$  decays after requiring `isMuon=0` on the bachelor  
 2511 is assessed in pseudoexperiments. Toy datasets are generated where the background  
 2512 is added in the generation step, which are then fitted with the default model. The  
 2513 background yield relative to signal and the mass shape are obtained from a sample  
 2514 of fully simulated decays for conditions corresponding to the run conditions in  
 2515 2012. The obtained bias in the toys is assigned as the systematic uncertainties:  
 2516 it is below  $0.1 \times 10^{-2}$  for all parameters.

2517 The systematic uncertainty relating to the presence of  $D^0 \rightarrow K_S^0\pi^-\mu^+\nu_\mu$  is  
 2518 estimated by repeating the bias studies of Section 5.3.3, but scaling the background  
 2519 yields to 10% to take into account the lepton veto on the  $D$  decay products. All  
 2520 biases are less than  $0.05 \times 10^{-2}$  in this case.

2521 **Swapped tracks**

2522 There is a peaking background present from  $B^\pm \rightarrow D(\rightarrow K^\mp\pi^\pm)K_S^0\pi^\pm$  decays where  
 2523 the kaon is reconstructed as the companion and the  $K_S^0$  is assigned to the  $D$  decay.  
 2524 The yield of this background is determined to be 0.5% of the signal yield in the  
 2525  $B^\pm \rightarrow DK^\pm$  channel in Section 5.3.5. The potential impact from the presence  
 2526 of the background is estimated by

- 2527 1. Calculating the expected  $B^\pm \rightarrow D\pi^\pm$  and  $B^\pm \rightarrow DK^\pm$  signal yields in each  
 2528 bin for physics parameters similar to the world average values.
  - 2529 2. Then calculating the background bin yields in each  $B^\pm \rightarrow DK^\pm$  bin, using  
 2530 a total yield equal to 0.5% of the signal yield, and the bin distribution  
 2531 from simulated samples of  $B^\pm \rightarrow D(\rightarrow K^\mp\pi^\pm)K_S^0\pi^\pm$  decays, produced via  
 2532 `RapidSim`. The study is carried out for multiple simulated samples, including  
 2533 decays where the  $K_S^0\pi$  pair in the  $B$  decay originate in different  $K^*$  resonances  
 2534 (generated with `EvtGen` and the proper resonance-spin models), as well as  $B$   
 2535 decays that are evenly distributed over the allowed phase space.
  - 2536 3. For each sample, the signal and background yields are added, and the new  
 2537  $B^\pm \rightarrow D\pi^\pm$  and  $B^\pm \rightarrow DK^\pm$  yields are fitted back with the default signal-  
 2538 yield expressions (including a fit of the  $F_i$  parameters).
- 2539 For each parameter, the most significant bias seen across the different `RapidSim`  
 2540 samples is taken as the related systematic uncertainty. The uncertainty is below  
 2541  $0.15 \times 10^{-2}$  for all parameters.

**Table 5.18:** Biases observed with alternative input parameters and the systematic uncertainty assigned for the bias correction. All numbers are quoted with an implicit  $\times 10^{-2}$ .

Input ( $\gamma, r_B^{DK^\pm}, \delta_B^{DK^\pm}, r_B^{D\pi^\pm}, \delta_B^{D\pi^\pm}$ )	$x_-^{DK^\pm}$	$y_-^{DK^\pm}$	$x_+^{DK^\pm}$	$y_+^{DK^\pm}$	$x_\xi^{D\pi^\pm}$	$y_\xi^{D\pi^\pm}$
(72, 0.080, 117, 0.005, 288)	-0.02	-0.01	-0.02	-0.02	0.03	0.00
(75, 0.100, 130, 0.005, 300)	-0.03	-0.04	-0.00	0.02	0.01	-0.03
(82, 0.112, 144, 0.005, 330)	0.00	-0.01	0.00	0.03	-0.03	0.02
(71, 0.099, 129, 0.005, 300)	-0.02	-0.04	-0.00	-0.00	0.05	-0.00
Syst. uncertainty	0.04	0.03	0.02	0.04	0.09	0.05

### 2542 5.6.10 Bias correction

2543 In the default sensitivity study, the bias was found to be compatible with zero.  
 2544 However, the size of a potential bias can vary depending on the input parame-  
 2545 ters. The size of the bias has been investigated with alternate input values of  
 2546  $(\gamma, r_B^{DK^\pm}, \delta_B^{DK^\pm}, r_B^{D\pi^\pm}, \delta_B^{D\pi^\pm})$ , obtaining the results in Table 5.18. A systematic  
 2547 uncertainty due to a potential, small bias is calculated as the difference between  
 2548 the maximum and minimum bias for a given parameter. The uncertainty assigned  
 2549 in this way is very small in general, and less than  $0.1 \times 10^{-2}$  for all parameters.

### 2550 5.6.11 Charmless backgrounds

2551 As discussed in Section 5.3.1, a small number of charmless background decays  
 2552 survive the  $D$  flight distance cut. In this section the systematic uncertainty related  
 2553 to those is assessed, in a series of pseudoexperiments. Toy datasets are generated,  
 2554 where a charmless background component is included, using the yields and shapes  
 2555 obtained in the studies of Section 5.3.1. The Dalitz-bin distribution is obtained  
 2556 by repeating the fits of that section for each bin individually. These datasets are  
 2557 subsequently fitted back using the default model, which does not include a charmless  
 2558 component. No statistically significant bias is observed.

2559 The study described above does not allow for charge-asymmetries in the charmless  
 2560 backgrounds, in terms of overall yields and phase-space distributions. These  
 2561 asymmetries are likely to be present, due to large local  $CP$ -violation in regions  
 2562 of phase space in  $B^\pm$  decays to hadrons []. The yields in the data-driven studies  
 2563 of Section 5.3.1 are not large enough to assess asymmetries, let alone asymmetric  
 2564 bin distributions with any degree of statistical precision. Instead, an extreme-case  
 2565 scenario is investigated, where *all* the charmless background is added to either the  $B^+$   
 2566 or  $B^-$  data sample in generation. In both cases, no statistically significant biases are  
 2567 observed, and it is concluded that the impact of charmless background is negligible.

**Table 5.19:** Overview of all sources of uncertainty on the measurement.

Source	All uncertainties are quoted with implicit: $\times 10^{-2}$					
	$\sigma(x_-^{DK^\pm})$	$\sigma(y_-^{DK^\pm})$	$\sigma(x_+^{DK^\pm})$	$\sigma(y_+^{DK^\pm})$	$\sigma(x_\xi^{D\pi^\pm})$	$\sigma(y_\xi^{D\pi^\pm})$
Statistical	0.96	1.14	0.96	1.20	1.99	2.34
Strong-Phase inputs	0.23	0.35	0.18	0.28	0.14	0.18
Efficiency correction of ( $c_i, s_i$ )	0.11	0.05	0.05	0.10	0.08	0.09
Mass-shape parameters	0.05	0.08	0.03	0.08	0.16	0.17
Mass-shape bin dependence	0.05	0.07	0.04	0.08	0.07	0.09
Lowmass physics effects	0.04	0.10	0.15	0.05	0.10	0.09
$CP$ violation of $K_S^0$	0.03	0.04	0.08	0.08	0.09	0.46
$D$ mixing	0.04	0.01	0.00	0.02	0.02	0.01
PID efficiencies	0.03	0.03	0.01	0.05	0.02	0.02
Fixed yield ratios	0.05	0.06	0.03	0.06	0.02	0.02
Dalitz-bin migration	0.04	0.08	0.08	0.11	0.18	0.10
Bias correction	0.04	0.03	0.02	0.04	0.09	0.05
Small backgrounds	0.11	0.16	0.13	0.12	0.08	0.13
Total LHCb systematic	0.20	0.25	0.24	0.26	0.32	0.54
Total systematic	0.31	0.43	0.30	0.38	0.35	0.57

### 5.6.12 Summary of systematic uncertainties

The complete set of included systematic uncertainties are summarised in Table 5.19. It can be seen that the measurement is statistically limited. The correlation matrix pertaining to the LHCb related systematics is given in Table 5.20. For studies where the systematic uncertainty is obtained by repeating fits to data multiple times while varying some input, the correlation matrix from the correlations of the fitted central values. For studies that are based on generating a large number of toy datasets and determining the average bias, the correlation of a systematic on two observables is taken to be +100 % if the biases are in the same direction, and -100 % if they are in opposite directions. The total systematic correlation matrix, including both LHCb-related systematics and that of the strong-phase inputs, is given in Table 5.21. The studies described in this section also allow for an estimate of the systematic uncertainties on the  $\mathcal{R}_i$  parameters of Eq. (5.20) or, equivalently the  $F_i$  parameters, in a completely analogous manner to how the uncertainty on the  $CP$ -violation observables was assigned. In all cases, however, the systematic uncertainty is found to be much smaller than the statistical uncertainties that were given in Table 5.10. The central values, statistical, and systematic uncertainties of the  $\mathcal{R}_i$  parameters have been made public in Ref. [?] because they can be employed in future LHCb measurements, as discussed in Section 5.5.2.

**Table 5.20:** Total LHCb-related systematic uncertainties and their correlation matrix.

Uncertainty ( $\times 10^{-2}$ )						
	$x_-^{DK\pm}$	$y_-^{DK\pm}$	$x_+^{DK\pm}$	$y_+^{DK\pm}$	$x_\xi^{D\pi\pm}$	$y_\xi^{D\pi\pm}$
$\sigma$	0.20	0.25	0.24	0.26	0.32	0.54

Correlations						
	$x_-^{DK\pm}$	$y_-^{DK\pm}$	$x_+^{DK\pm}$	$y_+^{DK\pm}$	$x_\xi^{D\pi\pm}$	$y_\xi^{D\pi\pm}$
$x_-^{DK\pm}$	1.000	0.864	0.734	0.897	0.349	0.318
$y_-^{DK\pm}$		1.000	0.874	0.903	0.408	0.362
$x_+^{DK\pm}$			1.000	0.771	0.563	0.447
$y_+^{DK\pm}$				1.000	0.507	0.451
$x_\xi^{D\pi\pm}$					1.000	0.484
$y_\xi^{D\pi\pm}$						1.000

**Table 5.21:** Total systematic uncertainties and their correlation matrix, including contributions due to strong-phase inputs as well as LHCb-related uncertainties.

Uncertainty ( $\times 10^{-2}$ )						
	$x_-^{DK\pm}$	$y_-^{DK\pm}$	$x_+^{DK\pm}$	$y_+^{DK\pm}$	$x_\xi^{D\pi\pm}$	$y_\xi^{D\pi\pm}$
$\sigma$	0.31	0.43	0.30	0.38	0.35	0.57

Correlations						
	$x_-^{DK\pm}$	$y_-^{DK\pm}$	$x_+^{DK\pm}$	$y_+^{DK\pm}$	$x_\xi^{D\pi\pm}$	$y_\xi^{D\pi\pm}$
$x_-^{DK\pm}$	1.000	0.301	0.156	0.576	0.265	0.231
$y_-^{DK\pm}$		1.000	0.437	0.218	0.183	0.170
$x_+^{DK\pm}$			1.000	0.445	0.414	0.310
$y_+^{DK\pm}$				1.000	0.353	0.243
$x_\xi^{D\pi\pm}$					1.000	0.502
$y_\xi^{D\pi\pm}$						1.000

## 5.7 Obtained constraints on $\gamma$

The measured values of  $(x_\pm^{DK}, y_\pm^{DK}, x_\xi^{D\pi}, y_\xi^{D\pi})$  can be used to put constraints on the possible values of the CKM angle  $\gamma$  and the hadronic nuisance parameters  $r_B^{DK\pm}$ ,  $\delta_B^{DK\pm}$ ,  $r_B^{D\pi\pm}$ , and  $\delta_B^{D\pi\pm}$ . This is handled using the `gammacombo` package, which is also used to combine all measurements of  $\gamma$  made by the LHCb collaboration [].

2592 **5.7.1 Statistical approach**

2593 The optimal central values determined in a maximum likelihood fit. The set of  
2594 all observables for which a measurement has been made is denoted  $A$ , and the set  
2595 of underlying physics parameters is denoted  $\theta$ . The physics parameters of course  
2596 determine the probability density function of measurement results of  $A$ ,  $f(A|\theta)$ .  
2597 Given a specific set of measurement results,  $A_{\text{obs}}$ , a likelihood function is defined

$$\mathcal{L}(\theta|A_{\text{obs}}) = f(A_{\text{obs}}|\theta) \quad (5.32)$$

2598 and the estimate of  $\theta$  is the set of parameters that maximize the likelihood

$$\hat{\theta} = \arg \max_{\theta} \mathcal{L}(\theta|A_{\text{obs}}). \quad (5.33)$$

2599 In practice, a  $\chi^2$  function is defined

$$\chi^2(\theta|A_{\text{obs}}) = -2 \ln \mathcal{L}(\theta|A_{\text{obs}}) \quad (5.34)$$

2600 and minimized instead. In the specific case where the likelihood profile is Gaussian,  
2601 it is given by the simple expression

$$\chi^2(\theta|A_{\text{obs}}) = (A_{\text{obs}} - A(\theta))^T \Sigma_{A_{\text{obs}}}^{-1} (A_{\text{obs}} - A(\theta)) + c, \quad (5.35)$$

2602 where  $\Sigma_{A_{\text{obs}}}$  is the covariance matrix for the measured observables,  $A(\theta)$  denotes the  
2603 value of the observables expressed in terms of the underlying physics parameters,  
2604 and  $c$  is a constant that is independent of  $\theta$ . In the specific case considered here

$$\begin{aligned} A &= (x_-^{DK}, y_-^{DK}, x_+^{DK}, y_+^{DK}, x_\xi^{D\pi}, y_\xi^{D\pi}) \\ \theta &= (\gamma, r_B^{DK\pm}, \delta_B^{DK\pm}, r_B^{D\pi\pm}, \delta_B^{D\pi\pm}). \end{aligned} \quad (5.36)$$

2605 The likelihood scan presented in Section ?? proved that the Gaussian expression  
2606 in Eq. (5.35) provides an excellent description of the likelihood profile of the  
2607 measurement, when  $\Sigma_{A_{\text{obs}}}$  is taken to be the covariance matrix obtained in that  
2608 section. Thus, the  $\chi^2$  function defined in Eq. (5.35) is minimised to determine  
2609 the best estimate of  $\gamma$ .

2610 Two different methods are employed to construct confidence regions for the  
2611 observables of interest, known within the `gammacombo` framework as the PROB and  
2612 PLUGIN methods. Both methods aim to construct confidence regions for some  
2613 subset,  $\phi$ , of the full parameter set  $\theta$ . The remaining parameters, dubbed nuisance  
2614 parameters below, are denoted  $\eta = \theta \setminus \phi$ . In practice,  $\phi$  most often denotes a single  
2615 parameter, and of special interest is of course the case where  $\phi = \gamma$ . Both methods  
2616 aim to solve the problem that due to the number of parameters in  $\theta$  (six in the case

2617 considered here, but up to X in the latest LHCb combination []), it is not feasible  
 2618 to derive the confidence regions from a full-fledged Neumann construction []. Under  
 2619 assumptions discussed below, the methods achieve reasonable coverage nonetheless,  
 2620 ie. had the measurement been repeated many times, the confidence region is  
 2621 expected to cover the true parameter(s) with a probability at least at large as  
 2622 the quoted confidence level (CL), independently of the true parameter value. The  
 2623 presentation follows the `gammacombo` manual [].

2624 The `PROB` method is a simple profile-likelihood method. The minimum value  
 2625 of the  $\chi^2$  function is denoted  $\chi_{\min}^2 \equiv \chi^2(\hat{\theta}|A_{\text{obs}})$ . To evaluate the CL for a specific  
 2626 value (set of values) of  $\phi_0$ , the  $\chi^2$  function is again minimised, this time under  
 2627 the constraint that  $\phi = \phi_0$ , resulting in a new minimum  $\hat{\theta}' = (\phi_0, \hat{\eta}')$ . In the  
 2628 approximation that all likelihoods are exactly Gaussian, the variable

$$\Delta\chi^2(\phi_0|A_{\text{obs}}) = \chi^2(\hat{\theta}'|A_{\text{obs}}) - \chi_{\min}^2 \quad (5.37)$$

2629 follows a  $\chi^2$  distribution with  $n$  degrees of freedom, where  $n$  is the number of  
 2630 parameters in  $\phi$  [?]. This can be used to evaluate CL at that point as

$$CL(\phi_0|A_{\text{obs}}) = F_n(\Delta\chi^2(\phi_0|A_{\text{obs}})) \quad (5.38)$$

2631 where  $F_n$  is the cumulative distribution function of a  $\chi^2$  distribution with  $n$  degrees  
 2632 of freedom. The method takes its colloquial name from the fact that this function  
 2633 is named `Prob` in the `ROOT` package. Confidence regions can be defined by scanning  
 2634 the values of  $\phi_0$  over a region of interest. These confidence regions assume that  
 2635 the estimates  $\hat{\theta}$  follow a Gaussian distribution centred on the true values, which is  
 2636 generally the case for maximum likelihood estimates in large samples []; in other  
 2637 cases they may not have good coverage properties. Given the Gaussian shape  
 2638 obtained in the likelihood scan of Section ?? the confidence regions are likely to  
 2639 be well behaved in the case considered here.

2640 However, for the purpose of comparing to the combination of several LHCb  
 2641 measurements in Section 5.5.3 below, the `PLUGIN` method is necessary. It foregoes  
 2642 the assumption that  $\Delta\chi^2$  follows a  $\chi^2$  distribution, and instead estimates the  
 2643 distribution in a bootstrapping scheme. The procedure is as follows: the values  
 2644 of  $\hat{\theta}$ ,  $\hat{\theta}'$ , and  $\Delta\chi^2(\phi_0|A_{\text{obs}})$  are determined as described above; then the following  
 2645 steps are carried out a number,  $N_{\text{toys}}$ , of times

- 2646 1. Generate a "toy" result,  $A_{\text{toy}}^i$ , following the distribution  $f(A|\hat{\theta}')$
- 2647 2. Determine  $\Delta\chi^2(\phi_0|A_{\text{toy}}^i)$  by minimising the  $\chi^2$  function for the results  $A_{\text{toy}}^i$   
 2648 twice, once where all parameters in  $\theta$  are free, and once where  $\phi = \phi_0$  is  
 2649 enforced

2650 Then the CL is defined by

$$CL(\phi_0) = 1 - \frac{N(\Delta\chi^2(\phi_0|A_{\text{obs}}) < \Delta\chi^2(\phi_0|A_{\text{toy}}^i))}{N_{\text{toys}}}. \quad (5.39)$$

2651 The method is described in Ref. [?], based on the hybrid resampling method pre-  
2652 sented in [?, ?]. While the coverage properties are not proven, evidence is presented  
2653 in terms of asymptotic results and simulation studies in those references. The  
2654 coverage properties have also been investigated in relation to LHCb combinations,  
2655 and the intervals were found to perform well in most cases [].

### 2656 5.7.2 Interpretation results

2657 The central values and confidence regions obtained for the physics parameters are

$$\begin{aligned} \gamma &= (68.7^{+5.2}_{-5.1})^\circ, \\ r_B^{DK^\pm} &= 0.0904^{+0.0077}_{-0.0075}, \\ \delta_B^{DK^\pm} &= (118.3^{+5.5}_{-5.6})^\circ, \\ r_B^{D\pi^\pm} &= 0.0050^{+0.0017}_{-0.0017}, \\ \delta_B^{D\pi^\pm} &= (291^{+24}_{-26})^\circ, \end{aligned} \quad (5.40)$$

2658 where the quoted uncertainties are obtained via the PLUGIN method. The one-  
2659 dimensional CL plots are shown in Fig. 5.49. It is also clear that the PROB and  
2660 PLUGIN confidence regions agree well; this is expected given the Gaussian likelihood.  
2661 A series of two-dimensional confidence regions are shown in Fig. 5.50, where it  
2662 can be seen that the observables define a single solution for  $\gamma$  as expected. It  
2663 is worth noticing that the uncertainty of this measurement alone is on par with  
2664 the current world average, due to the increased data sample, and the significant  
2665 reduction of systematic uncertainties due to the new measurement strategy and  
2666 updated inputs from BESIII.

2667 The contribution to the uncertainty on  $\gamma$  from each of the statistical, strong-  
2668 phase-related, and LHCb-related uncertainties in isolation can be estimated by  
2669 repeating the interpretation while only including subsets of the uncertainties on  
2670 the input parameters. Such studies have been performed using the PROB method.  
2671 Running with statistical uncertainties only yields an uncertainty on  $\gamma$  of  $5.05^\circ$ .  
2672 Including only the statistical and LHCb-related systematic uncertainties yields an  
2673 uncertainty on  $\gamma$  of  $5.08^\circ$ , suggesting that the LHCb-related systematics contribute  
2674 an uncertainty of  $0.6^\circ$ . This is a reduction compared to earlier analyses, where  
2675 the contribution was about  $2^\circ$ . A significant contribution to the improvement is  
2676 the efficiency-related systematic that has been avoided by promoting  $B^\pm \rightarrow D\pi^\pm$

2677 to a signal channel. Including only the statistical and the strong-phase-related  
 2678 uncertainties leads to an uncertainty on  $\gamma$  of  $5.09^\circ$ , showing the strong-phase-related  
 2679 uncertainty to be  $0.6^\circ$ , somewhat lower than the expectation of  $1.2^\circ$  presented in  
 2680 Ref. [?]. This is partly because the uncertainty estimate of that paper does not  
 2681 take into account the use of the  $D \rightarrow K_S^0 K^+ K^-$  channel, and partly because the  
 2682 uncertainty estimate depends on the specific central values.

2683 The obtained statistical uncertainty on  $\gamma$  is in excellent agreement with the  
 2684 expectation from pseudoexperiments. The interpretation procedure outlined above  
 2685 has been performed for each of the pseudoeexperiments performed to establish the  
 2686 feasibility of the  $CP$  fit in Section 5.5.1 (including only statistical uncertainties on the  
 2687 observables) and the central 90 % interval of the obtained uncertainties is  $[4.4^\circ, 6.0^\circ]$ .  
 2688 Similar studies have been carried out where no background decays are included in the  
 2689 generated toy data sets. In this case, the precision on  $\gamma$  is improved by about 30 %.

### 2690 5.7.3 Compatibility with other measurements

2691 It is worth comparing the obtained constraints on the physics parameters with the  
 2692 information available from other measurements, made at the  $B$  factories and by  
 2693 the LHCb collaboration using other decay channels. This comparison is made for  $\gamma$   
 2694 and the hadronic parameters in the  $B^\pm \rightarrow DK^\pm$  decay in Fig. 5.51, comparing to  
 2695 the results of the combinations of  $\gamma$  measurements by the Belle [?] and BaBar [?]  
 2696 collaborations presented in 2013, and the 2018 combination of LHCb results [?].  
 2697 For this purpose, the LHCb combination is re-performed, removing the input from  
 2698 earlier BPGGSZ measurements that use  $B^\pm \rightarrow DK^\pm$  decays, because they were  
 2699 made using data that is re-analysed in the present thesis; thus they need to be  
 2700 excluded to make the results that are compared independent. The combination  
 2701 employs the same statistical method outlined above, with the exception that the  
 2702 likelihood now depends on observables measured in a number of different analyses.  
 2703 The included measurements are summarised in Table ???. It can be seen in Fig. 5.51  
 2704 that the results obtained in this thesis agree well with the Belle and BaBar results,  
 2705 but are in some tension with the 2018 LHCb combination.

2706 The level of compatibility can be quantified by calculating the three-dimensional  
 2707  $\chi^2$  of the BPGGSZ results and those of the LHCb combination (without the earlier  
 2708 BPGGSZ measurements), with respect to the best fit values of  $(\gamma, r_B^{DK^\pm}, \delta_B^{DK^\pm})$   
 2709 when all measurements are combined. The two-dimensional confidence regions  
 2710 obtained in these three cases are compared in Fig. 5.52, where the tension in  $r_B^{DK^\pm}$   
 2711 and  $\delta_B^{DK^\pm}$  is visible again. The calculation is based on the PLUGIN uncertainties; for  
 2712 the LHCb combination these uncertainty estimates are slightly larger than the ones

**Table 5.22:** List of the LHCb measurements used in the combination that the results obtained in the present thesis is compared to. These correspond to the 2018 LHCb combination [?], except that the earlier BPGGSZ results made with  $B^\pm \rightarrow DK^\pm$  decays have not been included in the comparison. In the method column, TD stands for "time-dependent".

$B$ decay	$D$ decay	Method	Ref.	Data set
$B^+ \rightarrow DK^+$	$D \rightarrow h^+h^-$	GLW	[?]	2011-16
$B^+ \rightarrow DK^+$	$D \rightarrow h^+h^-$	ADS	[?]	2011-12
$B^+ \rightarrow DK^+$	$D \rightarrow h^+\pi^-\pi^+\pi^-$	GLW/ADS	[?]	2011-12
$B^+ \rightarrow DK^+$	$D \rightarrow h^+h^-\pi^0$	GLW/ADS	[?]	2011-12
$B^+ \rightarrow DK^+$	$D \rightarrow K_S^0K^+\pi^-$	GLS	[?]	2011-12
$B^+ \rightarrow D^*K^+$	$D \rightarrow h^+h^-$	GLW	[?]	2011-16
$B^+ \rightarrow DK^{*+}$	$D \rightarrow h^+h^-$	GLW/ADS	[?]	2011-16
$B^+ \rightarrow DK^{*+}$	$D \rightarrow h^+\pi^-\pi^+\pi^-$	GLW/ADS	[?]	2011-16
$B^+ \rightarrow DK^+\pi^+\pi^-$	$D \rightarrow h^+h^-$	GLW/ADS	[?]	2011-12
$B^0 \rightarrow DK^{*0}$	$D \rightarrow K^+\pi^-$	ADS	[?]	2011-12
$B^0 \rightarrow DK^+\pi^-$	$D \rightarrow h^+h^-$	GLW-Dalitz	[?]	2011-12
$B^0 \rightarrow DK^{*0}$	$D \rightarrow K_S^0\pi^+\pi^-$	BPGGSZ	[?]	2011-12
$B_s^0 \rightarrow D_s^\mp K^\pm$	$D_s^\pm \rightarrow h^+h^-\pi^+$	TD	[?]	2011-12
$B^0 \rightarrow D^\mp\pi^\pm$	$D^\pm \rightarrow K^+\pi^-\pi^+$	TD	[?]	2011-12
Measurements included in Ref. [?] but not in the present comparison				
$B^+ \rightarrow DK^+$	$D \rightarrow K_S^0h^+h^-$	BPGGSZ	[?]	2011-12
$B^+ \rightarrow DK^+$	$D \rightarrow K_S^0h^+h^-$	BPGGSZ	[?]	2015-16

2713 obtained via the PROB method. One obtains  $\chi^2 = \chi_{\text{GGSZ}}^2 + \chi_{\text{LHCb}}^2 = 0.7 + 9.1 = 9.8$ ,  
 2714 which for 3 degrees of freedom correspond to a  $p$ -value of 2 %, or a  $2.3\sigma$  deviation.  
 2715 However, this tension is expected to be reduced when other measurements in the  
 2716 LHCb combination are updated to include results based on the full Run 1 and 2 data  
 2717 set. The most important update is that of the two-body ADS/GLW measurement  
 2718 in  $B^\pm \rightarrow DK^\pm$  decays because that measurement, and the BPGGSZ measurement  
 2719 presented in this thesis, have the largest impact in the combination.

2720 The latest LHCb combination in which  $B^\pm \rightarrow D\pi^\pm$  parameters were determined  
 2721 is from 2016 [?]. Two solutions existed for  $(r_B^{D\pi^\pm}, \delta_B^{D\pi^\pm})$  which made the interpreta-  
 2722 tion problematic. As can be seen in Fig. 5.53 the measurement presented in this  
 2723 thesis picks out one of these solutions, with which it is in excellent agreement. This

<sup>2724</sup> solution agrees with the theoretically expected value of  $r_B^{D\pi^\pm} \sim 0.005$  [?]. Thus, the  
<sup>2725</sup> inclusion of the results presented here are expected to lead to a much less problematic  
<sup>2726</sup> inclusion of results from the  $B^\pm \rightarrow D\pi^\pm$  channel in future LHCb combinations.

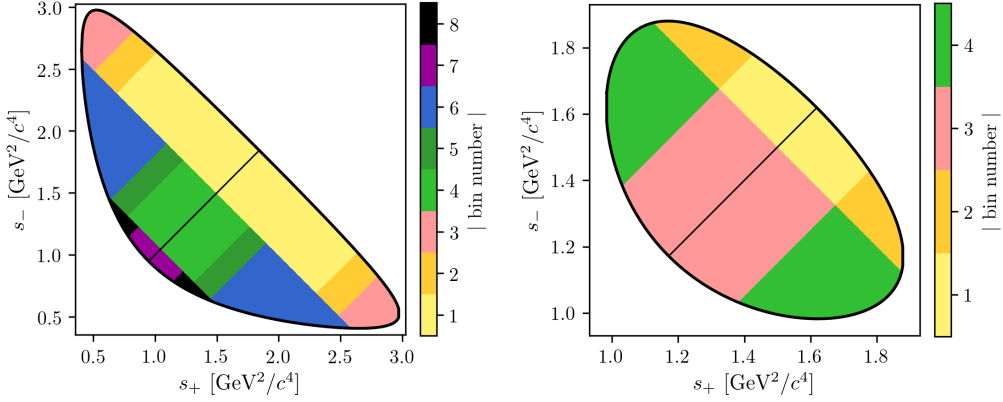


**Figure 5.42:** The rectangular binning schemes used to group candidates in (left) the  $D \rightarrow K_S^0\pi^+\pi^-$  and (right) the  $D \rightarrow K_S^0K^+K^-$  categories in a number of systematic uncertainty studies.

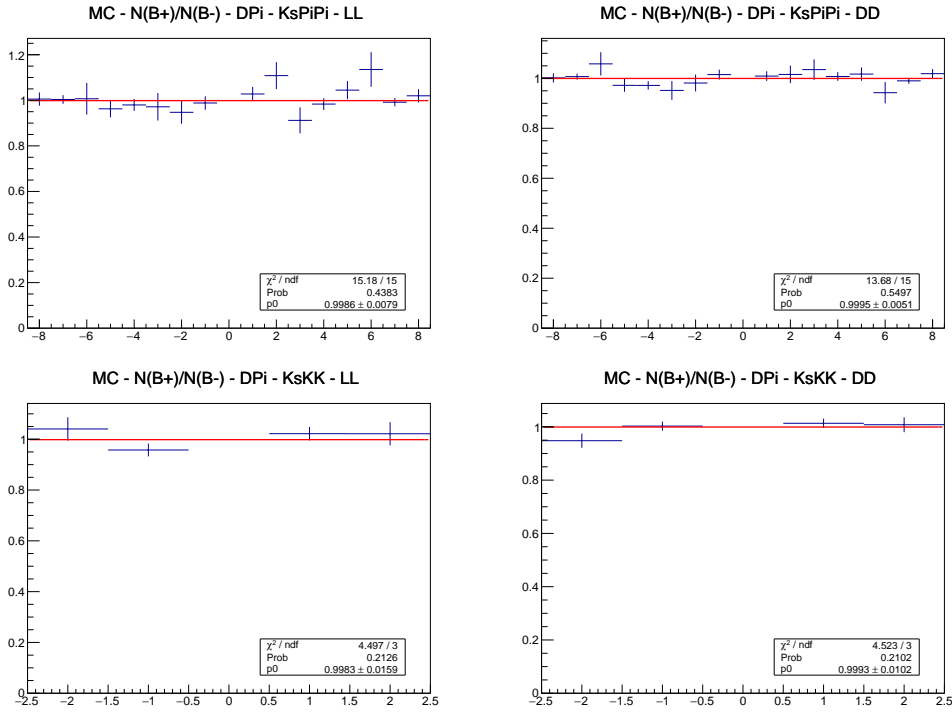


**Figure 5.43:** Comparison of the ratio of  $B^-$  decays reconstructed in bin  $+i$  to  $B^+$  decays reconstructed in bin  $-i$  for simulated  $B^\pm \rightarrow D\pi^\pm$  decays where (top)  $D \rightarrow K_S^0\pi^+\pi^-$  and (bottom)  $D \rightarrow K_S^0K^+K^-$ , also split into (left) the LL and (right) the DD categories. Calculated  $p$  values for the hypothesis that the ratio is flat are also shown, all of them being at least 20 %.

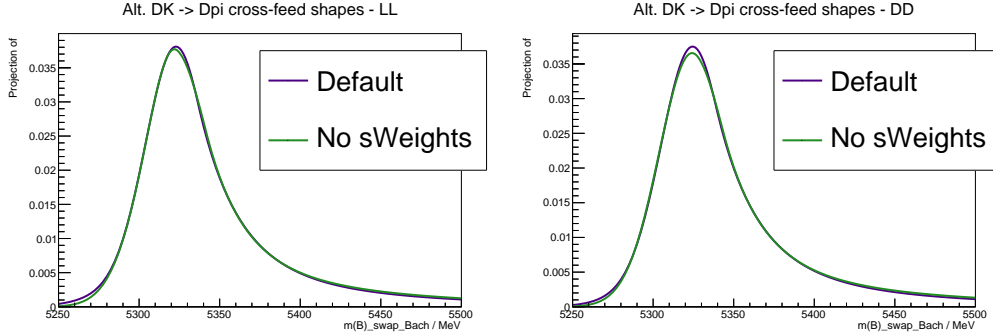


**Figure 5.44:** Comparison of the default and no-sWeights alternative shape for the  $D\pi \rightarrow DK$  cross-feed component in the (left) LL and (right) DD categories where  $D \rightarrow K_S^0\pi^+\pi^-$ . The binned fit obtains essentially the same central values for the  $CP$ -violation observables, independently of which shape is used.

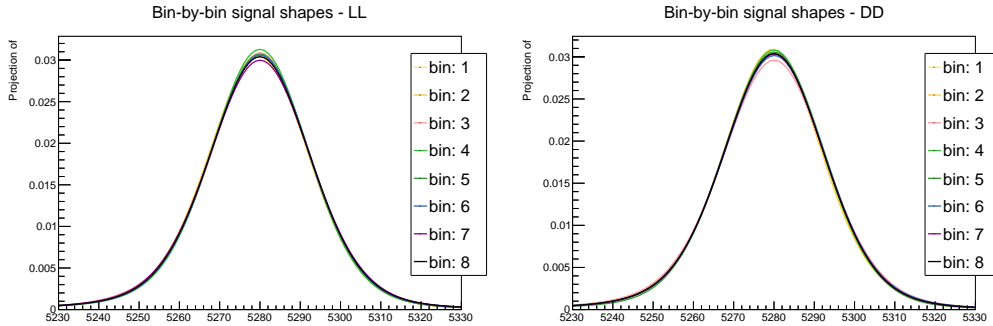


**Figure 5.45:** Signal shapes obtained in MC for individual Dalitz bins in the optimal binning scheme, for (left) LL and (right) DD candidates in the  $B^\pm \rightarrow D(\rightarrow K_S^0\pi^+\pi^-)\pi^\pm$  category.

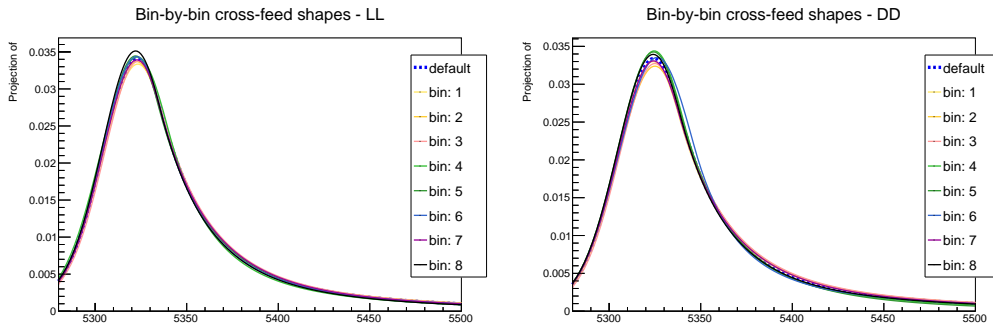


**Figure 5.46:** Mass shapes for  $D\pi \rightarrow DK$  cross feed obtained for individual Dalitz bins in the optimal binning scheme, for (left) LL and (right) DD candidates in the  $D \rightarrow K_S^0\pi^+\pi^-$  category.

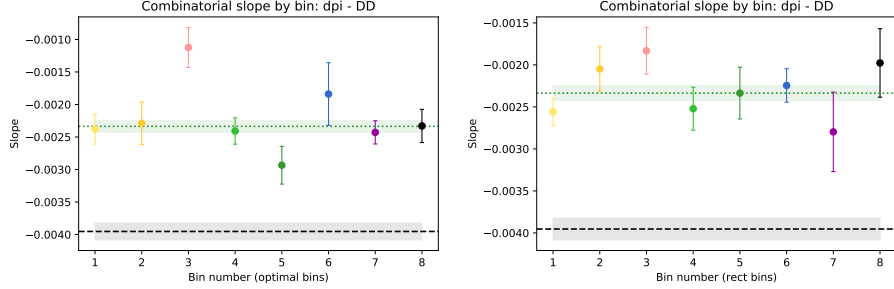


**Figure 5.47:** Plot of (dots) combinatorial slope in the high  $B$  mass background for each bin in the (left) the optimal binning scheme and (right) the rectangular binning scheme, for the DD  $B^\pm \rightarrow D(\rightarrow K_S^0\pi^+\pi^-)\pi^\pm$  category. The slope when all bins are combined (green, dashed line) is also shown, and compared with (black dashed line) the slope in the default fit region.

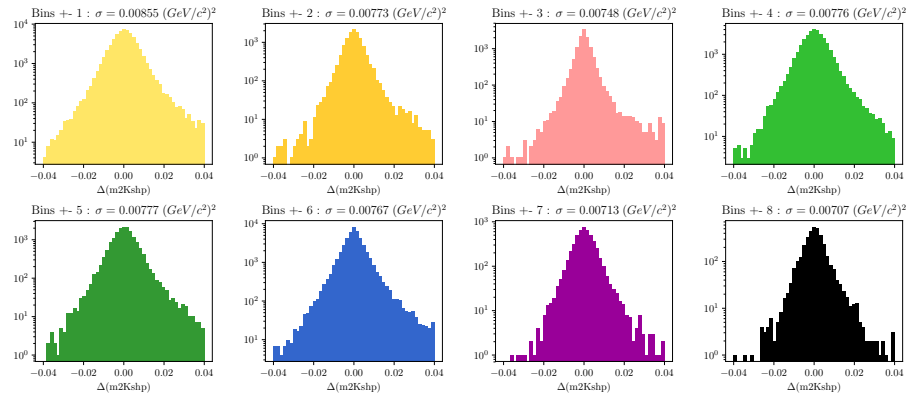


**Figure 5.48:** Distribution of the biases  $\Delta(m^2) = m_{true}^2 - m_{reconstructed}^2$  in simulation for  $m^2(K_S^0\pi^+)$  in bins of the rectangular binning scheme of Fig. 5.42.

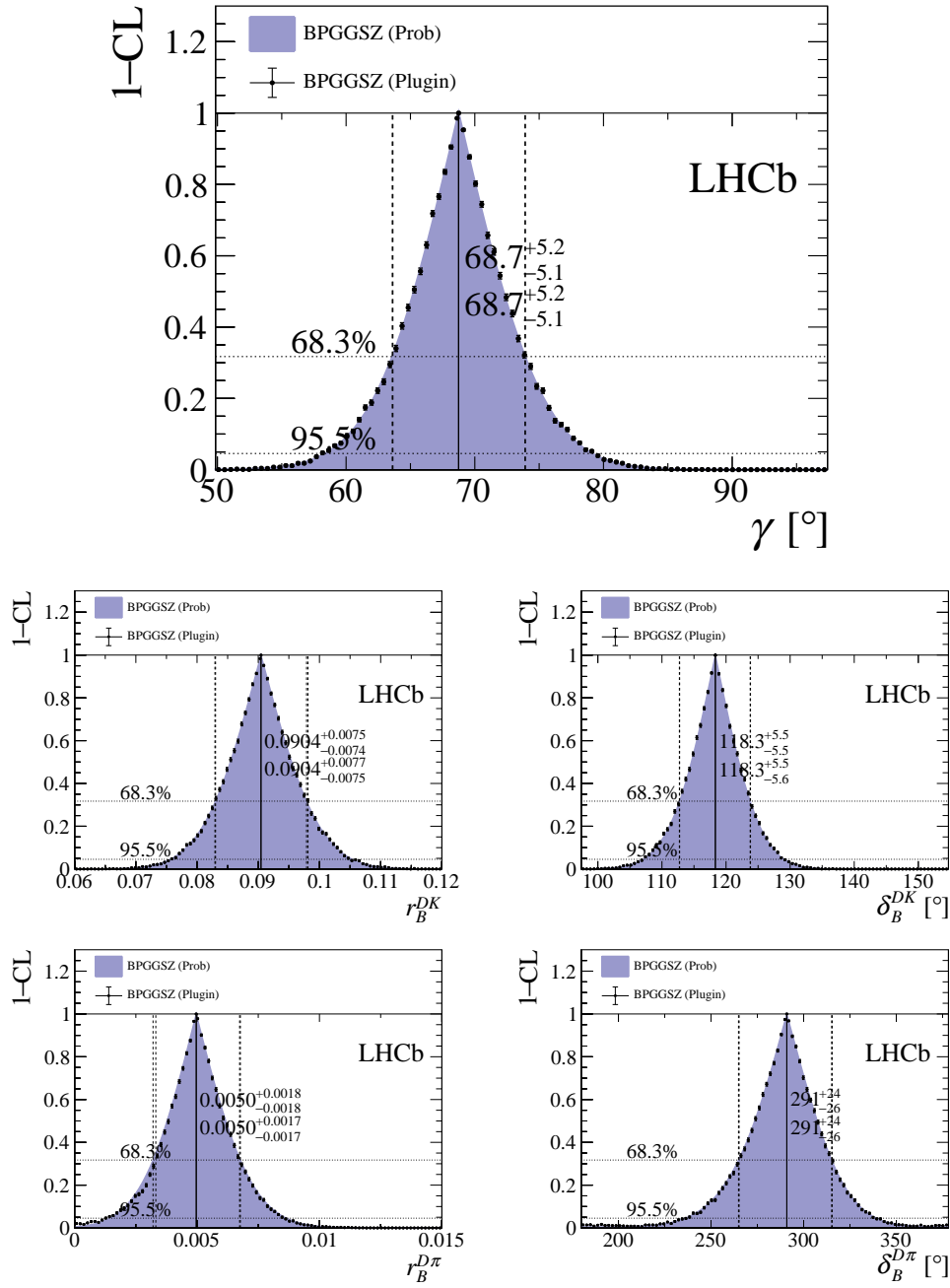


**Figure 5.49:** Confidence levels for the physics parameters of interest. The solutions are written on the plots, where the top number is given with PROB uncertainties and the bottom number with PLUGIN uncertainties.

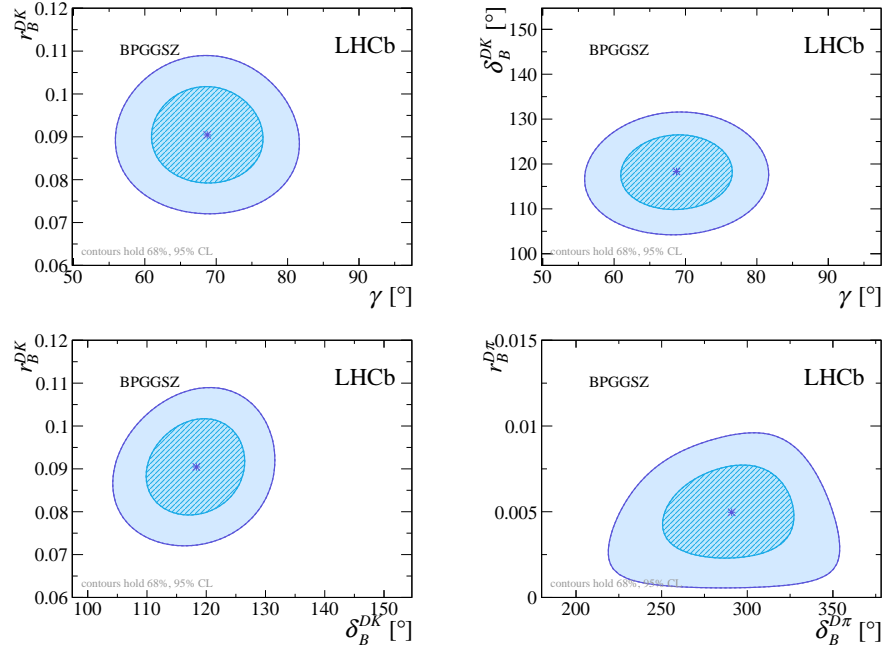


**Figure 5.50:** The 68 % and 95 % confidence regions for combinations of the physics parameters of interest, as obtained from the results of this measurement. The regions are calculated via the PROB method of gammacombo.

**Figure 5.51:** Caption here

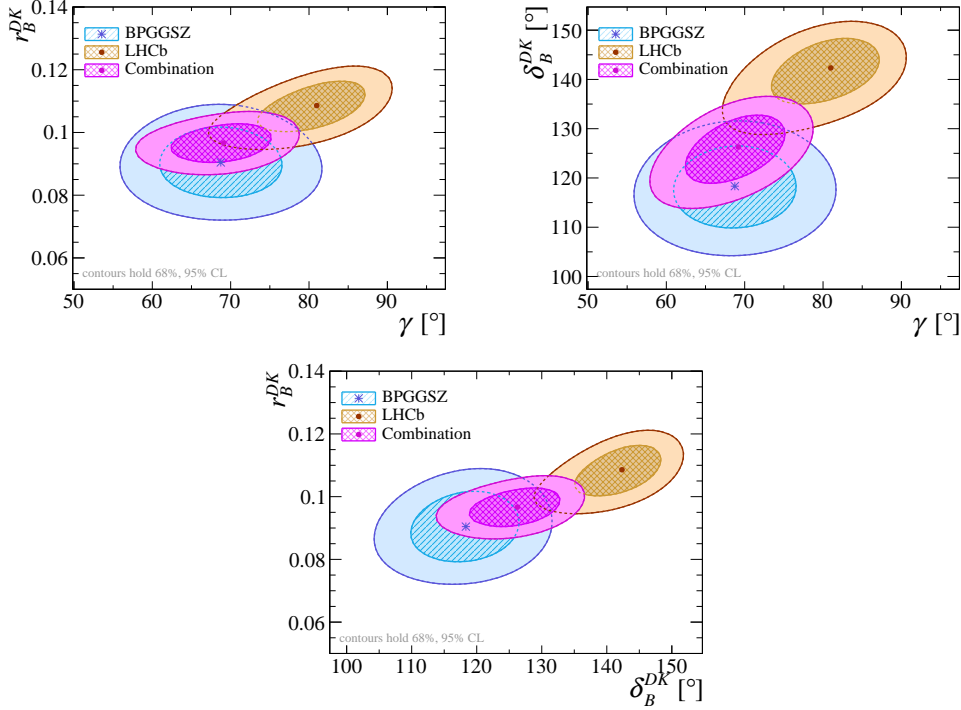


**Figure 5.52:** The 68 % and 95 % confidence regions for  $(\gamma, r_B^{DK\pm})$ ,  $(\gamma, \delta_B^{DK\pm})$ , and  $(\delta_B^{DK\pm}, r_B^{DK\pm})$  for this measurement, the 2018 LHCb combination [?] where the two-body ADS/GLW results have been updated to those from Ref. [?], and the combination thereof, calculated via the PROB method of `gammacombo`.

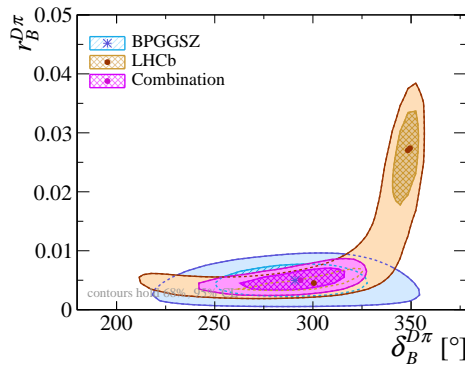


**Figure 5.53:** The 68 % and 95 % confidence regions for  $(\delta_B^{D\pi\pm}, r_B^{D\pi\pm})$  obtained from the results of this measurement, in the 2016 LHCb combination [?], and the combination thereof, calculated via the PROB method of `gammacombo`.

# 6

2727

2728

## Conclusions

2729 Say something clever

# Appendices

A

2731

2732

Projections of main fit to data